UNIVERSITÀ
DEGLI STUDI
DI PADOVA

UNIVERSITY OF PADOVA

CENTRE OF STUDIES AND ACTIVITIES FOR SPACE
"GIUSEPPE COLOMBO" - CISAS

Ph.D School in Space Sciences, Technologies and Measurements

Sciences and Technologies for Aeronautics and Satellite Applications

XXVIII Cycle

SIMULATION OF EUROPA'S WATER PLUME AND STRUCTURES RELATED TO ENERGETIC ACTIVITIES ON SOLAR SYSTEM BODIES FROM SATELLITE IMAGES

Ph.D School Director: Ch.mo Prof. Giampiero Naletto
Supervisor: Dr. Gabriele Cremonese
Co-supervisor: Ch.mo Prof. Francesco Marzari

Ph.D Student: ALICE LUCCHETTI

UNIVERSITÀ
DEGLI STUDI
DI PADOVA

UNIVERSITA' DEGLI STUDI DI PADOVA

CENTRO DI ATENEO di STUDI ed ATTIVITA' SPAZIALI - "GIUSEPPE COLOMBO" - CISAS

Scuola di Dottorato in Scienze Tecnologie e Misure Spaziali

Scienze e Tecnologie per Applicazioni Satellitari e Aeronautiche

Ciclo XXVIII

SIMULAZIONE DEL PLUME DI EUROPA E STUDIO DA IMMAGINI SATELLITARI DI STRUTTURE LEGATE A PROCESSI ENERGETICI SUI CORPI DEL SISTEMA SOLARE

Direttore Scuola di Dottorato: Ch.mo Prof. Giampiero Naletto
Coordinatore d'indirizzo: Ch.mo Prof. Giampiero Naletto
Relatore: Dr. Gabriele Cremonese
Correlatore: Ch.mo Prof. Francesco Marzari

Dottoranda: ALICE LUCCHETTI

"Quando ti metterai in viaggio per Itaca
devi augurarti che la strada sia lunga,
fertile in avventure e in esperienze.
I Lestrigoni e i Ciclopi
o la furia di Nettuno non temere,
non sarà questo il genere di incontri
se il pensiero resta alto e un sentimento
fermo guida il tuo spirito e il tuo corpo.
In Ciclopi e Lestrigoni, no certo,
nè nell'irato Nettuno incapperai
se non li porti dentro
se l'anima non te li mette contro.
Devi augurarti che la strada sia lunga.
Che i mattini d'estate siano tanti
quando nei porti - finalmente e con che gioia -
toccherai terra tu per la prima volta:
negli empori fenici indugia e acquista
madreperle coralli ebano e ambre
tutta merce fina, anche profumi
penetranti d'ogni sorta; più profumi inebrianti che puoi,
va in molte città egizie
impara una quantità di cose dai dotti.
Sempre devi avere in mente Itaca -
raggiungerla sia il pensiero costante.
Soprattutto, non affrettare il viaggio;
fa che duri a lungo, per anni, e che da vecchio
metta piede sull'isola, tu, ricco
dei tesori accumulati per strada
senza aspettarti ricchezze da Itaca.
Itaca ti ha dato il bel viaggio,
senza di lei mai ti saresti messo
sulla strada: che cos'altro ti aspetti?
E se la trovi povera, non per questo Itaca ti avrà deluso.
Fatto ormai savio, con tutta la tua esperienza addosso
già tu avrai capito ciò che Itaca vuole significare."
(Itaca, K. Kavafis)

Sommario

Il lavoro di tesi è focalizzato sull'analisi di processi fortemente energetici che agiscono e caratterizzano le superfici dei corpi del Sistema Solare (pianeti, satelliti e corpi minori), influenzandone anche l'ambiente circostante. Gli argomenti principali sviluppati in questo lavoro sono i seguenti: (i) simulazione e analisi della fisica dell'impatto su superfici planetarie, (ii) lo studio dei processi di frammentazione responsabili dell'origine dei molteplici massi presenti sulla superficie della cometa Churyumov-Gerasimenko 67P, e (iii) la caratterizzazione di fenomeni transienti che si manifestano sul satellite gioviano Europa, in particolare l'analisi di possibili "plumes" generati da fenomeni criovulcanici e lo studio accurato dell'ambiente esosferico.

Il primo tema affrontato è l'analisi del processo di craterizzazione da impatto tramite simulazioni numeriche, in quanto gli shock code rappresentano il miglior mezzo per esplorare condizioni non raggiungibili in laboratorio e capire quali siano le variabili maggiormente responsabili agenti della formazione del cratere. In questa tesi l'hydrocode iSALE è stato utilizzato per simulare due strutture di impatto presenti su due pianeti del Sistema Solare, Mercurio e Marte. Nel primo caso, la simulazione e analisi del cratere ha permesso di ottenere maggiori informazioni riguardo l'origine di una struttura conica circondata da materiale piroclastico, identificata dalle immagini acquisite dalla sonda MESSENGER (MErcury Surface, Space ENvironment, GEochemistry, and Ranging). Nel caso Marziano, invece, la simulazione numerica del cratere Firsoff, localizzato in Arabia Terra, ha permesso di capire quali siano i processi post-impatto che hanno determinato l'attuale morfologia del cratere e quale sia la struttura reologica caratterizzante quella regione. Dai risultati provenienti da entrambe le applicazioni emerge che la simulazione numerica dei crateri di impatto sia un importante e potente strumento per migliorare la conoscenza del Sistema Solare.

Il secondo argomento è stato sviluppato dopo l'inserimento in orbita di Rosetta attorno alla cometa 67P. Diversi processi energetici, come la sublimazione, frammentazione, outburts e crolli gravitazionali, sono stati considerati al fine di spiegare la genesi dei massi cometari, che si trovano ovunque sulla superficie. Per uno studio dettagliato dell'argomento sono state utilizzate le immagini acquisite dagli strumenti OSIRIS (Optical, Spectroscopic, and Infrared Remote Imaging System) e CIVA (Comet Infrared

and Visible Analyser), che sono le camere a bordo della sonda e del lander rispettivamente. I massi presenti sulle immagini sono stati analizzati quantitativamente, in termini di distribuzione in dimensioni, per comprendere quali siano i processi energetici che li generano e, in particolare, per determinare se tali processi avvengano ugualmente sulla cometa indipendentemente dalla scala spaziale considerata (m, cm, mm). A tale scopo, sono state ottenute le varie distribuzioni per i seguenti massi: (i) massi con un diametro maggiore di 7 m, (ii) massi con un diametro maggiore di 1 m (dall'analisi del sito Abydos, che è il luogo dove si suppone sia Philae) e (iii) grani (strutture su scala del mm-cm) presenti sulle immagini di CIVA.

Nell'ambito della missione futura ESA/JUICE e del nostro forte coinvolgimento nella camera JANUS (Jovis, Amorum ac Natorum Undique Scrutator), l'ultimo tema affrontato è incentrato sul satellite ghiacciato Europa. La presenza di un oceano subsuperficiale all'interno di Europa è un argomento di primaria importanza e, in aggiunta, la recente osservazione del plume al polo sud tramite le osservazioni di HST, ha alimentato le domande riguardanti l'interazione tra la subsuperficie, la superficie e l'ambiente circostante. In questo contesto, il primo obiettivo è stato quello di generare una simulazione che rappresentasse un possibile deposito di un plume generato da fenomeni criovulcanici, in modo da definire in quali condizioni l'evento sarebbe osservabile da JANUS durante i flybys di Europa. Inoltre, dato che lo studio dei "plume" necessita di un'accurata caratterizzazione dell'esosfera, è stato realizzato un dettagliato calcolo dei tassi di perdita dell'esosfera di Europa in relazione ai processi di ionizzazione e dissociazione per impatto di elettroni, di scambio di carica e di fotoionizzazione.

Abstract

This PhD thesis focuses on the analysis of different high energetic processes that affect the surface of planets, satellites and minor bodies as well as modify their surrounding environment. Specifically, this work concerns three main topics: (i) the simulation and analysis of one of the most geological energetic process, i.e. impact cratering; (ii) the investigation of the fragmentation processes that could have generated boulders on comet Churyumov-Gerasimenko 67P; (iii) the analysis of a possible transient plume originating from cryovolcanic events on Europa, the Jovian icy satellite, combined with an accurate characterisation of its exospheric background.

The first topic addresses the investigation of the impact formation process through numerical modelling. Shocks code represent the most feasible method for studying impact craters, as they can simulate a large span of conditions beyond the reach of experiments (e.g., velocity, size). The iSALE hydrocode was used to simulate two different impact structures located on Mercury and Mars. On Mercury, the simulation allows to determine the genesis of a particular landform, i.e. a steep-sided cone with associated pyroclastic deposits, which was revealed by images acquired by MErcury Surface, Space ENvironment, GEochemistry, and Ranging (MESSENGER) spacecraft. On Mars, the simulation of the Firsoff crater in Arabia Terra permits a better understanding the subsequent geologic processes that led to crater post modification, defining which rheological structure is more likely in that region. In both cases, we conclude that the numerical modelling of impact process is a powerful tool to improve the comprehension of the Solar System.

The second topic of the thesis has been developed after the Rosetta mission got inserted around the comet Churyumov-Gerasimenko 67P. We investigated the surface of comet Churyumov-Gerasimenko 67P focusing on the possible energetic events that lead to the formation of boulders; i.e. blocks that are ubiquitous on the surface of the comet. Different energetic formation processes were invoked to explain the presence of boulders, such as sublimation, fragmentation, outbursts and gravitational falls. Using images acquired by OSIRIS (Optical, Spectroscopic, and Infrared Remote Imaging System) and CIVA (Comet Infrared and Visible Analyser) cameras on board the spacecraft and the lander respectively, a quantitative analysis of different-size boulders has been performed

in order to understand if the same energetic formation processes occur equally on different scales on the comet (m, cm and mm). Specifically, by means of different resolution images, we obtained several size-frequency distribution for: (i) boulders larger than 7 m, (ii) boulders larger than 1 m from higher resolution images used to analyse the Abydos site, the location where Philae is supposed to be, and (iii) pebbles (mm-scale structures) visible on CIVA images.

The third topic is the icy satellite Europa in view of the future ESA/JUICE mission and because of our involvement in JANUS (Jovis, Amorum ac Natorum Undique Scrutator) visible camera. The presence of a subsurface ocean is a primary topic on Europa, in addition the recent discovery of a transient plume at the south pole by HST observations has raised many questions regarding the interaction between the subsurface/surface and the outer environment of Europa in terms of active processes affecting the icy surface. In this context, a possible plume deposit originating from cryovolcanic events was simulated to understand its detectability by JANUS camera during the Europa flyby phase of the JUICE mission. In addition, since the study of transient plumes has as a mandatory prerequisite an accurate characterisation of the exospheric background, a detailed study of the loss rates of Europa's tenuous atmosphere was performed. In particular, loss rates for electron impact dissociation and ionization processes, for charge-exchange (considering plasma torus, pick up and ionosphere ions) and for photo processes (for both cases of quite and active Sun) were calculated.

Acknowledgements

Working on the PhD has been an amazing and often overwhelming experience. When I started I was not even suspecting of how much I would have grown up either professionally and humanly during the following three years. Such an endeavour is time consuming and is not possible without persistence, perseverance, assistance, support, and encouragement of some inspiring people that in one way or another helped me and made my PhD an unforgettable period.

Foremost, I would like to express my sincere gratitude to my advisor Dr. Gabriele Cremonese for the continuous support of my PhD study and research, for his patience, motivation and enthusiasm. Thank you for trusting me and for giving me wonderful opportunities during these years. I would like to thank my co-advisor Prof. Francesco Marzari for his suggestions and constant help to solve our computer problems. Special thanks to Prof. Matteo Massironi for his precious help, support, encouragement, enthusiasm in sharing his vast knowledge, and the many conversations, as enlightening as always. I would like to acknowledge Prof. Nick Schneider for introducing me to Europa, for all your support and motivation. I have been so lucky to met you, you have been always active interested in my work and available to advise and help me. It gives me great pleasure to acknowledge to valuable suggestions, constructive criticism and incredible patience of Dr. Christina Plainaki. Thank you for gave me the opportunity to become part of the ISSI project and for your continuous support, motivation and scientific excitement. I would like to thank Prof. Francois Poulet for allowing me to spend a period in Paris, working there has been a great pleasure and has been important for my professional growth.

The thesis would not have come to a successful completion, without the precious help and support of all my colleagues, astronomers, geologists and engineers. They contribute in making the office such a stimulating, lively ad friendly place. They are friends more than colleagues, a special thank to Cristina for our friendship, for making office days funnier and for being always here for me, to Emanuele for his wise suggestions and patience, to Riccardo for being my favourite geologist. Thanks also to all MAPS group for being a wonderful research team!

I would like to acknowledge my flatmates, by now we could define us as a strange

family. I thank Andrea and Pamela for supporting me, but also for standing me. I enjoy my days here thanks to you. An additional thanks to Pamela with I'm sharing all the best and bad moments of my life since 8 years, thank you for our beautiful friendship.

I would like to thank my friends, in Padova and at home, and all the people I have met during this period because everyone enriched and helped me to grew and become what I am now. I would like to thanks all astronomers, in particular Andrea, Alessandra and Rosamaria, and friends that have been an important presence in my life or even in a part of my life, Galli, Allison, Teo, Alex, Cami. Special thanks to Paola, you have always trusted in me, supported my ideas and decisions and helped me to make the better choices of my life, you are a fantastic friend and I hope that your wise advices will be always with me. Thanks to Carolina, for her madness, for enjoying me with her amazing news and for being always present for me. Big thanks to friends that will be always part of my life despite the distance and years, India and Serena. I am sure that the stars will always watch over our friendship.

I would like to thank my family for all their unconditional love, endless encouragement and confidence in me. Words cannot express how grateful I am to my parents for all of the sacrifices that you have made on my behalf. Without my family I would never have been able to reach for my dreams. I would like to thank my brother Jacopo and Cristina for their constant presence and for helping and supporting me in any situation. Big thanks also to all my family, grandmothers, aunt, uncle and cousins because they have always kept me smiling.

Last, but not least, thanks to Maurizio for being on my mind most of the time and brightening up my day. Thank you for all your love and trust that you put into my work and me as a person. Often only your motivating words and your faithful and solid character gave me the motivation and the inner force to fulfil the expectations that people had for my work. Thank you for always being there especially during the hard times, for all your support, your warmth and for this big and amazing adventure of ours. For this and so much more, I love you!

Contents

List of Figures

List of Tables

Introduction

The subject of this PhD thesis is to analyse different structures and phenomena caused by high energetic processes that are present on Solar System bodies. Such processes affect the surface of planets, their satellites and of minor bodies modifying their surrounding environment too. In this work, we will focus on specific processes and planetary features visible by means of spacecraft images. Energetic processes act on the surface of all bodies, but the resulting features may be different. The first process here considered is impact cratering, i.e. one of the most energetic geological process. A hypervelocity impact crater is a structure resulting from the collision of a projectile with another body. It begins with the first contact of the two bodies and ends up with the final motions of debris around the crater (Melosh, 1989; Melosh & Ivanov, 1999; French, 1998). Impact cratering is a complex process that depends on several factors, such as the size, the velocity and the composition of the impacting body, as well as the gravity and the physical properties of the target, such as porosity and strength. It follows, that the study of impact craters offers a tool to investigate the subsurface structure and composition of the considered bodies. The current understanding of impact craters combines both observational data and computer simulations. The use of hydrocodes has allowed the investigation of the impact process on planetary scales because it can simulate conditions beyond the reach of experiments (e.g., velocity, size) and it allows an investigation of the complexity of crater collapse on a planetary scale. Within this frame, we made use of the iSALE hydrocode, which is a code used for modelling highly dynamic events, and in particular the propagation of the shock wave as well as the behaviour of geologic materials over a broad range of stress and deformation states. We simulated different impact craters on rocky bodies (Mercury and Mars) using both satellite images and the derived Digital Terrain Model. Indeed, by means of DTMs, we can provide the morphology of a crater, deriving its profile, that we consequently use for comparison with our output model. The impact crater simulations performed in the first chapter of the thesis are summarized as follows:

- Mercury case study: we analyse a particular landform on the Hermean surface. Images acquired by the MErcury Surface, Space ENvironment, GEochemistry, and Ranging (MESSENGER) spacecraft have shown a conical structure, surrounded

by a trough, lying at the centre of a large 23.000 km^2 diffuse-margined spectral anomaly that is brighter and red-sloped when compared to the Hermean average;

- Mars case study: the aim of simulating an impact process on a complex environment such as the Martian surface provides information about how different impact conditions (e.g., different impact velocities and compositional scenarios, thickness of the megaregolith) affect the crater formation but also gives an estimate of the post-impact modification processes entity. We present a numerical model for the formation of the Firsoff crater (90 km of diameter) which is a strongly degraded crater located in the equatorial southern highlands of Arabia Terra, thought to be an area of intense water interactions and subsequent modifications;

Assuming that all the Solar System bodies have been interested by impacts, we then focus our attention on Solar System minor bodies, in particular on comet Churyumov-Gerasimenko 67P. Since the arrival of the Rosetta mission on comet 67P, we decided to analyse its changeable surface through the images acquired by OSIRIS (Optical, Spectroscopic, and Infrared Remote Imaging System) instrument, the camera on board the Rosetta mission in which our team is involved. Material properties and images coming from OSIRIS reveal that no well-defined impact craters are present on its surface, but there are other features that are ubiquitous on the surface of this comet. These features, called boulders, are positive relief detectable in different images with the constant presence of an elongated shadow and seem to be detached from the ground where they stand. Previous studies of boulders, found on asteroids and planets, are usually related to impacts because they represent the largest fragments excavated by the collision which do not reach the escape velocity. For the specific case of 67P, the impact formation process is not sufficient to explain the presence of boulders since current collision rates for comets are very low and would imply that most blocks were created very early in the history of the comet. Nonetheless, this is very unlikely because of the activity of comet surface and because of comet lifetimes. Hence, it is reasonable to discard the impact origin for the boulders, and invoke other processes. Therefore, in the second chapter we focus our attention on the possible energetic formation processes that generate detached blocks. Firstly, we obtained the first size-frequency distribution of boulders on a comet analysing their spatial distribution and performing global and localized studies. After that, we described in detail the Abydos site, the location where the lander Philae is supposed to have come to rest, performing the boulder analysis by means of OSIRIS and CIVA images (the panoramic cameras on board the lander Philae). The latter, revealed a rough terrain dominated by fractures and agglomerates of consolidated materials, called pebbles, whose origin is still debated and very intriguing. A quantitative analysis of these structures was performed in order to compare the different distribution in order to correlate them and understand if the same energetic formation processes occur equally on different scales on the comet (m, cm and mm).

In the third chapter we focus on the outer part of the Solar System in view of the future JUICE/ESA mission and of our involvement in JANUS (Jovis, Amorum ac Natorum Undique Scrutator) camera. Specifically, we studied Europa, the icy satellite of Jupiter, that will be observed by two flybys during the mission. One of the objectives of JUICE is to explore for the first time the subsurface of Europa in the most recent active regions to understand the exchange processes from the subsurface to the surface and also to constrain the minimal thickness of the ice shell in the most active regions (ESA, 2014). JUICE will search and study present and/or recently active processes too considering that their manifestation can be found both on the moon's surface and in its atmosphere (plumes) and the ionosphere. The presence of a subsurface ocean is a primary topic on Europa, in addition the recent discovery of a transient plume at the south pole by HST observations (Roth et al., 2014b) has raised many questions regarding the interaction between the subsurface/surface and the outer environment of Europa in terms of active processes affecting the icy satellite. Therefore, in the third chapter we focused on different topics related to the presence of a subsurface ocean in order to achieve further information about the satellite and to support the observation planning of JUICE/JANUS. Firstly, we study the possible plume deposit that could be formed by cryovolcanic events. Indeed, spacecraft have observed plumes erupting from the geologically young surfaces of Io and Enceladus and, since Europa possesses a relatively young surface too, it has been proposed that many of its surface features are the result of material emplaced via ballistic cryovolcanism (i.e. plumes). These plumes have been long hypothesized but they were never directly observed until recent discoveries. In fact, a transient endogenic H_2O exosphere source, consistent with two 200-km-high plumes of water vapour, was recently discovered through the analysis of HI Lyman-α 1215.67 Å, OI 1304 Å and OI 1356 Å data obtained with HST/STIS (Roth et al., 2014b). On the other hand, in previous works, as in Fagents et al. (2000), ballistic cryovolcanism has been considered and modelled as a possible mechanism for the formation of low-albedo features, surrounding lenticulae and along triple band margins and lineae, on Europa's surface. In this context, we model a possible plume deposit originating from cryovolcanic events on Europa to understand if this feature could be observable by the JANUS camera during the flybys phases.

Furthermore, the study of the transient plumes, with their potential implications on the nature of the moon's inner ocean, will have as mandatory prerequisite an accurate characterisation of the exospheric background. For this reason, we performed a detailed study of the Europa's tenuous atmosphere loss rates on the basis of updated plasma condition in the vicinity of Europa (Bagenal et al., 2015). We studied the loss rates of the main components of Europa's tenuous atmosphere (O_2, H_2O, H_2), on the basis of energy-dependent reaction cross sections found in literature, and we then performed calculations for electron impact dissociation and ionization processes, for charge-exchange

(considering plasma torus, pick up and ionosphere ions) and for photo processes. This work is inserted into an ISSI international project, with the following title: "Towards a global unified model of Europa's exosphere in view of the JUICE mission", in which I am involved as a young scientist.

Finally, the summary of the results obtained will be presented in the Conclusion section, reporting possible future works that will be performed in next future.

Chapter 1

Impact craters

Impact cratering process is one of the most energetic geological process affecting planetary surfaces. Every body in the solar system has been subjected to the impact of objects such as comets, asteroids, or accretionary debris. This complex process depends on several factors (such as the size, the velocity and the composition of the impacting body, as well as the gravity and the physical properties of the target) and its study offers a tool to investigate the subsurface structure and composition of the planetary surfaces under investigation. In this context, observational data are usually coupled with computer simulations to better understand the impact cratering process.

In this chapter, after an overview of the impact cratering process and of the morphology of impact structures, we describe how numerical modelling works and, in particular, we focus our attention on the iSALE hydrocode. Then, we report two different numerical modelling application on rocky bodies (Mercury and Mars) using satellite images. Indeed, by using Digital Terrain Models (DTMs) generated through Mercury and Mars imagery, we can analyse in deep detail the geological context of what we are studying and obtain the crater profile that we use for comparison with our output model. On Mercury we analyse a particular landform revealed by images acquired by the MErcury Surface, Space ENvironment, GEochemistry, and Ranging (MESSENGER) spacecraft, while on Mars we present a numerical model for the formation of the Firsoff crater (90 km of diameter), which is a strongly degraded crater located in the equatorial southern highlands of Arabia Terra.

1.1 Impact crater morphology

The size of an impact crater depends not only on the amount of energy released by the impact, but also on the gravity field of the planet or satellite, and certain properties of the projectile and surface rocks. A crater is many times larger than the projectile that originated it, but, given the impact crater size, a larger crater will be created on a

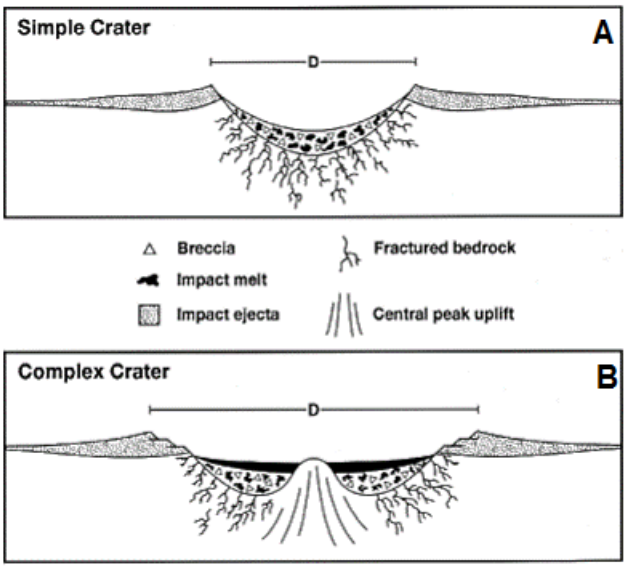

Figure 1.1: Schematic profiles of a typical A) simple crater and B) central peak crater. The breccia lenses are composed of a mix of impact melt and fragments of target rock.

planet with a weaker gravity field because it is easier to excavate the material. Impact structures follow a morphological progression as crater size increases (Figure 1.1) and they can be divided into three distinct groups: simple craters, complex craters and multi-ring basins.

1.1.1 Simple Craters

Simple craters are the most basic crater form (Figure 1.2). They are characterised by a smooth, bowl shape and a depth-to-diameter ratio of 1:3 - 1:5 (Melosh, 1989; Melosh & Ivanov, 1999). The slope of the crater wall is steepest close to the rim, decreasing in slope angle smoothly towards the crater centre forming an almost parabolic profile to the crater (Dence, 1973). As collapse of small cavities is governed by the internal friction of the target rocks, simple craters display an average rim slope roughly equal to the angle of repose of the target material ($\sim 25° - 30°$) independent of gravity (Melosh, 1989). The crater rim is elevated above the original surface topography by 4% of the crater diameter (Melosh, 1989) because of stratigraphic uplift and ejecta deposition. Fractured and melted target rock, which has fallen off the crater walls, creates a breccia lens inside the crater which overlays fractured country rock. There is no theoretical lower limit to the simple craters size, providing that the target has no significant cohesive strength and the impactor is travelling at a velocity greater than a few kilometres per second at the time of impact (Melosh, 1989). In reality, however, the minimum simple crater size is a function of the ability of the atmosphere to absorb small meteors. The upper limit to the size

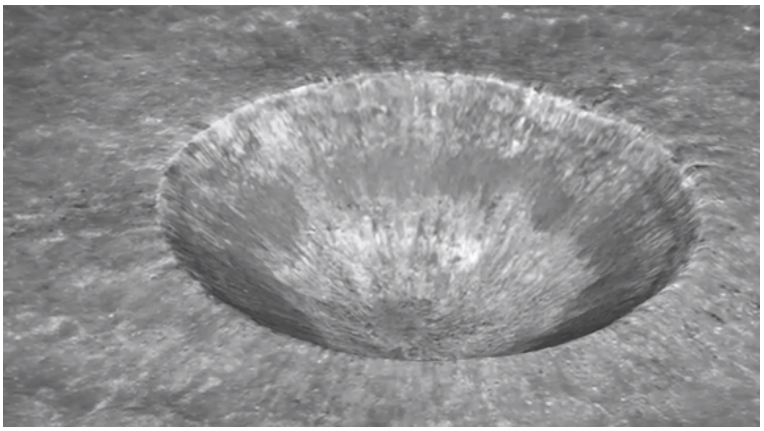

Figure 1.2: The Moon's Linné Crater is an example of a young and beautifully preserved simple crater. Image credit: NASA/GFSC/ASU.

of a simple crater occurs when the crater's morphology changes, becoming "complex". This modification, termed the simple-to-complex transition, occurs at different crater diameters on different planetary bodies. Simple craters begin the transition at a size which appears proportional to 1/g, where g is gravity (Figure 1.3): an higher transition diameter corresponds to a lower planetary surface gravity. The transition diameter is between 2-4 km on Earth, 5-10 km on Mars and 15-20 km on the Moon (Pike, 1988). The range in the transition diameters suggests that relative changes in target strength over the body could have some influence on crater formation. For example, on the Earth, the simple-to-complex transition diameter is ~ 2 km in sedimentary targets and ~ 4 km in crystalline targets (Grieve, 1987), while on the Moon central peak craters began at smaller diameters in mare units than in highland ones (Cintala et al., 1977).

1.1.2 Complex craters

Central-peak craters, which form above the simple to complex transition diameter, are typified by a dome sticking out from the centre of the crater, the central peak. The diameter of the central peak (D_{cp}) increases with crater diameter (D) (Pike, 1985) according to the following relationship: $D/D_{cp} = 0.22$. There is an area of relatively flat topography surrounding the central peak (located between the central peak and crater rim) that consists of a depression filled in by breccia. Terraces, which are defined as marginal collapse zones, are evident on the crater wall, where unstable material from the crater rim has collapsed towards the crater's interior. The lack of breccia in the central peak itself indicates that the uplift of the central region occurs rapidly, before debris has had time to slump in from the crater walls (Melosh, 1989). The depth of complex craters increases modestly with increasing diameter: Pike (1977) found that lunar complex craters has a depth-diameter ratio equal to 0.3, result that is in agree-

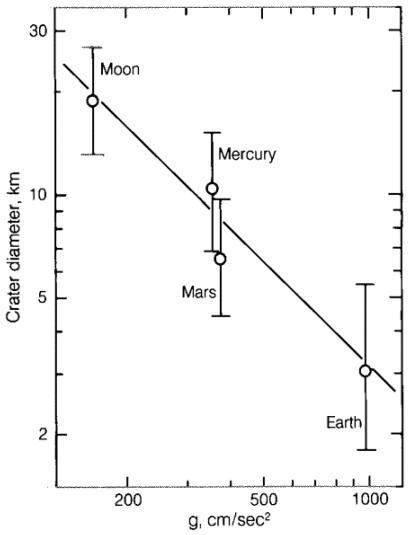

Figure 1.3: The simple to complex crater transition diameter for the Earth, Moon, Mercury, and Mars (data from Pike (1988), after Melosh (1989)).

ment with the depths of complex craters on Mercury and Venus. The morphology of the central peaks depends as well on crater dimension (Figure 1.4). At lower impact crater size, only one peak forms. At larger size, the central peaks complex begins to break up and an inner concentric ring of irregular mountain peaks develops, which is roughly half the rim-to-rim diameter (e.g. Melosh & Ivanov, 1999). During this transition, craters can have central peaks, peak-rings or both. Hartmann & Wood (1971) class craters that show both a peak and inner ring as "central peak basins". Craters with this "transitional" morphology are observed on the Moon, Mars and Mercury (McKinnon & Alexopoulos, 1994).

1.1.3 Multiring basins

The largest form of impact structures are called multi-ring basin (sometimes referred to as basins), which possess at least two asymmetric, inward-facing scarped rings, one of which may be the original crater rim (Hartmann & Wood, 1971; Spudis et al., 1984). Within the main crater rim, basin structure can resemble a peak-ring crater, though basins appear to lack the terrace structures of complex craters because covered by ejecta (Urrutia Fucugauchi & Pérez Cruz, 2009). This impact morphology does not seem to be originated by the same collapsing process of peak ring craters, since it does not follow the 1/g dependence (Melosh, 1989) suggesting that the rheological conditions of the target are important for their formation. In fact, multi-ring basins are likely to be affected by differences in crustal structure and composition (Melosh & McKinnon, 1978). Hartmann & Kuiper (1962) discovered that the spacing of adjacent rings occurs frequently in the

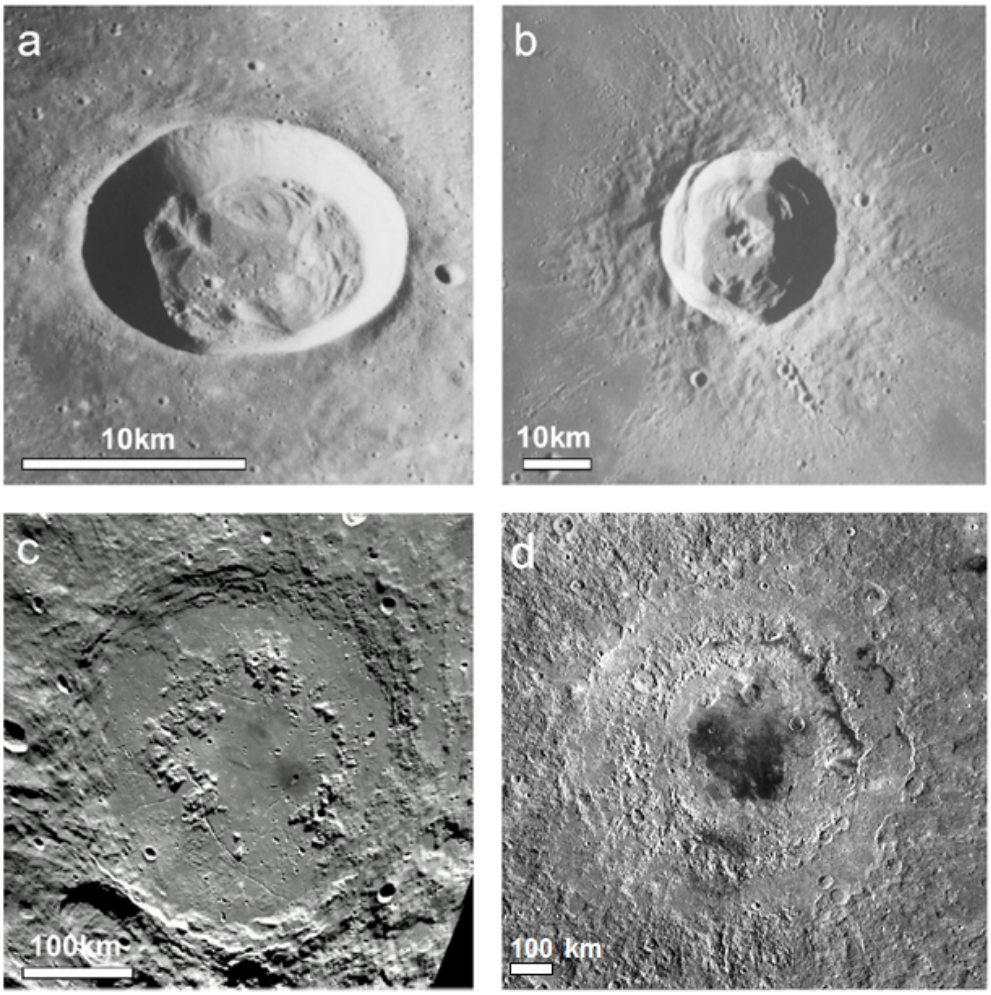

Figure 1.4: Progression of increasing crater sizes on the Moon: (a) Bessel, a 16 km impact crater belonged to the transition range from simple-to-complex morphologies (Courtesy of NASA, Apollo database (AS15-9328)), (b) Euler, a 28 km diameter central peak complex crater (AS17-2923), (c) Schrodinger, a 320 km diameter peak ring crater (mosaic of Clementine images processed by Ben Bussey, LPI), (d) Orientale, a 930 km diameter multi-ring basin (mosaic made from Wide Angle Camera images from NASA's Lunar Reconnaissance Orbiter Camera).

ratio of about $\sim$ 2:1, even if the validity of this geometric spacing remains unclear. The exact morphology of multi-ring structures varies spatially and on different bodies when compared to the typical basin morphology recorded for the Orientale basin on the Moon (Wieczorek & Phillips, 1999).

1.2 Impact cratering process

A hypervelocity impact crater is a structure resulting from the collision of a projectile with another planetary bodies, beginning with the first contact of the two bodies and ending with the final motions of debris around the crater (e.g. Melosh, 1989; French, 1998; Melosh & Ivanov, 1999). The impact formation process works through the propagation at supersonic velocity of a shock wave, i.e. a step-like discontinuity in pressure, density, particle velocity and internal energy (Melosh, 1989). Shock compression is a non–isentropic process (thermodynamically reversible) and results in the production of post-shock heat and in the melting or vaporization of the shocked material (Duvall & Fowles, 1963; Boslough & Asay, 1993). The energy transferred from the projectile to the target results in the motion of the material that begins to flow away from the impact site, against strength or friction forces and gravity. Although the impact process is continuous, it can be separated into three stages: contact of the projectile and compression of the rocks near the impact site, excavation of the crater and, finally, the modification of the impact crater driven by gravity, rock mechanics and erosion. (Figure 1.5).

1.2.1 Contact and Compression

The first stage of formation of a crater begins when the approaching projectile contacts the target surface at hypervelocity, i.e. at a velocity greater than the sound speed of the material (typically several kilometres per second or more). This process could be described as a kind of explosion due to the enormous kinetic energy supplied by the impactor. Upon impact, the impactor compresses the target material and accelerates it to a large fraction of the impactor velocity. Simultaneously, the projectile is rapidly decelerated. These velocity changes result in the formation of shock waves at the contact between the highly compressed and uncompressed material propagating away from the impact point, into both the projectile and target (Figure 1.6). Shock pressures developed during these early stages generally raise to more than 1 GPa (often reaching hundreds of GPa) (Okeefe & Ahrens, 1977). Once the shock wave reaches the back edge of the projectile, a release wave is produced which travels back through the projectile and into the target. During release, the projectile, which was heated during shock loading, may be melted and possibly even vaporised. The duration of the contact and compression stage is dependent on the size of the impactor, the velocity of the shock and its subsequent release wave in the impactor. After the rarefaction wave has reached the front end of

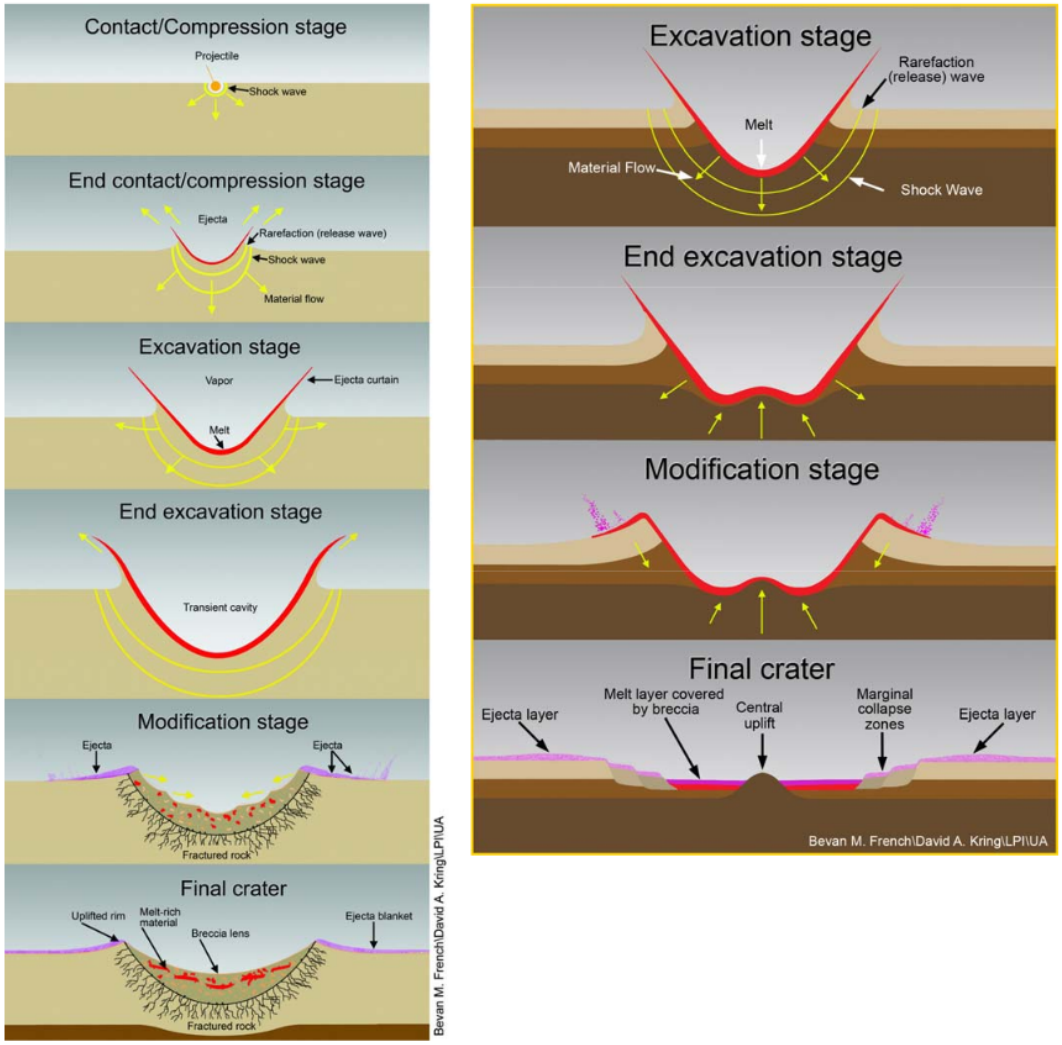

Figure 1.5: Cross-section diagrams showing the different stages of formation of an impact structure for both simple (left) and complex craters (right). The process begin with the so-called contact/compression stage, followed by an excavation stage that leads to the formation of the transient crater. The final stage of the cratering process is the modification stage that depends on the crater size. Image credit: French/Kring/LPI/UA.

the projectile and unloaded it completely, the projectile will play no further role in the formation of the impact crater, and the actual excavation of the crater is carried out by the expanding shock waves through the target rocks.

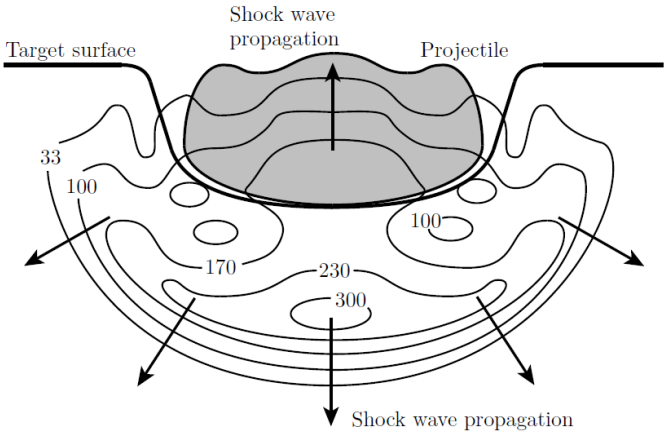

Figure 1.6: Schematic representation of the contact stage of an impact event. As the projectile (shaded grey) strikes the target surface, shock waves propagate into both the target and the projectile. Contours show the pressure levels in GPa, for a 15 km/s impact. Adapted from Melosh (1989).

1.2.2 Excavation phase

The excavation stage is characterised by two main processes: the shock wave and release wave expand through the target material, decaying in strength because of the larger area over which they are spread and because of irreversible losses involved in compressing material. This phase, which is dominated by complex interactions between the outward-directed shock waves and the downward-directed rarefaction waves with the target, leads to the formation of the so-called transient crater. Calculations and laboratory experiments suggest that on cessation of the excavation flow, the transient crater is approximately a parabaloid of revolution (Dence, 1973) with a depth-diameter ratio of between 0:3 − 0:4 (Melosh, 1989; Collins et al., 2002). During the excavation stage, the excavated material is deposited beyond the transient cavity rim, forming impact ejecta. Because the excavated zone contains material which has experienced a wide range of peak shock pressures, the ejected material may be a mixture of vaporised, melted, heated and fractured rock. The opening of the transient cavity stops when shock and rarefaction waves are not energetic enough to eject material beyond the cavity rim. The transient crater, typically 20-30 times larger than the projectile diameter (e.g. French, 1998), shows an uplifted rim. The entire excavation stage takes seconds to minutes to be completed, depending upon the crater size. About 6 seconds are nec-

essary to excavate a 1-km-diameter crater, while a 200-km-diameter crater is excavated in about one minute and thirty seconds (Melosh, 1989; French, 1998). After this, the forces retarding the excavation flow begin to collapse and modify the transient crater. Formation of the transient crater marks the end of the excavation stage; if the growth of the crater is driven purely by gravity, the timescale of excavation can be approximated by $\sqrt{H_f/g}$, where H_f is the depth of the transient cavity and g is gravity.

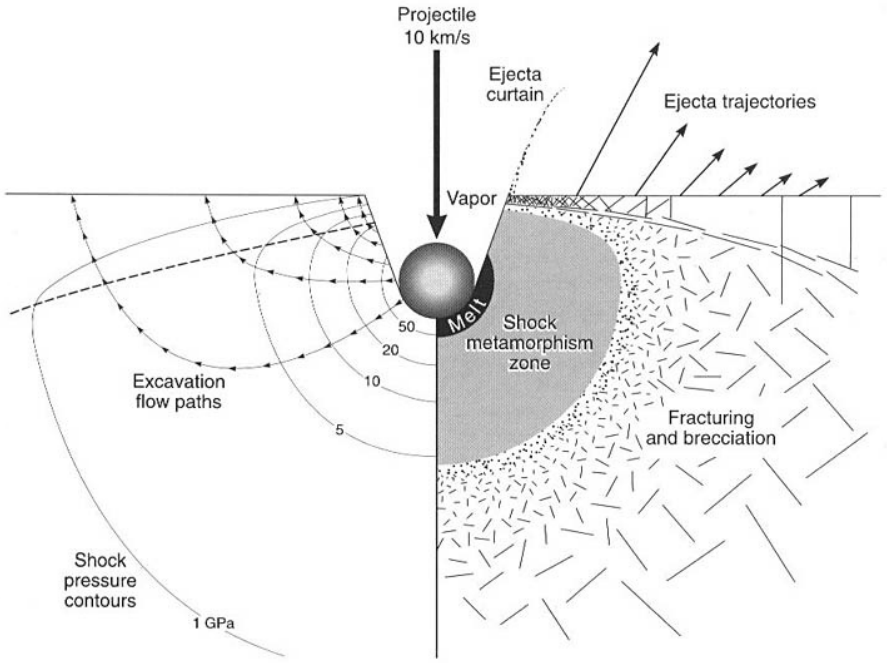

Figure 1.7: Illustration of the impact site during the excavation stage. Adapted from Melosh (1989).

1.2.3 Modification stage

The final stage of the cratering process is the modification stage. The collapse of the transient crater is dominated by gravity or target strength depending on the crater size. For smaller craters, the collapse is controlled primarily by the internal friction of the target rocks (Schmidt & Housen, 1987; Ivanov & Kostuchenko, 1998) and the main modification is the collapse of the upper crater walls. The simple bowl-shaped crater diameter may grow up to about 20% and it will be subjected to infilling from fallback ejecta and material slumping in from the walls and rim. The redeposited material form part of a breccia lens inside the crater. In larger impacts the collapse of the transient cavity is driven by the gravity of the target body rather than its material strength

resulting in complex morphology. The modification involves the formation of a central peak or rings and failure of the rim into wide zones of stepped terraces. The material motion during this stage results in a complex intermixture of breccia and impact melt inside the crater (Melosh, 1989). The timescale of the collapse may range from few tens of seconds to tens of minutes (for example the duration is few tents of seconds for 10 km diameter on Earth and nearly 10 minutes for 300 km diameter on the Moon), that is much shorter than most geological processes. After the collapse of the transient crater is complete, a last gravitational modification continue to shallower over geologically longer time periods leading to the leveling of the crater. This last process depends on crustal strength and crater size, for example the most prevalent process in post-impact modification on Earth is erosion of the exposed topography and infill of craters by fluvial or alluvial sediments (de Pater & Lissauer, 2001).

1.3 Numerical modelling: the iSALE hydrocode

The current understanding of impact cratering process combines both observational data and computer simulations. The use of hydrocodes has allowed the investigation of the impact process on planetary scales because it can simulate conditions beyond the reach of experiments (e.g., velocity, size) (e.g., Pierazzo & Collins, 2004) and it allows an investigation of the complexity of crater collapse on planetary scale (e.g., Collins et al., 2002). A hydrocode is a computer code used for modelling highly dynamic events, and in particular modelling the propagation of the shock wave as well as the behaviour of geologic materials over a broad range of stress states and deformation states (Anderson, 1987; Pierazzo & Collins, 2004). Over the last few decades, improvement of computer capabilities has allowed impact cratering to be modeled with high complexity and realism (Pierazzo & Collins, 2004).

This work uses the iSALE (impact Simplified Arbitrary Lagrangian Eulerian) hydrocode, a multirheology, multimaterial extension of the SALE hydrocode (Amsden et al., 1980), which was developed to model shock progression through geologic media (e.g., Melosh et al., 1992; Ivanov et al., 1997; Collins et al., 2004, 2011; Wünnemann et al., 2006). The original SALE code was capable of simulating only single-material, Newtonian-fluid flow; Melosh et al. (1992) implemented an elasto-plastic constitutive model in tandem with the viscous model, and incorporated the Grady-Kipp fragmentation algorithm and equation of state for impacts, including the Tillotson equation of state (Tillotson, 1962). Ivanov et al. (1997) advanced SALE's underlying solution algorithm by incorporating free surface and material-interface tracking in Eulerian mode, greatly improved the constitutive model by incorporating damage accumulation and strain-weakening, and implemented into the code the semy-analytical equation of state ANEOS (Thompson & Lauson, 1972). The result of these implementations was the first

extended release, now known as SALEB, capable simulating impact events from first contact of the impactor with the target, to cessation of the final gravity driven collapse of the crater (Ivanov, 2005; Ivanov & Artemieva, 2002). A second release, known as SALES-2, was improved to include a wider range of possible rheologic models and used to simulate impact crater collapse (Collins et al., 2002). Important improvements were incorporated in the iSALE release, such as the introduction of a third target material (Wünnemann & Ivanov, 2003), refinements to the constitutive model (Collins et al., 2004) and the inclusion of the $\epsilon - \alpha$ porous-compaction model (Collins et al., 2011; Wünnemann et al., 2006).

1.3.1 Hydrocode equations

Hydrocodes solve a set of equations to correctly describe the dynamics of continuous media and predict the material behaviour during the impact process. The first three differential equation are established through the application of the Newtonian law of physics, i.e. the conservation of mass, momentum and energy. In a reference frame that follows the material, these are (from Anderson (1987)):

$$Conservation\ of\ Momentum\ \frac{Dv_i}{Dt} = f_i + \frac{1}{\rho}\frac{\delta\sigma_{ji}}{\delta x_j} \tag{1.1}$$

$$Conservation\ of\ Mass\ \frac{D\rho}{Dt} + \rho\frac{\delta v_i}{\delta x_i} = 0 \tag{1.2}$$

$$Conservation\ of\ Energy\ \frac{DE}{Dt} = -\frac{p}{\rho}\frac{\delta v_i}{\delta x_i} + \frac{1}{\rho}\Sigma_{ij}\dot{\epsilon_{ij}}' \tag{1.3}$$

where v_i is the velocity, ρ is the material density, E is the specific internal energy and x is the position, f_i represents the external forces per unit mass, ϵ_{ij} is the deviatoric strain rate and σ_{ji} is the stress tensor, which is composed of a hydrostatic component, the pressure, P, and the deviatoric stress, Σ_{ij}. Subscriptes i and j refer to coordinate directions. To completely describe the response of material to deformation, two additional equations are needed. The first is an equation of state, that takes into account thermodynamic changes (e.g. heating via a shock event) and compressibility changes (e.g. increases in density under compression). The equation of state relates pressure to the density and internal energy and takes the following form:

$$P = P(\rho, E) \tag{1.4}$$

The second is a constitutive model that describes the effect of deformation (σ_{ji})(change in shape or strength properties) as a function of strain (ϵ_{ij}), strain rate ($\dot{\epsilon_{ij}}'$), internal

energy (E) or temperature (T) and damage (D).

$$\sigma_{ji} = g(\epsilon_{ij}, \dot{\epsilon_{ij}}', E, D) \tag{1.5}$$

1.3.2 Grid setup

Although Equations 1.1, 1.2 and 1.3 describe a material as a continuum flow, a computer is limited by a finite memory allocation. Therefore it is necessary to represent a continuous media as a mesh of elementary pieces, called cells. This process is known as discretization. In iSALE, the continuous media is approximated by a mesh of computational cells, that are defined by vertices connected by straight lines. For each cell, scalar quantities (e.g. pressure, density and mass) are assigned, while for each vertex vector, quantities are defined (for example velocity).

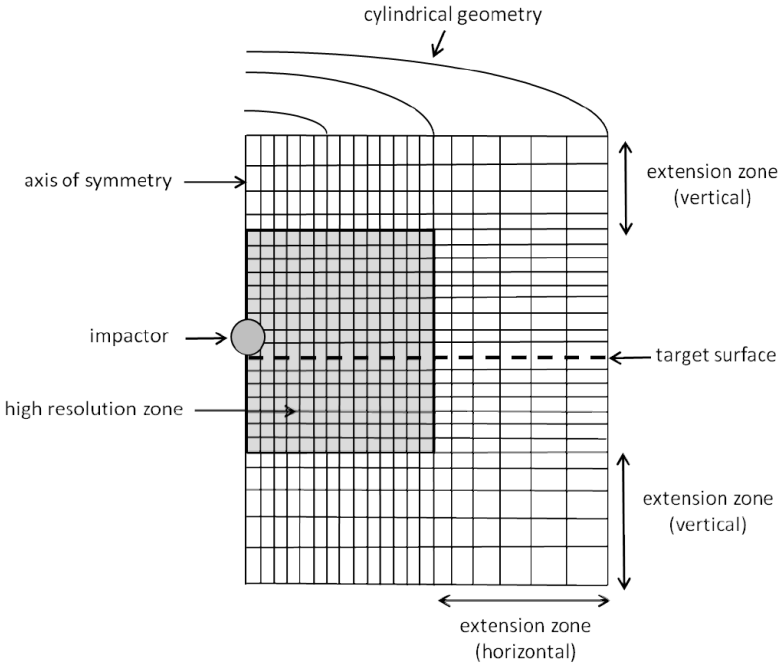

Figure 1.8: The computational mesh used in iSALE. Outside the high resolution zone (portion of the mesh within which the crater is likely to form), there is the extension zone useful to decrease computational time.

The two-dimensional coordinate system defined in iSALE is cartesian or cylindrical, even if a 3D dimensional version of iSALE has been developed and is currently being tested and validated (Elbeshausen et al., 2007). The iSALE computational mesh, which is schematically represented in Figure 1.8, consists of a central high-resolution zone, where the cell height and width are constant, that include the projectile and the portion of the mesh that is, normally, the zone in which the crater will form. Then, the mesh is

also characterised by an optional low resolution extension zones surrounding the high-resolution zone. In this part of the computational grid the cell height increases in a geometric progression away from the high-resolution. This low resolution part is needed to displace the mesh boundaries far away the cratering region and avoid the reflection effects from the boundaries (Collins et al., 2010).

Eulerian and Lagrangian method

The equation for motion for continuous media can be described by two different approach: Lagrangian or Eulerian, depending on the reference frame of the event (Figure 1.9). iSALE can utilize both representation as well a mixture of the two (Arbitrary Lagrangian Eulerian).

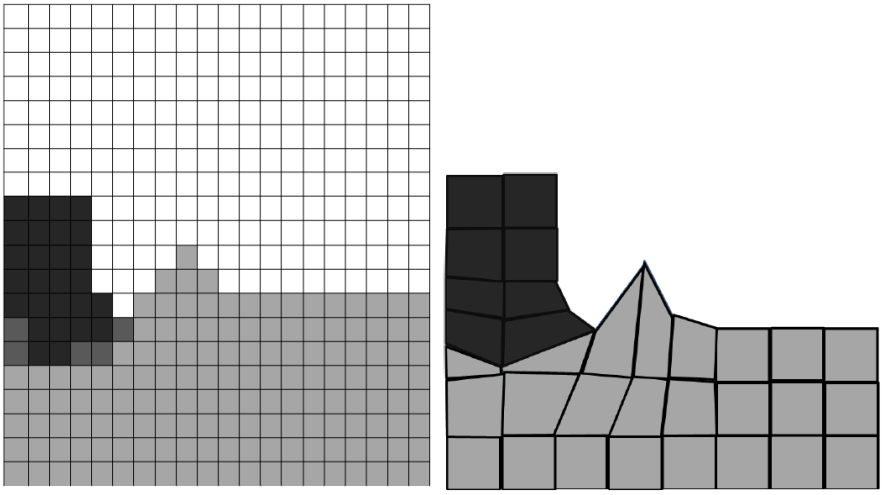

Figure 1.9: Comparison between the Eulerian (left) and Lagrangian (right) approach for a cylinder (dark grey) impacting a target (light grey). In the Eulerian method the computational mesh remains fixed and material moves between cells, while in Lagrangian method the material is fixed in the grid and the transport of material is calculated by the deformation of the cells. Image from Collins et al. (2010).

In the Eulerian description, the computational mesh is fixed in the space and the material flows between cells. This mass advection method makes it difficult to identify material interfaces at all times because leads to cell that contain a mixture of material or become partially filled. Determine with accuracy the material interfaces depends on the resolution of the mesh, therefore higher resolution of the mesh implies that the boundary is represented with more accuracy, but at the price of more computational zones (Pierazzo & Collins, 2004). This issue is not a problem for the Lagrangian method because the material is fixed in a computational cell and the transport of material is calculated by the movement and deformation of the whole grid in space. Free surfaces

and contact surfaces between different materials are easily determined, and remain distinct throughout the calculation (Pierazzo & Collins, 2004). The Lagrangian method provides a history of the material, whereas the Eulerian method can only record history at a fixed point. The major limitation for the Lagrangian method is the cell deformation, in fact cells can become highly elongated and, at extreme, can invert determining a physically impossible negative volume. A way to overcome the problem, again at the expense of accuracy in the determination of material interfaces, is to carefully rezone the computational grid, but it is a very time consuming process (Pierazzo & Collins, 2004). Hence, even if the Lagrangian method has advantages, all models shown in this work were carried out in the Eulerian mode of iSALE to avoid the inevitable extreme cell deformation.

1.3.3 Equation of state: Tillotson and ANEOS

Hydrocodes require the inclusion of an appropriate equation of state that describes the thermodynamic state of the material relating pressure to the temperature and density. The simple known equation of state is that of a perfect gas: $P = \rho RT$, where P is the pressure, ρ the density, T the temperature and R is the gas constant per unit mass. The equation of state for impact modelling is slightly different from the conventional EoS because of the strong interaction between the atoms (or molecules) of the medium. iSALE hydrocode support two different types of equation: parameters defining the Tillotson analytical EoS and data tables produced by ANEOS (e.g. Melosh, 1989).

The Tillotson EoS (Tillotson, 1962) is one of the most commonly used equations of state for impact modelling and was developed specifically for use in high-velocity impact simulations; it can be used over a wide range of pressures, densities and materials. The Tillotson EoS has two different formulations depending on the compression ($\rho/\rho_0 \geq 1$) or expansion ($\rho/\rho_0 \leq 1$) that the material experienced (taking also in account the vapour phase). When the material is compressed to a higher density with respect to its zero pressure form ($\rho/\rho_0 \geq 1$), the equation of state has the following formulation:

$$P = a + \left[\frac{b}{(E/E_o\eta^2) + 1}\right]\rho E + A\mu + B\mu^2 \tag{1.6}$$

where $\eta = \rho/\rho_0$, $\mu = \eta - 1$, and a, b, A, B and E_0 are the Tillotson parameters, empirically derived constants which vary for each material (Melosh, 1989). This form is also valid for a cold expanded state where the internal energy (E) is less than the energy of incipient vaporization (E_{iv}).

In the expanded states ($\rho/\rho_0 \leq 1$), when E exceeds the energy for complete vapor-

ization (E_{cv}), the Tillotson EoS is defined as:

$$P = a\rho E + \left[\frac{b\rho E}{E/E_0\eta^2 + 1} + A\mu \exp[-\beta(\rho_0/\rho - 1)]\right] \exp[-\alpha(\rho_0/\rho - 1)^2] \tag{1.7}$$

where α, β are constants that control the rate of convergence of the equation. The transition between these two regimes required an additional pressure equation, which combines the compressed and expanded form, since it involved the partial vaporisation of material for internal energies $E_{iv} < E < E_{cv}$.

$$P = \frac{(E - E_{iv})P_E + (E_{cv} - E)P_C}{(E_{cv} - E_{iv})} \tag{1.8}$$

where P_C and P_E are the pressure determined by the compressed and expanded state respectively.

The Tillotson EoS is limited in its applicability because provides no information about how to compute the temperature or the entropy of a material and is unable to model melting and vaporization (Pierazzo et al., 2008). Nevertheless, this type of equation of state is widely used in hydrocode simulations because of its simple form and because the vapour phase is not important for modelling impact crater formation (Bray, 2009).

iSALE hydrocode supports another type of equation of state, the ANalytical Equation Of State (ANEOS) (Thompson & Lauson, 1972), that is generated with a complex computer code and it relies on different physical approximations in different domains of validity. ANEOS is thermodynamically constant since pressure, entropy and internal energy are derived from the Helmholtz free energy. Typically, ANEOS is used to construct equation of state tables which are then used in a hydrocode (Melosh (2000) summarises the approach of ANEOS). ANEOS can predict (limited) phase changes including treatment of melt and vapour, as an advantage respect to other analytical equation of state, but it cannot treat solid-solid and solid-liquid phase changes simultaneously. One of the limitations of ANEOS is the treatment of gases as monoatomic species which causes it to overestimate the liquid-vapor phase and the critical point of most geologic complex materials (Pierazzo & Collins, 2004). A treatment of biatomic species has been introduced in ANEOS by Melosh (2000), but a lot of work is still needed. In addition, the Simon equation (Poirier, 1994) was implemented in iSALE to simplify the problems related to the liquid/solid phase transition in order to define the melt temperature as a function of pressure:

$$T_m = T_0 \left(\frac{P}{a} + 1\right)^{\frac{1}{c}} \tag{1.9}$$

where T_0 is the melt temperature at normal pressure, while a and c are material constants. In the recent years ANEOS equations of state for several materials of geologic interest have been developed and included in hydrocodes, but some limit are still un-

solved (an example is the treatment of biatomic species in vapour phase, like water).

The iSALE simulations presented in this thesis used ANEOS equation of state tables for basalt and Tillotson EoS to represent gabbroic anorthosite (Ahrens & O'Keefe, 1982), as it will be shown in next Sections.

1.3.4 Constitutive model

The constitutive model describes the response of a material to stress or deformation and is important to model the late phase of impact cratering modelling since the material strength defines the final morphology of the crater. A various number of strength model have been formulated and implemented into iSALE to determine different relationship between yield strength Y_i and pressure, strain rate, temperature. In iSALE the strength of intact and damaged rock is considered separately, in fact it is obvious that fractured rock is weaker than intact rock as component blocks are free to move within the fractured material. The yield strength for intact rock may be considered to have two components, a cohesive strength that is independent of overburden pressure, and a frictional component that is a function of overburden pressure and, hence, depth (Lundborg, 1968):

$$Y_i = Y_{i0} + \frac{P\mu_i}{1 + \frac{P\mu_i}{Y_m - Y_0}} \tag{1.10}$$

where Y_0 and Y_m are the shear strength at zero pressure (cohesion) and the limiting strength at high pressure (von Mises plastic limit) respectively, P is the pressure and μ is the friction coefficient. For damaged material the strength is defined as:

$$Y_d = min(Y_{d0} + \mu_d P, Y_{dm}) \tag{1.11}$$

where Y_{d0} is the cohesion, Y_{dm} the limiting strength at high pressure and μ_d the coefficient of internal friction. The amount of target damage caused by impact is highest close to the impact site and decreases with radial distance from the crater centre (e.g. Kenkmann & Scherler, 2002). The strength of the target material therefore also varies radially, increasing from the fully damaged strength at the crater centre, to the intact strength at larger distances (Bray, 2009).

There are many algorithm developed to describe dynamic fragmentation during the impact, in particular iSALE uses a damage parameter D to define the amount of rock fracturing (Collins et al., 2004). The damage parameter D depend on the plastic strain ranging between 0 (for completely intact, undamaged rock) and 1 (completely fractured, damaged rock). The amount of damage is then used to modify the cohesive strength of the material; for partially damaged rock ($0 < D \leq 1$) yield strength is defined as:

$$Y = (1 - D)Y_i + DY_d \tag{1.12}$$

1.3.5 Acoustic fluidization: the Block Model

The formation of large craters, hence the presence of central peaks and/or rings, must be explained with some additional weakening mechanisms since rock standard strength models are not able to take into account simultaneously the uplift of material from beneath the crater floor as well as the slumping of the transient crater walls (e.g. Dent, 1973; Melosh, 1977; Melosh & McKinnon, 1978; O'Keefe & Ahrens, 1993; Melosh & Ivanov, 1999; Collins et al., 2002; Ivanov & Artemieva, 2002). In order to reproduce the complex crater morphology, collapse requires significant weakening of the target material beneath the crater floor, but at the same time without loosing its plastic properties (Melosh, 1982). This weakening process must be transient acting over a timescale similar to that of crater collapse (Melosh & Ivanov, 1999). The formation of central peaks and peak-rings indicates that material is better described by a fluid-like movement, similar to cratering in water (Worthington, 1963). Hence, the target material can be described as a Bingham fluid, i.e. a material that responds elastically to stress until a critical strength (the yield strength or cohesion) is reached, while, once this limit is exceeded, it flows as a viscous fluid (Bingham, 1916). The nature of this fluidization is poorly understood at present and several weakening mechanisms have been suggested, as outlined by Melosh (1989) (thermal softening (O'Keefe & Ahrens, 1993, 1999), interstitial fluid and melt fluidization (Spray & Thompson, 1995) and Acoustic Fluidization (Melosh, 1979)).

Melosh (1979) proposed, following existing models of earthquake-induced landsliding (Seed & Goodman, 1964), that the presence of an acoustic field could cause impact rock debris to behave in a fluid-like manner only from a macroscopic point of view. In fact, impact crater events, creating seismic waves, induces a strong shaking that may have an important role in affecting debris around the crater (Melosh & Gaffney, 1983). Under normal conditions, material is under too high a overburden pressure to fail and, hence, it will not be able to flow. Therefore, acoustic fluidization suggests that the material may flow if vibrations of a random seismic wave field, generated by the impact shock and propagating through impact-fractured rocks, temporarily reduce overburden pressure (Potter, 2012). Hence, macroscopically, the debris mass appears to flow, the rapidity of which is a function of the frequency and amplitude of the failure events (Collins & Melosh, 2003). The material becomes frozen in place when vibrations dissipate, as the overburden pressure exceeds the local pressure.

The central equation of the acoustic fluidized model of Melosh (1979) describes the dependence of the strain rate $\dot{\epsilon}$ on the applied shear stress η in the acoustically fluidized material:

$$\dot{\epsilon} = \frac{\tau}{\rho\lambda\beta}\left[\frac{2}{erfc(\chi)-1}\right]^{-1} \tag{1.13}$$

where ρ is the bulk density, λ the wavelength of the acoustic field, β the bulk sound speed of the granular debris, erfc the complementary error function, and $\chi = \frac{1-\Omega}{\Sigma}$,

where $\Omega = \tau/\tau_{static}$ (with τ_{static} is the stress required to initiate failure in the absence of vibrations) is the dimensionless driving stress measure, which ranges from 0 to 1. The amplitude of the vibrations is represented by $\Sigma = \sigma/p$ (σ is the variance of the pressure fluctuations) and it is assumed to be distributed according to a Gaussian law (Crandall & Mark, 1973). The acoustic fluidization is valid if the vibration wavelength λ is much larger than the grain size d, i.e. $\lambda \gg d$ (Melosh & Ivanov, 1999). However, this model does not predict the wavelength of the vibrations dominating the flow, hence, a quantitative prediction of the rheology cannot be made (Melosh & Ivanov, 1999). The acoustic fluidization has the 1/g dependence, which facilitates the explanation of the simple-to-complex crater transition and the existence of some temporary weakening mechanism (Melosh & Ivanov, 1999).

iSALE, adopts a simple mathematical approximation of Acoustic Fluidization (AF) (Melosh, 1979), known as the Block Oscillation Model (Block Model) (Ivanov & Kostuchenko, 1998; Melosh & Ivanov, 1999), whose complete description is reported in Melosh & Ivanov (1999). The block model supposes that the target consists of a system of discrete blocks (rather than a continuum), with a characteristic size h, that oscillate periodically. A schematic description is reported in Figure 1.10. The amount and longevity of transient material weakening is controlled by two model parameters: the kinematic viscosity η of the fluidized region and the decay time of the block vibrations τ_v. The viscosity η is assumed to be proportional to density ρ, sound speed c and a length parameter comparable to the block size h (Wünnemann & Ivanov, 2003). The block length parameter for the determination of η could be scaled by some linear scale, based on the estimation of dominating fragment size changes at different-sized craters (Kocharyan et al., 1996). Nevertheless, there are still some uncertaintes, for example if the block system under a growing crater is activated during the crater growth process, the block characteristic size seems to be proportional to the transient cavity depth (Ivanov & Artemieva, 2002) or diameter (Collins, 2001). However, the transient cavity depth itself depends on the value of η. For a given impact velocity, the projectile dimension r may serve as a first approximation of the blocks fragment size. A linear proportionality is assumed and the viscosty η becomes:

$$\eta = \gamma_\eta(cr\rho) \tag{1.14}$$

Thus, the length parameter (block size or wavelength) is scaled by the projectile radius r and a dimensionless scaling parameter γ_η. Following the same approach, the damping of vibration is correlated linearly with the projectile size and the damping factor γ_T through the following relationship:

$$T_{dec} = \gamma_T \frac{r}{c} \tag{1.15}$$

From the equation reported above it is intuitive that larger impactors lead to higher viscosities and also to longer lasting than smaller projectiles. The parameters γ_η and γ_T represent the iSALE input parameters governing the fluidization mechanism (Wünnemann & Ivanov, 2003); these must be varied in simulations in order to achieve the best fit between data and modelling, such as the case of Sudbury crater (Ivanov & Deutsch, 1999), Chicxulub (Collins et al., 2002) and Chesapeake Bay (Collins & Wünnemann, 2005).

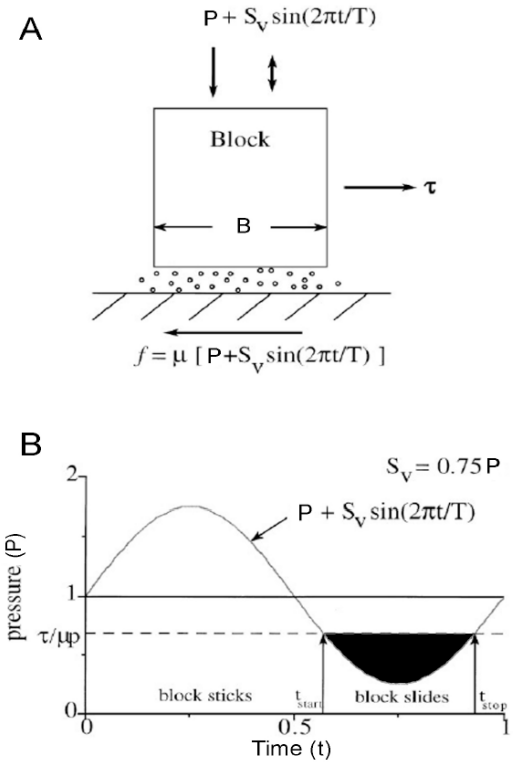

Figure 1.10: (a) The block slides along the underlying surface and it is subjected to different forces, as the overburden pressure p, the friction stress μp and the traction stress τ. The varying acoustic pressure is indicated with a double-ended arrow. Acoustic energy sets the block oscillating in a vertical manner with a period, T, and amplitude, S_v, resulting in a sinusoidal variation in the normal stress. (b) Plot of the net pressure, relative to the overburden pressure, against time for one period of oscillation. The "block slides" region represents times at which the block is free to slide along the underlying surface. The block will remain stationary if $p + S_v \sin(\frac{2\pi t}{T}) >$ traction (μp). From (Melosh & Ivanov, 1999).

1.3.6 Porosity model

The compaction model, used in iSALE, is the so-called $\epsilon - \alpha$ compaction model (Wünnemann et al., 2006), which describes the compression of pristine porous materials compris-

ing four regimes: elastic compaction, exponential compaction, power-law compaction, and compression. The porosity model formula represents the relative volume of pore space using the distension α parameter instead of porosity ϕ:

$$\alpha = \frac{1}{1-\phi} = \frac{V_s + V_v}{V_s} = \frac{\rho_s}{\rho} \tag{1.16}$$

where V_s and V_v are the volume of the solid matrix and void respectively, and ρ_s and ρ are the densities of the solid matrix and the material bulk respectively. A non-porous body ($\phi = 0$) will therefore have a distension, α, of 1. As well as the initial compaction, release from the applied stress must also be considered. In the crushing of pore space, the amount of reversible (elastic) stress is relatively small and can be neglected; the majority of the applied stress is irreversible (compaction) and therefore upon release from the applied stress pore space is not re-introduced into the material (Potter, 2012).

1.4 Numerical modelling application: Mercury

The surface of Mercury has numerous interesting features, including a variety of craters, ridges, and terrains ranging from heavily cratered to nearly crater free. Craters on Mercury range in diameter from small bowl-shaped cavities to multi-ringed impact basins and different crater types can be seen, including young craters, new craters on top of old craters, craters with peaks in the center, and craters with lines or "rays" of bright material pointing out from the central crater. These features are affected by different type of degradation, from relatively fresh crater to highly degraded crater remnants. It is also interesting to note that one side of the planet is more cratered than the other one, which is characterised by the presence of smooth plains, near the Caloris basin. This latter structure is the largest impact crater (with a diameter of 1550 km) presented on the planet and its formation was so energetic to cause lava eruptions and left a concentric ring surrounding the crater.

In this work, despite the different craters presented on the planet, we analyse a particular impact landform. In fact, images acquired by the MErcury Surface, Space ENvironment, GEochemistry, and Ranging (MESSENGER) spacecraft have shown a conical structure, surrounded by a trough, that lies at the centre of a large (23.000 km^2) diffuse-margined spectral anomaly that is bright and red-sloped compared to the Hermean average (Figure 1.11). This type of relatively bright and red anomaly have been interpreted elsewhere on the planet as a pyroclastic deposit (Kerber et al., 2009, 2011; Goudge et al., 2014). Hence, this morphology could suggest a genesis that involves explosive volcanism; this hypothesis is also supported by the fact that on other planets, like Earth and Mars, volcanism constructs steep-sided edifices by deposition of ballistically-ejected particles (e.g. Hasenaka & Carmichael, 1985; Brož & Hauber, 2012) or by flow of viscous lava. On the other hand, on Mercury, the ballistic range of particles ejected at a particular velocity is larger than on Mars and Earth, due to a lack of air-resistance and weaker gravity, therefore, structures formed in this way would be expected to have relatively low relief (McGetchin et al., 1974; Brož et al., 2014). In addition, compositional data do not at present support the presence of evolved lavas able to form these type of structure through effusion (Denevi et al., 2013; Nittler et al., 2011; Weider et al., 2012). Finally, it would be the only example of a volcanically-constructed cone on Mercury. For this reason, we made and tested the alternative hypothesis that the cone is the intrinsic central peak of an impact crater, in fact the cone lies within an encircling trough, which is in turn encircled by a ridge that could be interpreted as the rim crest of a 43-km diameter. In this scenario the cone occupies the location where a central uplift structure would be expected (Pike, 1988) and the spectrally red-sloped deposit, formed through explosive eruption from the trough, is interpreted as a volcanic vent encircling the crater's central uplift (Thomas et al., 2015). This would be consistent with the observation that pits associated with pyroclastic deposits on Mercury are co-

located with regions of structural weakness in impact craters (Gillis-Davis et al., 2009), and would support the hypothesis that such structures play a controlling role in explosive volcanic eruptions on Mercury (Thomas et al., 2014). In order to evaluate the feasibility of this hypothesis, we have studied the most likely original morphology of an impact crater of this size on Mercury through two different method: i) measuring topographic cross-sections across relatively fresh craters with similar diameters, and ii) performing an impact crater numerical modelling using iSALE hydrocode. Both procedures allow us to asses our hypothesis and to make quantitative conclusions.

1.4.1 Landform description and proposed mode of formation

The steep-sided cone-like structure lies at the centre of a circular pit. This is in turn surrounded by a topographic rise, which we interpret as the rim crest of a 43-km diameter impact crater (Figure 1.11b). We proposed that such a landform assemblage, which lies at the centre of a 92-km radius spectral anomaly, could have formed in the following way. The first stage of formation of this landform assemblage was the creation of a 43-km diameter crater with a central uplift through an impact event (Figure 1.12a), in fact craters with a diameter larger than 12 km (defined as complex) are expected to have a central peak where the cone occurs (Pike, 1988). After an unknown period, magma rose beneath the crater along a sill or dyke, either as a result of or independently of the impact crater formation (Figure 1.12b). This magma may have stalled in the low-density fractured zone beneath the crater, in a manner similar to that hypothesised to result in floor-fractured craters on the Moon (Schultz, 1976). During a period of sub-surface magma storage, crystallization of volatile-poor minerals may have enhanced the volatile content of the remaining melt. The Dyke propagation to the surface occurs along planes of crustal weakness, possibly aided by an increase in overpressure due to volatile exsolution, this occurred subvertically due to the presence of zones of weakness in the overlying crust (Parfitt et al., 1993), particularly those bounding the central uplift. Volatiles within the magma expand at the surface and eject juvenile and vent-wall material. This falls along ballistic pathways to form deposits with a relatively bright and red-sloped spectral character. To assess this hypothesis, we analyse the morphology, dimensions and topography of the cone, pit, host crater and deposit, and we also compare the present-day topography to two independent estimates of the original host crater topography: the first derived from similar-diameter craters (fresh craters) with no evidence of explosive volcanism and the second from a hydrocode model of the original impact. We will refer to this crater as AP1 through this work ('Annular Pit 1').

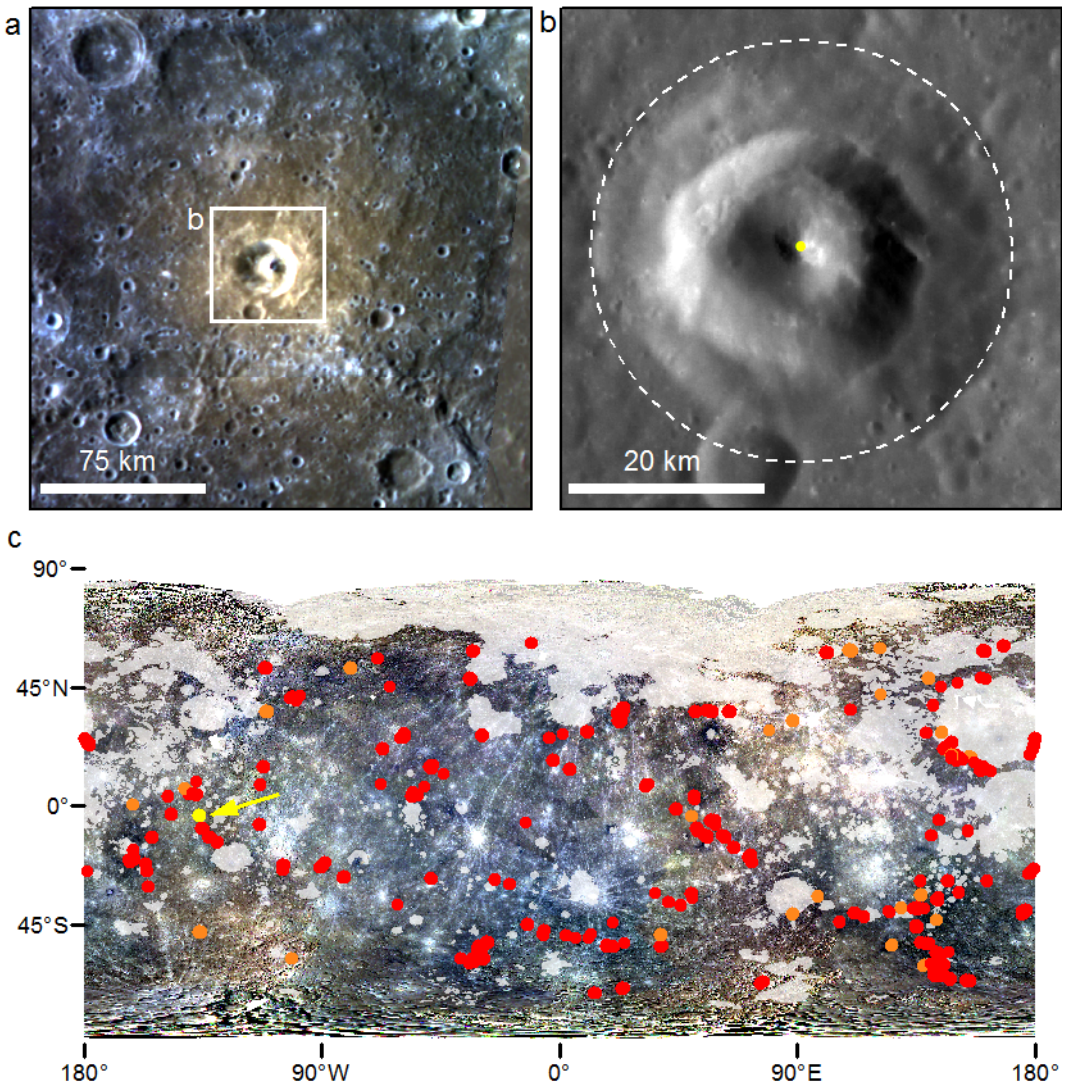

Figure 1.11: A steep-sided cone associated with putative explosive volcanic products (-136.7° E, -3.5° N). (a) The cone lies at the centre of a widespread relatively bright and red-sloped spectral anomaly characteristic of explosive volcanism. White rectangle: extent of (b) (Image: colour composite of images EW0262430050I, EW0262430054F and EW0262430070G). (b) Close-up showing that the cone lies within a pit, which is encircled by a ridge (dashed white line), interpreted as the rim-crest of an impact crater. Yellow dot: central point used for determining the median elevation profile in Figure 1.13 (Image EN0212284006M). (c) Global location of the cone (yellow dot, yellow arrow) relative to endogenic pits with (red dots) and without (orange dots) a surrounding relatively bright and red-sloped spectral anomaly (identified by Thomas et al. (2014)). White areas indicate smooth volcanic plains (from Denevi et al. (2013)). (Base image: MESSSENGER global colour mosaic v5). Images in (a) and (b) were obtained by MESSENGER's Wide-Angle (10.5° field-of-view) and Narrow-Angle Camera (1.5° field-of-view) respectively. Figure from Thomas et al. (2015).

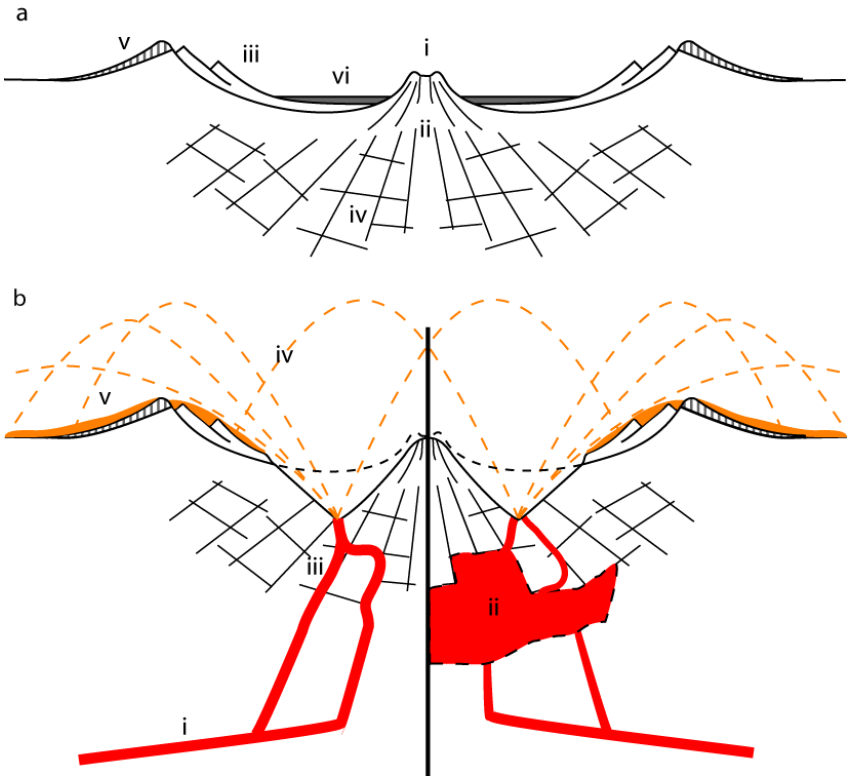

Figure 1.12: Proposed model of formation of a crater-centered cone surrounded by pyroclastic deposits by vent formation around the central uplift of the impact crater. (a) Schematic of a complex impact crater with (i) a central uplift with (ii) internal steeply-dipping faults (Senft & Stewart, 2009; Scholz et al., 2002), (iii) slump structures forming terraces, (iv) an underlying fracture zone, (v) ejecta and (vi) impact melt deposits forming a flat floor. (b) Proposed morphology of the crater during explosive volcanic activity, with (left) or without (right) shallow magma storage. (i) Volatile-bearing magma rises from depth along a sill or dyke, possibly forming a (ii) shallow magma chamber or sill beneath the low density fractured zone (right; dashed outline indicates the margins may be gradational). (iii) Dyke propagation to the surface occurs along planes of crustal weakness, possibly aided by an increase in overpressure due to volatile exsolution. (iv) Volatiles within the magma expand at the surface and eject juvenile and vent-wall material. This falls along ballistic pathways to form (v) deposits with a relatively bright and red-sloped spectral character (dashed line indicates the original crater profile). Figure from Thomas et al. (2015).

1.4.2 Methods

(a) Planform morphology

We analysed all images of the landform location up to September 17, 2013 in order to study the morphology of the cone and its associated deposit. These images were taken by the MDIS camera onboard MESSENGER, which consists of a 1.5° field-of-view monochrome Narrow Angle Camera (NAC), and a 10.5° field-of-view multispectral Wide Angle Camera (WAC). After radiometric and photometric corrections using the ISIS3 (Integrated System for Imagers and Spectrometers) software produced by the U.S. Geological Survey, we were able to combine images taken with different filters (at 966 nm, 749 nm and 433 nm in the red, green and blue bands respectively) to derive colour images. This procedure allow us to make a distinction between pyroclastic deposits (Kerber et al., 2009; Goudge et al., 2014) and general difference in albedo and colour between regions of Mercury's surface (Denevi et al., 2009). We used Graphics and Shapes tools (Jenness) within ArcGIS software to make geodetic planform measurements of the dimensions of the cone, associated landforms and deposit.

(b) Present-day topography

Due to MESSENGER's highly elliptical orbit around the planet, the Mercury Laser Altimeter (MLA) has not been able to obtain elevation data at the location of interest to this study. We therefore determined the present-day topography by creating a digital terrain model (DTM) using NAC stereo images EN0257648861M and EN0227259475M (Figure 1.13). The DTM generation has been performed following a photogrammetric workflow that consider many steps and several tools. The files have been fed into ISIS3 (Eliason, 1997), radiometrically calibrated and finally the images are ortho-rectified with cam2map program (i.e. projected onto the reference surface of the Mercury spheroid). The correlation phase have been performed with the Area Based image matching software named "Dense Matcher" (Re et al., 2012). As far as the triangulation stage is concerned, the Ames Stereo Pipeline (ASP)(Moratto et al., 2010) routine have been used by suitably modifying the Dense Matcher disparity map to produce an input data in the format accepted by ASP. Any Bundle Block Adjustment have been performed and the obtained GeoTiff raster DTM (with a 215 m/pixel resolution) has been imported in a GIS software package in order to extract the profiles.

(c) Original crater topography

It is necessary to define the pristine morphology of the surface to assess the cone formation hypothesis. Hence, we determine the original morphology of the host crater, taking into account that the cone lies at the centre of an impact crater. We investigated this in

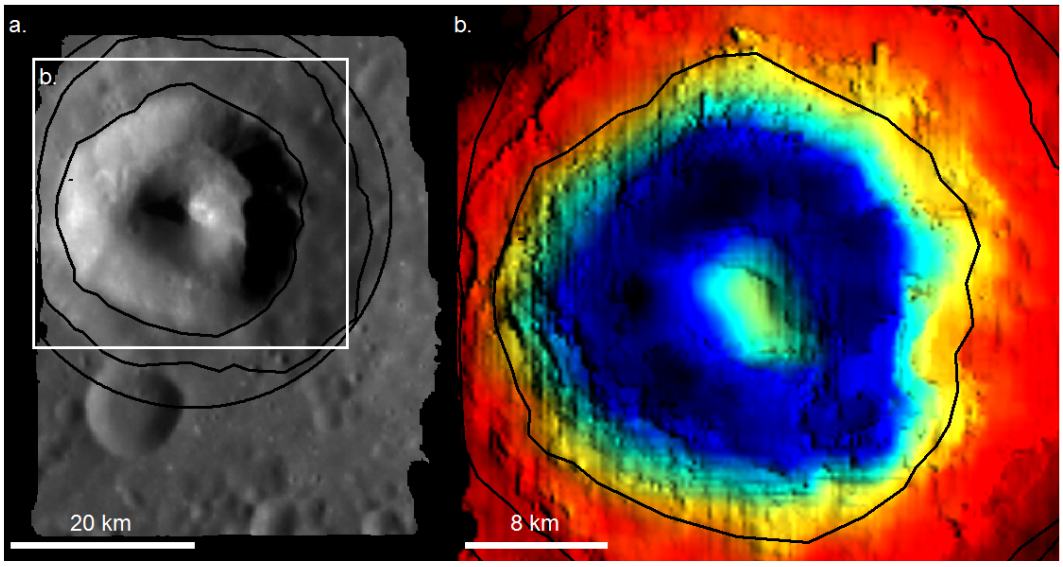

Figure 1.13: Extent of the stereo-derived DTM of the cone and surrounding pit and crater (based on images EN0257648861M and EN0227259475M). (a) An orthorectified image showing the extent of the DTM. Black lines indicate the position of the pit and crater rims. White rectangle: extent of (b). (b) Colorized shaded relief produced from the DTM (blue, green, red indicate increasing elevation) showing irregularities in the depth of the pit floor, probably mass wasted material. Image from Thomas et al. (2015).

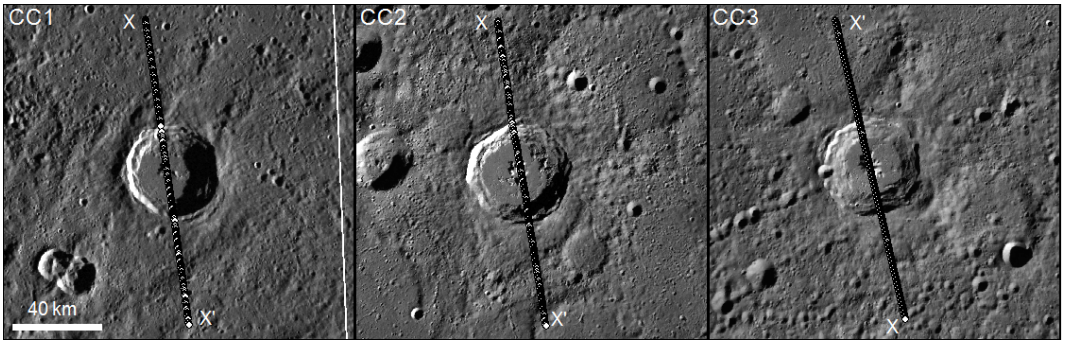

Figure 1.14: $\sim$ 43 km diameter morphologically fresh impact craters used as a control on the original crater shape and on the simulation. Outlined dots indicate MLA data points from X to X′. CC1: 177.1° E, 50.9° N, MLA track MLASCIRDR1109231307 (orbit 380); CC2: -107.5° E, 49.2° N, MLA track MLASCIRDR1208272313 (orbit 1198); CC3: -122.1° E, 63.8° N, MLA track MLASCIRDR1203061631 (orbit 715). Only channel 1, high threshold, MLA pulse returns were used to avoid incorporating noise. All the panels have the same horizontal scale as that indicated for CC1 (Base image: MDIS global monochrome mosaic v9). Image from Thomas et al. (2015).

two ways: (i) by obtaining topographic cross-sections across relatively fresh craters of a similar size but with no evidence for explosive volcanic activity and (ii) by performing a hydrocode impact simulation to reproduce the morphology of a crater of this size.

(i) Topography of undegraded craters of a comparable size

We identified 3 impact craters ranging in diameter between 43 and 47 km on the basis of MLA tracks available, that cross their central peak structures (Figure 1.14). These were used as a control on crater morphology and to assess the plausibility of the results of our simulations. We specifically chose undegraded impact craters (Mansurian age) (Spudis & Guest, 1988), which are characterised with intact ejecta blankets and little sign of terrace modification, and therefore approximate the morphology of the impact crater being studied not long after its formation. We underline that the pyroclastic deposits obscure the original topography of the crater containing the cone (AP1), so we are not able to assess how degraded it was prior to the pyroclastic activity. Our comparison assumes that the crater was relatively fresh at the time of this activity.

(ii) Impact crater numerical model

We simulated the formation of the impact crater using the iSALE (Impact Simplified and Arbitrary Lagrangian Eulerian) hydrocode. The structure and composition of the projectile was simplified to spherical and homogeneous basalt impacting at an angle of 90°. iSALE has a 2D capability that limits the study impact events on normal incidence angles and obviously can only model vertical impact orientation. The only way to include the effect of different impact angles is assuming that the projectile indeed has an average impact speed, but impact at 45° impact angle. Therefore, the impact speed use in the simulation is $v_{average} * \sin(45°)$ to have a more reliable initial condition. This is commonly accepted practice in the impact cratering studies. We employed an impact velocity of 30 km/s (Marchi et al., 2005), and estimated a porosity of 10% derived from the average of the meteorite types proposed by Britt et al. (2002). We estimated an impactor size of 2.4 km diameter by comparing profiles obtained in a series of runs at low resolution to the topographic profile of the present topography and cross-sections of the similar-sized control craters. We took an Eulerian approach, defining the number of computational cells per projectile radius (CPPR) as the resolution of our impact model. We used the Eulerian setup because of the inevitable extreme cell deformation that occurs with the alternative Lagrangian approach (Pierazzo & Collins, 2004). The crater was modelled on a computational mesh of 400 x 600 cells, with a cell size of 150 m and a projectile size of 8 CPPR. We used a spatially constant gravitational acceleration of 3.7 m/s^2. The Hermean surface was approximated as a homogeneous layered half-space made up by a brecciated 5 km basalt layer overlying an intact basalt layer. This depth was chosen on the basis of the thickness estimation of the fractured layer derived by Schultz (1993) and on the crater size frequency distributions predicted by the MPF (Model Production Function) for analogue smooth plains (Marchi et al.,

2011; Giacomini et al.). The thermodynamic response for both the projectile and target in our simulations was approximated with an equation of state table for basalt derived using ANEOS (Thompson & Lauson, 1972). The material properties of these layers are summarized in Table 1.1, while the output simulations are shown in Figure 1.15 and Figure 1.16.

		Projectile	**Target**	
			1°layer	2°layer
	Material type	Basalt	Fractured Basalt	Intact Basalt
Variable	Description			
D	Impactor diameter (km)	2.4		
R_i	Impactor radius $(CPPR)$	8		
v_i	Impact velocity (km/s)	30		
ϕ_i	Material porosity	10%	5%	0
ρ_i	Material density (kg/m^3)		2850	2850
Y_0	Cohesion for intact material (MPa)		10	10
Y_d	Cohesion for damaged material (MPa)		0	1
Y_m	von Mises plastic limit (GPa)		3.5	3.5
μ_i	Coefficient of internal friction		1.2	1.2
μ_d	Coefficient of friction (damaged material)		0.6	0.6
T_m	Melt temperature (°K)		1500	1500
η	Kinematic viscosity (m^2s^{-1})		120000	120000
τ	Decay time (s)		48	48

Table 1.1: Numerical model parameters used in the simulation.

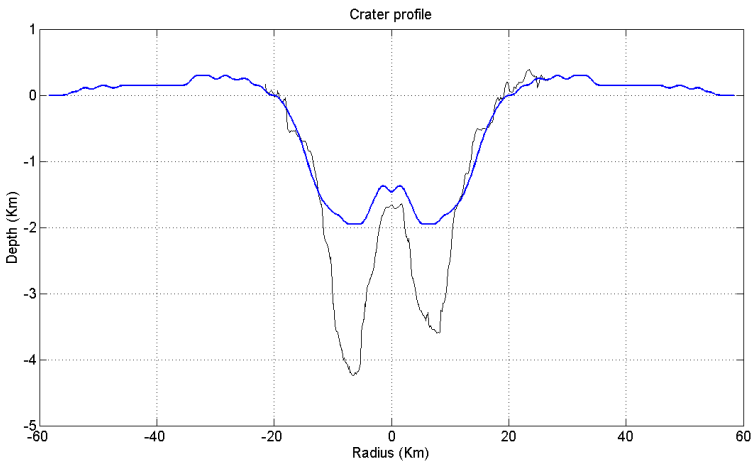

Figure 1.15: DTM profile (black line) and iSALE (blue line) simulated profile of the pit crater.

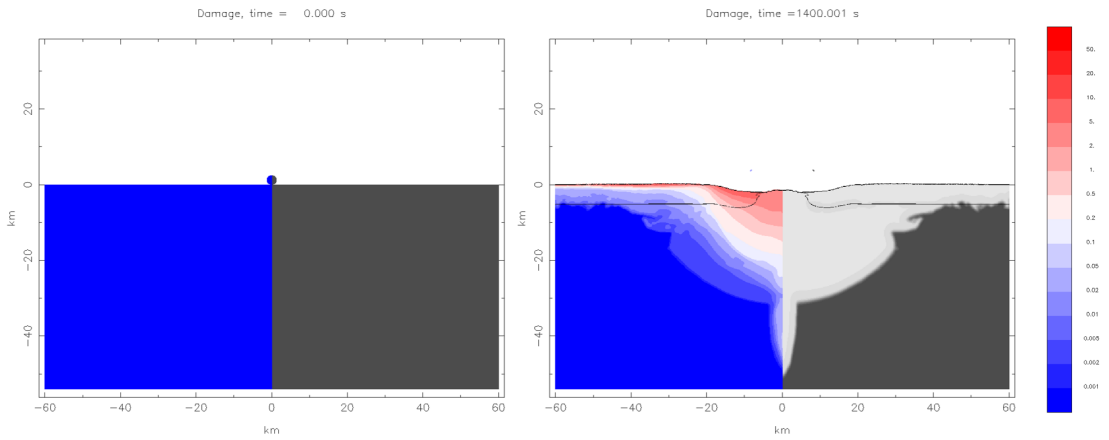

Figure 1.16: Snapshots of the crater formation: right side shows the amount of damage on gray scale (white = maximum level of damage); left side shows plastic strain contours in a color scale (red = maximum deformation, blue = no deformation).

1.4.3 Results

Present-day morphology and deposit extent

The crater's average diameter is 43.2 km with a cone of $\sim$ 12.5 km basal diameter. It stands up to 2.2 km above the floor of the pit surrounding it and its summit is 1.8 km below the rim crest of the host crater (Figure 1.17).

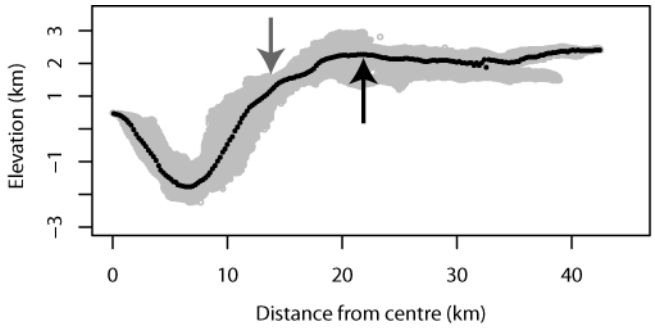

Figure 1.17: Present-day topography of the crater. (a) Average present-day topography from the centre of the cone. Light grey circles mark the elevation of each pixel of the DTM against its distance from the cone centre. Black dots mark the median elevation within 215 m radial bins. Grey arrow: average location of the pit margin, black arrow: average location of the rim crest. Image from Thomas et al. (2015).

It lacks a summit crater and has steeply-dipping flanks, averaging 26°. The pit margins are similarly steep, averaging 30°. More gently-sloping deposits are visible at the base of the pit's wall scarp in some places, consistent with landslided material (Figure 1.13b). This suggests that the original slope of the pit walls may have been greater prior

to mass wasting. The area between the rim-crest and the outer pit margin measures on average 8.5 km wide on the orthorectified image. This may be a terrace formed by wall-slumping, draped by volcanic deposits. The spectral anomaly with the relative bright, red sloped character is the second most areally-extensive such anomaly on the planet (Thomas et al., 2015) and its extension from the centreline of the pit is $\sim$ 92 km.

Topography of the control craters

In this study we use three different control craters (named as craters CC1, CC2 and CC3) with a diameter equal to 41.8 km, 46.7 km and 43.2 km, respectively. Their cross-sections were normalised to give a crater diameter of 43.2 km in order to compare the control craters profiles with the present-day topography of AP1. Because a smaller impact crater would be expected to have a smaller ratio of rim-crest to floor depth, this necessitated a relatively minor adjustment to elevation values across CC1 and CC2. To achieve this goal we calculated the expected rim crest to floor depth of the crater on the basis of the Pike (1988) relationship, which was obtained for complex craters on Mercury:

$$d = 0.353D^{0.496} \tag{1.17}$$

where d is the depth and D the diameter. We calculated the ratio between the depth indicated by this method for the control crater and for a 43.2-km diameter crater and multiplied the MLA elevation values by this value. To compare the morphology of the craters, we have plotted them so that distance along the cross-section is equal at the rim crest and elevation is equal at the base of the outer slope of the raised rim (known as the rim flank). The latter feature was chosen as the best point of reference because the topography beyond the craters (Figure 1.18) is very uneven due to the presence of other impact craters, so it is impractical to identify a "regional datum" at any greater distance. The control craters have similar profiles, excepting that the floors of CC1 and CC2 are shallower (2.3 km and 2.1 km) and the peak height above the floor is lower (0.4 km and 0.7 km) than those of CC3 (with a depth of 2.7 km and a peak height of 1.2 km) (Figure 1.18). This suggests that the interiors of CC1 and CC2 have experienced more infilling than CC3, either by retention of a higher volume of impact melt during the modification stage of their formation, or by post-formation volcanic flooding (Thomas et al., 2015).

Numerical simulation

A projectile with a diameter of 2.4 km, penetrating the target at 30 km/s (in accordance with Marchi et al. (2005)), generates a crater diameter in agreement with the DTM profile considering that the final output of iSALE (Figure 1.15) has a 4% radius uncertainty, a value found from code validation against laboratory experiments (Pierazzo

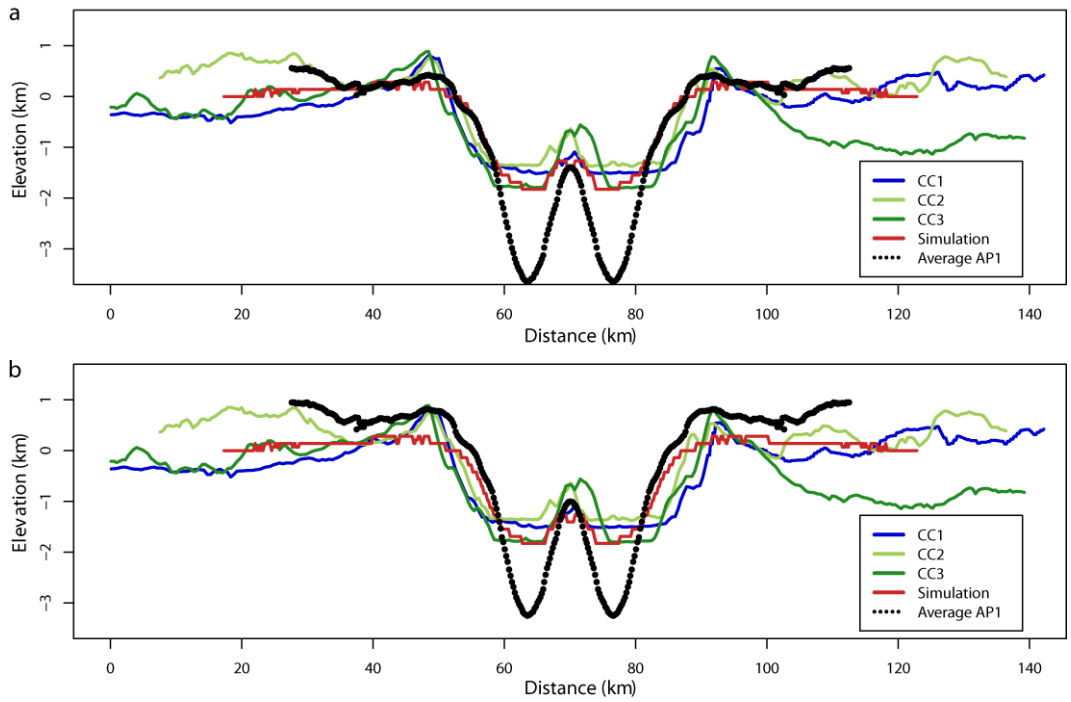

Figure 1.18: Comparison between the average DTM elevations across the present-day landform, MLA cross-sections through the control craters, and the results of the hydrocode simulation, showing general agreement between complex crater morphology and the morphology of the cone in AP1. (a) Values on the distance axis are equal at the leftmost rim crest, and elevations are equal at the base of the leftmost rim flank. (b) Horizontal location and elevations are matched as in (a), except that the DTM profile is placed so that the rim-crest elevation equals the average elevation of the leftmost rim crests of the control craters. Image from Thomas et al. (2015).

et al., 2008). We observe a good match in terms of dimension while the morphology appears slightly different with the observed crater. This is due to the pyroclastic event that affects this crater generating an asymmetric collapse of several hundred meters by explosive volcanism. The simulation shows a best fit with the crater diameter and the interior morphology of the control craters with a decay time of 48 s and a kinematic viscosity of 120,000 m/s^2.

As with the control craters, both horizontal and vertical values along the simulated cross-section were adjusted for comparison to a 43.2-km diameter crater (Figure 1.18). Results from the simulation are in accordance with depth-diameter ratios observed in impact craters in large morphometric datasets for Mercury. Pike (1988) found a best-fit to the depth-diameter values of 58 craters between 30 and 175 km diameter with the relationship given in Equation 1.17. Using this relationship, a 43.2 km wide crater would be expected to be 2.3 km deep; the simulated crater has a depth of 2.3 km (2.1 km after adjustment of its depth to take into account its larger diameter). More recent

study based on MESSENGER data (Baker & Head, 2013) found a mean depth-diameter ratio of 0.034 ± 0.010 for complex craters greater than 50 km in diameter. Applying this relationship to our case study, we expect a depth of 1 - 1.9 km, which is shallower than the simulated crater, but this could be due to data extrapolation for crater with a diameter smaller than 50 km. Following this similar method of extrapolation for the peak height data, the expected height of the central peak would be in the range of 0.3 - 0.9 km. The height of our simulated central peak above the crater floor is 600 m, or 570 m after adjustment for the greater crater diameter, and so is in agreement with this estimation. This indicates that though the simulated central peak is lower than those of the control craters, it lies within the range of possible values on Mercury. The simulated central peak width (8.7 km, or 7.8 km after adjustment for crater diameter) is somewhat narrower than the relationship $D_{cp} = 0.44D^{0.82}$ observed by Pike (1988) between crater diameter D and central peak width D_{cp} in 138 craters that predicts a width of 9.7 km. When vertically matched with the control craters at the base of the rim flank, the elevation of the floor of the simulated crater almost exactly matches that of CC3, which we have previously identified as the least likely to have undergone significant infilling. However, the height of the rim crest relative to the base of the rim flank is much lower (140 m) in the simulation than in the control craters (averaging 780 m). Additionally, the wall slope is shallower than in the control craters. In the simulated profile the wall slope is steeper, but this strong difference should be explained by the relative "freshness" of the simulated crater versus modification of the control craters over a period of up to 3.5 Ga.

Comparison of estimated original and present morphologies

We compare the present topography with the control craters and the simulated original topography using two possible vertical tie-points. The first plots all cross-sections so that the elevation at the base of the rim flank is equal (Figure 1.18a). This requires the assumption that there is not an appreciable thickness of pyroclastic material in this area, as this would increase the elevation of the original ground surface. The second comparison plots the topographic profile derived from the DTM such that its rim crest is at the average elevation of the rim crests of the control craters (Figure 1.18b). This would be a valid match if the original crater AP1 has undergone a similar amount of degradation as the control craters and if pyroclastic deposition has not increased the ground elevation at the rim crest. We judge that the first comparison leads to a better match between the interior and exterior morphology of AP1 and the morphology of the simulated and control craters, so we prefer to use this in the proceeding analysis (Thomas et al., 2015).

The height of the cone (820 m above the expected floor height indicated by CC3 and the simulation, and 1.4 km below the rim crest) is in agreement with that expected from

simulation and control craters (Figure 1.18a), in addition it is similar with the value found using the relationship of Baker & Head (2013) (predicting a height of 0.3 - 0.9 km above the crater floor). The width of the cone at the elevation of the floors of the simulated crater and CC3 is 4.3 km, which is narrower than expected for the central peak of a crater of this size (9.7 km) (Pike, 1988). The slope of the walls is similar to that of the simulation, but shallower than seen in the control craters. This could indicate that AP1 is younger than the control craters, since the simulation profile represents the crater shape just after its formation and the control craters belong to Mansurian age (3-5 - 1 Gyr). However, the rim crest of AP1 is also lower than those of the control craters, which indicates that it is more degraded and thus older. For this reason, the shallower wall slopes could be the result of wall slumping in AP1. There is some evidence for pyroclastic deposition in the region between the rim crest and the pit margin: it has the same smooth texture here and outside the rim, with no boundary between the two surfaces (Figure 1.11b). Similar deposits may contribute to the broad, high-elevation region inwards of the rim crest and the relative narrowness of the crater walls. However, it is not possible to distinguish relief resulting from pyroclastic deposition from that resulting from crater degradation processes.

The pit represents a large loss of material: the average pit floor is 1.4 km below the expected crater floor depth (Figure 1.18a) and the volume difference (calculated using ArcGIS) is 350 km^3. This is an approximate value for the volume of material lost because shadows in the images used to construct the DTM do not allow us to calculate the volume loss in the eastern part of the pit, and because the vertical match is uncertain. If the volume loss from the pit equals the volume of a pyroclastic deposit over the area indicated by the bright, red-sloped spectral signature, that deposit would average $\sim$ 20 m thick when scaled to take into account the different densities of basalt rock and pyroclastic fall (2760 kg m^{-3} vs. 2000 kg m^{-3} (Wilson et al., 2014). Elsewhere on Mercury, putative pyroclastic deposits ranging from 29 to 567 m thick have been identified in close ($\sim$ 6 km) proximity to vent margins (Thomas et al., 2014). Because of the uncertain vertical match between the original and present-day topography, we cannot define the thickness of the AP1 deposit near the vent, even if the wide high-elevation area inwards of the rim crest and the narrowness of the crater walls are in some part the result of pyroclastic deposition.

1.4.4 Discussion

Mode of formation of the landform assemblage

There is no evidence that the cone was constructed by volcanism: it lacks a summit caldera or vents, has no flow features on its flanks and has a similar slope to that of the outer scarps of the pit surrounding it. Conversely, its position, elevation, slope and morphology is consistent with a residual central peak of an impact crater, surrounded by an annular pit. This type of feature, a pit associated with pyroclastic deposits at the centre of an impact crater, is not the only example to this location. Indeed, we identified 150 sites were endogenic pits are surrounded by a bright, red-sloped spectral anomaly interpreted as pyroclastic deposits (Thomas et al., 2014). In this global survey, 118 of these structures occur within impact craters, and 52 (excluding AP1) are at the crater centre. In other cases the pit is in place of an expected central peak or peak ring, but in 31 cases it is concentric to the peak or central region (Figure 1.19). There are small pits existing around the crater centre (Figure 1.19c) in addition to conjoined pits form arcs around the centre (Figure 1.19b). In rare cases (e.g. Figure 1.19a), a pit or conjoined pits entirely surround the crater centre, though not forming so distinctive a "cone" as seen at AP1. Terrestrial seismic surveys and numerical models indicate that such impact crater central uplifts are bounded by deeply-penetrating high-angle faults (Scholz et al., 2002; Senft & Stewart, 2009). Mercury's crust has been in a global state of compression for much of its history (Strom et al., 1975), inhibiting the ascent of magma to the surface, so it is to be expected that any magma ascent that did occur would be localised in pre-existing zones of weakness such as these. It is interesting to note that, though it has previously been stated that endogenic pit formation appears to be structurally-controlled by host crater structures (Gillis-Davis et al., 2009), our findings suggest that pits most commonly occur at the crater centre or along a peak ring, and less commonly at other fault-bounded structures such as the terraces or rim area (Thomas et al., 2015).

Mode of pit formation

A structural control on pit formation has been taken as evidence that Mercury's endogenic pits form by collapse along planes of weakness during magma withdrawal from a shallow magma chamber (Gillis-Davis et al., 2009). It is possible that our case study was subjected to subsidence, in fact the cone's peak is at the lower of the range of probable original central peak heights, even if this low peak elevation cannot be conclusively attributed to post-formation modification. The pit was clearly the locus of intense explosive volcanism, so it is probable that a significant amount of wall-rock erosion contributed to pit-formation (and possibly reduction in peak height). The maximum dispersal of pyroclasts ejected on ballistic trajectories in the airless conditions of Mercury, as discussed by

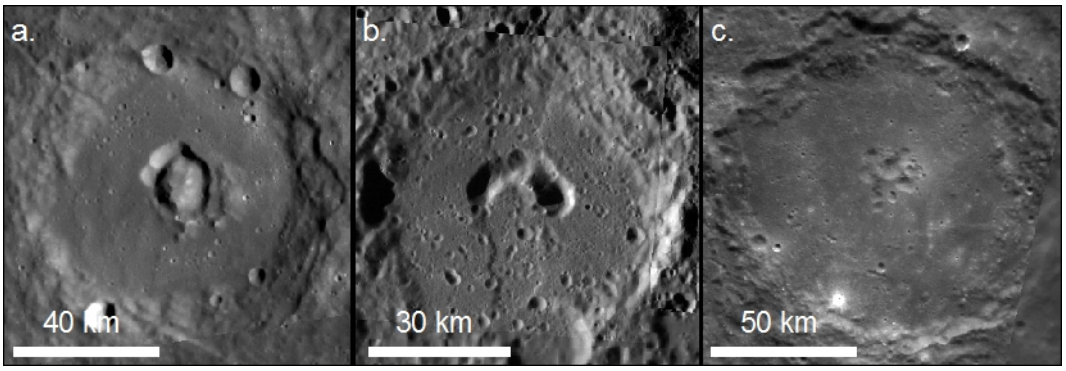

Figure 1.19: Endogenic pits with surrounding pyroclastic deposits circumferential to the impact crater centre. (a) A pit entirely encircles the central uplift (72.4° E,-21.1° N). (b) Pits circumferential to the centre of an impact crater where the central peak is not visible, probably due to volcanic infill prior to pit formation (140.5° E, -11.1° N). (c) Multiple small pits occurring circumferential to the crater centre (6.5° E, -48.4° N). Image from Thomas et al. (2015).

Kerber et al. (2009), is $X = v^2 \sin(2\theta/g)$. Taking X as 92 km, the maximum horizontal radius of the deposit from the pit centreline, g (gravity) as 3.7 m/s^2 and θ as the angle at which dispersal is greatest (45°), the minimum velocity at the vent is 580 m/s. On Earth, such velocities are typical of high-energy Plinian eruptions, in which significant vent-widening occurs (Wilson et al., 1980). However, we do not measure the volume of material ejected and subsequently the kinetic energy involved in this activity, so it is not possible to determine the relative importance of magma chamber drainage versus wall-rock excavation for pit formation. These information could be only constrained by future higher-resolution compositional data, that could potentially be acquired by the forthcoming BepiColombo mission (Fraser et al., 2010; Rothery et al., 2010).

Evidence for magma storage prior to eruption

Previous work (Thomas et al., 2014) has suggested that the horizontal scale of the largest pyroclastic deposits on Mercury (of which the 92 km radius AP1 deposit is the second-largest example) is consistent with their emplacement by either strombolian eruption or by high flux steady eruption where the majority of the magma is disrupted into large particles, 10 mm to 1 m diameter (Wilson & Head, 1981). In either case, thick deposits would be expected near the vent and thinner deposits at greater distance. The extreme dispersal of the deposits indicates a high volatile content in the magma, and this is also consistent with slow magma rise or stalling at shallow depths prior eruption. On the basis that the kinetic energy during eruption is approximately proportional to the released magma gas fraction by mass (Wilson et al., 2014) (as discussed by Thomas et al. (2014)) we find that that ejection of pyroclasts to 92 km on Mercury requires 5.4 wt% CO_2 or 4.2 wt% H_2O if each of these were the sole volatile. These are very high

values: in non-subduction settings on Earth, melt inclusions indicate 0 - 0.25 ppm CO_2 and 0.2 - 0.8 wt% H_2O in basaltic melts (Metrich & Wallace). Chemical equilibrium models suggest a combination of more reduced species such as N_2, CO, S_2, CS_2, S_2Cl, Cl, Cl_2, and COS would be present in Mercury's magmas (Zolotov, 2011). Due to their high molecular weights, a concentration greater than, or equal to, 7.6 wt% would be necessary to form the deposit if any of them were the sole volatile. As there is no reason to believe Mercury to be more volatile-rich than Earth, it is probable that such high volatile concentrations were reached by some process causing volatile enrichment in the erupted magma (Thomas et al., 2014). If magma ascend very slowly and/or is stored at shallow depths, it may become oversaturated due to crystallisation and volatiles will exsolve in the low pressure near-surface environment.

1.4.5 Summary

Our results shows that it is improbable that a steep-sided cone with associated pyroclastic deposits is a volcanic construct, but confirm the hypothesis that this feature on Mercury was formed by explosive volcanic eruption from a vent encircling a residual central peak of an impact crater. We find that the landform at this location likely represents the extreme end-member of a large class of volcanic vents circumferential to impact-crater central peak structures, indicating that crater-related faults control explosive volcanism at such locations. The scale of the pyroclastic deposit indicates that the magma had a high volatile content relative to basaltic eruptions on Earth, supporting the idea that it was stored for some time in the low-density fractured zone beneath the impact crater prior to eruption. The numerical modelling result was fundamental to assess the beginning hypothesis and impact craters simulations could be useful also in the future to determine the origin of similar structures.

1.5 Numerical modelling application: Mars

Crater modelling on Mars is very difficult due to the degradation processes which occur all over the planet. In particular, a variety of processes have been involved in crater degradation, including superimposed impacts, weathering, mass wasting, fluvial erosion and deposition, ice-related processes, lacustrine processes, lava and ash infilling, aeolian saltation, airfall deposition from dust storms (Arvidson et al., 2006; Evans et al., 2010; Rodriguez et al., 2010), regionally distributed ejecta from large impacts and impact-induced hydrothermal activity (Abramov & Kring, 2005; Schwenzer & Kring, 2009; Schwenzer et al., 2012). Impact craters strongly modify planet landscape and control fracture systems and surface/subsurface hydrology (e.g., Rodríguez et al., 2005). In fact, impact processes produce a pervasive network of fractures related to the propagation of the rarefaction waves (Melosh et al., 1992; Collins et al., 2004, 2011; Wünnemann et al., 2006) and thus favouring fluids circulation within the crust. The aim of simulating an impact process on a complex environment such as the Martian surface provides information about how different impact conditions (e.g., different impact velocities and compositional scenarios, thickness of the megaregolith) affect the crater formation but also give an estimate of the post-impact modification processes entity.

In this work we present a numerical model for the formation of the Firsoff crater (90 km of diameter) which is a strongly degraded crater located in the equatorial southern highlands of Arabia Terra at 2.6° N - 350.8° E (Mars), thought to be a locus of intense water interactions and subsequent modifications (Andrews-Hanna & Lewis, 2011; Franchi et al., 2014; Pondrelli et al., 2011, 2015; Michalski et al., 2013; Pozzobon et al., submitted). Firsoff crater is characterised by a large central layered bulge (35-40 km diameter, 1600 m elevation) and numerous mound-like landforms within it, often interpreted as mud volcanoes or spring deposits sources (Pondrelli et al., 2011; Franchi et al., 2014; Pozzobon et al., submitted) (Figure 1.20). Central inner crater bulges often display a widespread inner stratification that fills the whole interior such as Firsoff and Crommelin cases (Franchi et al., 2014; Pondrelli et al., 2011, 2015).

Among craters with bulges, Firsoff was chosen for the wide dataset available of high-resolution images as well as different resolution DTMs (MOLA, HRSC, and HiRISE respectively onboard Mars Global Surveyor, Mars Express and Mars Reconnaissance Orbiter missions) (Zuber et al., 1992; Jaumann et al., 2007; McEwen et al., 2007). Moreover, with its 90 km diameter is a representative sample of most of the Arabia Terra craters displaying the peculiar bulge that characterises some similar craters.

Through impact modelling we could better understand the subsequent geologic processes that led to crater post-impact modification, define which rheological structure of the Martian upper crust is more likely in Arabia Terra and if there are local conditions that favour the formation of central bulges.

Taking into account that Firsoff crater has been strongly affected by degradation, we

used morphometric relationships to reproduce the original morphology of the crater at time of its formation in order to have a comparison with the results of the simulations. Using iSALE hydrocode, we run a series of simulation with different set up to understand how specific parameters could affect the morphology of the Firsoff crater. Specifically, for a target composed by a double basalt layer we consider different impact velocity of the projectile (from the most probable value of 7 km/s to 12 km/s) and various thickness of the first megaregolith layer of the target (beginning from 8 km to larger thickness). Furthermore, we consider as a minor case the introduction of an anorthosite layer in the target to verify if this type of composition is likely in Arabia Terra because of recent anorthosite detection on Martian highlands (Carter & Poulet, 2013).

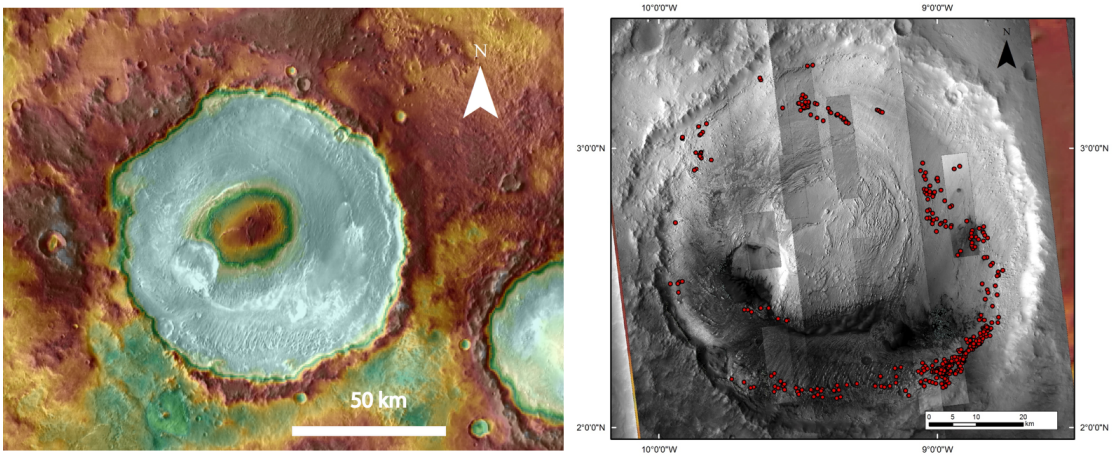

Figure 1.20: On the left Shaded relief MEGDR MOLA 128px/deg DTM, while on the right the distribution of mounds in Firsoff crater.

1.5.1 Geological context

As mentioned above, Firsoff impact crater is located in Arabia Terra at 2.6° N - 350.8° E. This region is located at the Martian topographic dichotomy with a difference in height of 4 km over a distance of 2500 km (average slope = 0.0016°). Most of the impact craters within the region display a central bulge, bearing a well-preserved stratification and a wide range of smaller morphologies like pitted cones, mounds and knobs (Pondrelli et al., 2011).

Firsoff is characterised by a big central bulge of 35-40 km of diameter located where the central peak should be. The bulge is $\sim$ 1 km above the crater floor and displays a light albedo layered sequence (Pondrelli et al., 2011; Pozzobon et al., submitted). Its shape is slightly elliptic with the major and minor axes measuring respectively 30 and 40 km, with an average areal extent of $\sim$ 1000 km^2. According to the global geologic map

from Tanaka et al. (2014) and to the more detailed map from Pondrelli et al. (2011), Firsoff Crater is located within a plateau sequence named Cratered Unit in this particular area, consisting of an etherogeoneous mixture of pyroclastites, lava flows and brecciated material (Franchi et al., 2014). The layered unit within Firsoff Crater is a sequence of thin layers present also outside the crater and overlaying in unconformity the Cratered Unit. Locally this light albedo thin stratified formation is named equatorial layered deposits (ELD). In addition many small mounds that are widespread in Firsoff crater's interior, are interpreted to have worked as pathways for subsurface fluids (Pondrelli et al., 2011; Franchi et al., 2014) and their origin and timing of formation is still under investigation (Pozzobon et al., 2013). These landforms appear as sub-circular conical features going from tens to hundreds of meters in diameter, often presenting a central orifice (Pondrelli et al., 2011). Their spatial distribution is peculiar and roughly surrounds Firsoff's central inner bulge. Most of them are clustered in the south-eastern part, while the remaining are located in the NE and SW sectors bordering the bulge. The mounds are almost absent in the NW side. According to Pondrelli et al. (2011, 2015) some of them are aligned along fault traces and fractures and seem to be genetically linked to the ELDs. These observations constrain the presence of a structural control on their formation linked to a percolating fracture network evolution and to a deep fluid source (Pozzobon et al., 2013).

The case study area involves a well-defined compositional scenario. The upper crust can be composed of a fractured basaltic megaregolith overlying an intact basalt layer, given the common basaltic composition and the widespread Noachian/Hesperian volcanic resurfacing of the Martian surface in Arabia Terra (e.g., McSween et al., 2003, 2009; Taylor et al., 2010), The thickness of this fractured basaltic megaregolith overlying an intact basalt layer is an important parameter that is under investigation since there is only a lower limit of this depth threshold, equal to 8 km, according to Pozzobon et al. (2013), defined as where the depth of a likely fluid source is linked to the surface by a hydraulically-connected fracture network. Another minor compositional scenario, that is considered in this study, consists of jointed basaltic flows on anorthosite rich crust, as it happens for the Moon highlands (Wieczorek et al., 2013). This scenario is indeed plausible given the recent discovery of anorthosite in the nearby Noachis Terra (Carter & Poulet, 2013). In particular, we do not exclude its important presence in the Martian highlands in patches corresponding to local ascent of anorthositic plutonic bodies (Carter & Poulet, 2013; Wray et al., 2013).

1.5.2 Morphological analysis

As testified by the numerous yardangs and dunes in the topographically lower parts of the crater and by the layered deposits in the central bulge (Pondrelli et al., 2011; Franchi et al., 2014), it appears that Firsoff crater has been strongly affected by eolian and

water-related degradation and infilling processes. Moreover slumping and gravitational collapses of the crater walls along listric sliding planes faults are likely (Pondrelli et al., 2011; Franchi et al., 2014). The central layered bulge formation has been interpreted as due shallow fluid interaction processes, and thus not linked to the normal crater degradation occurring on Mars by exogenous processes (Pondrelli et al., 2011; Franchi et al., 2014). The central bulge is eroded on its sides and its summit's height is roughly the same as the crater rims, while the ELD formation present in the topographically lower parts of Firsoff is still present and well preserved. This seems to support the hypothesis that some other modification processes other than normal wind degradation occurred after the impact crater formation.

MOLA (Mars Orbiter Laser Altimeter, Mars Global Surveyor mission) MEGDRs (Mission Experiment Gridded Data Records) topographic data (128 px/deg) (Zuber et al., 1992) were used for our analysis, in particular the reference topographic section was obtained with MOLA averaging the two profiles taken along the NW-SE and NE-SW direction, as shown in Figure 1.21.

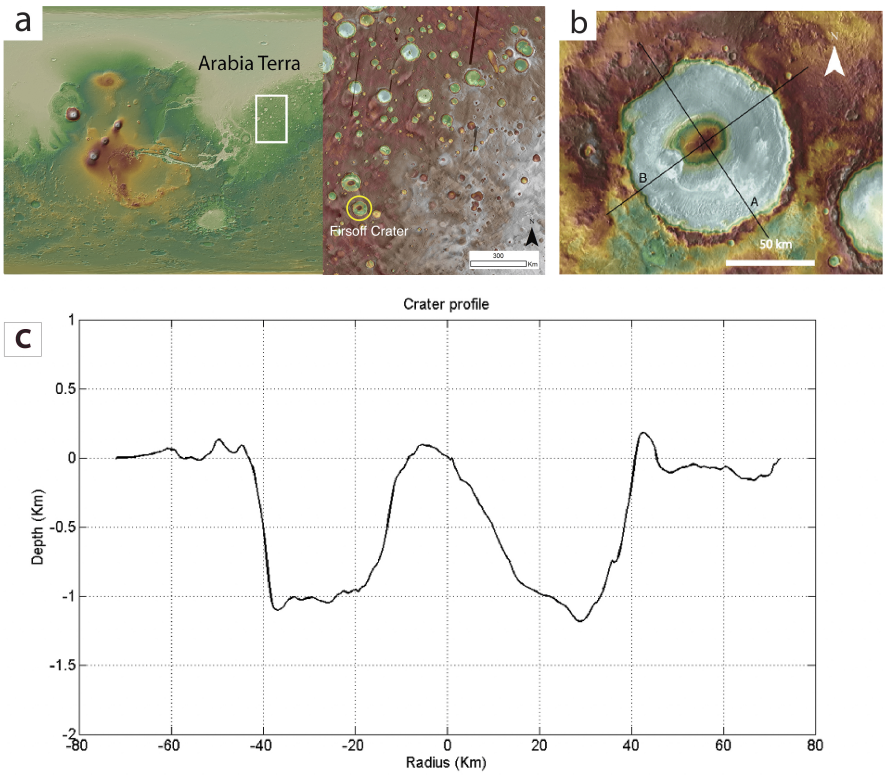

Figure 1.21: a) MOLA (Mars Orbiter Laser Altimeter) global map and detail of Arabia Terra. **b)** THEMIS daytime infrared image draped on MOLA 128px/deg DTM. **c)** Topographic section obtained averaging the two profiles taken along the NW-SE and NE-SW directions (A and B in Fig. 1.21b).

Since Firsoff crater has been also strongly affected by degradation, we expect that its pristine shape is quite different in respect to the current morphology. In fact, Firsoff appears to be heavily degraded, both by wind (widespread presence of yardangs and dunes in the southern part) and layered formations (ELDs) (Pondrelli et al., 2011, 2015). More in detail, the strong presence of ELDs suggest a pervasive interaction of the crater with acqueous environment (Pondrelli et al., 2011, 2015; Rossi et al., 2008). According to Forsberg-Taylor et al. (2004), that provides estimates of craters degradation that undergoes pervasive fluid-related modification (and also take into account airfall deposition, eolian degradation, fluvial erosion and sedimentation), we assume that the pristine diameter of this crater must have been 10% less than the current diameter that is equal to 90 km, and should have been filled up to more than half its depth. Degradation processes affect the crater morphology in different ways and all of them are responsible for the modification of the crater that results in an increase of the diameter, an important infilling and rim dismantling that lowered its height.

Therefore, adopting a pristine diameter equal to 80 km, we applied to the Firsoff case the morphometric relationships of Garvin et al. (2003), shown in Table 1.2. These equations, that link the crater diameter with the impact crater parameters such as rim height, central peak height and diameter, were defined by Garvin et al. (2003) on the basis of MOLA topographic profiles of 6000 martian impact craters. By comparing three-dimensional geometric properties, several equations were generated describing the relations between the different features of impact craters, thus allowing the original geometry of the impact craters to be reconstructed.

Parameters	Complex crater relationships	Firsoff crater case
Depth	$d = 0.36D^{0.49}$	3 km
Rim Height	$H = 0.02D^{0.84}$	0.8 km
Central Peak Diameter	$D_{cp} = 0.25D^{1.05}$	2.5 km
Central Peak height	$h_{cp} = 0.04D^{0.51}$	0.3 km

Table 1.2: Morphometric relationship derived from Garvin et al. (2003) and applied to the Firsoff case.

The same method of Garvin et al. (2003), has been utilized by Robbins & Hynek (2012) to find the complex depth/diameter relationship over different terrains, for example the relationship characterising impact craters located in the region from $-40°$ to $40°$ latitude is $d = 0.28D^{0.579}$, that implies a crater depth value in agreement with that found by Garvin et al. (2003) for the Firsoff impact crater. In Figure 1.22 it is shown the pristine crater profile, that has been reconstructed according to the parameters obtained applying the morphometric relationships of Garvin et al. (2003), and the degraded crater

profile, that has been reconstructed reducing the diameter, lowering the rim height and filling the crater, in agreement with Forsberg-Taylor et al. (2004).

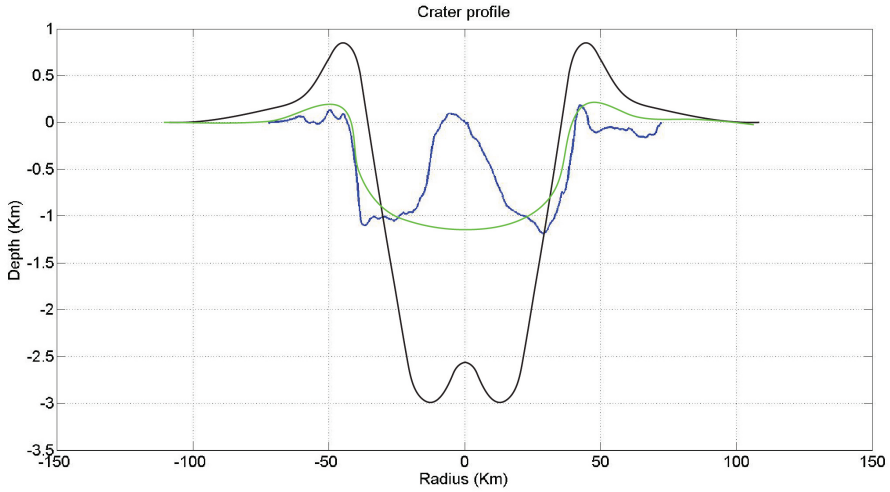

Figure 1.22: Pristine crater profile, reconstructed according to the parameters shown in Table 1.2, is shown in black, while the respective degraded crater profile is shown in green and it has been reconstructed reducing the diameter, lowering the rim height and filling the crater, in agreement with Forsberg-Taylor et al. (2004). The degraded crater profile is in agreement with MOLA topographic profile (blue).

1.5.3 Numerical modelling: model setup

The Firsoff impact involves the collision of an asteroidal origin projectile and due to the axisymmetric nature of the 2-D iSALE hydrocode, we adopt a head-on geometry, where the projectile hits perpendicularly the target surface. We have used an Eulerian approach, i.e., the mesh is fixed in space and the material flows through it (Pierazzo et al., 2008), and the resolution in our impact model was defined by the number of computational cells per projectile radius (CPPR). A spatially constant gravitational acceleration of 3.7 m/s^2 was used in the simulation. We run a series of simulation with different set up to understand how specific parameters could affect the morphology of the Firsoff crater. Specifically, we consider different impact velocity of the projectile and various thickness of the first layer of the basalt target. Furthermore, we consider as a minor case, the introduction of anorthosite media to verify if this type of composition is likely in Arabia Terra.

The basic scenario consists of a projectile which was simplified to spherical and homogeneous basalt impacting at an angle of 90°. Departure of the impact angle from the more statistically likely value of 45° is necessary due to the axissymetric nature of the iSALE hydrocode. From the Mars probability distribution for impact speeds calculated

by Le Feuvre & Wieczorek (2011) the mean impact velocity is equal to 10 km/s, but we have to include the effect of different impact angles. To take it into account the projectile speed would be $v_{average}(\sin 45°)$ which results in an impact velocity equal to 7 km/s. We approximate our impactor to a spherical basalt projectile, with a porosity of 10 % which is derived from the average of the meteorite types proposed by Britt et al. (2002). The impactor size has been estimated from the comparison between the profiles obtained by a series of runs at low resolution and by the topographic profile obtained with MOLA. Given the common basaltic composition and the widespread Noachian/Hesperian volcanic resurfacing of the Martian surface in Arabia Terra (e.g., McSween et al., 2003, 2009; Taylor et al., 2010), the upper crust can be composed of a fractured basaltic megaregolith overlying an intact basalt layer.

		Projectile	**Target**	
			1°layer	2°layer
	Material type	Basalt	Fractured Basalt	Intact Basalt
Variable	Description			
R_i	Impactor radius ($CPPR$)	15		
v_i	Impact velocity (km/s)	7		
ϕ_i	Material porosity	10%	5%	0
ρ_i	Material density (kg/m^3)		2850	2850
Y_0	Cohesion for intact material (MPa)		10	15
Y_m	von Mises plastic limit (GPa)		3.5	3.5
μ_i	Coefficient of internal friction		1.2	1.2
μ_d	Coefficient of friction (damaged material)		0.6	0.6
T_m	Melt temperature (°K)		1400	1400
ϵ	Thermal softening		1.2	1.2
η	Kinematic viscosity (m^2s^{-1})		100000	100000
τ	Decay time (s)		120	120

Table 1.3: Numerical model parameters used in the simulation.

Hence, the target structure was modeled as a double basalt layer with the depth of the first layer fixed at 8 km depth. This depth threshold has been chosen according to Pozzobon et al. (2013), where the depth of a likely fluid source is linked to the surface by a hydraulically-connected fracture network. This layering in Arabia Terra is justified by Andrews-Hanna et al. (2010), in fact this work inferred the presence of deep basalt-weathering fluids, testified also by the presence of Fe/Mg smectites on the surface. The presence of a thick basaltic level with a percolating fracture network (Michalski et al.,

2013) is also likely and provides a pathway for fluids that over deeper intact basalts. In the simulation the thermodynamic behaviour and compressibility of each material in the model is described by an equation of state (EoS). Tables generating using an Analytical EoS (ANEOS) (Thompson & Lauson, 1972) for basalt are used to represent the layering of the Martian subsurface and also the impactor. We fix a porosity equal to 5% for the top layer (8 km thickness) since a fractured basalt has a lower density (and higher porosity) than an intact basalt just by nature of cracks and larger amounts of pore space (Melosh, 2011). According to Pierazzo et al. (2008), we use T $\sim$ 1400 K as typical incipient melting temperature for basalt from estimates for its main components, namely plagioclases and pyroxenes (Ahrens & O'Keefe, 1972). We use acoustic fluidization to reproduce complex crater collapse and in the absence of better information, we assume that all materials have the same acoustic fluidization parameters. We chose parameters that give a reasonable agreement to measured crater geometries beginning from the values used by Collins et al. (2002)) and Wünnemann & Ivanov (2003) for the Moon. After investigation of kinematic viscosities we determined for the basic scenario set up a best-fit viscosity of 10^5 $m^2 s^{-1}$ with a corresponding decay time of 120 s. In Table 1.3 we summarize all the model parameters and the material properties used for our numerical simulations, where the parameters used for basalt are in agreement with those assumed in Pierazzo et al. (2005). From this basic scenario we change the impact velocity and the thickness of this top layer in order to understand how these parameters affect the impact crater formation.

Comparing different impact velocity

It is well established that changing the impact velocity will result in differences in the energy and momentum coupling to the target (Housen & Holsapple, 1990; Melosh & Ryan, 1997). The Mars impact velocity distribution is derived from Le Feuvre & Wieczorek (2011) and we can consider a possible 90° impact since the ejecta distribution surrounded the Firsoff crater is roughly symmetric (Pondrelli et al., 2011, 2015). We consider different impact velocities equal to 7 km/s, 10 km/s and 12 km/s. The first value (7 km/s) corresponds to the mean impact velocity including the effect of different impact angles, but also to the first peak of the impact velocity distribution of Le Feuvre & Wieczorek (2011). The value of 10 km/s corresponds to the mean impact velocity, while 12 km/s velocity is related to the second peak of the impact velocity distribution of Le Feuvre & Wieczorek (2011).

The resolution in our impact models was defined by the number of computational cells per projectile radius (CPPR) (Wuennemann et al., 2008) equal to 15 CPPR for each velocity case. Larger impact velocities need smaller projectile to obtain the same crater diameter, for this reason we consider different cell size dimensions as shown in Table 1.4. The results obtained from this set of simulation are shown in Figure 1.23.

Additionaly, we report the outcome of the hydrocode simulation that consider a 7.5 km projectile diameter impacting the target with impact velocity equal to 7 km/s in Figure 1.24.

Parameters	Value		
Impact velocity (km/s)	7	10	12
Cell size (m)	300	270	250
Impactor diameter (km)	9	8.1	7.5
Mesh size (CPPR)	340x430	370x480	400x520

Table 1.4: Simulation cell size dimension for a 15 CPPR projectile for different velocities.

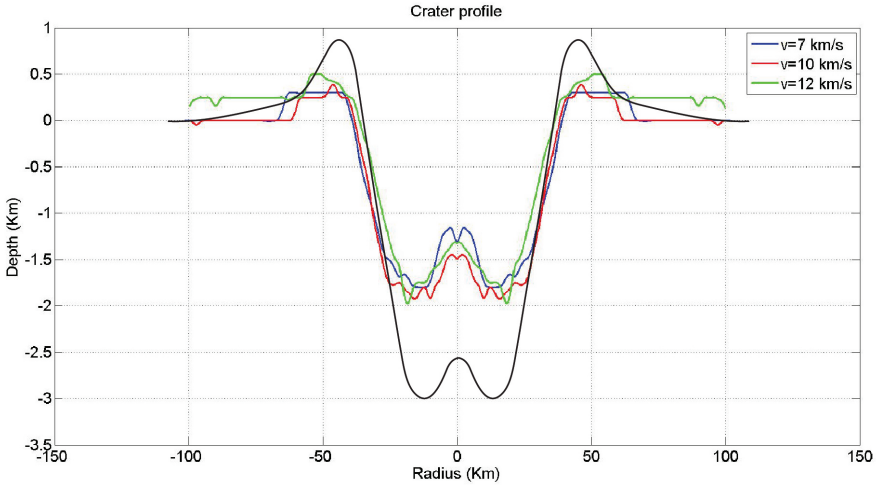

Figure 1.23: Results of the basalt case simulation compared with the pristine profile reconstructed from Garvin et al. (2003). The latter is shown in black, while the profiles involving velocity value equal to 7 km/s, 10 km/s and 12 km/s are shown in blue, red and green respectively.

Comparing different basalt thickness layer

Since the hydrocode simulation output at different velocities shows that the crater depth is not well fitted, we changed the thickness of the fractured basalt layer in order to understand how this parameter affects our result. This is also supported by the fact that the Figure 1.24 shows a damaged layer with significant plastic deformations reaching tens of kilometers beneath the crater floor. Therefore, we change the thickness of the fractured layer considering several values from 8 km to 50 km (Figure 1.25).

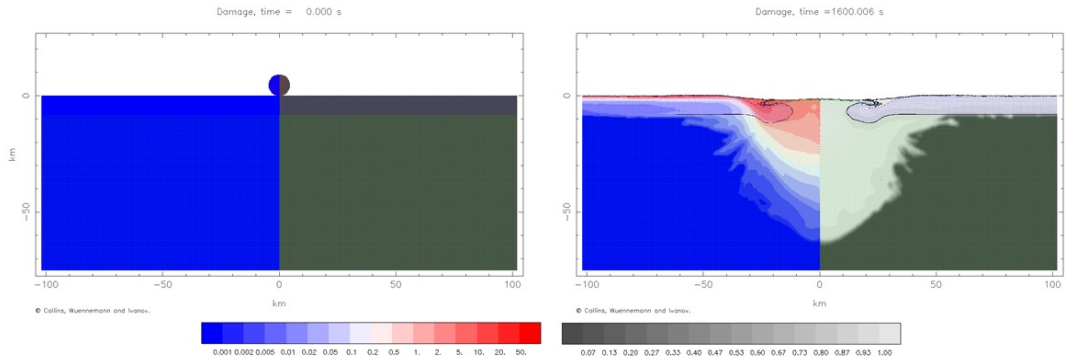

Figure 1.24: Hydrocode snapshots of the Firsoff crater formation. On the left side of each plot, contours of the amount of damage are shown on a gray scale where white corresponds to the maximum level of damage. On the right side of the plot, plastic strain contours are illustrated for the same cross section in a color scale where red corresponding to the maximum deformation while blue means node formation.

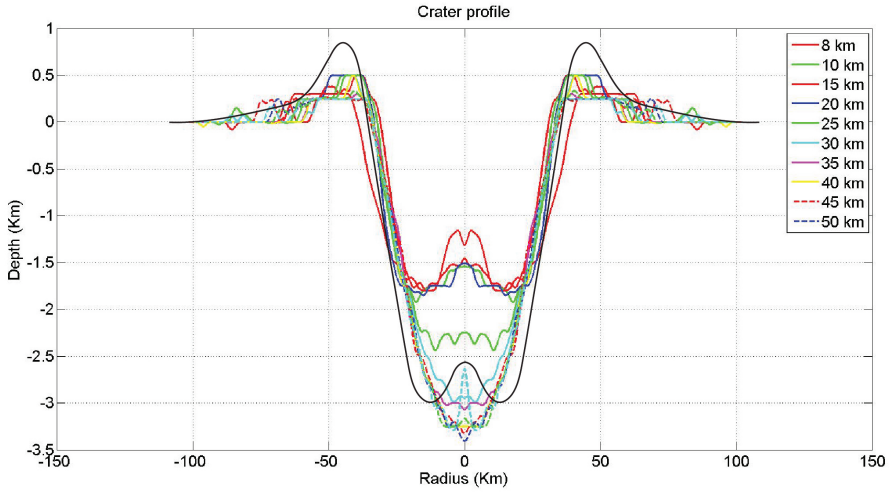

Figure 1.25: Results of the simulation compared with the pristine profile reconstructed from Garvin et al. (2003). The latter is shown in black, while the profiles involving different fractured basalt thickness are shown in different colors.

Anorthosite substratum

Another compositional scenario considered in this study consists of jointed basaltic flows on anorthosite rich crust. In fact, significant amounts of anorthositic bodies could have been produced either globally during magma ocean differentiation or primordial serial magmatism as proposed for the Moon, or locally by fractional crystallization, assimilation, or partial melting of an already evolved source (Carter & Poulet, 2013). The few

anorthosite detections on Mars would argue against a primordial crust composed of pure ferroan anorthosite as inferred for the Moon (Wieczorek et al., 2013), as well as petrological analyses on Martian meteorites. However, some volcanic activities (often associated with large crustal intrusions as in Noachis Terra (Carter & Poulet, 2013)) around the highlands were recently spotted in Arabia Terra by Michalski et al. (2013); Wray et al. (2013). They have catalogued felsic outcrops in Noachis Terra among a global population of crater floor bedrocks and attributed this lithology to impact generated volcanism from relatively high-silica reservoirs at depth. Indeed, recent CRISM observations of feldspar-rich materials in widely scattered ancient exhumed outcrops may be consistent with such reservoirs. Alternatively, feldspar-rich crater floors could have been emplaced through partial melting of basaltic crust followed by slow cooling and crystal density separation (Carter & Poulet, 2013; Wray et al., 2013). Because the literature involving anorthosites on Mars, we do not exclude their presence in patches in the Martian highlands. This not necessarily imply a Moon-like crustal formation (Wieczorek et al., 2013). We model the target as a double layer made up by a fractured basalt layer on top of rather intact anorthosite. This second layer of the target is described by a Tillotson EoS for gabbroic anorthosite (Ahrens & O'Keefe, 1982). From the model setup reported in Table 1.3 we change the intact basalt layer in an anorthosite intact layer with material properties reported in Table 1.5, in agreement with those reported in Potter et al. (2012).

Variable	Description	Intact anorthosite
ϕ_i	Material porosity	0
ρ_i	Material density (kg/m^3)	2940
Y_0	Cohesion for intact material (MPa)	50
Y_m	von Mises plastic limit (GPa)	2.5
μ_i	Coefficient of internal friction	1.5
μ_d	Coefficient of friction (damaged material)	0.6
T_m	Melt temperature (°K)	1500
ϵ	Thermal softening	1.2

Table 1.5: Numerical model material parameters for anorthosite intact layer.

We run a set of simulation considering different impact velocities, as in the basalt case, equal to 7 km/s, 10 km/s and 12 km/s. The results obtained from this set of simulation are shown in Figure 1.26.

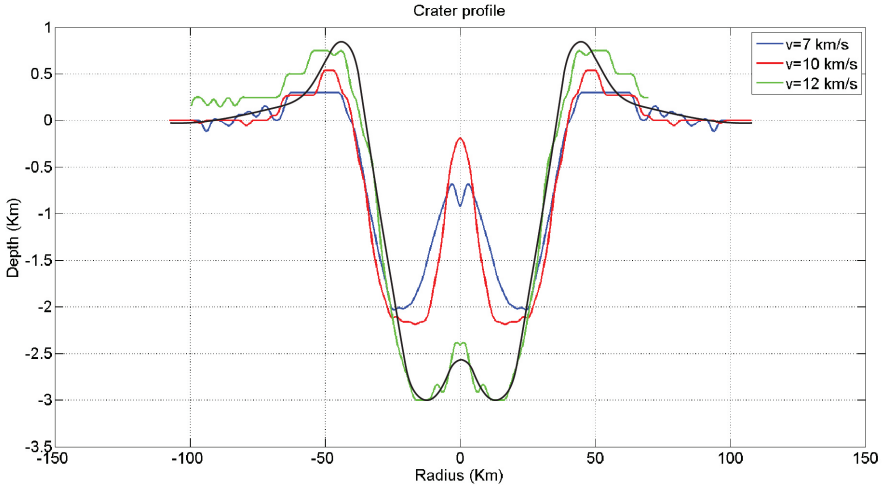

Figure 1.26: Results of the anorthosite case simulation compared with the pristine profile reconstructed from Garvin et al. (2003). The latter is shown in black, while the profiles involving velocity value equal to 7 km/s, 10 km/s and 12 km/s are shown in blue, red and green respectively.

1.5.4 Modelling results and discussion

In figure 1.23 are shown the hydrocode results coming from the set of simulations regarding the variation of impact velocities for a double layer of basalt (megaregolith with a thickness of 8 km overlying an intact basalt layer). It appears that the resulting simulation outputs are slightly similar taking into account the values from code validation against laboratory experiments (Pierazzo et al., 2008). In fact, the depth and central peak height are comparable considering that the final output of iSALE has a 3 - 4% radius uncertainty and a 12% depth uncertainty. It is noteworthy that all simulated profiles give a depth that is 1 km lower than what is expected from Garvin et al. (2003), while the central peak height is $\sim$ 0.5 km, slightly higher than what calculated from Garvin et al. (2003) (Figure 1.23).

Since a shallower crater for each velocity case was obtained, we fixed the velocity equal to 7 km/s, that is the most probable impact speed on Mars, and changed the megaregolith thickness from 8 km (minimum expected according to Pozzobon et al. (2013)) to 50 km in order to understand how this parameter affects the crater formation. This choice is supported by the fact that Arabia Terra is heavily cratered and the damage below the impact extends for ten of kilometers, as shown in Figure 1.24. Figure 1.25 underlines that the increase of the megaregolith thickness directly affects the depth of the resulting crater and the presence of the central peak. In addition, it is shown how overcoming the threshold of 20 km the crater depth predicted by Garvin et al. (2003) is reached, although we do not obtain any central peak. In accordance with the widely acceped hypothesis of the whole basaltic crust on Mars (McSween et al., 2003, 2009;

Taylor et al., 2010), considering each variaton set up of the impact model, the predicted pristine profile was never obtain. However, since we do not meet the expected pristine features calculated from Garvin et al. (2003) and because his statistic involves the whole planet, we can hypothezise a different local compositional scenario for Firsoff and most likely for bulged craters in general. For this reason a compact anorthosite layer below the basalt megaregolith was introduced, on the basis of anorthosite detection on Martian highlands (Carter & Poulet, 2013; Wray et al., 2013). A set of simulations for different impact velocities were performed as previously done on the double basalt layer. As it is shown in figure 1.26, the simulation profiles obtained for the impact velocity cases of 7 km/s and 10 km/s display similar pristine crater morphology, while the simulation corresponding to the 12 km/s impact velocity case fits correctly the calculated pristine crater depth.

From these results it is noticeable that changing the impact velocity for a double basalt layer with a megaregolith thickness of 8 km determines a crater shallower than what it is expected according to Garvin et al. (2003), while the pristine profile is well-fitted increasing the thickness of the megaregolith, especially with a depth greater than 20 km. We could advance the hypothesis that the megaregolith basalt stratum in Arabia Terra is at least 20 km and the absence of the central peak can be plausible since there are other craters in Arabia Terra with a diameter similar to Firsoff crater without a central peak or bulge.

Alternatively, the configuration involving the anorthosite media (with a thickness of 8 km) and an impact velocity equal to 12 km/s well fits the pristine profile. This can be explained by the fact that the global database of thousands of topographically characterised craters cannot consider different target properties and composition, so other different compositional scenarios should be taken into account.

For all simulation set up the simulated morphology of the central peak is not well reproduced with respect to the reconstructed pristine one, but this is an open problem also because we could only hypothesize its actual shape from Garvin et al. (2003) based reconstructions. In addition, since the present morphology of Firsoff crater is affected by later sedimentary infilling, the central bulge is not reproducible with simulations. Therefore, from the geological analysis alone is not possible to understand which part of the crater floor and central bulge should be attributed to the central peak. On the basis of the relevant difference in elevation ($\sim$ 700 m) between the central bulge and the pristine central peak, our results are consistent with the hypothesis that a latter processes occurred after Firsoff impact crater formation and subsequent degradation, such as spring related constructional processes (Pondrelli et al., 2011).

1.5.5 Summary

We have numerically modeled the formation of the Firsoff crater to define which rheological structure of the Martian upper crust is more likely in Arabia Terra and if there are local conditions that favour the formation of central bulges. According to hydrocode modelling outputs resulted two possible realistic scenarios that fit correctly the pristine crater morphology (Garvin et al., 2003). The first compositional scenario involves a basaltic crust with a fractured megaregolith whose thickness must be at least 20 km, in agreement with the fact that Arabia Terra is heavily cratered and the damage below the impact extends for ten of kilometers; in this case the crater depth is well reproduced while the central peak is absent. The second scenario involves the presence of an intact anorthosite layer below the fractured megaregolith (with a thickness of 8 km) that well reproduces the pristine crater profile, in particular the crater depth while the central peak is slightly higher. As previusly explained, the anorthosite hypothesis is consistent with the recent discover of anorthosite patches in Martian highlands, nearby Arabia Terra (Carter & Poulet, 2013). Moreover, Garvin's statistic is target independent since the morphometric relationships were defined on the basis of MOLA topographic profile and different compositional scenarios should be considered.

Therefore, Firsoff numerical modelling can give an overall idea of the behaviour of other similar craters formation that are concentrated in Arabia Terra, such as Crommelin crater. In addition, being a representative sample of the majority of Arabia Terra major craters displaying the peculiar bulge, it can provide useful data to build up hypotheses on the entity of geological processes that led to this feature's formation.

Chapter 2

Blocks formation through energetic events on a changeable surface: the case of comet 67P

In this chapter we investigate the surface of the comet Churyumov-Gerasimenko 67P to analyse its mutable nature through the images acquired by the OSIRIS instrument, the camera on board the ROSETTA spacecraft. In particular, we focus our attention on the possible energetic events that lead to the formation of boulders, i.e. blocks that are ubiquitous on the comet surface: we underline that the "boulder" terminology is not to imply any structural similarity to the meant boulders normally seen on Earth. Previous works performed on asteroids and planets link the boulders origin with impacts, but for the comet's case this process is not sufficient to explain their presence. Hence, we invoke other possible energetic formation processes that could generate these features, such as sublimation, fragmentation, outbursts and gravitational falls. Firstly, we present the size-frequency distribution of boulders on 67P, which was obtained analysing their spatial distribution and performing global and localized studies (Pajola et al., 2015). Then, in order to understand if these energetic processes occur equally on different spatial scale (m, cm and mm), we analyse higher resolution images from OSIRIS and CIVA (the panoramic cameras on board the lander Philae) instruments for a specific target region. Then, we study the Abydos site, i.e. the location where Philae is supposed to have come to rest, describing the blocks present on different spatial scale images (m-boulders on OSIRIS images and cm-pebbles on CIVA ones) to understand if they are formed by the same energetic process and if there is a possible correlation between blocks of different dimension.

2.1 Rosetta

Rosetta is a planetary cornerstone mission in ESA's Horizon 2020 long-term program which was successfully launched on 2 March 2004. This mission is currently studying its main target, the Jupiter-family comet 67P/Churyumov-Gerasimenko (hereafter 67P), with a combination of remote sensing and in situ measurements. During the cruise phase, Rosetta has observed asteroid 2867 Steins, in September 2008, and asteroid 21 Lutetia, in July 2010, secondary objective of the mission. From these two asteroids flybys, Rosetta obtained a wealth of high-quality scientific data, that lead to the high-resolution analysis of the surfaces, craters, densities and mineralogical composition (e.g. Keller et al., 2010; Sierks et al., 2011). The Rosetta spacecraft is constituted by two parts: the orbiter that has 12 scientific instruments, and the lander PHILAE which has 9 scientific experiments. All instruments are summarized in Table 2.1 and Table 2.2, respectively.

Rosetta arrived at the comet on 6 August 2014 following a 10-year journey through the Solar System. Between August and November 2014, the spacecraft orbited the comet and gathered data to characterise the nucleus and its environment. On 12 November 2014, Rosetta's lander Philae was deployed to the surface. The Rosetta orbiter tracked the comet through perihelion (August 2015), examining its behaviour before, during and after this event. Rosetta is carrying out a global characterisation of the comet, a detailed study of the physical evolution of cometary activity and of dynamic properties, surface morphology and chemical composition of this primitive body, providing the most detailed study of a comet ever attempted. The nominal end of the mission was scheduled for December 2015, but Rosetta mission has been extended until September 2016. Figure 2.1 displays an illustration of the Rosetta spacecraft and its scientific equipments, while Figure 2.2 is a representation of the instruments onboard the lander Philae.

2.1.1 OSIRIS

OSIRIS, the Optical, Spectroscopic, and Infrared Remote Imaging System (Keller et al., 2007) is the scientific camera system onboard Rosetta.

OSIRIS was built by an international collaboration of scientific institutions from six different European countries, all designing, building, integrating or supporting different parts of the camera system. The instrument comprises a Narrow Angle Camera (NAC) and a Wide Angle Camera (WAC) with a field of view (FOV) of $2.20° \times 2.22°$ and $11.35° \times 12.11°$, respectively. The NAC has a high angular resolution of 18.6 μrad/px resulting in a spatial resolution of 1.86 cm/px at 1 km distance, while the WAC has a lower angular resolution than the NAC, 101 μrad/px resulting in a spatial resolution of 10.1 cm/px at 1 km distance. Both cameras use a 2048×2048 pixels backside illuminated CCD detector with a UV optimised anti-reflection coating. The NAC is

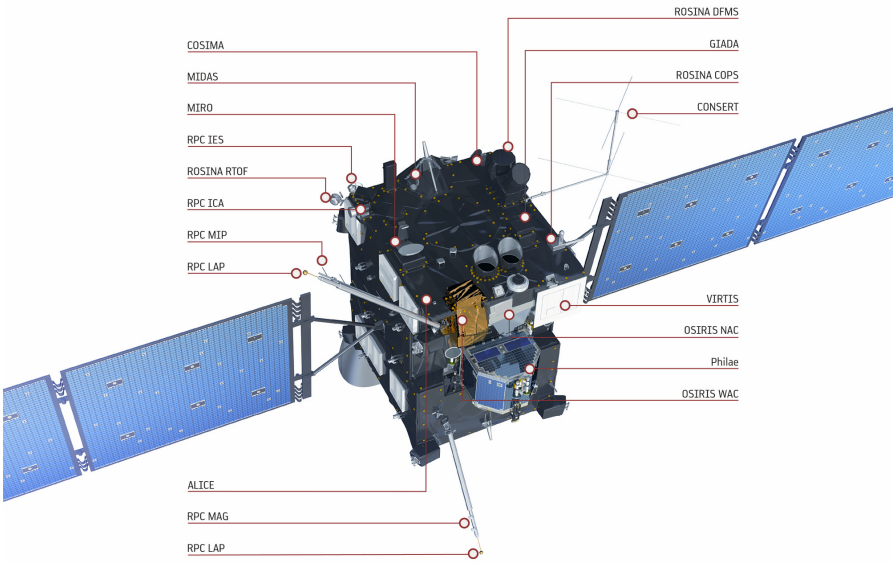

Figure 2.1: Payload instruments onboard Rosetta spacecraft.

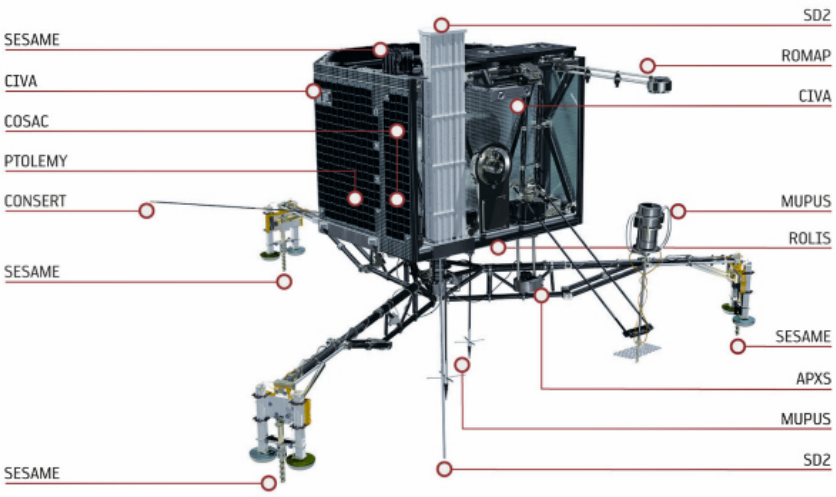

Figure 2.2: Payload instruments onboard Philae lander.

Instrument	**Scientific Goal**
ALICE	UV imaging spectrograph, analysing gases in the coma and tail of the comet, detecting water, carbon monoxide, and carbon dioxide.
CONSERT	COmet Nucleus Sounding Experiment by Radiowave Transmission, examining the nucleus interior by analysing reflected radio wave transmitted between the spacecraft and the lander.
COSIMA	Secondary Ion Mass Analyser, investigating the chemical compositions of the cometary dust.
GIADA	Grain Impact Analyser and Dust Accumulator, measuring the number, mass, momentum and velocity distribution of dust grains.
MIDAS	Micro Imaging Dust Analysis System, examining the dust surrounding the comet and delivering details of particle population, size, shape and volume.
MIRO	Microwave Instrument of the Rosetta Orbiter, verifying the abundance of molecules in the cometary nucleus and essential isotope ratios, determining the nucleus surface and subsurface temperatures and measuring the surface outgassing rate.
OSIRIS	Optical, Spectroscopic and Infrared Remote Imaging System, Multi-Color camera system with a Narrow and a Wide Angle Camera to take high resolution and wide-angle images of the nucleus.
ROSINA	Rosetta Orbiter Spectrometer for Ion and Neutral species Analysis, specifying the composition, temperature and the bulk velocity of the gas in the comet's atmosphere and ionosphere.
RPC	Rosetta Plasma Consortium, monitoring entirely the plasma environment around the comet.
RSI	Radio Science Investigation, using the frequency shifts of the spacecraft's radio signals to calculate the mass and gravity.
VIRTIS	Visible and Infrared Thermal Imaging Spectrometer, recording in details the temperature of the nucleus' surface, monitoring the comet gases, constraining the physical characteristics of the coma.

Table 2.1: Scientific instruments on board the Rosetta orbiter.

Instrument	Scientific Goal
APXS	Alpha Particle, X-ray spectrometer, measuring the elemental composition of the surface material.
CIVA	Comet nucleus Infrared and Visible Analyser panoramic and microscopic imaging system to characterise the samples and record the IR spectra of samples.
CONSERT	The lander PHILAE equipped with the CONSERT instrument which has the same task as the one on the Rosetta orbiter.
COSAC	COmetary SAmpling and Composition experiment, a gas analyser to detect organic molecules in the comet materials.
MUPUS	MUlti PUrpose Sensor for surface and subsurface science, measuring the thermal and mechanical properties of the surface layers.
ROLIS	ROsetta Lander Imaging System, a downward looking camera for exploring and photographing the landing site before and after Philae has landed.
ROMAP	ROsetta lander MAgnetometer and Plasma monitor, exploring the magnetic field and plasma of the landing site, evaluating the interaction between the landing site environment and the solar wind.
SESAME	Electrical, acoustic and dust impact monitoring at the surface.
SD-2	Drill, Sampler and Distribution (SD2) subsystem, extracting the soil of comet nucleus at discrete depths.
PTOLEMY	Gas chromatograph and isotope ratio mass spectrometer, studying the comet surface and subsurface from mass spectroscopy point of view.

Table 2.2: Scientific instruments on board the lander Philae

.

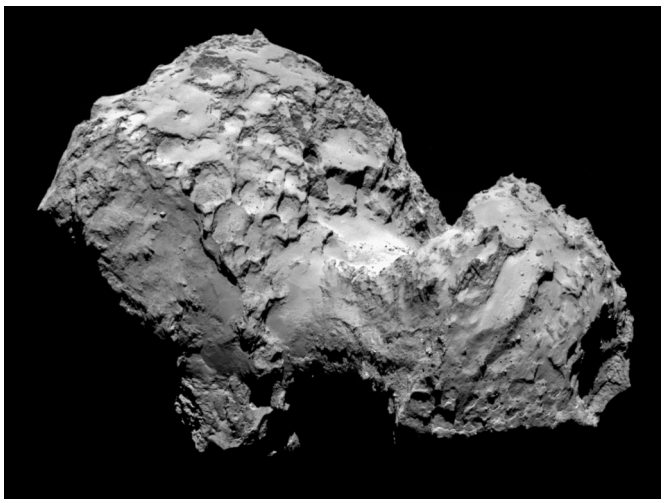

Figure 2.3: Comet 67P/Churyumov-Gerasimenko by Rosetta's OSIRIS narrow-angle camera on 3 August 2014 from a distance of 285 km. The image resolution is 5.3 metres. Image Credit: ESA/Rosetta/MPS for OSIRIS Team MPS/UPD/LAM/IAA/SSO/INTA/UPM/DASP/IDA

equipped with 11 filters covering a wavelength range of 250 - 1000 nm, while the WAC has 14 filters covering a range of 240 - 720 nm. The camera system has been designated to focus on the detailed exploration of nucleus surface as well as the dust ejection and gas emission processes near the nucleus. The main task of the NAC is to perform high resolution imaging of the comet's nucleus to investigate the structure and mineralogy of the surface and the dust ejection process. The main task of the WAC is to image the three-dimensional flow field of dust and gas in the comet's coma. In Figure 2.3 it is shown an image of the comet 67P acquired by OSIRIS NAC instrument.

2.1.2 Philae - CIVA

CIVA, Comet Infrared and Visible Analyser, is an integrated set of imaging instruments, designed to characterise the 360° panorama (CIVA-P) as seen from the Rosetta Lander Philae, and to study surface and subsurface samples (CIVA-M) (Bibring et al., 2007). CIVA-P is a panoramic stereo camera, while CIVA-M is an optical microscope coupled to a near infrared microscopic hyperspectral imager. Here, we focus on the set of CIVA-P images acquired in situ to characterise the surface materials surrounding the lander on comet 67P, reporting a brief description of the instrument from Bibring et al. (2007). CIVA-P is a set of seven identical miniaturized microcameras, implemented as five single cameras and one stereoscopic pair of two coaligned cameras with their optical axes separated by 10 cm; CIVA-P acquires a $\sim 360°$ panoramic field of view (FOV) by six adjacent FOVs of 60° each. The angular sampling of CIVA-P is ~ 1.02 mrad, which corresponds to 1 mm size feature at the distance of the landing legs, 1 m, and up to a few cm at the local horizon. The spectral response of each broadband camera extends from 400 to 1100 nm. After the descent of Philae, images were collected twice: just after touchdown, and after Philae finally came to rest, where it acquired a full panorama.

2.2 Boulders formation on comet 67P

The nucleus, its activity and the surface morphology of 67P, as observed by OSIRIS cameras, are described in Sierks et al. (2015) and in Thomas et al. (2015). Between the different morphological features characterising the surface of the comet, we focus our attention on boulders, i.e. large blocks that are ubiquitous on the surface of the comet (head, neck and body). This is the first time that boulders are observed on a cometary nucleus thanks to the high resolution images acquired by OSIRIS with respect to previous observations.

We consider multiple energetic processes to explain the boulders formation, such as thermal stress fragmentation coupled with activity and jets, pit formation, gravitational phenomena, and possibly impacts. Moreover, if the gas drag force acting on the surface is similar to the gravity, the boulders seen at a given point of the surface might have

been lifted from a different area and been redeposited on the surface, possibly undergoing fragmentation after landing.

We analyse the spatial distribution of boulders located on the surface of 67P, obtaining the first ever size-frequency distribution of a comet, which is derived using the Rosetta/OSIRIS cameras images of the nucleus. Therefore, we derive the global size distribution of boulders measured on the illuminated regions of the nucleus, which corresponds to the Northern hemisphere and covers $\sim 70\%$ of the total surface. In addition, we investigate the different distributions on localized areas of the comet discussing the possible boulders formation processes, that are summarized below (from Pajola et al. (2015)).

- **Fragmentation and sublimation.** Cracks and fractures on the cometary surface and also on single boulders (Figure 2.4) might be due to rapidly mutable insolation conditions and associated thermal stresses, in addition to outgassing of volatiles and dust from active areas (Sierks et al., 2015; Thomas et al., 2015). Moreover, some few meter-sized boulders, showing highly reflective patches with a distinctly bluer spectrum on their surfaces, could be made of H_2O ice (Pommerol et al., 2015) and so being affected by sublimation (and hence fracturing while 67P approaches the Sun). Therefore, we expect that fragmentation by thermal stress and sublimation can justify the presence of meter-sized boulders all over the surface of 67P, also considering that they are composed by dust components mixed with different super-volatile material. Fragmentation by thermal stress and sublimation activity can be two of the main causes that mutually increase the population of smaller boulders with respect to larger boulders and eliminate the smaller blocks by reducing them into dust or grains. The first effect results in a steepening of the size-frequency slope, while the second tends to make the slope fainter.

- **Outburst and gravitational falls.** The presence of niches and terraces on different areas of the comet (see, e.g., the Seth region studied in Massironi et al. (2015), Figure 2.5) with localized debris accumulation at their bases suggest that gravitational phenomena induced by differential erosion could generate fields of boulders. In particular, a differential erosion by sublimation might affect strata with different content of material prone to volatilization (more erodible strata are the ones richer in volatiles).

- **Impacts**. Previous studies of boulders, which are found on asteroids and planets, are usually related to impacts because they represent the largest fragments excavated by the collision which do not reach the escape velocity after the impact. Blocks on asteroids have been described in detail by Lee et al. (1986) for Phobos and Deimos, by Geissler et al. (1996) and Lee et al. (1996) for (243) Ida, by Thomas et al. (2001) for (433) Eros, by Küppers et al. (2012) for (21) Lutetia,

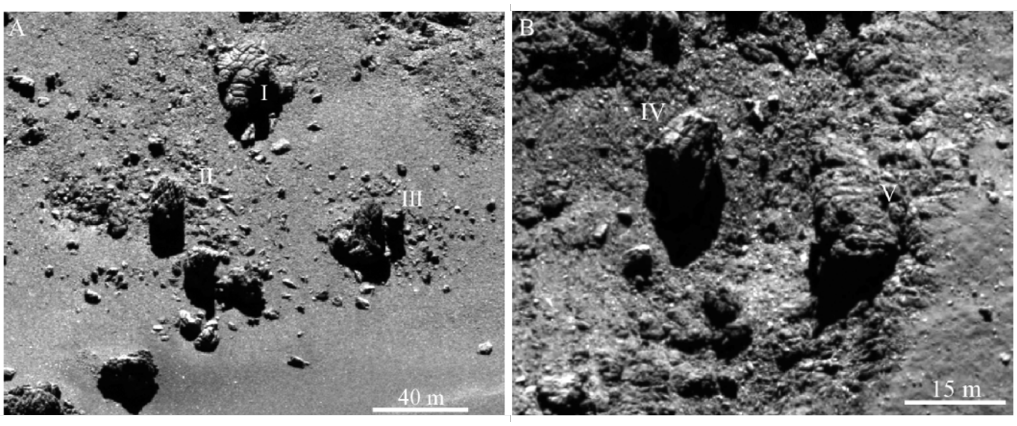

Figure 2.4: **A**) OSIRIS NAC image taken on 29 November 2014 at a distance of 16.94 km from the surface of 67P. The scale of the image is 0.32 m/px. This area is located in the Imhotep region (Thomas et al., 2015); I is a 30 m boulder crossed by multiple fractures, i.e., a good candidate for future fragmentation. II and III show examples of split materials located around a 18 m boulder (II) and a 34 m boulder (III). **B**) OSIRIS NAC image taken on 22 October 2014 at a distance of 8.1 km from the surface of 67P. The resolution of the image is 0.15 m/px. IV and V are 10 m boulders with multiple fractures surrounded by split material. Image from Pajola et al. (2015).

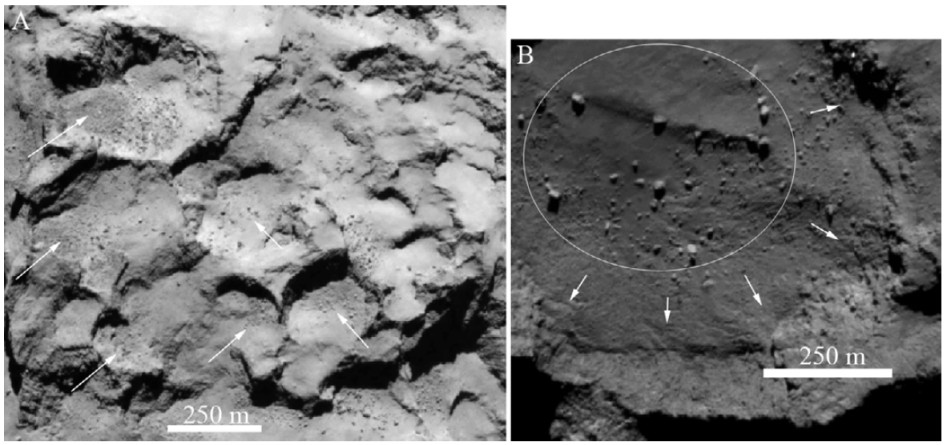

Figure 2.5: **A**) subframe of a NAC image taken on 6 August 2014. Pits in the Seth region are indicated with white arrows together with the corresponding gravitational falls. **B**) subframe of a NAC image taken on 6 August 2014 showing a subsection of the Hatmehit depression. At its center, the boulders representative of the remnant part of the past surface area are indicated with the white circle. At the margin of this depression (white arrows) there are deposits related to gravitational phenomena and differential regressive erosion by sublimation. Image from Pajola et al. (2015).

and by Michikami et al. (2008) for (25143) Itokawa. In 67P comet case, the impact formation process is not sufficient to explain the presence of boulders since current collision rates for comets are very low (see Belton et al. (2013); Vincent et al. (2014)) and would imply that most blocks were created very early in the history of the comet, but it is very unlikely because of the activity of comet surface and because of comet lifetimes (Kresak, 1981; Levison & Duncan, 1994). Hence, it is reasonable to discard the impact origin for the boulders, and invoke other processes.

- **Lifting boulders.** Another possibility to explain the presence of isolated boulders in some areas of Ma'at, Seth, Ash and Imhotep is that, once formed they can be fragmented and lifted up by cometary activity (Pommerol et al., 2015; Thomas et al., 2015). Their flight would possibly terminate because of a change in the gas density or velocity and they might land in a different location with respect to the cradle where they formed.

2.2.1 Dataset and Methodology

We used images acquired by the OSIRIS Narrow Angle Camera (NAC) on 5 and 6 August 2014, shown in Table 2.3, when Rosetta spacecraft completed its rendez-vous with the comet 67P and entered the comet orbit. The dataset, presented in Table 2.3, imaged the comet in full frame and covers the comet nucleus during an entire rotation, allowing a global study of the surface of the comet and obtaining a global, as well as localized, boulders size frequency distributions (Pajola et al., 2015). In order to obtain an homogeneous dataset and considering the scale of these images (2.44 - 2.03 m/px), we decided to consider boulders $\geq$ 7 m, which is a value above the three pixel sampling which minimizes the likelihood of misidentifications (Nyquist, 1928). The value of 7 m derives from the lowest resolution of the image obtained on 5 August at 19:43 UT, even if we were able to identify also smaller features (two pixels in diameter, $\sim$ 4 - 5 m) from their elongated shadow since the images were taken with an average phase angle of 50°. We define as "boulder" a positive relief detectable in different images with the constant presence of an elongated shadow (if the phase angle is greater than 0°) whose extension depends on the illumination geometry, in addition, a boulder seems to be "detached" from the ground where it stands. These features were identified and manually extracted from the datasets with the software ArcGIS, hence, we measured their position on the surface of the comet, and assuming their shapes to be circumcircles, we derived their maximum length, that is the diameter, and the corresponding area (Figure 2.6). We got the cumulative size-frequency distribution per km^2 using the corresponding area calculated from the 3D shape model of 67P (Preusker et al., 2015).

Day	UT	Distance from 67P center (km)	Scale (m/px)
05-08-2014	19:43	131.5	2.4
05-08-2014	21:43	126.9	2.4
05-08-2014	23:20	123.5	2.3
06-08-2014	01:20	119.3	2.2
06-08-2014	02:20	117.2	2.2
06-08-2014	04:20	113.4	2.1
06-08-2014	06:20	109.8	2.0

Table 2.3: The OSIRIS NAC images used in the analysis (from Pajola et al. (2015)).

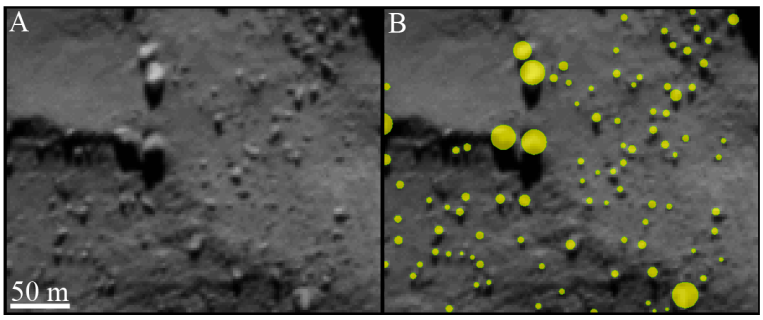

Figure 2.6: Example of the methodology used to identify the boulders on the surface of comet 67P. **A**) Subframe of a NAC image taken on 6 August 2014 at a distance of 119.3 km from the surface of 67P. The scale of the image is 2.2 m/px. **B**) the same image with the detected boulders indicated in yellow circles are presented. Image from Pajola et al. (2015)

2.2.2 Global distribution and interpretation

Boulders are ubiquitous on the head, neck, and the body of 67P. The global statistics we performed on the surface of the comet consists of 4976 boulders, whose number reduces to 3546 when we take into consideration only the boulders with diameters larger than 7 m. In Figure 2.7, the 67P global distribution of the boulders and the resulting statistic are presented. We got the cumulative size-frequency distribution of boulders over the entire illuminated side of the comet nucleus considering the 3D surface of 67P which is 36.4 km^2 (Sierks et al., 2015), finding a power-index value equal to -3.6 +0.2/-0.3. We then performed the same analysis by considering the body, the head and the neck of the comet as separate regions (Figure 2.8), in order to understand if there are any size-frequency differences between them (Pajola et al., 2015). The main results are summarized and reported in Table 2.4.

Despite the fact that the two lobes of 67P seem to be constituted by the same material, the small lobe shows a more pendent global size-frequency distribution with respect to the main one, possibly due to a more pervasive fracturing. Therefore, the power slope

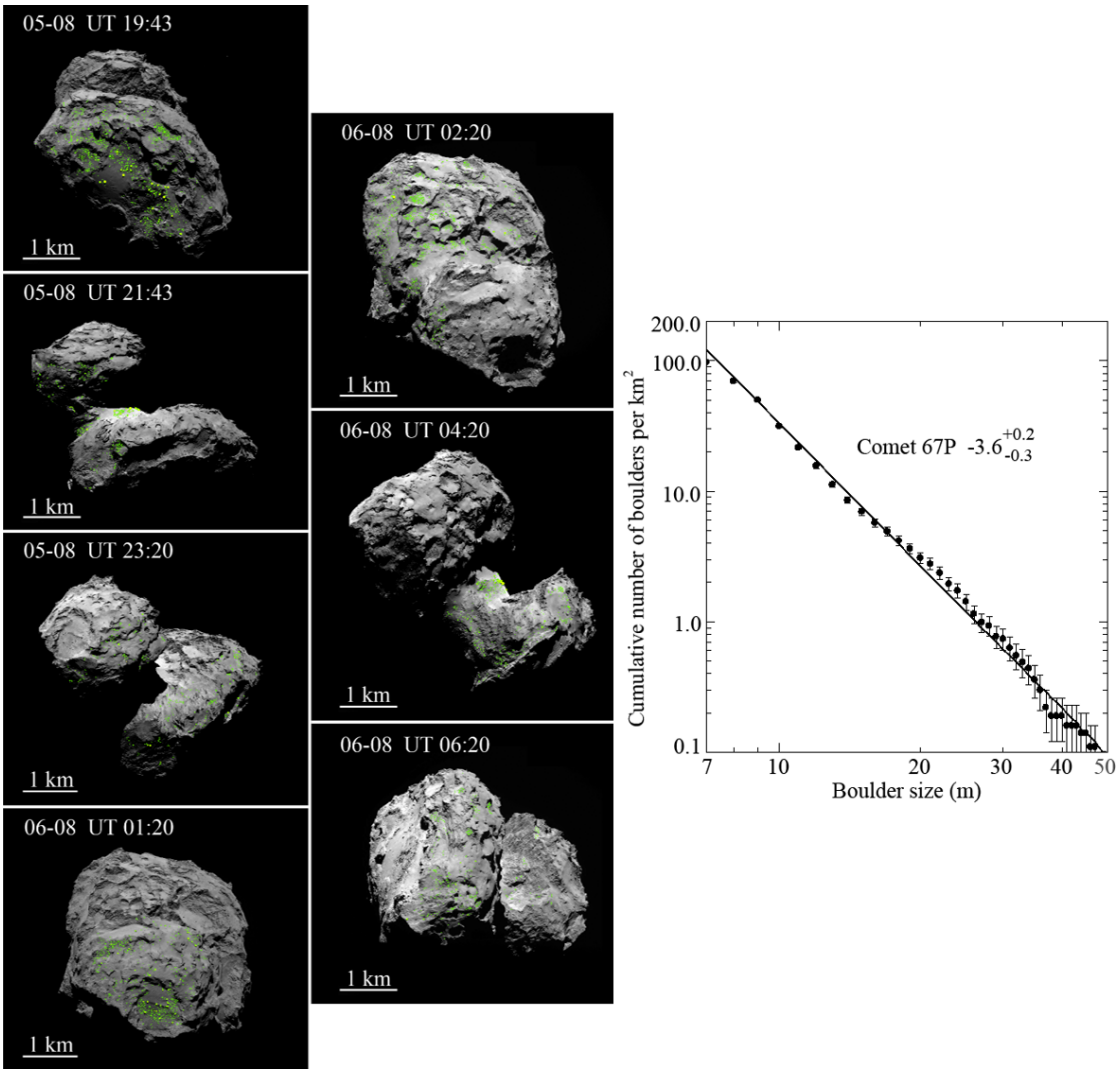

Figure 2.7: On the left the spatial distribution of the $\geq$ 7 m boulders on the illuminated side of 67P (75% of the total surface, equivalent to 36.4 km^2), derived from NAC images presented in Table 2.3. On the right the cumulative size-frequency distribution of boulders $\geq$ 7 m per km^2 over the illuminated surface of 67P. The bin size is 1 m and vertical error bars indicate the root of the cumulative number of counting boulders (as from Michikami et al. (2008)). The fitting regression line gives a power-law index of -3.6 +0.2/-0.3. Image from Pajola et al. (2015).

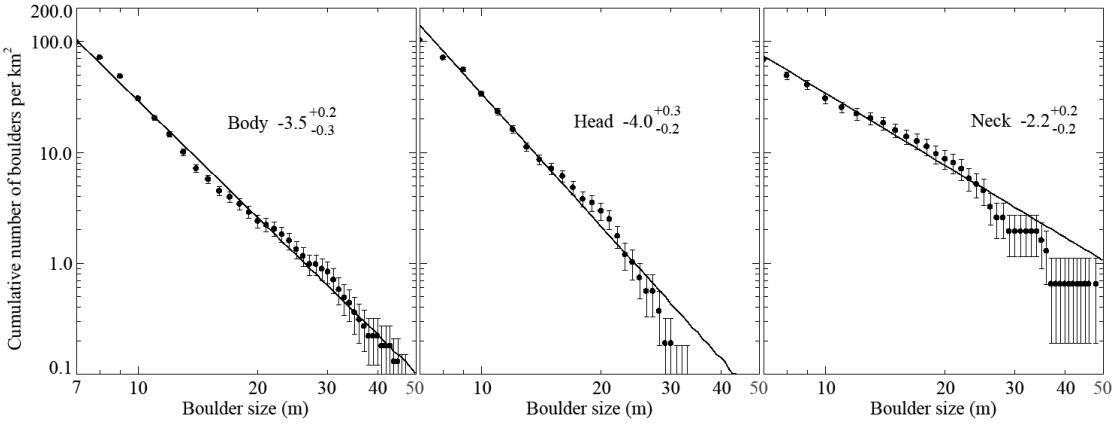

Figure 2.8: Cumulative size-frequency distribution of $\geq$ 7 m boulders per km^2 on the body, head, and neck. The fitting regression lines gives a power law index of -3.5 +0.2/-0.3, -4.0 +0.3/-0.2 and -2.2 +0.2/-0.2 for body, head and neck respectively. Image from Pajola et al. (2015)

Name	Area$_{3D}$ (km^2)	Tot # boulders $\geq$ 7 m	# 7 m boulders per km^2	Power-index	+	-
All	36.4	3546	97	-3.6	0.2	0.3
Body	22.5	2218	99	-3.5	0.2	0.3
Head	10.8	1115	103	-4.0	0.3	0.2
Neck	3.1	213	69	-2.2	0.2	0.2

Table 2.4: Names of the different regions, their area from the 3D shape model, the total number and surface density of boulders $\geq$ 7 m, power-law index, and associated error.

of boulders distribution is a measure of the degree of fracturing: higher values being related to more pervasive fracturing (i.e. more small-size boulders with respect to the larger ones). From this analysis, we can say that similar processes occurring on the surface should produce a more pendent global size-frequency distribution on the head, with respect to the body on the basis of the pre-existing structural framework and fracture density (Pajola et al., 2015).

On the other hand the neck shows a power-slope distribution, i.e. -2.2 +0.2/-0.2, that is different from those of body and head, suggesting that the boulder field located on the neck area is the result of blocks falling from the contiguous Hathor cliff.

2.2.3 Size-frequency distribution of localised areas and interpretation

We then derived the size-frequency distribution per km^2 of localized areas on 67P assuming the naming convention used to identify the regions on 67P of Thomas et al.

(2015) (Figure 2.9). In particular for the main body we have chosen three areas representative of the layered/niches region of Seth and Ash (region 1) (Massironi et al., 2015), one depression on Ash, a smooth region within Imhothep (Auger et al., 2015) and a layered region in Khepry (region 2). On the head, besides the blocks distinguishable at the Hathor layered cliff, we focused on the talus of the Nut and Hatmehit depressions (El-Maarry, M. R. et al., 2015; La Forgia et al., 2015). We derived the cumulative size-frequency distribution per km^2 using the corresponding area computed by the 3D shape model of 67P for each different morphological area. The purpose of this analysis is to understand how the size-frequency distribution slopes differ when considering specific geomorphological contexts and possible different origins of boulders deposits.

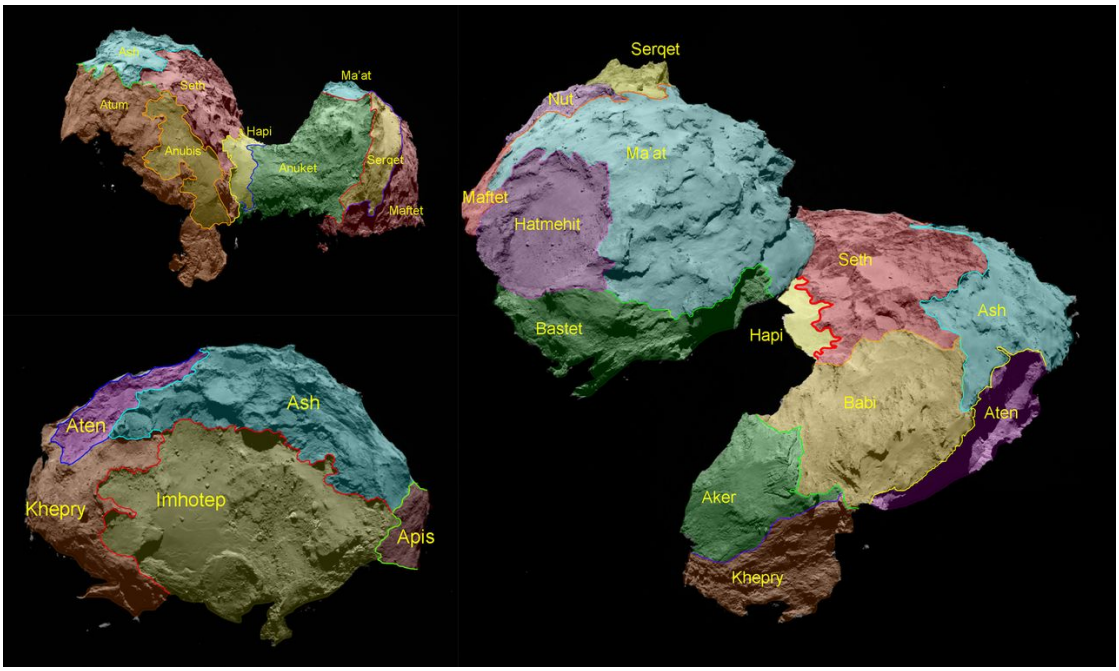

Figure 2.9: Regional definitions and nomenclature based on large-scale unit boundaries. Image from Thomas et al. (2015)

In Table 2.5 we reported all power-index values obtained on the specific locations of the comet 67P, dividing them in the following way (from Pajola et al. (2015)):

- Body 1 A consists of a rough layered region with niches and cliffs and a layered terrain mainly dominated by terraces covered by smooth deposits. The power-law index, equal to -4.2, is lower respect to the specific pit (B and C) locations; this could be justified by the contribution of boulders produced by gravitational processes not necessarily accompanied by jet activity and sublimation processes;
- Pit regions (i.e., body 1 B, body 1 C and body 2 C) show an higher power-law

index (from -5.8 to -6.5) and they are representative of a pervasive fragmentation, probably caused by related jet activity and active sublimation. The origin of these pits can be explained by roof collapses induced by sublimation of sub-surface layers, possibly accompanied by short-lived mini-outbursts (Vincent et al., 2015). After formation, such pits can expand in diameter via sublimation and retreat of their enclosing walls. Sublimation and gravitational falls likely control the walls retreat which can eventually collapse. The final result is that the enlarged to collapsed pit floors are covered by dust and debris falling from the enclosing walls. The highest fragmentation we see on these areas can be then related to the fact that such boulders formed during the collapse, but afterwards local activity and jets, that likely accompanied the boulders' genesis too, kept working locally, further fragmenting the remains and hence, steepening the power-law indices. The pit region located on the body 2 presents similar behaviour of the two pits present on Seth, therefore it is possible that this area has been affected by the same mechanism;

- Two depressions covered by boulder deposits, i.e. Body 2 A and Head B, where possibly an extended collapse occurred in the past, leaving the big boulders as "remnants" of the event. Both regions present a size-frequency distribution dichotomy that can be explained by two different deposits with boulders, i.e. talus deposit at the depression margins and smooth terrain with boulders. Smaller material at the foot of the scarps surrounding such depressions can be interpreted as the down-fallen remains of the outgassing, sublimation activities occurring at the walls, whereas deposits with boulders located at the center of the depression are likely related to the former genesis of the depression through roof-collapse phase, hence they are older and not renovated. In both cases two power indeces are present, a first trend ranging between -3.6 and -3.4 and a second trend with a slope of -1.0. The fact that older deposits show lower slopes than the fresher, repeatedly renewed ones, is an important hint that fragmentation of bigger boulders is dominant in an early stage of the deposit generation and development, whereas disappearance through sublimation of smaller boulders become much more relevant in later stages and longer periods;

- two regions, i.e. Body 2 B and Head A, where gravitational taluses are present, showing a similar power-indeces ranging between -3.8 and -3.9. The first area is located at the boundary between Kephry and Ash, while the second is located on Nut. It is worth noting that this distribution is very similar to the steeper trends of the talus located at the two depressed region.

By comparing the cumulative size-frequency distributions of akin geomorphological settings, we derive similar power-index values. This suggest that, despite the selected loca-

Name	Geographical unit	Area$_{3D}$ (km^2)	# 7 m boulders per km^2	Power index	+	-
Body1 A	Seth/Ash	4.96	100	-4.2	0.7	1.1
Body1 B	Seth	0.10	950	-6.5	0.3	0.4
Body1 C	Seth	0.08	688	-5.8	0.3	0.5
Body2 A trend 1	Imhotep	0.19	485	-3.6	0.1	0.2
Body2 A trend 2	Imhotep			-1.0	0.1	0.1
Body2 B	Khepry/Ash	0.29	385	-3.8	0.1	0.2
Body2 C	Ash	0.16	769	-6.4	0.3	0.4
Head A	Nut	0.17	424	-3.9	0.3	0.2
Head B trend 1	Hatmehit	0.49	350	-3.4	0.2	0.1
Head B trend 2	Hatmehit			-1.0	0.1	0.2

Table 2.5: Power indices of the slope of the cumulative boulder size-distribution per km^2 of localized areas on comet 67P.

tions are on different and often opposite sides of the comet, similar sublimation/activity processes, pit formation or collapses, as well as thermal stresses/fracturing events widely occurred on several areas of the comet, shaping its surface into the appearance we see today.

Therefore, we classified the boulder formation and evolution as below (from Pajola et al. (2015)):

1. collapses/pit formation and creation of depressions with subsequent escape of high-pressure volatiles and consequent high fracturing are characterised by power-law indeces of about -5 to -6.5;

2. gravitational events triggered by sublimation and/or thermal fracturing causing regressive erosion present power-law indeces of about -3.5 to -4;

3. evolution of the original material formed during both the collapsing or the gravitational event, not particularly renewed, or present in areas where continuous and high sublimation occurred or is still occurring show power-law indeces of about -1 to -2.

2.3 Abydos site

By using OSIRIS NAC and CIVA images, we analyse the distribution of boulders and pebbles located on the Abydos region, where Philae is expected to be. The distribution comparison is relevant in order to correlate and understand if the same energetic formation processes occur equally on different scales on the comet (m, cm and mm). In fact, by means of different resolution images, we obtained several size-frequency distribution for: (i) boulders larger than 7 m from the study reported in Pajola et al. (2015), (ii) boulders up to 1 m from higher resolution images used to analyse the Abydos site (Lucchetti et al., 2016), (iii) pebbles (mm-scale structures) visible on CIVA images.

Before presenting the boulders analysis, we summarize below the Philae descent and the identification of its plausible location, describing its geological context (from Lucchetti et al. (2016)). Philae lander was delivered on the nucleus on 12 November 2014, when the comet was at 3.0 AU from the Sun and first touched down at 15:34 UT at the selected Agilkia "J" landing site on the head of the nucleus of 67P failing to anchor to the surface. Then, it bounced three times for an additional two-hour flight (Biele et al., 2015) before finally landing at a site later named Abydos, about 1 km away from the first touchdown. During the lander descent the comparison between high resolution images acquired by ROLIS (ROsetta Lander Imaging System) on board Philae (Mottola et al., 2007; Mottola et al., 2015) with those obtained by OSIRIS (Optical, Spectroscopic, and Infrared Remote Imaging System, Keller et al., 2007) allowed the identification of the first touchdown point. In addition, Philae's ROMAP (Rosetta Lander Magnetometer and Plasma Monitor, Auster et al., 2007) provided precise timing of the various contact points through magnetic field measurements and subsequently identifying the final settling of the lander in Abydos site at 17:32 UT (Heinisch et al., 2015). During the nearly 57 hours of prime Philae mission the CIVA camera (Comet Infrared and Visible Analyser, Bibring et al., 2007) took images providing a panorama of the final landing site revealing a rough terrain dominated by agglomerates of consolidated materials similar to cm-sized pebbles (Bibring et al., 2015; Poulet et al., 2015). After Philae exhausted its remaining power on 15 November 2014, a huge multi-instrument attempt was performed in order to find the lander exact location. Thanks to CONSERT experiment (Comet Nucleus Sounding Experiment by Radio wave Transmission, Kofman et al., 2007), it was possible to indirectly identify the location of the lander within an ellipse of 16 x 160 meters in size by using radio signals sent between Philae and Rosetta. This ellipse is located just outside the rim of the Hatmehit depression, but it could be refined because it strongly depends on the assumed shape model of the comet. Afterwards, the comparison between OSIRIS Narrow Angle Camera (NAC) images taken before and after the landing allowed the possible identification of Philae on images acquired in mid-December 2014 at a distance of approximately 20 km (ESA Rosetta blog, 2015; Lamy et al., 2015).

The putative Philae's position was reported as a few bright pixels on OSIRIS NAC

images acquired in mid-December 2014, at very close proximity to the ellipse derived from CONSERT instrument (ESA Rosetta blog, 2015). This identification was found after a comparison with an image taken before the landing with similar geometric conditions. Despite the different spatial resolution, all topographic details match in both images except for one bright spot located on the post-landing image (Lamy et al., 2015). Some bright pixels at the same location were also seen on another OSIRIS NAC image taken on 6 December 2014 at 10:52:53 UT (Figure 2.10A, top panel). The image was acquired using the Orange filter (649.2 nm) with a phase angle of about 90° and at a distance of approximately 20 km above the nucleus surface, resulting in a spatial scale of 38.7 cm/pixel. Even if Philae is expected to be in the shadowed part, we chose this image because its better viewing geometry allows a more accurate analysis of the area surrounding the lander.

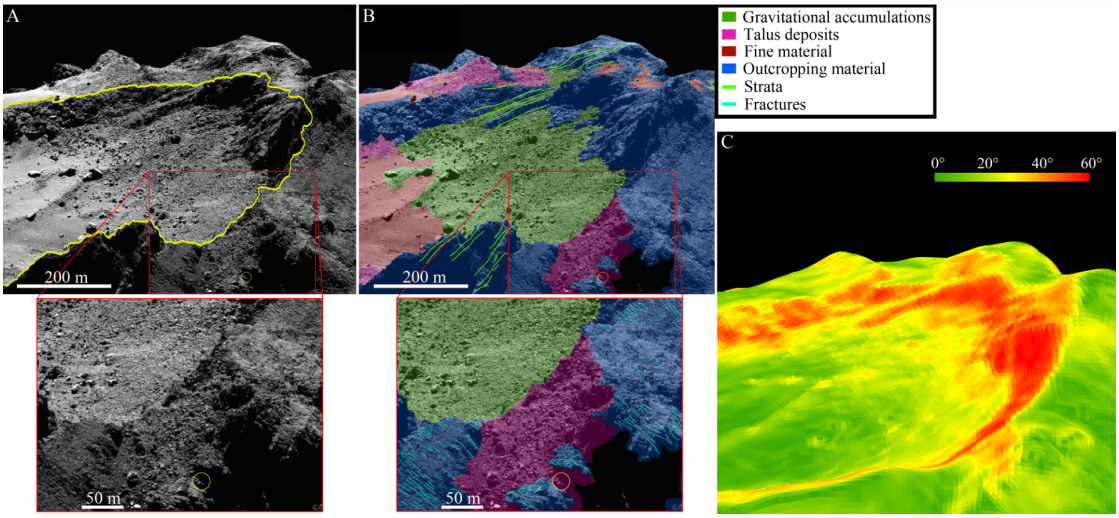

Figure 2.10: [**A**] OSIRIS NAC image acquired on 6 December 2014 at 10:52:53 UT at an average phase angle of 90° (top panel) with a close up of the Abydos site (bottom). The region surrounding the putative landing site of Philae **is** identified here by a yellow circle, while the Hatmehit depression is outlined in yellow on the top panel. [**B**] The geomorphological map identifying the main geological units, produced on the image shown on the top panel of Figure 2.10A, is displayed at the top panel with the close up of the Abydos site showing both geomorphological units and linear features (bottom panel). [**C**] Gravitational slope map of the image obtained using the 3D shape model, derived with the the Stereo-Photoclinometry (SPC) technique, and the gravitational potential model derived assuming an homogeneous nucleus and accounting for the centrifugal force due to the nucleus rotation. Image from Lucchetti et al. (2016).

Geomorphological analysis

In Figure 2.10 the geomorphological map of the Abydos site and its close surroundings is presented. The site where Philae came to rest is located on the small lobe of 67P,

next to the Hatmehit depression (Thomas et al., 2015). We made use of the image's high spatial resolution to identify distinct geomorphological units:

1. on the Hatmehit depression, we confirmed the results of La Forgia et al. (2015) regarding the distinction between the gravitational accumulation deposits (green unit, Figure 2.10B) and the fine material covering the layered consolidated terrain (pink unit, Figure 2.10B);

2. the surrounding structure of Hatmehit is characterised by the presence of outcropping material that is often layered as well as fractured (mapped as blue unit, Figure 2.10B). The fractures are typically 30 - 50 m-long, roughy parallel to each other, and show a preferred propagation orientation roughly perpendicular to the rim of Hatmehit. This fracturing pattern is similar to patterns observed in the neighboring Bastet region (Thomas et al., 2015; El-Maarry et al., 2015) but on a smaller scale. Fractures are ubiquitous on the surface of the comet, particularly in consolidated regions (El-Maarry et al., 2015). Therefore, their presence around the Abydos site is an indication of a high degree of consolidation in the region whereas their propagation pattern suggests that they could be linked to the formation of the Hatmehit depression;

3. the Abydos landing region is a 0.02 km^2 unconsolidated talus deposit distinct from the surrounding blue unit also by the presence of numerous boulders within what appears unconsolidated material. The suggested Philae landing site location is on this bouldered deposit, but limited by two outcrops that limit its horizon (Bibring et al., 2015).

In addition, we analysed the gravitational slopes of the Abydos site in order to describe the gravitational framework of the region using the 3D shape model of the comet, which was created on the basis of the entire NAC dataset that has provided multiple stereo coverage of the cometary surface. For our calculation we have used the shape model derived with the Stereo-Photoclinometry (SPC) technique (Jorda et al., 2012, submitted). The gravitational slope is defined as the angle between the local surface normal pointing inside the nucleus and the gravity vector. The region surrounding the putative Philae's position is found in correspondance with high gravitational slope ranging from 20° to 50°, usually associated to collapse due to erosion by sublimation (Figure 2.10C).

2.3.1 Boulders distribution

A large quantity of boulders is present in the Abydos region, specifically on the talus deposit. The identification of boulders has been performed with the same method explained previously. We manually identified these features as polygonal shapes deriving

their maximum length, i.e., the diameter, and the corresponding area. Since the higher resolution of the image, we decided to identify the boulders as polygons and not as circumcircles (as in Pajola et al. (2015)). By using the 3D SPC shape model, we geo-localized each boulder on the surface of the comet in terms of coordinates and distance (of about $\sim$ 18 km for each boulder), hence we calculated the exact diameter. In this

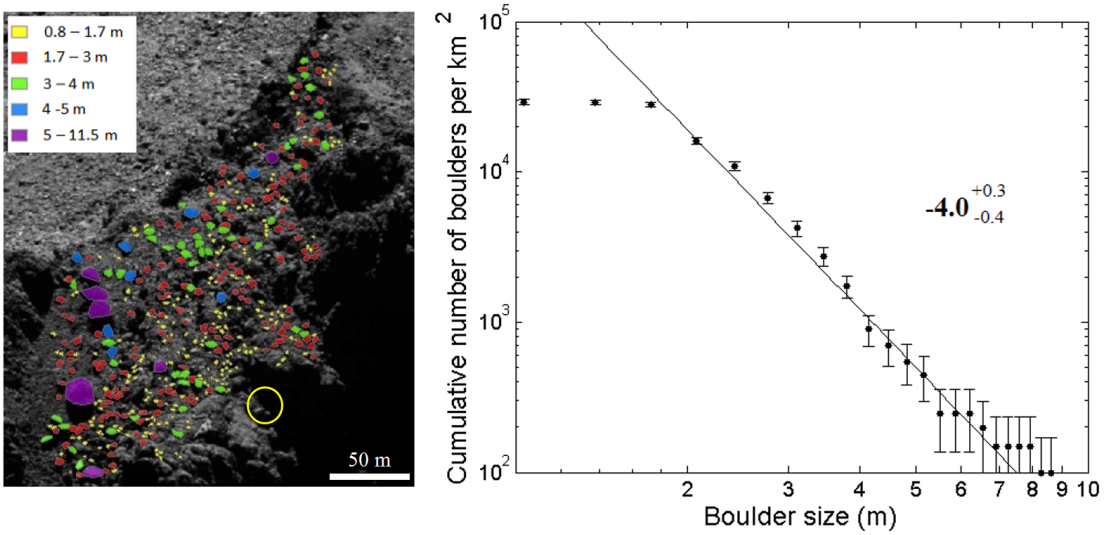

Figure 2.11: Left panel shows the spatial distribution of boulders on the Abydos site, where Philae is identified by a yellow circle. Boulders smaller than 1.7 m, where the boulder size corresponds to the length calculated from the corresponding area, are in yellow and are not taken into account in the statistic. The right panel shows the cumulative size-frequency distribution of boulders larger than 1.7 m identified on the Abydos site. The bin size is 34 cm and vertical error bars indicate the root of the cumulative number of counting boulders (as from Michikami et al. (2008)). The fitting regression line gives a power-law index of $-4.0 + 0.3/ - 0.4$. Image from Lucchetti et al. (2016).

analysis, we considered boulders larger than 1.7 m, which is a value above the three pixel sampling which minimizes the likelihood of misidentifications (Nyquist, 1928), even if we are able to identify also smaller features from their elongated shadow since the image was taken with a phase angle of 90°. We did not include boulders smaller than 1.7 m in the statistical analysis because the slope of the size-frequency distribution naturally drops off approaching the three pixel detection limit (Mazrouei et al., 2014). The total numbers of boulders identified in this analysis is 447, 323 of which have diameters larger than 1.7 m. Figure 2.11 shows the spatial distribution of boulders in the Abydos region. We obtained the cumulative size-frequency distribution per km^2 using the corresponding area (0.02 km^2) calculated from the 3D shape model of 67P (Preusker et al., 2015) through the triangulation of boulder point cloud. We then derived the cumulative size-frequency distribution of boulders using a constant-size bin of 34 cm (approximately one

pixel resolution of the OSIRIS NAC image in the Abydos region at a distance of 18 km). A power law index of -4.0 +0.3/-0.4 is found (Figure 2.11, right). The fitting regression line used to obtain the power-law index does not consider those points that are equally cumulatively repeated above 6 m because they represent a poor statistic that has not to be considered by the fit. This effect has been already observed for bigger boulder sizes as presented in Pajola et al. (2015) and Michikami et al. (2008).

Interpretation

The resulting power law index of the boulders cumulative size frequency distribution is correlated with the morphological unit where the boulders are located. This unit is identified as the talus deposit, shown in Figure 2.10, that has a gravitational source and it could be interpreted as rockfall material deposit that is originated from erosion, as supported by high slopes ranging from 20° to 50°. We compared the power law index obtained in this work (-4.0 +0.3/-0.4) to the results of global and local boulders distribution of Pajola et al. (2015), reported in subsection 2.2.3. The talus bouldered deposit under study shows a similar size-frequency distribution of other talus deposits located on different areas of the comet, as the one located at the boundary between Khepry and Ash and the one on Nut. Boulders on this type of area are classified as those correlated with gravitational events triggered by sublimation and/or thermal fracturing causing regressive erosion. Hence, we can give the same explanation for the Abydos talus deposit too, since the derived power coefficient (-4.0 +0.3/-0.4) is similar to the power law index of second type of boulders (power law from -3.5 to -4).

2.3.2 Pebbles distribution

The CIVA cameras onboard Philae provided the first ever in situ images of the surface of a comet (Bibring et al., 2015). The panorama acquired by CIVA at the landing site on the 67P comet, the Abydos region, reveals a rough terrain dominated by fractures and agglomerates of consolidated materials. A quantitative analysis of the microscopic structures is presented here, in particular we obtained the pebble size-frequency distribution, which will be compared to the size distribution of boulders surrounding the landing site (Lucchetti et al., 2016) and of $\geq$ 7 m sized boulders globally distributed on the comet (Pajola et al., 2015). Between the images collected by CIVA, we used those acquired by the camera 3 and camera 4 (hereafter referred to image 3 and image 4), which have been mosaicked in Figure 2.12 to show the sunlit part of the nucleus surrounding Philae (at the time the images were acquired).

In image 3, it is identified one Philae foot most likely in contact with the neuclus, while in image 4, the CONSERT antenna is visible in contact with surface (Figure 2.13). The dimensions of the Philae foot and CONSERT antenna (5 mm in diameter, 693 mm

long), apparently in contact with the nucleus, enable us to estimate the distance of this cometary material, and the scale of the structures we identified (Bibring et al., 2015).

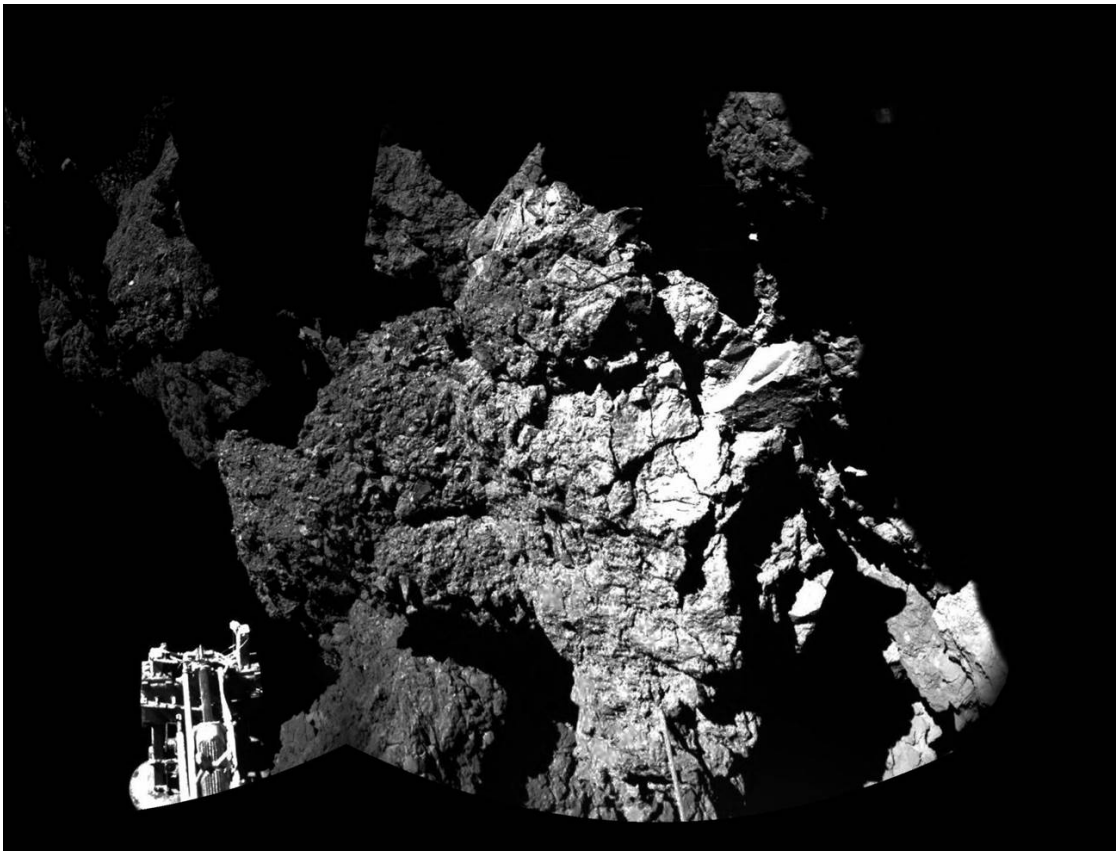

Figure 2.12: Mosaic of CIVA images acquired by cameras 3 and 4 (Bibring et al., 2015).

We have counted 283 and 412 pebbles on images acquired by camera 3 and 4 respectively, as shown in Figure 2.14. We manually identified them with the same method explained before, i.e deriving their diameter and the corresponding area. The resolution of the CIVA images and the orientation of the surface are unknown, hence, we can import errors in obtaining the pebbles size-frequency distribution. To solve this problem, we decided to take into account only pebbles that are in specific parts of the images. In image 3, there is one Philae foot and from its known dimension we can approximate the resolution of the image that is valid only for pebbles located on the right bottom part. On image 4 there is the CONSERT antenna that seems to be in contact with the comet surface, hence, we can achieve the pixel scale that is valid only for pebbles that are on the left part of the image. Therefore, we decided to use this set of pebbles, which are 449, to obtain the pebbles size-frequency distribution using a pixel scale equal to 0.91 mm/px for image 3 and 0.625 mm/px for image 4. The pebbles considered in this analysis are

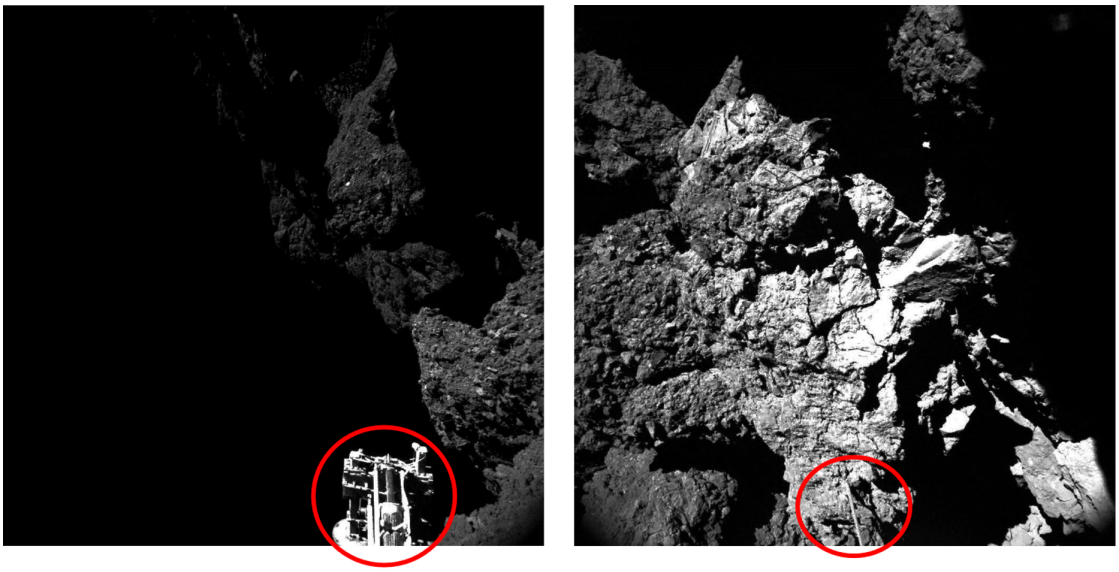

Figure 2.13: On the left the image acquired by camera 3, exhibiting the foot likely in contact with the nucleus (red circle). On the right the image acquired by camera 4, exhibiting one CONSERT antenna, in contact with the nucleus (red circle). Images from Bibring et al. (2015).

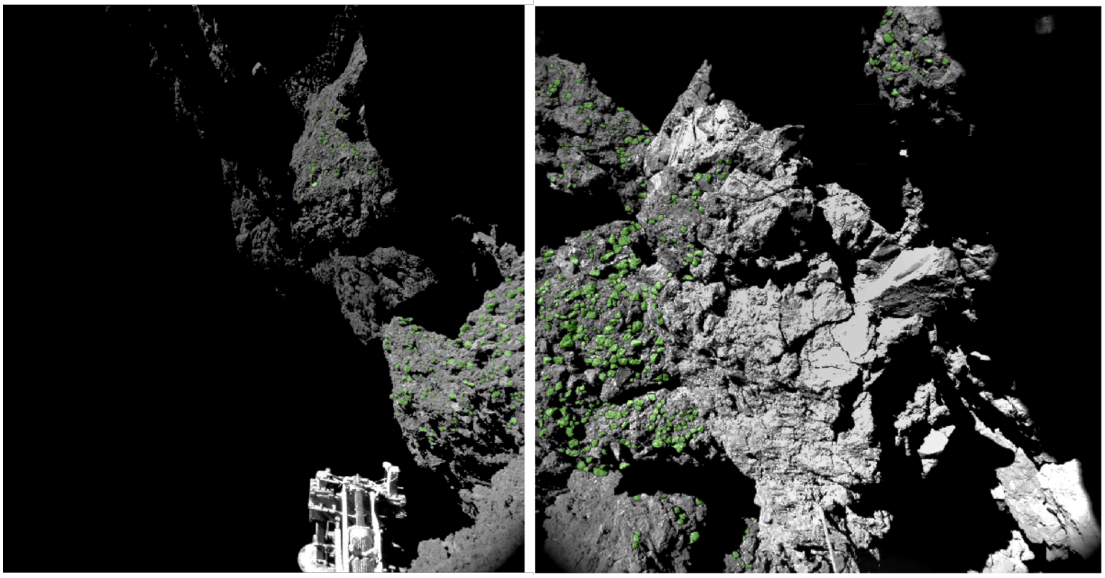

Figure 2.14: On the left the spatial distribution of the pebbles on the image acquired by camera 3, while on the right the spatial distribution of pebbles present on the image acquired by camera 4.

shown in Figure 2.15. We consider a bin of 0.625 mm, which is approximately one pixel resolution of the CIVA image 4, and pebbles larger than 3.2 mm, value above the three pixel sampling which minimizes the likelihood of misidentifications (Nyquist, 1928). We did not include pebbles smaller than 3.2 mm because no pebbles were identified with this dimension.

Respect to previous boulders analysis, we could not find a fitting regression line capable to fit all data, but we obtain two different behaviour for 2 different size ranges. For pebbles between 3 and 5 mm, whose number is 92, we obtained a power-index value of -0.36 +0.01/-0.01, while for 321 pebbles between 5 and 11 mm we obtained a value of -2.94 +01/-0.2. Regarding pebbles larger than 11 mm, we did not find a power slope since the statistic is poor (only 32 pebbles with dimension larger than 11 mm). Hence, we got the cumulative size-frequency distribution for pebbles, which is presented in Figure 2.16.

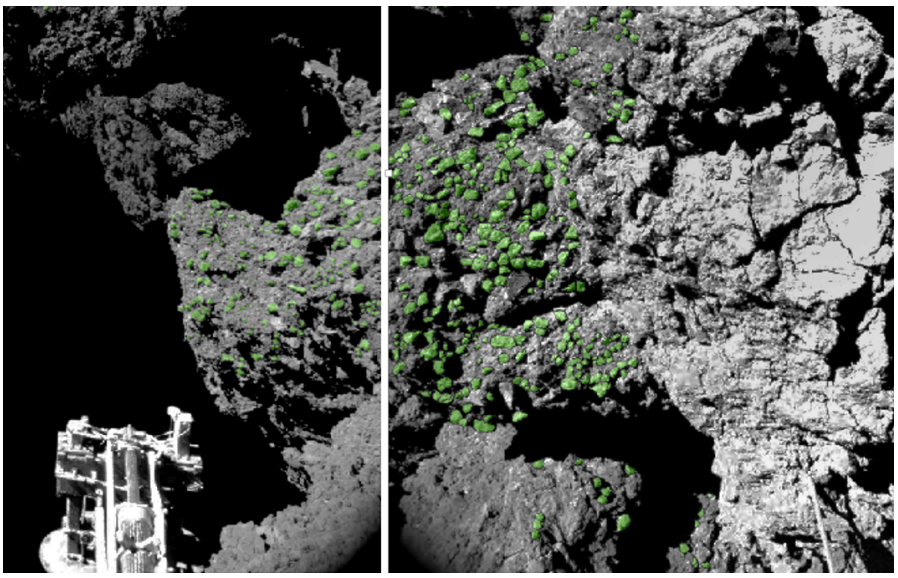

Figure 2.15: The set of 449 pebbles used is shown in these two images. The choice is determined by the resolution of the images, that can be approximated by the dimension of the Philae foot and CONSERT antenna in image 3 and 4 respectively. The pixel scale is equal to 0.91 mm/px for image 3, while it is 0.625 mm/px for image 4.

Interpretation

The nature of pebbles might be discussed in relation to both endogenic and exogenic processes that could explain their formation.

The analysis of the Abydos region is helpful for the interpretation of CIVA data analysis. As stated before, the putative Philae's position is on a 0.02 km^2 bouldered deposit,

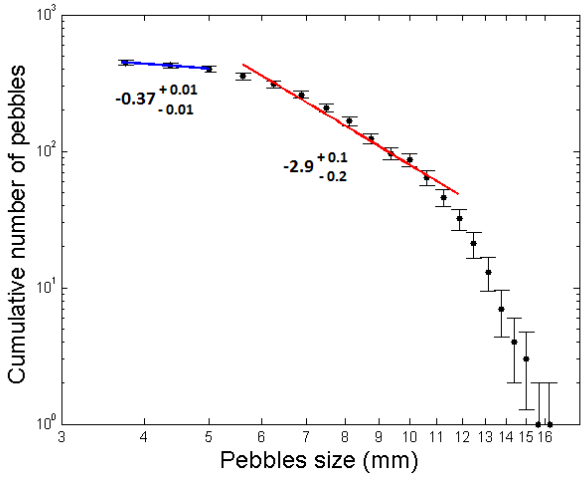

Figure 2.16: The panel shows the cumulative size-frequency distribution of pebbles larger than 3.2 mm identified on the CIVA images. The bin size is 0.625 mm and vertical error bars indicate the root of the cumulative number of counting boulders (as from Michikami et al. (2008)). The fitting regression line is not unique, but we can see two different distribution with power indeces equal to -0.36 +0.01/-0.01 and -2.9+0.1/-0.2, respectively.

limited by two outcrops that are fractured and layered. We recognized fractures in the Abydos region that suggest a brittle nature of outcropping material and often cut across strata heads. The evidence of these parallel linear features on the region is in agreement with the presence of stratification as a dominant structural aspect of 67P throughout its entire bilobed-shape (Massironi et al., 2015). As explained in Massironi et al. (2015) the comet stratification shows that the two lobes are the expression of two independent objects, perhaps formed as pebble-pile planetesimals, that are evidently characterised by onion-like stratification several hundred meters thick. Hence, the consolidated material strata belonging to outcrops can be representative of primordial stratification. This interpretation can support the hypothesis that Philae could be on primordial terrain. In this respect, the rough terrain dominated by agglomerates of consolidated materials, cm-sized pebbles (Poulet et al., 2015), revealed by CIVA image acquired by cameras 3 and 4 (Bibring et al., 2015), could be indicative of the formation process from which the initial nucleus formed. This view is also supported by numerical simulations in which small icy bodies in the outer Solar System formed from collapsing clouds of small pebbles (e.g., see Wahlberg Jansson & Johansen (2014) for a review).

On the other hand, comparing the pebbles size frequency distribution with the boulders analysis on 67P is useful to understand if boulders and pebbles are produced by the same fragmentation process and, hence, the same mechanisms occur equally at different scale (m, cm or mm scale). In fact, as recent structures, they could be the result of current erosive processes that affect the comet (fracturing microscopic process, sublima-

tion processes, non-escape and redeposition of particles previously emitted from other regions of the comet). Unfortunately, the power-law index found for both pebbles behaviour is not similar to the ones found by previous boulders analysis. In addition, we have only few images of CIVA and at the moment we do not know if future images will be downlinked because of the Rosetta orbit. From this consideration we can conclude that the pebbles could be formed primordially or, on other hand, we still do not know how fragmentation processes act in detail on the comet surface, and on the formation of smaller features as pebbles. In this context, a more powerful and detailed study about fragmentation process must be performed to better understand the pebbles origin and give the right explanation to the size-frequency distribution we see from the images.

2.4 Summary

In this chapter it is presented the first ever size-frequency boulders distribution per km^2 of a comet, 67P/Churyumov-Gerasimenko, using the ESA Rosetta/OSIRIS images of the nucleus (Pajola et al., 2015). We obtained the size-frequency distribution of boulders larger than 7 m on the entire illuminated side of the nucles (which corresponds to 70% of the comet surface at the beginning of August, 2014), as well as the boulders distribution on the body, head and neck. In addition to this, we derived the size-frequency distribution per km^2 of localized areas on 67P that are located on different and often opposite sides of the comet. Nevertheless, we obtained similar cumulative size-frequency distributions when akin geomorphological settings are present, suggesting that similar activity processes, pit formation or gravitational collapses, as well as thermal fracturing events likely occurred in different areas of the comet. To understand if these energetic processes occur equally on different spatial scale of 67P, we performed a detailed analysis of the Abydos site using higher resolution images. Firstly, through OSIRIS images, we found that the boulders deposit, around the Philae plausible location is strictly related to the geomorphological unit where it stands. This is in agreement with what found previously on low resolution scale, in particular with the results coming from the different localised areas. Indeed, the derived power coefficient of the Abydos talus deposit (-4.0 +0.3/-0.4) is similar to the power law index of second type of boulders (power law from -3.5 to -4) and, hence, can be correlated with gravitational events triggered by sublimation and/or thermal fracturing causing regressive erosion. In addition, we analyse images coming from the panorama acquired by CIVA at the landing site to assess the hypothesis that boulders formation processes explained before occur also on smaller spatial scale. A quantitative analysis of one ubiquitous microscopic structure (grains that look like pebbles) has been presented and the pebble size distribution are reasonably well fitted by power-laws having different cumulative indeces. As recent structures, they could be the result of current erosive processes that affect the comet (fracturing microscopic process,

sublimation processes, non-escape and re-deposition of particles previously emitted from other regions of the comet), but a more powerful and detailed study about fragmentation process must be performed. In fact, the power law indeces found for pebbles are not consistent with those found for boulders and, hence, it is more difficult to classify the pebbles distribution in the same way of the previous case studies (Abydos site and localised areas of boulders larger than 7 m). On the other hand, given the consolidated nature of the pebble agglomerates, a formation in an inhomogeneous granular media could be however preferred. Indeed, an intriguing possibility is that these particles may be left over relics of the formation process, as there are several lines of evidence (especially lack of thermal and aqueous alteration processing as expected if it would be the collisional relics of larger bodies) that the nucleus could be primordial (Davidsson et al., submitted), and not a collisional rubble piles of a large body (Morbidelli & Rickman, 2015).

Chapter 3

Europa

The Jovian satellite Europa was discovered in 1610 by Galileo Galilei and it is the smallest of the four Galilean moons named in his honor. The space exploration of Jupiter's satellite system began with the Pioneer mission. The first close-up view of Europa was provided by the two Voyager flybys in March and July 1979. A bright smoothed surface was discovered, crossed by long cracks that implied a crust subject to tectonic stress. In addition, the lack of impact craters suggested a relatively young surface (Smith et al., 1979b,a).

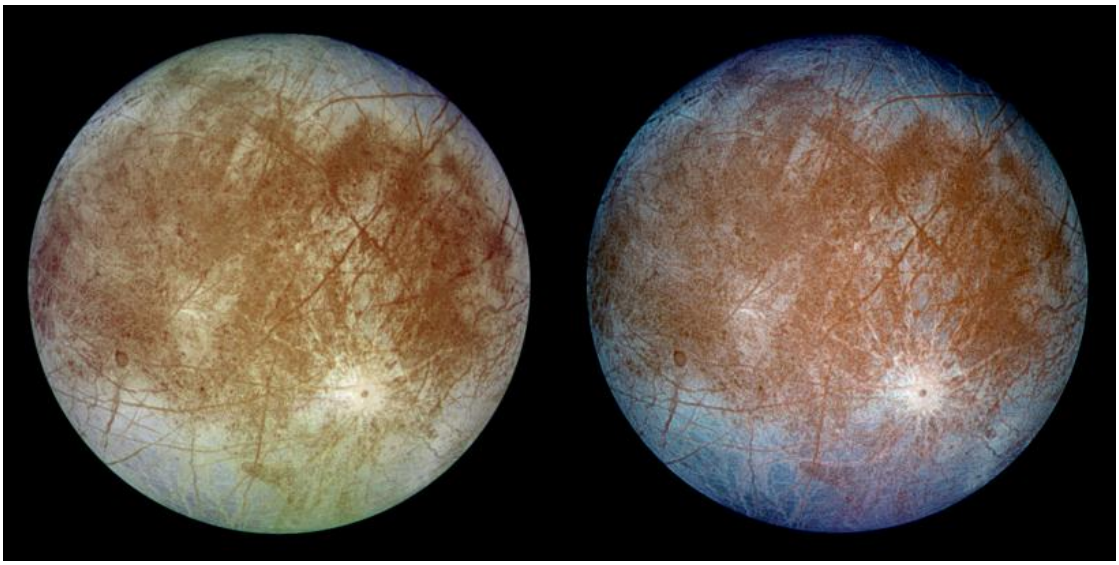

Figure 3.1: This image, taken by Solid State Imaging (ISS) on board Galileo Orbiter, shows two views of the trailing hemisphere of Jupiter's ice-covered satellite, Europa. The left image shows the approximate natural color appearance of Europa. The image on the right is a false-color composite version combining violet, green and infrared images to enhance color differences in the predominantly water-ice crust of Europa. Image credit: NASA/JPL/DLR.

New insights about Europa were provided by the Galileo mission, which orbited the Jupiter system since December 1995 to September 2003. During the Europa flybys, multiple instruments on board the satellite collected a wealth of data providing a huge step forward in the knowledge of the satellite. High resolution images data, obtained with the Solid State Imaging (SSI) system (Belton et al., 1992), confirmed a smooth surface of the satellite with very few impact craters, whose size frequency distribution returned an estimation of the surface age equal to 40 - 90 Myr (Bierhaus et al., 2009). High resolution observations revealed different features on Europa surface such as chaos regions, large ringed features, lineae, maculae and lenticulae (e.g. Doggett et al., 2009), as shown in Figure 3.2.

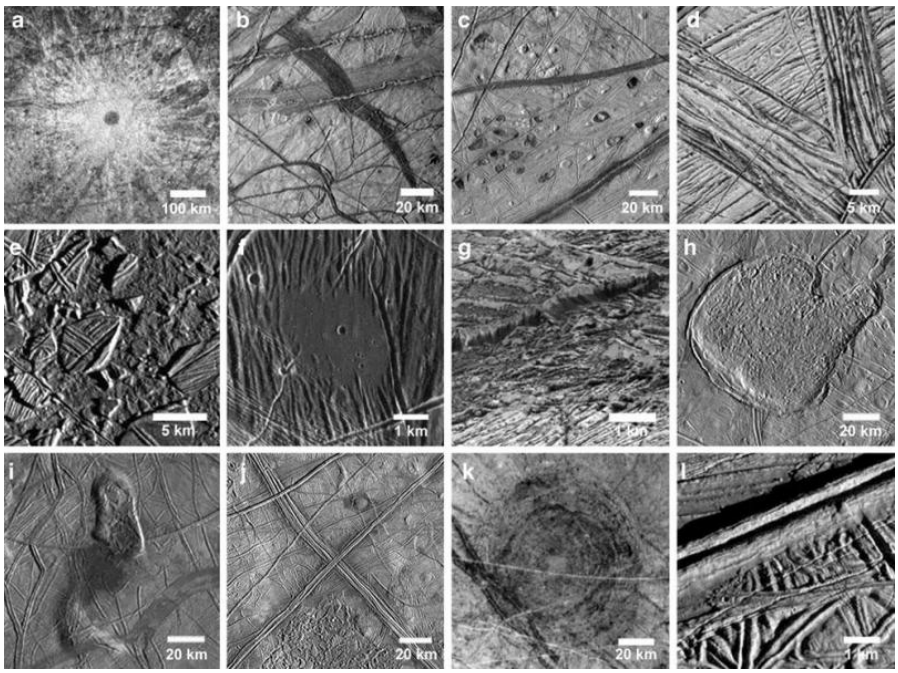

Figure 3.2: Variety of surface features on Europa. Shown here are (a) the impact crater Pwyll, the youngest large crater on Europa; (b) pull-apart bands; (c) lenticulae; (d) ridge complexes at high resolution; (e) Conamara Chaos; (f) dark plains material in a topographic low; (g) very high-resolution image of a cliff, showing evidence of mass wasting; (h) Murias Chaos, a cryovolcanic feature which appears to have flowed a short distance across the surface; (i) the Castalia Macula region, in which the northernmost dome contains chaos and is ∼900 m high; (j) regional view of two very large ridge complexes in the Conamara region; (k) Tyre impact feature, showing multiple rings; and (l) one of Europa's ubiquitous ridges, at high resolution. Image from Pappalardo et al. (2013)

Moreover, the data returned from the Galileo spacecraft suggested the presence of a subsurface ocean; indeed (i) geological observations provided indirect evidence for a liquid ocean (e.g. Carr et al., 1998; Pappalardo et al., 1999) and (ii) the observed tectonic

patterns can be explained by non-synchronous rotation of the interior, which requires a decoupled crust, i.e. a thin ice shell above a liquid water ocean (Geissler et al., 1998; Greenberg et al., 2000). In addition, thermal models of the interior suggest that a portion of the outer icy shell could be liquid today (e.g. Schubert et al., 1986; Spohn & Schubert, 2003). The tidal heating, caused by the three-body Laplace resonance with Io and Ganymede, is considered the energy source required to maintain a liquid water ocean; this possibly compensates the loss due to heat conduction or convection through the crust (e.g. Cassen et al., 1979). In addition, the detection of an induced magnetic field is consistent with the presence of a shallow conductive subsurface ocean (Khurana et al., 1998; Kivelson et al., 2000; Zimmer et al., 2000; Schilling et al., 2007).

Analyses of the radio Doppler data suggest that Europa is differentiated, consisting of a metallic core, a rocky mantle and a ice-liquid water outer shell (Anderson et al., 1997, 1998). The radius of the metallic core is unknown because of its uncertain composition, while the thickness of the outer ice-liquid water shell ranges from 80 to 170 km (Sohl et al., 2002). Gravity data cannot distinguish between the solid ice and liquid water layers because of their similar densities, but there are estimates of the icy shell thickness that range between $\leq$ 1 km (e.g. Carr et al., 1998; Billings & Kattenhorn, 2005) to 20 km (Schenk, 2002). On the other hand, thermal models suggest that the liquid ocean below the crust should be located at a depth of 30 to 60 km (Hussmann et al., 2002; Spohn & Schubert, 2003). A detailed review of Europa's interior and surface properties is reported in Part II and Part III of Pappalardo et al. (2009).

Europa possesses a tenuous atmosphere too (called exosphere as it is not permanent and it is not dominated by collisions) which comprises mainly the following populations: H_2O, released mainly through ion sputtering caused by the energetic ions of Jupiter's magnetosphere that impact the moon's surface (Brown et al., 1982; Plainaki et al., 2010, 2012; Cassidy et al., 2013) and secondarily through sublimation (Shematovich et al., 2005); O_2 and H_2, both species produced through chemical reactions among different products of H_2O radiolytic decomposition (Johnson, 1990; Shematovich et al., 2005; Cassidy et al., 2010; Plainaki et al., 2010, 2012, 2013); and some minor species like Na and K (Brown & Hill, 1996; Brown, 2001; Leblanc et al., 2002, 2005) and H, O, HO_2, and H_2O_2 (Baragiola, 2003).

A direct measurement of the main atmospheric species has not been performed yet, since the limited available observations are just proxies of the bulk constituents (e.g. the OI UV emission can be a proxy for O_2). The discovery of an O_2 atmosphere was made by Hall et al. (1995, 1998) using the Hubble Space Telescope (HST) observations of ultraviolet line emission of atomic oxygen. The ratio of the two observed emission lines at 1304 Å and 1356 Å was used to identify dissociative excitation of O_2 as the origin of the emissions. Later, the observations of the Ultraviolet Imaging Spectrograph (UVIS) onboard Cassini confirmed the existence of a tenuous O_2 atmosphere during

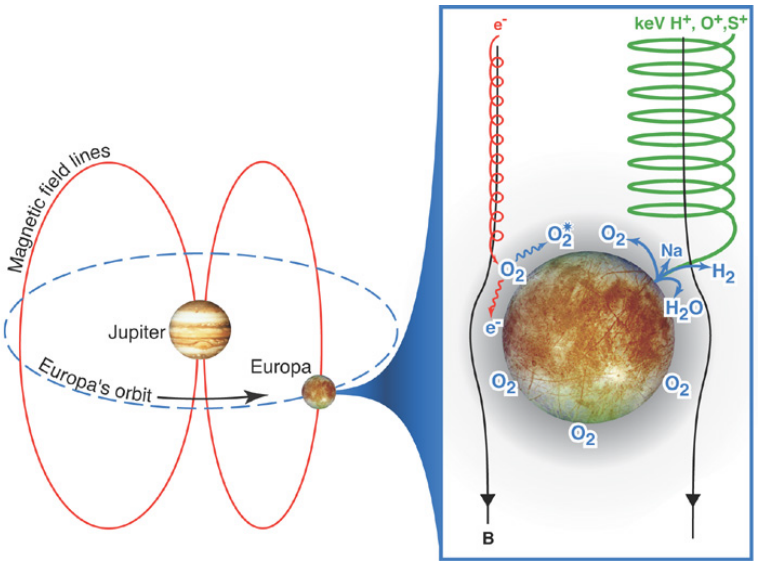

Figure 3.3: Schematic of the formation of Europa's neutral gas environment. Ions (green) and electrons (red) alter and erode the surface, producing a tenuous atmosphere composed mostly of O_2. H_2 and Na (and other trace species) form an extended cloud, whereas H_2O freezes upon contact with the surface. Image from Johnson et al. (2004).

Cassini's flyby of Jupiter (Hansen et al., 2005). Recent observations with HST have revealed surpluses of hydrogen Lyman alpha and atomic oxygen emissions above the moon's southern hemisphere, that have been interpreted as evidence of transient vapor water plumes (Roth et al., 2014b). It is worth noting, however, that the plumes have not been detected afterwards and never confirmed, hence the status is at the current moment unclear (Roth et al., 2014a).

Nowadays, there are still many uncertainties regarding the issues presented above; therefore new observations of the icy satellite are required. For this reason, two different mission are planned for the Europa exploration: (i) the JUICE/ESA mission that will perform two flybys at Europa and (ii) the Europa/NASA mission that will perform multiple flybys around the satellite.

In this chapter we focus our attention on the JUICE/ESA mission and, in particular, on the JANUS visible camera in which we are involved. In the first section we briefly describe the mission, the instrument and the Europa flyby phase. Then, we present a simulation of a possible transient plume originating from cryovolcanic events on Europa whose surface deposit could be detectable by JANUS camera. One of the objectives of JUICE is to explore for the first time the subsurface in the most recent active regions in order to understand the exchange processes from the subsurface to the surface and also to constrain the minimal thickness of the ice shell in the most active regions (ESA, 2014). In addition, JUICE will search and study present and/or recently active processes by

considering that their manifestation can be found both on the moon's surface and in its atmosphere (plumes) and related ionosphere, as supported by the HST observation. The study of the transient plumes and their implications on the nature of the moon's inner ocean, have as mandatory prerequisite an accurate characterisation of the exospheric background. For this reason, we performed a detailed study of the Europa's tenuous atmosphere loss rates on the basis of update plasma condition in the vicinity of Europa (Bagenal et al., 2015). This study is inserted into an ISSI international project, with the following title: "Towards a global unified model of Europa's exosphere in view of the JUICE mission" whose one of the main objective is the definition of suitable observation strategies for the two mentioned future missions in order to discriminate between the existing exosphere models. Finally, we report a work in progress regarding the estimation of the icy shell thickness through the application of a fractal method on Europa's surface features.

3.1 JUICE mission

The JUICE (JUpiter ICy moons Explorer) spacecraft of the European Space Agency (ESA) is dedicated to the detailed study of Jupiter and its moons. It was selected by ESA in May 2012 to be the first L-class mission within the Cosmic Vision Program 2015-2025 and it will provide the most comprehensive exploration to date of the Jovian system in all its complexity.

The focus of JUICE is to characterise the conditions that may have led to the emergence of habitable environments among the Jovian icy satellites, with special emphasis on the three ocean-bearing worlds, Ganymede, Europa, and Callisto. Ganymede is identified for detailed investigation since it provides a natural laboratory for analysis of the nature, evolution and potential habitability of icy worlds in general, but also because of the role it plays within the system of Galilean satellites, and its unique magnetic and plasma interactions with the surrounding Jovian environment. Hence, throughout the mission JUICE will map the Galilean satellites, observe Jupiter's atmosphere and magnetosphere, small moons and the interaction of all four Galilean satellites with the gas giant planet. The main science objective of JUICE are listed in Table 3.1.

JUICE is planned for launch in September 2022 with an Ariane 5 and will arrive at Jupiter in July 2030 after an Earth-Venus-Earth-Earth gravity assist strategy and an interplanetary cruise of 7.6 years. The spacecraft will perform a dozen flybys of Callisto, the most heavily cratered object in the Solar System, and will fly past Europa twice in order to make the first measurements of the thickness of its icy crust. JUICE will end up in orbit around Ganymede, where it will study the moon's icy surface and internal structure. JUICE will be set in a polar orbit around Ganymede, becoming the first spacecraft in history to enter orbit around an icy satellite in the outer solar system. The

Explore the habitable zone: Ganymede, Europa, and Callisto	
Ganymede as a planetary object and possible habitat	Characterise the extent of the ocean and its relation to the deeper interior; Characterise the ice shell; Determine global composition, distribution and evolution of surface materials; Understand the formation of surface features and search for past and present activity; Characterise the local environment and its interaction with the Jovian magnetosphere.
Europa's recently active zones	Determine the composition of the non-ice material, especially as related to habitability; Search for liquid water under the most active sites; Study the recently active processes.
Callisto as a remnant of the early Jovian system	Characterise the outer shells, including the ocean; Determine the composition of the non-ice material; Study the past activity.
Explore the Jupiter system as an archetype for gas giants	
The Jovian atmosphere	Characterise the atmospheric dynamics and circulation; Characterise the atmospheric composition and chemistry; Characterise the atmospheric vertical structure,
The Jovian magnetosphere	Characterise the magnetosphere as a fast magnetic rotator; Characterise the magnetosphere as a giant accelerator; Understand the moons as sources and sinks of magnetospheric plasma.
The Jovian satellite and ring systems	Study Io's activity and surface composition; Study the main characteristics of rings and small satellites.

Table 3.1: Scientific objectives of JUICE (ESA, 2014).

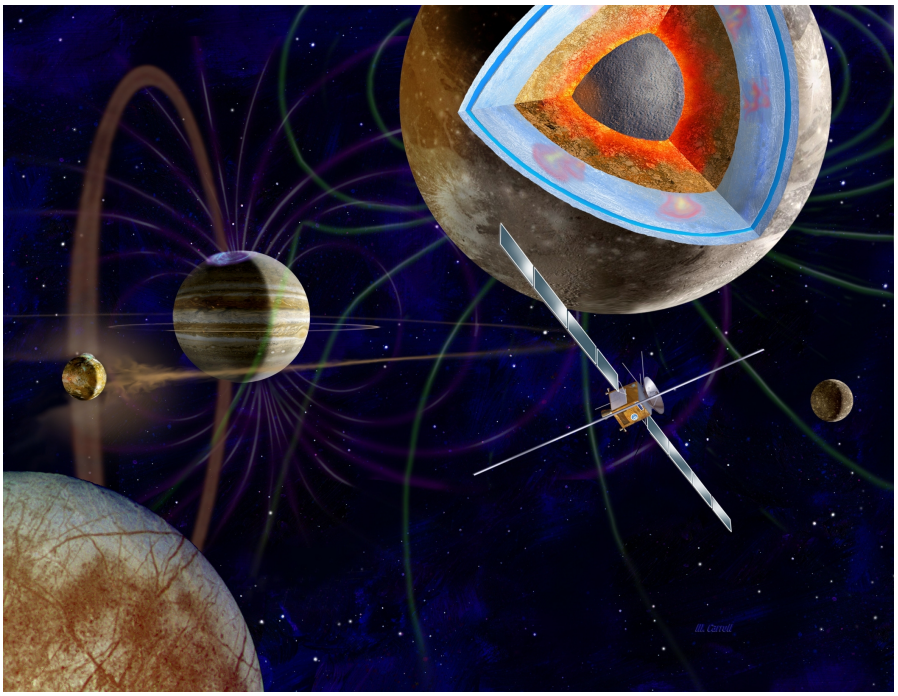

Figure 3.4: Artist's impression of the JUICE spacecraft in the Jovian system. Credit: Artist M. Carroll.

current nominal end of mission scenario is after 3,5 years from the Jupiter orbit insertion and involves spacecraft disposition on Ganymede. The JUICE spacecraft will carry a highly capable suite of ten scientific instruments, including remote sensing and in situ packages, that are summarized in Table 3.2.

3.1.1 JANUS instrument

JANUS (Jovis, Amorum ac Natorum Undique Scrutator) is the instrument designed to meet the scientific requirements foreseen for imaging at visible wavelengths aboard the JUICE mission. JANUS will conduct an in-depth comparative study of Ganymede, Callisto and Europa, and explore most of the Jovian system and Jupiter itself. The science objectives of the camera instrument reflect the imaging tasks stated by the JUICE Science Requirements:

- Characterise Ganymede, Callisto, and Europa as planetary bodies, including their potential habitability, with special focus on Ganymede; this implies an in-depth geological study including tectonics, mass wasting, cryovolcanism, impact structures, crater relaxation history and surface ages, orbit, rotation status and interior, color characteristics, potential water plumes source;

Instrument	Scientific Goal
Radio Science Experiment (3GM)	Interior state of Ganymede, presence of a deep ocean and other gravity anomalies. Ganymede and Callisto surface properties. Atmospheric science at Jupiter, Ganymede, Europa and Callisto, and Jupiter rings.
Laser Altimeter (GALA)	Topography and tidal deformation of Ganymede.
Imaging System (JANUS)	Local-scale geologic processes on Ganymede, Europa, and Callisto; Io Torus imaging, Jupiter cloud dynamics and structure. Global morphology of the Ganymede surface. Global to regional scale morphology of the Callisto and Europa surface. Physical and dynamical properties of minor moons and rings.
Magnetometer (J-MAG)	Ganymede's intrinsic magnetic field and its interaction with the Jovian field. Induced magnetic field as evidence for subsurface ocean on Ganymede, Europa and Callisto.
Visible-Infrared Hyperspectral Imaging Spectrometer (MAJIS)	Composition of non-water-ice components on Ganymede, Europa and Callisto; State and crystallinity of water ice. On Jupiter: tracking of tropospheric cloud features, characterisation of minor species, aerosol properties, hot spots and aurorae.
Particle Package (PEP)	Complete plasma composition and distribution in the Jovian magnetosphere. Interaction between Jovian magnetosphere and Ganymede, Europa and Callisto. Energetic Neutral Atom imaging of neutral and plasma tori of Europa and Io, and magnetospheric energetic particle injections. Composition and structure of exospheres and ionospheres of the moons, and response to plasma precipitation.
Ice Penetrating Radar (RIME)	Structure of the Ganymede, Europa and Callisto subsurface; identify warm ice water "pocket" and structure within the ice shell; search for ice/water interface.
Radio and Plasma Wave Instrument (RPWI)	Ganymede: Exosphere and magnetosphere; Callisto and Europa: Induced magnetic field and plasma environment; Jovian magnetosphere and satellite interactions.
Submillimetre Wave Instrument (SWI)	Dynamics of Jupiter's stratosphere; Vertical profiles of wind speed and temperature; Composition and structure of exospheres of Ganymede, Europa and Callisto.
Ultraviolet Imaging Spectrograph (UVS)	Composition, structure and dynamics of the atmospheres of Ganymede, Europa, Callisto and Jupiter and their interactions with the Jovian magnetosphere and plasma tori; search for water vapour plumes/geysers.

Table 3.2: JUICE mission payload.

- Characterise and study the physical properties of other satellites of the Jupiter system, including Io, the irregular and inner satellites;
- Study Jupiter's troposphere, imaging of the active dynamical processes, cloud systems, waves, vortices, and other instabilities, determining the vertical cloud structure within discrete features, and detecting lightning;
- Observe Jupiter's stratospheric aerosol variability due to vigorous water meteorology and disturbances from large vortices, such as the Great Red Spot;
- Investigate Jupiter's upper atmosphere by imaging auroral activity and particle precipitation in the form of polar hazes.
- Contribute to the study of the interaction between the Jovian magnetosphere and the bodies embedded within it;
- Perform a physical characterisation of the ring system.

The long trade-off between different design solutions, performed by the JANUS team in order to satisfy all JUICE mission's scientific requirements and to take into account the new selected nominal detector, has led to the following architectural choices:

- a catoptric telescope with excellent optical quality is coupled with a CMOS detector, avoiding any scanning mechanism; no mechanisms are needed or implemented for yaw steering compensation;
- a fine tuning of instrument parameters allows us to have an instrument designed to perform low, medium and high-resolution imaging on different targets in the Jupiter system taking advantage of the complex mission design;
- instrument operations are flexible enough to optimize the acquisition parameters with respect to the many different observation requirements and conditions that JANUS will face. The instrument design will allow us to adjust the resolution through binning, the field of view through windowing, the signal levels and SNR through integration time, the instrument calibration parameters through in-flight calibration and data pre-processing;
- cold redundancy is implemented for all critical electronic parts;
- use of broad-band and narrow-band filters is allowed by the implementation of a filter wheel with high heritage and high redundancy.

In Table 3.3 are reported the main characteristics of the instrument, in Figure 3.5 a sketch of the JANUS optical head and, finally, in Table 3.4 are listed the main spectral characteristics of the JANUS instrument.

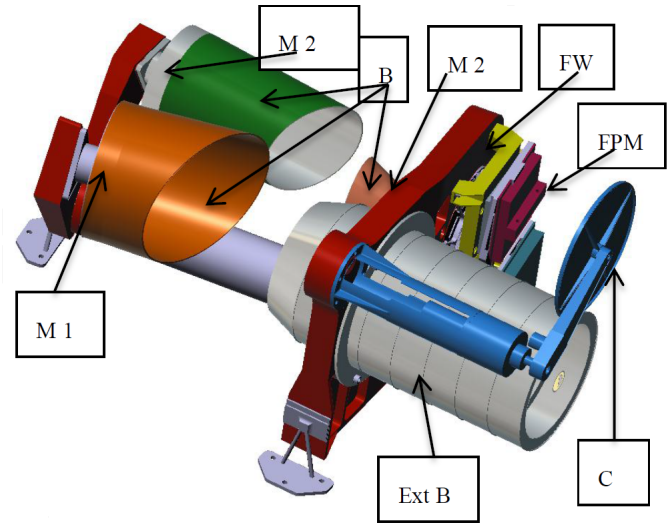

Figure 3.5: The schematic characteristics of the JANUS telecope with schematic showing the main modules: the mirror (M2), the Filter Wheel (FW), the Focal Plane Module (FPM), including the detector, the cover (C) and the baffles (B).

Specification	**Value**
Effective focal length	467 mm
F/#	4.67
Field of View	1.72 × 1.29 degrees^2
Detector format	2000 × 1504 pixels^2
Pixel size	7 μm
Pixel scale	15 μrad/pixel
Spectral range	350 - 1050 nm

Table 3.3: First order optical properties of the camera and the detector.

Filter	Central Wavelength /Bandpass (nm)	Note
FPAN	650/500	Panchromatic – monochromatic imaging
FBLUE	450/60	Blue – satellite colours
FGREEN	530/60	Green, background for Na – satellite colours
FRED	656/60	Red, background for Ha – satellite colours
CMT medium	750/20	Continuum for strong Methane band on Jupiter, geology
Na	590/10	Sodium D-lines in exospheres
MT strong	889/20	Strong Methane band on Jupiter
CMT strong	940/20	Continuum for medium Methane band on Jupiter, Fe^{2+} on satellites
MT medium	727/10	Medium Methane band on Jupiter
Violet	410/80	UV slope of satellites surfaces
NIR 1	910/80	Fe^{2+}, Io lava spots
NIR 2	1000/150	Fe^{2+}, Io lava spots
Ha	656/10	Hα-line for aurorae and lightning

Table 3.4: JANUS filters list

.

Based on these considerations and the chosen instrument architecture, JANUS will perform all kind of observations foreseen for visible imager onboard the JUICE mission. In particular, the driver requirements for the design of JANUS, as for the most of JUICE instruments, are the observation of Ganymede and Europa flybys.

3.1.2 Europa Flyby

Due to the initial phase of the mission, the information hereafter reported and used through this work are probably not the final solution that will be defined for JUICE. However, in this work we focus on a particular phase of the JUICE mission: the Europa flybys, planned on 13 and 29 February 2030 (we consider these dates representative of the two flybys, even if they could be changed in next future because of the initial phase of the mission), reporting below the main phase characteristics from ESA (2014).

Europa flybys are fundamental to answer to the main open questions regarding the icy satellite. They will focus on the surface regions with traces and recent activities to:

- Characterise the composition of the non-ice material, especially as related to habitability;
- Search for liquid water under the most active sites;
- Study the active processes.

During this phase, JUICE should provide imaging and spectroscopy of Europa's surface geology, composition and thermophysical properties across the broad wavelength range, radar sounding of the Europan sub-surface and laser altimetry for topography at closest approach. In addition, JUICE should provide limb observations to study aurorae, airglow and the tenuous Europan exosphere, satellite ephemerides and gravity measurements, detailed characterisation of the magnetospheric and plasma environment surrounding the satellite and a search for Europan plumes (ESA, 2014).

These objectives drives specific requirements to the mission to enable, at least, one Europa flyby with closest approach with distance $\leq$ 500 km above the regions of interest. The spacecraft shall be capable of performing high spatial resolution imaging and spectral imaging in the broad wavelength range of selected sites on Europa, as well operating all instruments simultaneously within the distance of 150000 km from the moon during approach and departure. The two flybys will take place at middle latitudes over

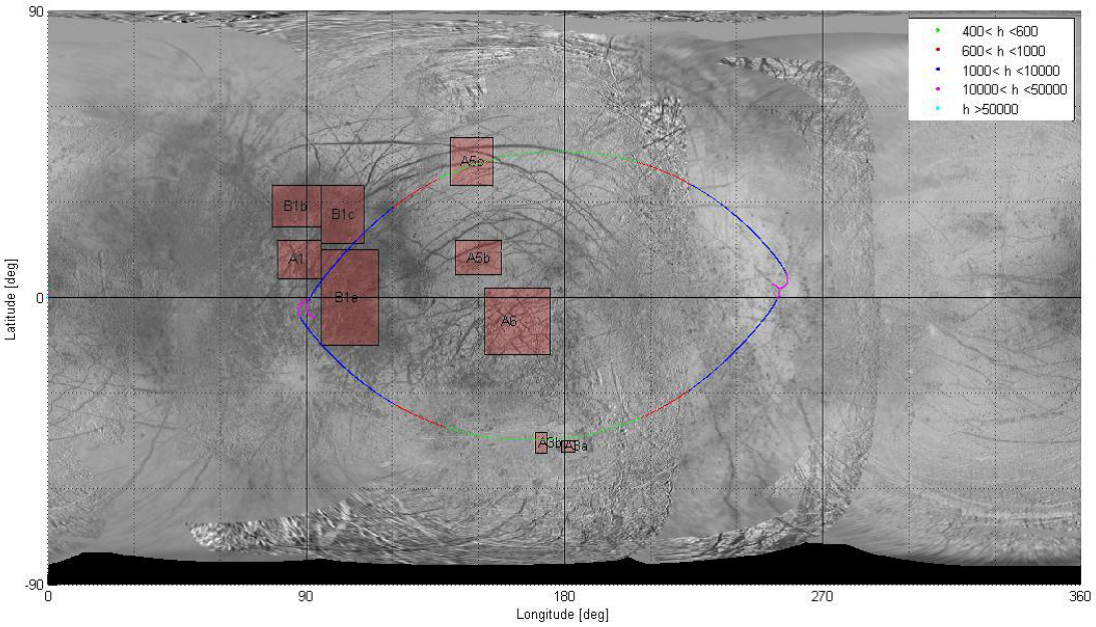

Figure 3.6: Ground track of the spacecraft during Europa flybys. The image shows an Europa surface map with the areas of specific interest indicated by red rectangles. The ground tracks of the two flybys are indicated in coloured lines, with the colour indicating the altitudes in 1000 km (see the colour legend in the upper right) (ESA, 2014).

the Northern and Southern hemispheres of Europa with a closest approach altitudes of $\sim$ 400 km and within 15° of the 180° longitude (centre of the far side). The relative velocity for both Europa flybys ranges from 3.6 to 3.9 km/s. The ground tracks and illumination conditions are given in Figure 3.6 and 3.7. Each flyby will last for several days, during which the data will be collected and stored in the spacecraft mass memory.

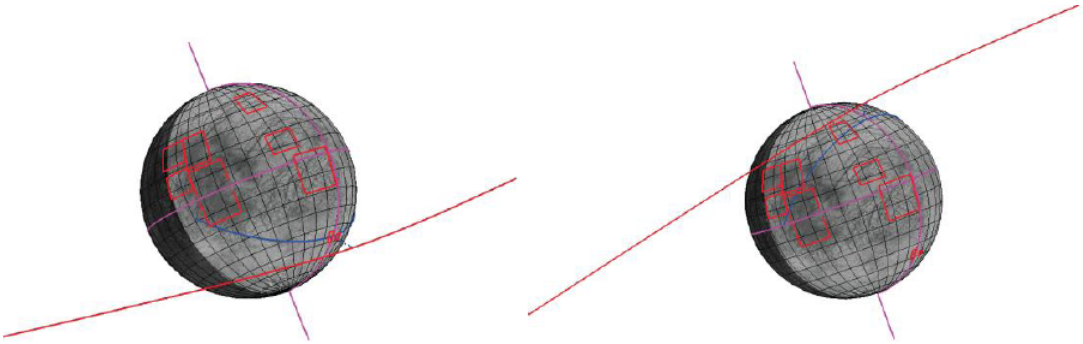

Figure 3.7: 3D representation of the first (left) and second (right) Europa flyby (ESA, 2014).

The data will be downloaded after the flyby, and will require a significant number of ground station passes ($\sim$ 8 hours each). This scenario requires a significant amount of mass memory on the spacecraft itself, and presents the sizing case for the spacecraft ability to cope with the highest data flow and on board mass memory.

Manoeuvering slews of the spacecraft will provide the scan mosaics required by the imaging experiments: 5 slews (3 for JANUS and 2 for MAJIS) are envisaged during each of the approach and departure phases within 12 hours of closest approach (CA) with yaw steering enabled to maximise spacecraft power. The slews extend beyond the disc to enable both surface imaging and remote sensing of the limb and exospheres. During the 120 minutes surrounding closest approach (CA$\pm$60 mins), the spacecraft suspends yaw steering. Spacecraft slews are executed for MAJIS, JANUS, UVS and SWI surface coverage until CA-30 mins, when nadir pointing is acquired and all instruments switch to push-frame mode (JANUS operating in single-filter panchromatic imaging for CA$\pm$17 mins; MAJIS using its scanning mechanism for motion compensation for CA$\pm$13 mins). GALA and RIME observations will operate within CA$\pm$7 mins when the distance to the surface is at a minimum. Finally, yaw steering is recovered at CA$\pm$60 mins and the approach sequence is repeated in reverse. Depending on the data volume constraints, distant observations of Europa (e.g., plume searche, satellite mutual events) will be executed during the pre- and post-flyby phases two days either side of closest approach (ESA, 2014).

3.2 Europa's water plume

Surface venting is quite common on some outer solar system satellite, as Io and Enceladus, and spacecrafts have observed plumes erupting from their geologically young surface, that reflect the possible material exchange between the subsurface and the surface of the satellite. Voyager 1 observed an enormous plume reaching several hundred kilometers above Io's surface providing the first spectacular evidence of active volcanism beyond

Earth (Morabito et al., 1979). Cassini-Huygens mission (2004-current) discovered active jets of water vapour and icy particles above Enceladus' south pole, i.e., plumes, providing a unique opportunity to probe the composition of its subsurface (Porco et al., 2006; Spencer et al., 2006; Hansen et al., 2006; Waite et al., 2006). On Enceladus, episodic plumes are thought to emanate from a set of fractures, known as the "tiger stripes" (Nimmo et al., 2014) which exhibit temperatures higher than that of the surrounding terrain (Porco et al., 2014). The five fractures are thought to be sites of active strike-slip or transtension/transpression tectonics resulting from cyclic tidal deformation (Smith-Konter & Pappalardo, 2008). During extensional or transtensional deformation phases, volatiles may be exposed allowing eruptions to occur (Hurford et al., 2007). Similar tectonic deformation is observed on Europa, which also presumably formed in response to temporally varying tidal stresses (e.g. Greenberg et al., 1998; Hoppa et al., 1999).

Plumes on Europa have been long hypothesized but they were never directly observed until recent observations, made with the Space Telescope Imaging Spectrograph (STIS) of the Hubble Space Telescope (HST). November and December 2012 observations reported significant surpluses of hydrogen Lyman alpha and oxygen OI 130.4 nm emissions above the southern hemisphere (Roth et al., 2014b), as shown in Figure 3.8.

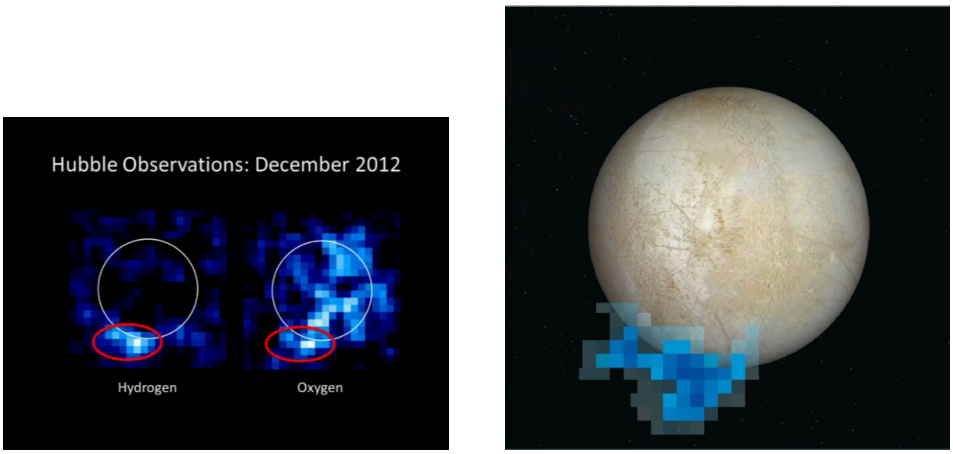

Figure 3.8: On the left: HST observation from Roth et al. (2014b). On the right: artist impression of the Europa south polar plume. Credit: NASA, ESA, and L. Roth (Southwest Research Institute and University of Cologne, Germany)

These emissions were persistently found in the same area over 7 hours, suggesting atmospheric inhomogeneity, and were best explained by two 200 km high plumes of water vapour. Non detections in November 2013 and in previous HST images from 1999 suggests varying plume's activity that might depend on changing surface stresses based on Europa's orbital phases, since plumes were identified in observations taken when Europa was near apocenter. Similarly, Enceladus plumes are linked with eccentric tides

and show an intensity change depending on the orbital position. However, tidal origin of plumes on Europa is still uncertain because no plumes were detected in following HST/STIS observations taken when Europa was again near apocenter.

On the other hand, in previous works (Fagents et al., 2000) it has been proposed that many surface features of Europa are the results of material emplaced via ballistic cryovolcanism (i.e. plumes). In fact, Europa possesses a relatively young surface, whose average age is estimated to be 40 - 90 Myr (Bierhaus et al., 2009), suggesting that it has undergone heavy resurfacing in current geological time, like Io and Enceladus. In Fagents et al. (2000), ballistic cryovolcanism has been considered and modeled as a possible mechanism for the formation of low-albedo features, surrounding lenticulae and along triple band margins and lineae. These features are considered as the expression of ongoing or recent cryomagmatic processes and, in some cases, may be the result of effusive cryovolcanism (Wilson et al., 1997; Head et al., 1998; Pappalardo et al., 1999; Fagents et al., 2000; Figueredo et al., 2002; Fagents, 2003; Prockter & Schenk, 2005). The work of Fagents et al. (2000) predicts smaller plume dimension with respect to what Roth et al. (2014b) have found, but this could be explained by hypothesising that plume, as that observed by HST, may be a rare event, or it occur frequently but on smaller spatial scales not observable by HST.

Our aim is to understand if possible water plumes could be detectable by the JANUS camera, in particular we are interested in the detection of plume deposits. We made a simple simulation of the plume deposit that may be formed after cryovolcanic events basing our assumption on Fagents et al. (2000) work. Firstly, we focus on the Europa flybys, and in particular on the specific phase of the first flyby, hereafter referred as E9 phase as defined in JUICE mission scenario, providing JANUS operation and possible observing strategies adopted. Then, we present our plume deposit model, from which we obtained an albedo distribution that is used to understand the detectability of the phenomenon by the JANUS camera. We therefore will search evidence of these phenomena in targeted regions that display activity, in addition to limb observation at the south pole, i.e where Roth et al. (2014b) identified the debate plume. We know that there is only one plume direct evidence from HST observations, but Europa's surface features and behaviour are suggesting the presence of these phenomena.

3.2.1 JANUS operation during flyby

One of the 2 foreseen flybys of Europa has been deeply studied to simulate a possible observing strategy applicable in order to address the specific JANUS science requirements. The flyby E9 is assumed to last 24 hours around the Closest Approach (CA, 13/2/31 13:49), and it is divided in 2 (time-)symmetric phases around the CA. Each phase is further divided in 2 phases, the Approach Phase (AP) and the Close Approach Phase (CAP). In each of them a different operation profile is foreseen: in Table 3.5 it is

reported the detailed profile of the Approach phase (AP).

JANUS would acquire full frame images in four filters (adding exosphere filters where necessary) on, at least, seven occasions during approach/departure phases when within ± 150000 km and under yaw steering. As the distance to Europa decreases, JANUS will switch from full-frame imaging (8 colours) to mosaics of 4 - 8 images in 4+ filters using the spacecraft slews (5 slews either side of the CA, 3 devoted to JANUS). Then surface scans in push-frame mode from CA-60 mins to CA-30 mins will be performed, before finally switching to nadir-pointing push-frame mode for single filter panchromatic images during closest approach. This sequence enables context imaging of half of the moon's surface (day side) and limb with resolution from 2 km/px to 0.1 km/px in all JANUS filters and panchromatic imaging of the most active regions along the flyby trajectory with resolution up to 6 m/px.

AP sub-phase	**a**	**b**	**c**	**d**	**e**
Time before CA	-11.5 h ÷ -5.7 h	-5.7 h ÷ -4.3 h	-4.3 h ÷ -3.9 h	-2.65 h ÷ -2.25 h	-1.95 h ÷ -1.20 h
Simulated timeframe	02:19 ÷ 08:05	08:07 ÷ 09:29	09:31 ÷ 09:55	11:09 ÷ 11:33	11:53 ÷ 12:27
$d_{S/C}$ [km]	138895 - 71953	71551 - 54784 1st JANUS mosaic	54368 - 49354	33633 - 28463 2nd JANUS mosaic	24131 - 16726
Pointing	Nadir	Yaw steering, Slew from 1.65° to -1.65° along Y,in 330 s, Offset by 0.8° to the sunlit side (Z)	Yaw steering, Slew from -1.8° to 1.8° along Y, in 1440 s, Offset by 0.85° to the sunlit side (Z)	Yaw steering, 2 slews from +3° to -3.05° then from -3.2° to +3.3° along Y in 550 s then 590 s (300 s between slews for stabilization); Offset by 0.8° then 2.4° to the sunlit side (Z)	Yaw steering, 1 slew from +3.3° to -4.7° along Y in 2200 s; Offset by 0.85° to the sunlit side (Z)
JANUS operation strategy	2 sets of surface images (in 8 colors: FPAN, 3×BB, NIR, Violet) + 2 set of limb images (Na, Na_{bkg})	3 sets of surface images (in 4 colors: FPAN, 3×BB) + 2 sets of limb images (Na, Na_{bkg})	Ride-along: 3 sets of surface images (in 4 colors: FPAN, 3×BB)	8 sets of surface images (in 4 colors: FPAN, 3×BB) + 4 sets of limb images (Na, Na_{bkg})	Ride-along: 8 sets of surface images (in 4 colors: FPAN, 3×BB)
JANUS pixel scale [m]	2083 - 1079	1073 - 822	816 - 740	556 - 427	362 - 251
On-ground S/C velocity [m/s]	38 - 71	71 - 96	97 -107	144 -188	220 -313
Dwell time [s]	54 - 15	15 - 8.5	8.4 - 6.9	3.2 - 2.3	1.6 - 0.8

Table 3.5: Summary and operation strategy and profile during the E9 approach flyby phase (AP a-e sub-phase).

Radiometric model

To estimate the JANUS performance during scientific operations in the Jupiter-satellites system, a Radiometric Model (RadMod) has been developed in order to retrieve the expected instrument SNR. The RadMod is a software tool organised in three modules, which can be adapted to different observation and/or operative constraints. The input modules are:

1. the S/C trajectory and/or orbit in the different mission operative phases, which defines the observation geometry and gives constraints on operations (e.g., integration time, binning, filters to be used), following the preliminary Flight Operations Concept (FOC);

2. the environmental conditions during the different phases (e.g., planet or satellite albedo, the full-disk albedo spectra described in Karkoschka (1994) have been used);

3. the instrument design, especially in terms of optics (e.g., IFOV, optics transmission), detector and electronics (e.g., quantum efficiency, noise sources, saturation), filters (central wavelength, bandwidth).

For our purpose the JANUS SNR has been performed for E9 flyby, and the S/C trajectory and the JANUS operation planes and strategies, as described in ESA (2014), have been adopted. These operative plans are only indicative, designed to provide input for a preliminary analysis. Typical sequence of operations used should be considered as sample timelines. Figure 3.9 shows the full-disk albedo spectra described in Karkoschka (1994) used for the SNR simulations in each mission phase.

Between the different phases of the Europa flyby, we analyse the E9 Ap-d sub-phase to derive the SNR expected during observations and understand if plumes could be detectable. We adopt this sub-phase because both surface and limb images will be acquired.

E9 AP-d phase

In this sub-phase, the S/C approaches the moon, with sub-S/C point always very close to the equator and very close to the terminator. Europa does not fill the JANUS FOV (see Figure 3.10). Slews from +3° to -3.05° then from -3.2° to +3.3° along Y (roughly along the terminator) are foreseen, with a pointing offset by 0.8° and 2.4° to the sunlit side, respectively, in order to complete the JANUS mosaic map of the Sun-illuminated Europa half-disk (see also Table 3.5). Figure 3.11 gives a schematic example of how the 4 (sets of) images of the first slew from N to S are distributed along Y (roughly, along the latitude arc) to perform the mosaic (in 4 colors). The β angle for this slew is $\sim 60°$.

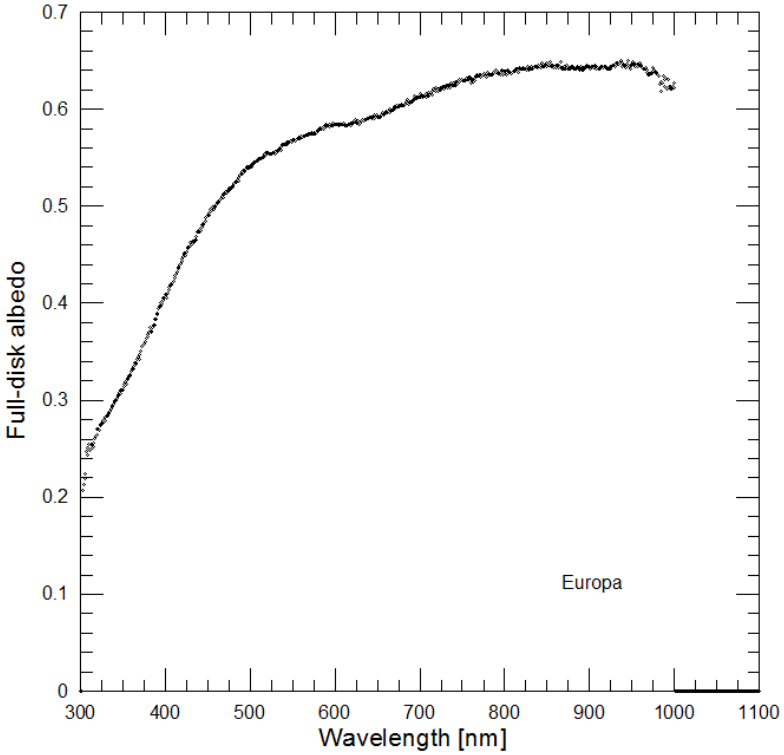

Figure 3.9: Full disk albedo of Europa (VIMS data) (ESA, 2014).

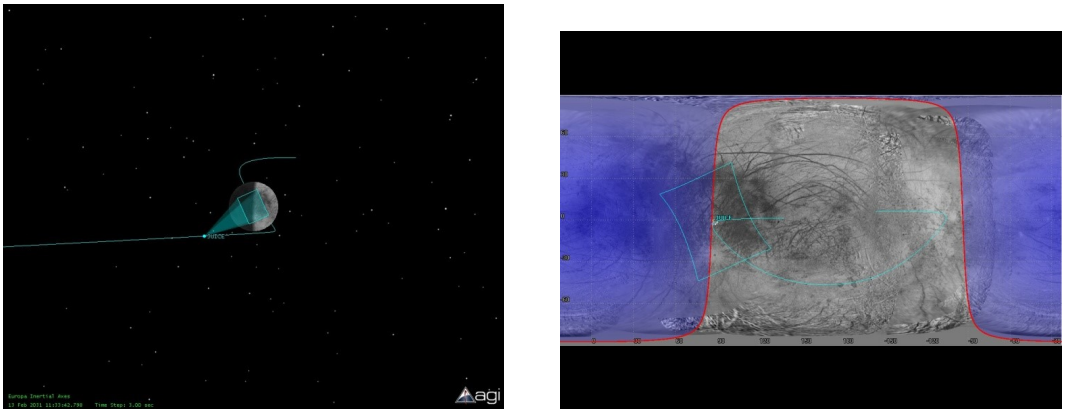

Figure 3.10: Europa in the JANUS FOV at the end of AP-d (13/2/31 11:33). (Left) 3D vision of JANUS FOV projected on the moon's surface (without pointing offset). (Right) 2D vision of JANUS FOV projected on the moon's surface (without pointing offset), together with projection of the whole FB trajectory.

The second slew will be performed from S to N, with a further pointing towards the sunlit side, with a β angle $\sim 30°$. The 4 sets of images in the first slew will be performed at average latitude of $\sim$60°N, $\sim$20°N, $\sim$20°S, $\sim$60°S (on the reverse order in the second slew). The pixel scale for this sub-phase ranges from 556 to 427 m. Table 3.6 summarises

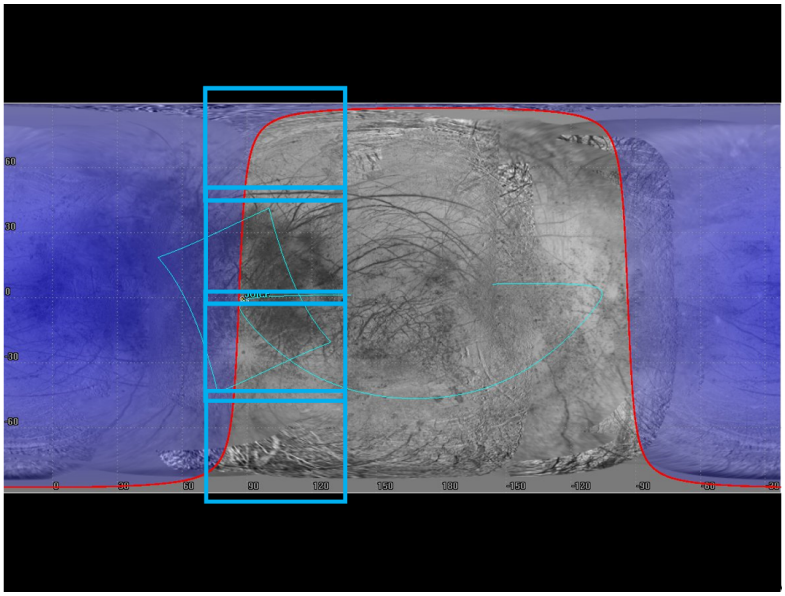

Figure 3.11: A schematic example of how the 4 sets of images of the first slew are distributed along Y (i. e., roughly, along the latitude arc) to perform the mosaic map (in 4 colors) of the Sun-illuminated Europa half disk. The thin blue line is the projection of the whole FB trajectory, together with the JANUS FOV (its orientation is still somehow arbitrary). The thick blue rectangles are schematic representations of 4 images obtained during the first slew (from N to S). The second slew goes from S to N, with pointing tilted towards the sunlit side to cover the half illuminated Europa disk.

an example of the expected JANUS SNR for this operative case, when integration times perfectly compatible with the dwell time in this phase are adopted. In addition, we have done a further simulation with RadMod for observing at a latitude of 88° S (where the plume was observed by Roth et al. (2014b)) with different illumination conditions, discrete and optimal, obtaining a SNR in FPAN equal to 98 and 134 respectively with the increase of the integration time to 0.02 s, in agreement with the dwell time of Ap-d sub-phase. Therefore, we generate a simple model to understand the detectability of the plume deposits under these conditions.

3.2.2 Methodology - model assumptions

We consider as a plume deposit the material falling after a cryovolcanic event on the Europa's surface basing our model on Fagents et al. (2000) work (a similar approach has

First slew (β=60°)				
	Latitude α=60°		Latitude α=20°	
	t_{exp}(s)	SNR	t_{exp}(s)	SNR
Filter FPAN	10^{-2}	211	5×10^{-3}	204
Second slew (β=30°)				
	Latitude α=60°		Latitude α=20°	
	t_{exp}(s)	SNR	t_{exp}(s)	SNR
Filter FPAN	5×10^{-3}	196	2×10^{-3}	170

Table 3.6: An example of the expected JANUS SNR in FPAN filter achievable during the 2 slews foreseen during the Europa E9 AP-d sub-phase, with pixel scale from 556 to 427 m.

been already adopted by Quick et al. (2013)). As stated before, Fagents et al. (2000) suggested that many surface features of Europa are the results of material emplaced via ballistic cryovolcanism, such as dark deposits surrounding lenticulae and along triple band margins and linae, an example is shown in Figure 3.12. They derived the particles velocity, the deposit composition and the extension from surface features analysis. Assuming that particles follow ballistic trajectories, they concluded that the deposits could have been emplaced by plumes that consisted of 0.1-20 wt% volatile content (CO_2, SO_2, CO, etc.), whose particles had initial eruption velocities between approximately 30 and 250 m/s, and that extended 0.4 to 25 km above Europa's surface.

Our model considers solid particles that follow ballistic trajectories after eruption and formed plume deposits that could be detectable. We consider the detection of these deposits with JANUS camera, that operates between 300 -1050 nm, centred at 600 nm and assuming particles size and water production rate from Enceladus case because of their similarity. In Fagents et al. (2000) model, cryoplumes deposits contain also volatile components, but in this work we consider only icy particles that would be ejected and fall back on the Europa's surface forming snow deposit (albedo of snow is approximately 0.8-0.9). In this context, we expect to observe high albedo regions in contrast with the background albedo of Europa surface, whose average value is 0.6. Therefore, we obtain an albedo distribution of particles in order to understand the real detectability of the deposit. For simplicity, we assume that the number of particles that will be ejected during the plume event is equal to the number of particles that land on the Europa's surface.

At a first case, by considering that particles follow ballistic trajectories, we made several simple assumptions: (i) we neglect loss processes of particles; (ii) we fix a single ejection velocity for all particles; (iii) we choose a launch angle cone from 45° to 90° and inside this range, the particles are assumed to be ejected uniformly; and (iv) an azimuth

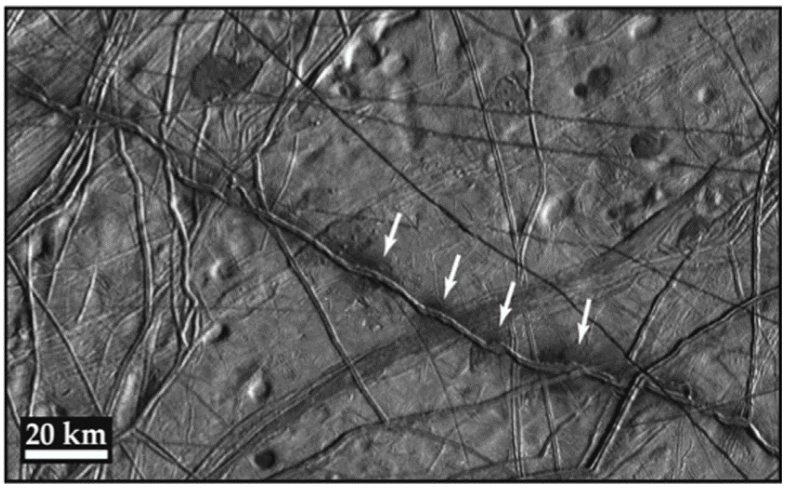

Figure 3.12: Deposits along Rhadamanthys Linea as indicated by white arrows. The horizontal range, R, of dark deposits is measured from the center of the feature (i.e. linea, ridge, lenticula), in this case, Rhadamanthys Linea, to the edge of the deposit on either side. R for these deposits ranges from 2 to 6.8 km (Table 1 in Fagents et al. (2000)). Image from Galileo Orbit E15 at ∼ 230 m/pixel. Adapted from Quick et al. (2013).

angle that changes from 0° to 360°. Assuming ballistic trajectories and a well-defined velocity, the maximum height for the cryoplume is $H_{max} = \frac{v^2}{2g}$, while the maximum extension of the plume deposit on the surface is defined by $R_{max} = v^2/g$, where g is the gravity acceleration on Europa equal to g = 1.314 m/s^2. Fixing the ejection velocity equal to 0.2 km/s, particles reach a maximum height of 15 km and a maximun range of 30 km, that is roughly in agreement with the estimates reported in Fagents et al. (2000). The left panel of the Figure 3.13 shows the landing site particle distribution for the case above, while the right panel reports the particle distribution converted to a pixel image choosing an average value of 500 m bin (in agreement with the AP-d sub-phase in which the pixel scale is 556-427 m).

As we expected, the deposit is brighter at the outer ring than in the centre (Figure 3.13 on the right). This exact high contrast of brightness between the outer part of the deposit and the inner part is due to the same ejection velocity of the particles and to the small size of pixels.

A more realistic assumption is a Gaussian velocity distribution $f(v) = \frac{1}{\sigma\sqrt{2\pi}} \exp \frac{-(x-\mu)^2}{2\sigma^2}$ of particles peaked at 0.2 km/s and with a variable σ (10, 20, 30 and 40) in order to have a more realistic situation.

As a result, we report in Figure 3.14 the particles landing site in pixel scale for a Gaussian velocity distribution peaked at 0.2 km/s and with a width of 20 (pixel scale of 500 m/px). The distribution is more uniform with respect to single ejection velocity case: indeed, more particles land in the outer part of the deposit while less particles are

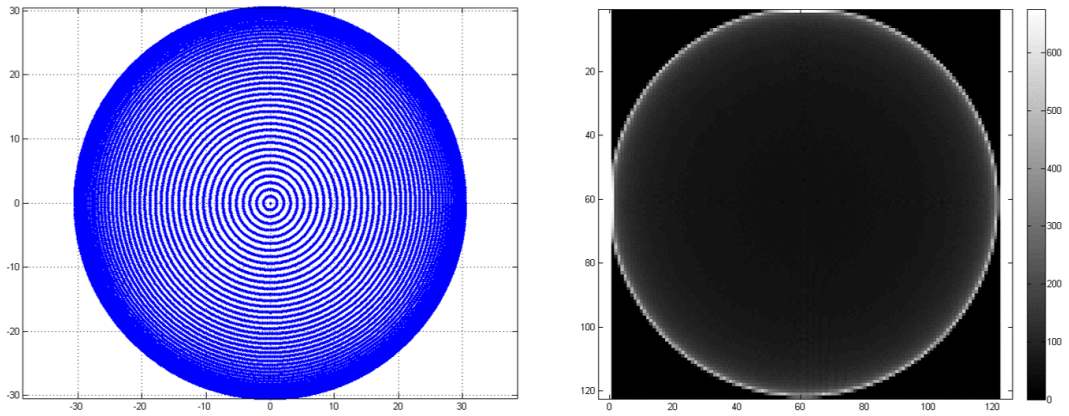

Figure 3.13: On the left the real particles distribution on the surface of the satellite considering a fix velocity equal to 0.2 km/s, while on the right it is shown the same particles distribution converted in a pixel distribution using the pixel scale of Ap-d sub-phase, equal to an average value of 500 m/px.

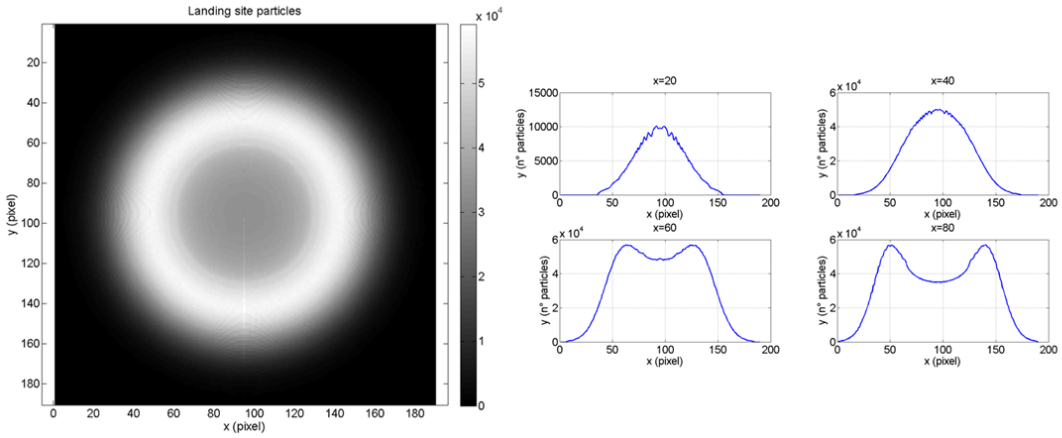

Figure 3.14: On the left the particle landing site pixel distribution for a Gaussian velocity distribution peaked at 0.2 km/s, while on the right it is shown the behaviour of the distribution along different directions representing how particles are distributed inside the plume deposit.

present in the inner part. Contrary to the previous analysis, the contrast between these two different landing sites is lower. In addition, we report also the cross section of this landing site distribution along different horizontal directions to show how particles are distributed inside the plume deposit.

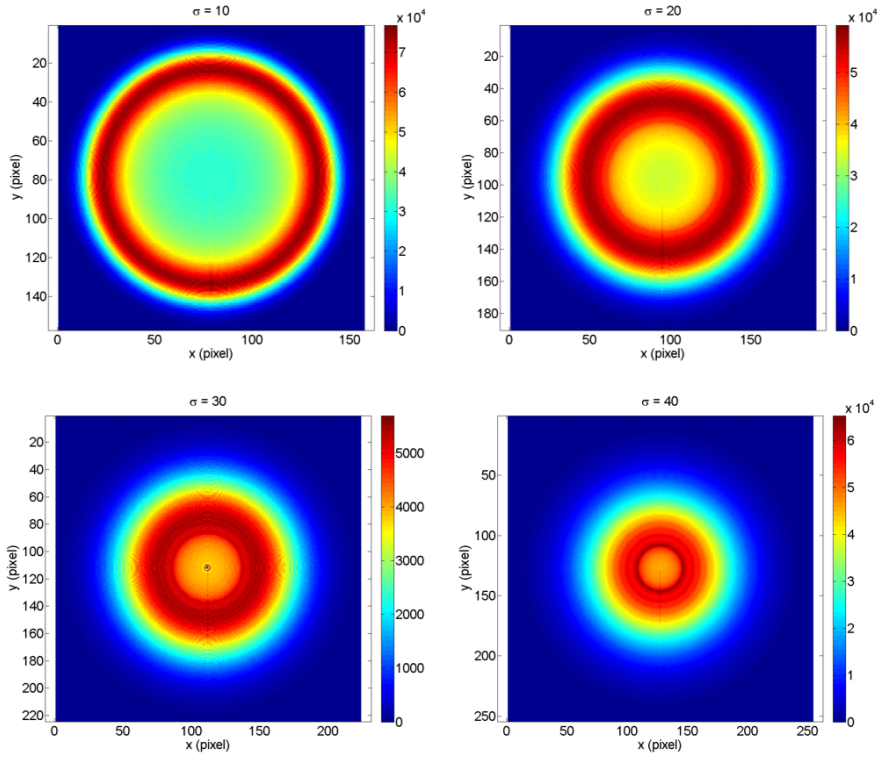

Figure 3.15: Images of particle landing site distributions in pixels changing the sigma of the Gaussian velocity distribution: increasing the width of the Gaussian velocity distribution implies that more particles land in a wider area. The deposit becomes less distinct.

Albedo particles distribution

In the following, we obtain the surface albedo distribution in order to understand the detectability of the plume deposit with JANUS. To calculate the real number of particles landed on the surface we correlate the number of particles ejected from the plume with the simulated particles. We assume a water production rate equal to 200 kg/s (mean value from Enceladus case (Hansen et al., 2006)) finding the real number of particles included in each pixel. Subsequently, we define the optical thickness of our plume deposit calculating the column density for each pixel in order to obtain the surface albedo distribution.

When doing so, we assume an icy particles radius equal to 0.5 μm and an ice density

equal to 918 kg/m^3, in agreement with the size ranges of plume particles observed on Enceladus (Porco et al., 2006; Kempf et al., 2008; Postberg et al., 2008; Kieffer et al., 2009; Ingersoll & Ewald, 2011). Considering observation in FPAN filter (Table 3.6), peaked at 0.6 μm, and assuming a dielectric constant for ice of 3 at 273 K (Cumming, 1952) (as in Quick et al. (2013)), the scattering cross section of particles is equal to $\sigma_{scat} = \frac{8\pi^3 r_p^3}{5\lambda}$, which is valid in Mie scattering condition (i.e. $r_p = \lambda$) by non-absorbing particles (so that $\sigma_{scat} = \sigma_{ex}$ (van de Hulst, 1957; Bohren & Huffman, 1998)). Hence, we calculated the optical thickness as $\tau = N \times \sigma_{scat}$, where N is the column density in $1/m^2$ and σ_{scat} the scattering cross section. Then, since the plume deposit is optically thick, we apply the Lamber-Beer law $I/F = \exp(-\tau)$ in order to achieve the intensity of radiation that we could see from this deposit. As stated before, considering the plume deposit as snow deposit, we calculate the albedo distribution in order to understand if the contrast with the surface of Europa permits the detection of the deposit. Therefore, we scaled our data to a range of values between 0 and 0.2 adding a fix value of 0.6, that is the albedo background of Europa in the FPAN filter. In this way, we obtained a range of data between 0.6 and 0.8, where 0.8 is assumed to be the snow albedo (we consider 0.8 instead of 0.9 (albedo of pure snow) because we expect that the deposit will be composed by dirty snow). The albedo particles distribution for a plume lifetime of 3.5 day orbital period is shown in Figure 3.16.

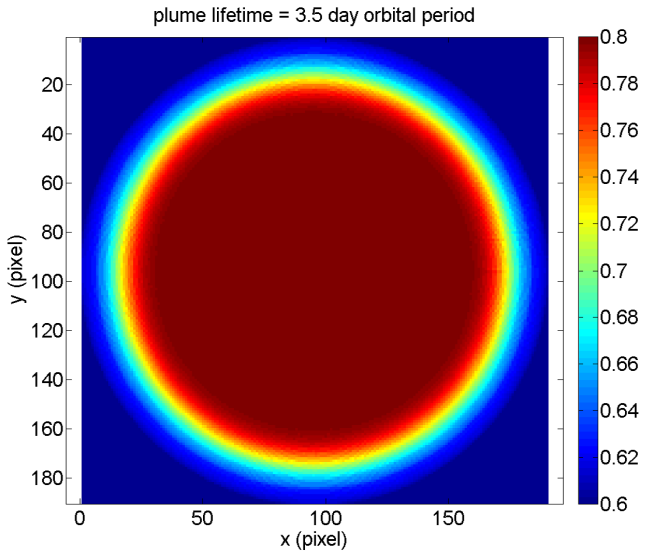

Figure 3.16: This image represent the distribution of surface albedo. When assuming a plume lifetime of 3.5 day orbital period, we obtain a deposit that is much more bright and, hence, detectable in its inner part. On the other hand, the outer part of the deposit has an albedo comparable with the Europa surface albedo.

In this model we consider different plume lifetimes in order to understand how the

deposit evolves with time. We consider as lower lifetime limit the diurnal tides time equal to 1 day, in agreement with the fact that cracks could open and close over a Europa's orbital period (Greenberg et al., 1998). On the other hand, since the lenticulae and dark deposits surrounding them are genetically linked with chaos regions as suggested by previous works (Spaun et al., 1999; Riley et al., 2000), we assume as an upper lifetime limit the chaos region's age equal to 1 Myr (Pappalardo et al., 1999).

In Figure 3.17, it is shown the evolution of the plume deposit, ranging from 3.5 orbital day to 1 Myr. We can say that the plume deposit becomes more uniform in brightness with increasing time (the optical thickness increases) and in the last case, corresponding to 1 Myr, the brightness becomes equal on the entire deposit.

To understand if the plume deposit is detectable in Ap-d sub-phase, we apply a Gaussian noise on the simulation result, that is shown in Figure 3.18. We consider different SNR in order to understand the limit of the detectability of the plume deposit. Considering the SNR listed in Table 3.6, we can say that the plume deposit (if exists) is detectable in Ap-d sub-phase (the minimum simulated SNR for Europa observation is $\sim$ 100) and it could be detectable also with lower SNR, as it is shown in Figure 3.18. The deposit could be visible by the JANUS camera as a small bright area on the detector. In addition to the SNR listed in Table 3.6, we consider the SNR values obtained for the simulation at $\sim 88°$. This is made in order to understand if the plume deposit is still visible at the south pole too, i.e. the region where the unique plume observation was made (Roth et al., 2014b). For this case too, the plume deposit could be detectable since the deposit is still visible even with lower SNR (the minimum simulated SNR for south pole observation is $\sim$ 100).

3.2.3 Discussion

JUICE will arrive at Europa observing the trailing hemisphere. During approach, JUICE will cover the regions above the trailing terminator. This configuration favours the direct search for the occurance of possible plumes also in the northern hemisphere as well as the detection of plume-material (possibly scattered from condensates) originating from the southern hemisphere. In this section, we built up a plume deposit model using a Gaussian velocity distribution peaked at 0.2 km/s, that implies a 30 km extension of the deposit, in order to understand if this plume deposit could be detectable by JANUS visible camera. In doing so, we examined the E9 flyby AP-d sub-phase when JUICE s/c will be at $\sim$ 30000 km from Europa with a phase angle of ~ 87 °. Using the radiometric model, we simulate possible observational scenario obtaining the SNR expected during this phase, as reported in Table 3.6. We conclude that the plume deposit could be visible as a small bright spot on the detector covering at least 60 pixel. In addition, we applied the radiometric model to possible observation at the south pole (88°), achieving a SNR which allows the detection of the plume deposit in this case too. Limb observations will

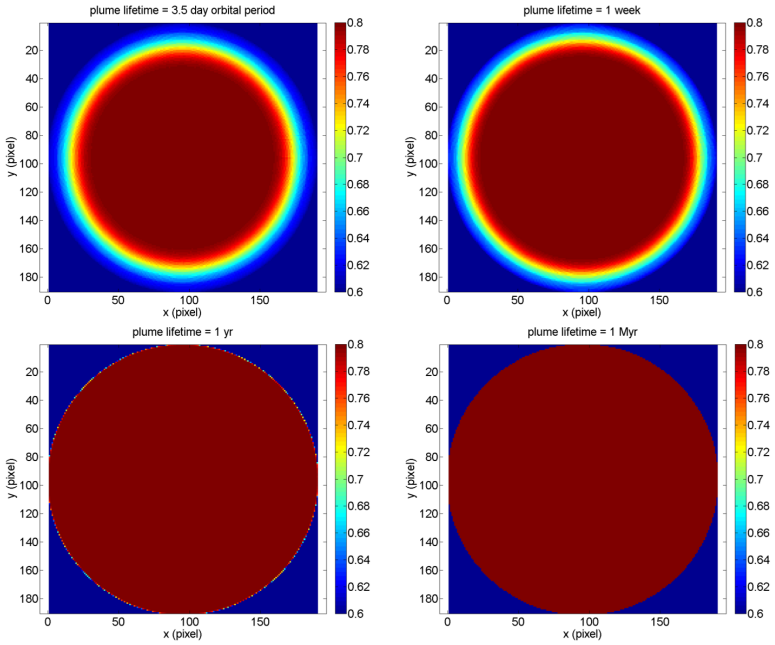

Figure 3.17: The evolution of the surface albedo distribution with the plume lifetime: the deposit becomes more uniform in brightness with the increasing of time.

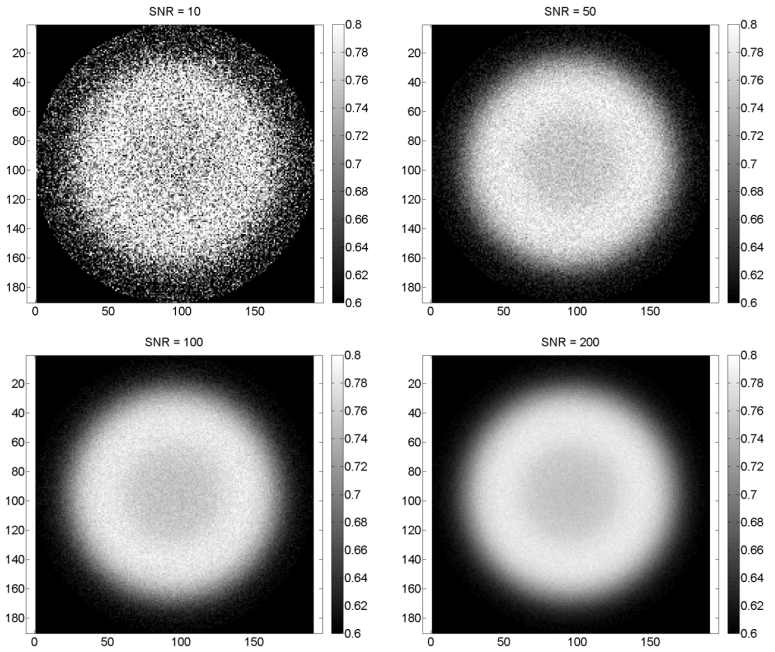

Figure 3.18: Surface albedo distribution combined with Gaussian noise applied to obtain different SNR. We emphasize that the deposit can be visible and detectable even at lower SNR than those listed in Table 3.6 (The lower simulated SNR for Europa observation is $\sim$ 100).

be done during the Ap-d phase too, but the observational scenario is not yet defined. We report in Figure 3.19 the hypothetical particles distribution at limb, which is obtained under the same assumption adopted for modelling the plume deposit.

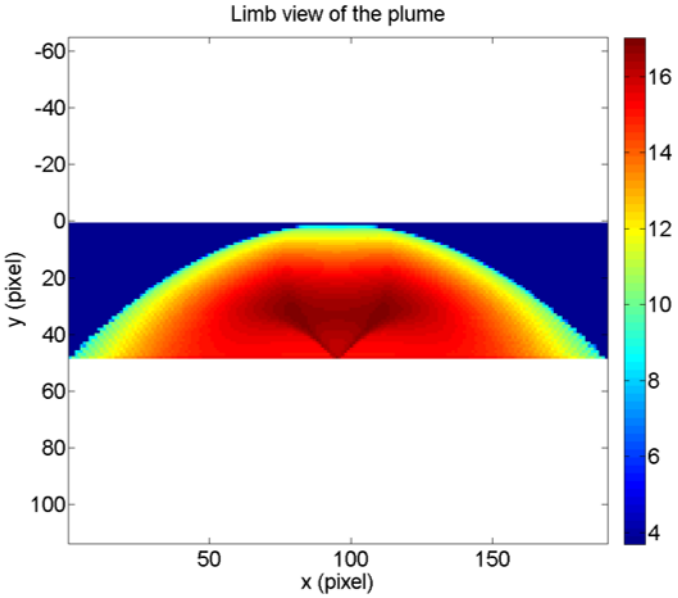

Figure 3.19: Logarithmic plot of the plume limb view assuming a Gaussian velocity distribution (μ= 0.2 kmm/s, σ = 20) and a pixel scale equal to 500 m.

The conclusions reported above came from different assumptions, but we know that changing some parameters could affect the reliability of our results. For example, if we consider lower velocities (as the lower value of 30 m/s reported in Fagents et al. (2000)), the plume deposit will be a very small spot on JANUS detector and, hence, not possible to observe in Ap-d sub-phase. On the other hand, considering the observation made by Roth et al. (2014b), the maximum extension of the plume deposit would be roughly 400 km (considering an erupting velocity of 720 m/s resulting from the plume height observed equal to 200 km) and, hence, it will cover a large area on the detector, which would correspond roughly to its half size. However, we do not consider this latter case as the most probable one because plumes have not been detected after the HST observation. In addition, null plumes detection were reported by imagers on Voyager 2, Galileo and New Horizons, but it could be due to the possibility that erupting venting was not at the limb when those images were acquired.

In our model we consider observations in FPAN filter, even if color images will be acquired too. From the expected performances of JANUS during AP-d sub-phase, it is computed that the SNR color filter is similar to the FPAN one. For this reason, the plume deposit could be observable also with other different filters since the feature

remains recognizable.

In this work, we took the Ap-d phase as a representative observational case since surface imaging and limb observation will be acquired. Obviously, this method could be applied to other AP flybys phase too (Table 3.5), even if in AP phases prior to AP-d the detection will be more challenging due to the smaller pixel scale.

Concerning the CAP, the closest approach phase that begins 1 hour prior the CA, the S/C will move faster and faster towards the CA (13/2/31 13:49), occurring at 403 km from the surface, CA_{lat} = - 47°, CA_{long} = 174°. At CA, the conditions will be quite demanding in terms of integration time, and will be the worst expected during the flyby. JANUS will scan the surface in 4 colours up to 2870 km from the surface (end of sub-phase CAP-d), then will operate in push-frame mode, initially in 4 colours and then in the only panchromatic filter. This trajectory will be the most powerful timeframe in term of achievable pixel scale on the Europa's surface (from $\sim$ 40 to 6 m), and will allow unprecedented investigations on surface geological details on many surface portions and/or specific surface targets. Therefore, the search of plume deposits (with the dimension assumed before) is more difficult and not the primary objective of this phase. On the other hand, if the plume deposit is smaller than our assumption, there could be the possibility to observe this feature in CAP phase too.

3.3 Loss rates of Europa's tenuous atmosphere

The study of the transient plumes (Roth et al., 2014b), with their potential implications on the nature of the moon's inner ocean, will have as mandatory prerequisite an accurate characterisation of the exospheric background. For this reason, we performed a detailed study of the Europa's tenuous atmosphere loss rates that are dominated by plasma-neutral interactions (Lucchetti et al., in press).

The source processes responsible for the generation of the tenuous atmosphere of Europa as well as the chemistry between exospheric neutrals and Jupiter's magnetospheric plasma have been discussed many times in the past (see in Plainaki et al. (2012, 2013); Cassidy et al. (2010, 2013); Krupp et al. (2010); Dalton et al. (2010); Coustenis et al. (2010); Bagenal et al. (2004); Pappalardo et al. (2009)). In particular, the plasma-neutrals interactions have been mainly studied either on the basis of Voyager and Galileo flyby data (Kabin et al., 1999; Bagenal et al., 2004; Schilling et al., 2008; Lipatov et al., 2010) or through analytical (Saur et al., 1998) and Monte Carlo models (Shematovich et al., 2005; Smyth & Marconi, 2006; Plainaki et al., 2012). However, the lack of a sufficient series of in situ measurements able to: a) further constrain the estimations obtained through the above mentioned studies and b) determine the variability of the magnetospheric plasma properties around Europa, has significantly limited our knowledge on the plasma-neutrals interactions and the temporal and spatial variability of the

exosphere loss rates. On the other hand, our understanding of the tenuous atmosphere sources has been significantly expanded by the results of a series of related laboratory ice experiments (Brown et al., 1978; Baragiola, 2003; Teolis et al., 2015; Galli et al., 2015). Nevertheless, a thorough and detailed determination of the balance between atmosphere sources and losses is expected to come once new in situ data will be obtained (i.e. during the ESA/JUICE and NASA/Europa missions).

In view of preparation for future missions to Europa, an accurate estimation of the loss rates for the main constituents of the exosphere of Europa, based on state to the art models providing the plasma-properties nearby the satellite as well as on laboratory derived cross sections for different plasma-neutral interactions, is of significant help. We provide detailed estimations of the loss rates of Europa's exosphere, based on the updated plasma conditions at the moon's vicinity, calculated recently by Bagenal et al. (2015) based on the analysis of Galileo data. We provide a broad and long list of reactions, not discussed thoroughly in previous Monte Carlo modeling papers, and we estimate for the first time their impact to the Europa's neutral environment for three sample plasma environment cases (hot and low density, cold and high density and an intermediate case that in this work is referred to as "medium"). All previous studies including estimations of the loss rates were based: a) on Voyager-1 data (e.g. Sittler & Strobel, 1987) or b) Cassini data (Delamere et al., 2005) or c) on plasma properties information provided by the earlier Bagenal (1994) model (e.g. Saur et al., 1998; Smyth & Marconi, 2006; Shematovich et al., 2005; Plainaki et al., 2012, 2013). We also include, for the first time, temporal variability of the loss rates due to the large variability in plasma properties. The tilt of Jupiter's magnetic field is another source of temporal variability as it brings Europa in and out of the dense plasma near Europa's centrifugal equator. With this work we provide an add-on to current knowledge, which can be used as a resource for the improvement of future plasma and atmosphere/exosphere models. Additionally, we investigate the role of different charge-exchange interactions between ionosphere/pickup ions and atmospheric neutrals, for all three dominant atmosphere species, namely water, oxygen and hydrogen. In previous studies (Shematovich et al. (2005); Smyth & Marconi (2006)) charge exchange processes were found to be of negligible importance. For completeness, we provide information also on photoreactions for both cases of quiet and active Sun.

3.3.1 Loss processes: rates and variability

Interactions of the tenuous atmosphere of Europa with Jupiter's magnetospheric plasma and, to a lesser extent, solar UV photons, lead to the ionization and/or dissociation of its constituents. Whereas such mechanisms result in the actual atmosphere loss, they provide also a supply of fresh ions and new atoms to the near-Europa space environment. Fresh ions can contribute to the further ionization of the neutral environment (Dols

et al., 2016). Moreover the freshly dissociated molecules modify the composition of the tenuous atmosphere, creating inhomogeneities in the nominal neutral distribution around the moon. Interactions in the near-Europa space environment, therefore, result in both dynamical changes of the plasma composition and temperature and effective atmosphere loss.

Plasma-neutral interactions

Cross sections for plasma-neutral interactions are energy dependent and hence the respective reaction rates depend on the speed distribution of the plasma, as well as the densities of each reactant (Burger et al., 2010). Therefore, in order to address the role of the different loss mechanisms, the external plasma environment has to be considered first. The plasma properties in the space environment in which Europa is embedded have been identified in detail in the past through the plasma model by Bagenal (1994), which was based on Voyager-1 Ultraviolet Spectrometer (UVS) data (Shemansky, 1987; Bagenal et al., 1992) and Plasma Spectrometer (PLS) measurements in Jupiter's inner magnetosphere. According to this model, the plasma electron population at Europa's orbit includes a core cold and a hot component that can be approximated by two Maxwellian distributions (at 20 and 250 eV, respectively). Moreover, the plasma properties were shown to have a variability depending on the location of Europa with respect to the JPS. In particular, due to the tilted (with respect to JPS) orbit of Europa, the plasma density falls off north/south of above/below the centrifugal equator with a scale height of $\sim 1R_J$ for 50-100 eV plasma (Kivelson et al., 2004). As Europa moves in its orbit, it effectively moves up and down the JPS and the density and temperature of the local plasma change remarkably. The Bagenal (1994) model predicted for the electron density at the orbit of Europa values of $\sim 35 - 40\ cm^{-3}$ off the equator and values of $80 - 100\ cm^{-3}$ near it, depending on the strength of the equatorial current. Observed electron densities over Galileo flybys of Europa ranged from 18 cm^{-3} to 250 cm^{-3} (Gurnett et al., 1998; Kurth et al., 2001). Ion-mixing ratios in the vicinity of Europa were estimated by Delamere et al. (2005) on the basis of the Cassini Ultraviolet Imaging Spectrograph (UVIS) data (Steffl et al., 2004). We note that the earlier models based on analyses of Voyager UVS data had lower abundances of S_2^+ and higher abundances of O^+ than the ones estimated by Steffl et al. (2004). Such differences between model outputs may be due to differences in the analysis techniques, different coverage of the UV spectrum, or actual changes in the torus conditions at the time of the measurements. Recently, Bagenal et al. (2015) analysed the available Galileo PLS and Plasma Wave Instrument (PWS) data to derive electron density, azimuthal speed and ion temperature of the plasma in the vicinity of Europa's orbit (away from Europa itself, though). They found that the flow speed has a narrow distribution around a median value that is equal to 83% of the corotation speed. Based on the observed temporal variability of

the plasma, Bagenal et al. (2015) provided three cases of plasma conditions: (a) Low density, high temperature; (b) Medium conditions of density and temperature; and (c) high density, low temperature. We use these updated plasma electron and ion conditions in the near-Europa space environment, as given in Bagenal et al. (2015), to estimate the loss rates of the tenuous atmosphere. These are provided in Table 3.7.

Table 3.7: Plasma properties in the near-Europa space environment as estimated by Bagenal et al. (2015) on the basis of previously unprocessed data. The ion composition is based on the physical chemistry model by Delamere et al. (2005). From Lucchetti et al. (in press).

	Plasma condition:	**(1) Low/Hot**	**(1) Medium**	**(1) High/Cold**	**Note**
$\boldsymbol{T(S^+)(eV)}$	S^+ temperature	500	130	70	
$\boldsymbol{T(S^{2+})(eV)}$	S^{2+} temperature	250	65	40	
$\boldsymbol{T(S^{3+})(eV)}$	S^{3+} temperature	170	45	25	
$\boldsymbol{T(O^+)(eV)}$	O^+ temperature	500	130	70	
$\boldsymbol{T(O^{2+})(eV)}$	O^{2+} temperature	340	90	50	
$\boldsymbol{T(H^+)(eV)}$	H^+ temperature	70	17	10	
$\boldsymbol{T_i}$ **(eV)**	ion temperature	340	88	48	from the Galileo/PLS instrument
$\boldsymbol{V(km/s)}$	flow speed	123	98	76	from the Galileo/PLS instrument
$\boldsymbol{T_e}$ **cold (eV)**	electron temperature (cold component)	30	20	10	
$\boldsymbol{T_e}$ **hot (eV)**	electron temperature (hot component)	1200	300	200	
$\boldsymbol{N_e cm^{-3}}$	(cold) electron density	63	158	290	from the Galileo/PLS instrument
$\boldsymbol{N_e(hot)/N_e}$	hot to cold electron density ratio	0.1	0.05	0.02	
$\boldsymbol{N(S^+)/N_e}$	S^+ composition	0.02	0.02	0.02	Delamere et al. (2005)
$\boldsymbol{N(S^{2+})/N_e}$	S^{2+} composition	0.14	0.14	0.14	Delamere et al. (2005)
$\boldsymbol{N(S^{3+})/N_e}$	S^{3+} composition	0.04	0.04	0.04	Delamere et al. (2005)
$\boldsymbol{N(O^+)/N_e}$	O^+ composition	0.3	0.3	0.3	Delamere et al. (2005)
$\boldsymbol{N(O^{2+})/N_e}$	O^{2+} composition	0.08	0.08	0.08	Delamere et al. (2005)
$\boldsymbol{N(H^+)/N_e}$	H^+ composition	0.12	0.12	0.12	Delamere et al. (2005)
$\boldsymbol{< A_i >}$	assumed mass of the dominant heavy ion species (amu)	18	18	18	Delamere et al. (2005); Bagenal et al. (2015)
$\boldsymbol{< Z_i >}$	assumed charge of the dominant heavy ion species (amu)	1.5	1.5	1.5	Delamere et al. (2005); Bagenal et al. (2015)
$\boldsymbol{B(nT)}$	background magnetic field	480	450	423	Delamere et al. (2005); Bagenal et al. (2015)

Whereas the available in situ measurements guide the construction of plasma torus models in the near Europa space environment, the plasma properties in the near surface regions are currently known with less certainty and they are mainly provided by models. 3D hybrid models (Lipatov et al., 2010, 2013, e.g) or 3D MHD models (Schilling et al., 2007; Rubin et al., 2015) of plasma interaction provide some insights into the near the surface plasma environment. Although a) strong evidence for the existence of an ionosphere has been provided through the Galileo Radio Science observations (Kliore et al., 1997) and b) so far substantial progress in modeling has been made, there are still substantial uncertainties considering the specific characteristics (e.g. height and thickness) of an ionosphere layer between the impinging magnetospheric ions and the moon's surface. Indeed, Sittler et al. (2013) discussed the complexity of inferring Europa's ionospheric scale height from Galileo Radio Science observations and concluded that the inferred electron density should be interpreted combining also the knowledge obtained through a global interaction model (e.g. Lipatov et al., 2010). Moreover, these authors noted that several plasma modeling efforts of the past could not resolve the problem of determining the characteristics of the ionopause due to either the modeling technique itself (for example the MHD models by Schilling et al. (2007, 2008) guiding-center approximation for the ions) or due to low model-resolution (for example, equal to $\sim$ 150 km in the model by Lipatov et al. (2010)).

Understanding the characteristics of Europa's ionosphere is of significant importance in order to determine the exosphere loss rates. In general, in a planetary (or lunar) atmosphere, below the ionopause, i.e. the transitional region between ions of magnetospheric origin and ionospheric ions, the external plasma does not penetrate, the convective electric field of the external flow is near zero and the gyroradius of the local ions is essentially zero. At altitudes above the ionopause the pick-up ions dominate, the plasma flow is non-zero and the convective electric field will be relatively large. If the thickness of the ionopause is large with respect to its height then the ionopause does not occur and the external plasma flow can penetrate down to the moon's surface. Recent simulations by Sittler et al. (2013) showed that at Europa the plasma flow can extend down near the surface when the O_2 column density is low enough. In particular, they showed that for a column density equal to $\sim 5 \times 10^{14} cm^{-2}$ the plasma flow stopped essentially at the altitude of 40 km defined as the height of the occurrence of the ionopause. Moreover, the model by Sittler et al. (2013) provides the density profile of pick up ions of different species for altitudes up to 200 km from the surface (see in Sittler et al. (2013), Fig.9). The ionosphere and pick up ion properties provided by Sittler et al. (2013) are used in this work in order to estimate the exosphere loss rates.

Based on the above description, the interactions, between the plasma and Europa's exosphere leading to the actual loss of the neutral population, refer either to electron-neutral or to ion-neutral collisions. In the latter case, the interactions refer (potentially)

to three ion populations, namely the ions in the plasma torus (with origin from Io), dominating at altitudes $\geq$ 200 km; the ionosphere ions, originating from the ionization of the sputtered neutral exosphere, dominating at altitudes $\leq$ 40 km; the pick-up ions, being the ionized neutrals that once generated they are immediately accelerated and picked-up by the corotating magnetic field. The term potential refers to the uncertainty for the existence of an ionosphere layer at Europa. In this work, we estimate the loss rates corresponding to electron and ion interactions with the neutral exosphere for the three plasma torus conditions given in Table 3.7 and the main ionosphere and pick up ion populations provided in Sittler et al. (2013). Here, we consider only the main constituents of Europa's exosphere, namely H_2O, O_2 and H_2. Although the expected ice irradiation processes at Europa do not exclude the existence of some other less abundant exosphere species, such as OH and H (Watanabe et al., 2000) or H_2O_2 and HO_2 (Kimmel et al., 1994; Orlando & Kimmel, 1997) and other minor components of the surface, laboratory measurements of ice irradiation experiments have shown that water molecules dominate the total release yield at lower temperatures ($<$ 120 K) and molecular oxygen and hydrogen at higher ($>$ 120 K) temperatures (Johnson & Kanik, 2001).

Electron-neutral interactions

Plasma electrons impacting the exosphere of Europa can dissociate and/or ionize its various constituents. The dissociation (or ionization) rate due to electron impact processes is computed by

$$\nu_e = \kappa(V_e) N_e \tag{3.1}$$

where N_e is the electron density and κ is the rate coefficient of the reaction (in $cm^3 s^{-1}$), determined from the cross section of the reaction and the velocity distribution function $f(V_e)$, where (V_e) is the velocity of the electrons measured relative to the neutrals. For electron impact processes, the plasma flow speeds (also called bulk velocities) can be ignored since the electron thermal speeds are much larger. For example, cold 20 eV electrons (Medium case in Table 3.7) have velocities of $\sim 2.7 \times 10^3$ km/s which are much larger than the measured flow speed in the near-Europa space, equal to 98 km/s (Bagenal et al., 2015). Therefore, for a thermalized (Maxwellian) electron population, the rate coefficient is a function of the electron temperature:

$$\kappa(T_e) = \int f(V_e)\sigma(V_e) dV_e \tag{3.2}$$

where $f(V_e)$ is the velocity distribution function of the electron population and σ is the experimentally determined cross section of the reaction. In order to estimate κ, we approximately consider the mean electron velocity $< V_E >= \frac{2}{\sqrt{\pi}} \sqrt{\frac{2k_b T_e}{m_e}}$ of a Maxwellian distribution function. Our results for different plasma electron populations are resented

in Table 3.8.

Table 3.8: Electron impact reactions rates for different plasma conditions. From Lucchetti et al. (in press).

Reaction	**(1) Low/Hot**		**(2) Medium**		**High/Cold**		**Note**
			$\nu(10^{-6}s^{-1})$				
	Cold	**Hot**[a]	**Cold**	**Hot**	**Cold**	**Hot**	
$H_2O + e \rightarrow OH + H + e$	3.0		3.31	1.28	0.92	0.96	[1,2]
$H_2O + e \rightarrow H_2O^+ + 2e$	1.88	0.58			0.18[b]	0.61	[2]
$H_2O + e \rightarrow OH^+ + H + 2e$	0.37	0.19	1.94	0.84		0.2	[2]
$H_2O + e \rightarrow OH + H^+ + 2e$	0.99	0.15	0.069	0.28		0.19	[2]
$H_2O + e \rightarrow H_2 + O^+ + 2e$	0.0085	0.026	0.013	0.26		0.039	[2,3]
$O_2 + e \rightarrow O + O + e$	1.43		0.0014	0.05	1.57[b]	0.16[c]	[4]
$O_2 + e \rightarrow O_2^+ + 2e$	1.5	0.79	2.58		0.082[b]	0.76[c]	[4]
$O_2 + e \rightarrow O^+ + O + 2e$	0.28	0.42	1.18	1.1		0.47[c]	[5]
$H_2 + e \rightarrow H + H + e$	1.24		0.091	1.66	3.55		[6]
$H_2 + e \rightarrow H_2^+ + e$	1.48	0.27	3.55		1.32	0.45	[7]
$H_2 + e \rightarrow H^+ + H + 2e$	0.019	0.016	1.32	0.45	0.024	0.036	[7]

[a] The cross section for the hot electron population are reported for an energy equal to 1000 eV (instead of 1200 eV) because cross sections for higher electron temperature are not reported in [2,3].
[b] The cross section are reported for an energy equal to 13.5 eV.
[c] The cross section are reported for an energy equal to 198 eV.
Reaction 1 Cross sections measured over an energy range from threshold to 300 eV [1].
Reaction 2,3,4,5 Reaction cross section measured from threshold to 1000 eV [2, 3].
Reaction 6 Cross sections measured over an energy range from 13.5 eV to 198.5 eV [4].
Reaction 8 Cross section corresponding to an electron temperature of 10 eV is below the threshold [5].
Reaction 9 Cross sections measured over an energy range from 9 eV to 80 eV [6].
Reaction 10,11 Cross sections measured over an energy range from threshold to 1000 eV [7].
Table References: [1] Harb et al. (2001); [2] Itikawa & Mason (2005); [3] Shirai et al. (2001); [4] Cosby (1993); [5]Itikawa (2009); [6] Yoon et al. (2008); [7] Straub et al. (1996).

Ion-neutral Interactions

Ion-neutral reactions refer to collisions between plasma ions and neutral species. The charge-exchange (also called "charge transfer") is a collisional process that takes place during the interaction between a relatively fast (energetic) ion and a cold neutral. During this process the fast ion and the cold neutral exchange their charge hence an energetic neutral atom (ENA) and a cold ion are being formed. If the projectile and the target

particles are of the same species, charge exchange is a symmetric (resonant) process (Hasted & Hussain, 1964) and the newly created ENA retains approximately both the energy of the colliding energetic ion and its direction (e.g. Milillo et al., 2005). In case of different species, either a non-resonant process (e.g. proton projectile and He target) or an "accidental resonance" in ionization energies (e.g. O^+ projectile and H target) can occur (Fite & Brackmann, 1963). The "accidental resonance", by which it is meant that the energy defect is almost zero but the two ions are not chemically identical, permits charge exchange to proceed rapidly in thermal energies (Banks & Kockarts, 1973). If the mean free path of the newly created ENAs is long enough, such an ENA can transport information out of the generation region, thus allowing remote sensing of the interaction process (e.g. Roelof et al., 1985; Roelof, 1987; Daglis & Livi, 1995; Orsini & Milillo, 1999; Barabash et al., 2001; Milillo et al., 2001; Orsini et al., 2001).

Charge-exchange rates are also determined by Equation 3.1 and 3.2 substituting the electron density and velocity, with the ion density N_i and velocity relative to the neutrals (V_i), respectively. Because ions are more massive than electrons, the relative bulk motion between the ions and neutrals is significant hence it needs to be taken into account when calculating the respective reaction cross section. The charge-exchange rate coefficient is given by:

$$\kappa(V_i) = \int f(V_i)\sigma(V_i)dV_i \tag{3.3}$$

where $V_i = V - V_{orb}$, with V_{orb} being the orbital velocity of Europa, equal to 14 km/s, and V being the flow velocity of the plasma as derived from the Galileo PLS measurements (Bagenal et al., 2015). We note that if the thermal temperature is large then both the thermal (random) motions of the ions and the bulk motion of the plasma relative to the neutral gas must be considered. Such is the case of plasma being slowed as flowing through satellite exospheres or the Enceladus plume (Burger et al., 2010). Johnson et al. (2006) showed that the presence of H_3O^+ in the Saturnian plasma implied reactions between neutral and ionized water molecules at low relative velocities because the cross section for H_3O^+ production is large for speeds below $\sim$ 10 km/s (Lishawa et al., 1990). For the Europa case, the random thermal ion velocities estimated by Bagenal et al. (2015) are in general lower than the flow velocity hence in the current study we do not take their effect to the relative velocity into account. Future in situ measurements of course will provide more detailed information on the plasma properties in the near-surface environment of Europa allowing hence a more accurate evaluation of the rates of the plasma-neutral interactions.

In our loss rate estimates corresponding to the interactions between the plasma torus ions and the neutrals (see Table 3.9), we take into account only the S^{++} and O^+ ions, since they are the dominant species of the sub-corotating plasma, with densities equal to 15% and 20% of the electron density, as inferred from UV observation in Steffl et al. (2004), in consistency also with the model by Delamere et al. (2005). We underline that

the low energy plasma composition was not measured directly by Galileo but it was inferred through the spectra and Mach numbers of the measured flows (Sittler et al., 2013). Indeed these measurements could not distinguish O^+ from S^{++} hence the relative abundances for these species are currently known only through remote observations plasma Io torus that do not include Europa's orbit. The complete composition of the plasma in the near-Europa space environment is presented in Table 3.7. We note that in the model of Delamere et al. (2005) the proton density ($\sim$ 12% of the electron density) is derived as additional ion charge to match electron density and to satisfy charge neutrality. Since the H^+ composition is not a direct measurement, in the current study we do not estimate rates corresponding to plasma neutral reactions involving H^+.

Table 3.9: Plasma flow charge exchange reactions rates given for reactions between S^{++} and O^+ ions and O_2, H_2 and H_2O neutrals. The ion velocity is equal to $V - V_{orb}$, where V_{orb} is the orbital velocity of Europa (equal to 14 km/s) and V is the flow velocity of the plasma as derived from the Galileo PLS measurements (Bagenal et al., 2015). The S^{++} and O^+ ion densities used to calculate the reaction rates are based on the physical chemistry model by Delamere et al. (2005), see Table 3.7. From Lucchetti et al. (in press)

	(1) Low/Hot	**(2) Medium**	**High/Cold**	**Note**
V_{ions} (km/s)	109	84	62	[1]
$N(S^{++})\ cm^{-3}$	9	22	41	[2]
$N(O^+)\ cm^{-3}$	19	47	87	[2]
Reaction	$\boldsymbol{\nu(10^{-6}s^{-1})}$	$\boldsymbol{\nu(10^{-6}s^{-1})}$	$\boldsymbol{\nu(10^{-6}s^{-1})}$	
$S^{++} + O_2 \rightarrow S^+ + O_2^+$	0.15	0.28	0.38	[3]
$O^+ + O_2 \rightarrow O + O_2^+$	0.27	0.51	0.7	[3]
$S^{++} + H_2 \rightarrow S^+ + H_2^+$	0.09	0.32	0.42	Copy of the below
$O^+ + H_2 \rightarrow O + H_2^+$	0.09	0.32	0.42	[4]
$S^+ + +H_2O \rightarrow S^+ + H_2O^+$				
$O^+ + H_2O \rightarrow O + H_2O^+$		0.7	0.11	[5]

Reaction 3 The cross section is not available and we used the value of the cross section of the reaction below (as Dols et al. (2016)).
Reaction 5 Cross section value not found in literature.
Reaction 6 Cross section studied in the energy range 1 to 400 eV.
Table References: [1] Bagenal et al. (2015); [2] Delamere et al. (2005); [3] McGrath & Johnson (1989); [4] Tawara et al. (1985); [5]Turner & Rutherford (1968).

Regarding the loss rate estimates corresponding to the interactions between the iono-

sphere ions and the neutrals, we attempt to provide an upper limit of the respective charge-exchange reactions considering the O_2^+, H_2O^+, and H_2^+ ionosphere densities at the height of the ionopause (where they become maximum). Considering the interactions between pick-up ions and exosphere, in this work we provide estimations for altitudes $>$ 200 km, since the region between the height of 200 km and the ionopause is a transition region where the density of the pick-up ions is highly variable (see Sittler et al. (2013), Fig. 9). For the pick-up ions at the altitude of 200 km we assume a relative speed equal to the one of the plasma torus (see Table 3.7). We underline that our estimated loss rates due to pick-up ion interactions are in consistency with the overall plasma neutrality. Note that Delamere et al. (2005) estimated that whereas the addition of pickup O^+ ions and O_2^+ ions to the torus increases the net temperature from 130 eV and 100 eV to 300 eV and 200 eV respectively, the modification they bring to the plasma torus composition is minor. For the ionospheric ions, originating from the ionization of the sputtered neutral exosphere and dominating at altitudes $<$ 40 km, we assume a velocity equal to $\sim$ 10 km/s as given by Sittler et al. (2013). Our results are presented in Table 3.10. Although we did not perform any detailed calculations corresponding to the transition region between the ionopause and the altitude at which the plasma torus becomes dominating (assumed to be equal to $\sim$ 200 km, as in Sittler et al. (2013)), we expect that the respective loss rates will vary between the values provided in Table 3.9 and Table 3.10.

Table 3.10: Pick up and ionosphere charge exchange reactions rates given for reactions between O_2^+, H_2^+ and H_2O^+ ions and O_2, H_2 and H_2O neutrals. We assume for pick up ions a relative speed equal to the one of the plasma torus. The pick up ion density is provided by Sittler et al. (2013) (Figure 9) and it is equal to 10 cm^{-3} for the three ions species (O_2^+, H_2^+, H_2O^+), which is valid for the different plasma condition cases. The ionosphere ion velocity (10 km/s) and the ionosphere ion density are provided by Sittler et al. (2013). We assume an ion density equal to 10000, 50 and 25 cm^{-3} for O_2^+, H_2^+, H_2O^+ ions respectively. From Lucchetti et al. (in press).

	PICK UP IONS			**IONOSPHERE**	**Note**
	(1) Low/Hot	**(2) Medium**	**High/Cold**		
V_{ions} (km/s)	109	84	62	10	[1] pick up ions, [2] ionosphere ions
$N(O_2^+)cm^{-3}$	10	10	10	1000	[2]
$N(H_2^+)cm^{-3}$	10	10	10	50	[2]
$N(H_2O^+)cm^{-3}$	10	10	10	25	[2]
Reaction	$\boldsymbol{\nu(10^{-6}s^{-1})}$	$\boldsymbol{\nu(10^{-6}s^{-1})}$	$\boldsymbol{\nu(10^{-6}s^{-1})}$	$\boldsymbol{\nu(10^{-6}s^{-1})}$	
$O_2^+ + O_2 \rightarrow O_2 + O_2^+$		0.05	0.04	15	[3]
$H_2^+ + O_2 \rightarrow H_2 + O_2^+$	0.027	0.027	0.027	1.35	[4]
$H_2O^+ + O_2 \rightarrow H_2O + O_2^+$	0.002	0.002	0.002	0.005	[5]
$O_2^+ + H_2 \rightarrow O_2 + H_2^+$	0.066	0.034	0.019	0.005	[6,7]
$H_2^+ + H_2 \rightarrow H_2 + H_2^+$	0.082	0.067	0.054	0.12	[8]
$H_2O^+ + H_2 \rightarrow H_2O + H_2^+$					
$O_2^+ + H_2O \rightarrow O_2 + H_2O^+$					
$H_2^+ + H_2O \rightarrow H_2 + H_2O^+$	0.44	0.42	0.36		[9]
$H_2O^+ + H_2O \rightarrow H_2O + H_2O^+$				0.025	[10]

Reaction 1 Cross section measured for energy up to 1000 eV [3]. **Reaction 2,3** The reaction rate coefficients for references [4,5] are published for a fixed gas temperature or a limited range of temperatures. These values are equal to 2.7×10^{-9} and 0.2×10^{-9}, which are reported from [4] and [5] respectively.**Reaction 4** Cross section measured from 100 eV [6,7]. **Reaction 6,7** Values not found in literature. **Reaction 8** Cross section measured for incident ion energy range 30 - 500 eV. **Reaction 9** Cross section measured for energy up to 60 eV.

Table References: [1] Bagenal et al. (2015); [2] Sittler et al. (2013); [3] Benyoucef & Yousfi (2014); [4] Kim & Huntress (1975); [5]Fehsenfeld et al. (1967); [6]Irvine & Latimer (1997); [7]Hasan & Gray (2007); [8]Vance & Bailey (1966); [9]Coplan & Ogilvie (1970); [10]Lishawa et al. (1990).

Photoreactions

Photoreaction rates are given at 1 UA by Huebner et al. (1992). These rates are inversely proportional to the distance of Europa from the Sun squared. The values listed in Table 3.11 are for quiet and active Sun at Europa's orbit (5.2 UA) for H_2O, O_2 and H_2 Photo-Reactions.

For completeness, we mention the contribution coming from fresh photoelectrons that have enough energy to dissociate and ionize the neutrals. We estimate that the rate resulting from this secondary process is about 10% - 30% of the photoreaction rate. This is a standard approximation used in the aeronomic studies, that was checked and validated in the accurate calculations of the photo and photoelectron rates for different planetary atmospheres (see, for example, Hubert et al. (2012) and Ionov et al. (2014)).

Table 3.11: Photoreaction rates for H_2O, O_2 and H_2 from Huebner et al. (1992). From Lucchetti et al. (in press).

Photo-Reaction	$\nu(10^{-6}s^{-1})$
$H_2O + h\nu \rightarrow H + OH$	$0.38 - 0.65$
$H_2O + h\nu \rightarrow H_2 + O(^1D)$	$0.022 - 0.055$
$H_2O + h\nu \rightarrow H + H + O$	$0.028 - 0.71$
$H_2O + h\nu \rightarrow H_2O^+ + e$	$0.012 - 0.031$
$H_2O + h\nu \rightarrow OH^+ + H + e$	$0.0021 - 0.0056$
$H_2O + h\nu \rightarrow OH + H^+ + e$	$0.00048 - 0.0015$
$H_2O + h\nu \rightarrow H_2 + O^+ + e$	$0.00022 - 0.00082$
$O_2 + h\nu \rightarrow O(^3P) + O(^3P)$	$0.0052 - 0.0082$
$O_2 + h\nu \rightarrow O(^3P) + O(^1D)$	$0.15 - 0.24$
$O_2 + h\nu \rightarrow O(^1S) + O(^1S)$	$0.0015 - 0.0035$
$O_2 + h\nu \rightarrow O_2^+ + e$	$0.017 - 0.044$
$O_2 + h\nu \rightarrow O + O^+ + e$	$0.004 - 0.013$
$H_2 + h\nu \rightarrow H(^1S) + H(^1S)$	$0.0018 - 0.004$
$H_2 + h\nu \rightarrow H(^1S) + H(2s, 2p)$	$0.0013 - 0.003$
$H_2 + h\nu \rightarrow H_2^+ + e$	$0.002 - 0.004$
$H_2 + h\nu \rightarrow H + H^+ + e$	$0.00035 - 0.0011$

3.3.2 Discussion

Overall results on the H_2O, H_2, and O_2 loss rates

For the H_2O constituent of the atmosphere we find that the dominant loss is due to electron impact dissociation. As shown in Table 3.8, such process is expected to have an efficiency that varies with the assumed plasma conditions (i.e. density and temperature).

We note that such plasma conditions (taken from the Bagenal et al. (2015) model) depend on both the location of Europa with respect to the JPS and on the epoch of the Galileo observations on which the plasma model was based. Maximum loss is expected for the orbital phases of median plasma conditions (Case (2) in Table 3.8) and it is estimated to be equal to $3.31 \times 10^{-6} s^{-1}$. Production of minor species H and OH is favoured during these phases. We note that the cold plasma electron population is the main responsible for the H_2O exosphere loss.

For the H_2 we find that the dominant loss process is electron impact ionization (leading to the production of H_2^+) when Europa is under median plasma conditions, and electron impact dissociation when Europa is found under conditions of high plasma density and low plasma temperature (Case (3) in Table 3.8). Both processes have a rate equal to $3.55 \times 10^{-6} s^{-1}$. The dissociation process populates the exosphere with H atoms that, given their low mass, can easily escape the moon's gravity and make part of Europa's neutral cloud (gravitationally bounded to Jupiter).

For the O_2 exosphere, we find that charge-exchange reactions between the ionospheric O_2^+ and exospheric O_2 molecules have the highest rates with respect to all other loss process. In particular, we find that the $O_2^+ - O_2$ reaction rate, equal to $\sim 15 \times 10^{-6} s^{-1}$ is by a factor of ~ 6 and ~ 10 higher than the ones corresponding to electron impact ionization (medium case in Table 3.8) and electron impact dissociation (High/cold case in Table 3.8) processes, respectively. Of course this result is also due to the actual assumption on the reactant's density, which in this study was considered as in Sittler et al. (2013). Nevertheless, the domination of the $O_2^+ - O_2$ charge exchange over all other loss processes is in agreement with Dols et al. (2016), who used different assumptions to estimate the importance of this process as well as a multi-species chemistry model. As in case of H_2O and H_2 exospheres, also here the efficiency of the electron impact processes depends strongly on the position of Europa with respect to the JPS determining the actual plasma conditions. In particular, the electron impact ionization loss rate varies by a factor up to ~ 3.4 and the dissociation rate by a factor up to ~ 31 among the three considered cases of plasma conditions. Although these processes are not the ones determining the actual loss of exosphere molecules, their rates can be used in order to roughly estimate the production of ionosphere O_2^+ and atomic oxygen. Information on such intermediate products of the plasma-neutral interactions, however minor, can be useful during the interpretation of remote sensing measurements of Europa's exosphere (as for example: the ultraviolet line emission of atomic oxygen).

Volume-integrated O_2 loss rates using the EGEON model

In order to calculate the volume integrated neutral loss rates we use the O_2 tenuous atmosphere described by the EGEON model (Plainaki et al., 2012, 2013), including the release yields revised described in Plainaki et al. (2015). We consider two different

configurations between Jupiter, Europa and the Sun: **Conf. 1** subsolar point coincides with the leading hemisphere apex and **Conf. 3** subsolar point coincides with the trailing hemisphere apex [1]. For case **Conf. 1** the spatially averaged O_2 column density given by the revised EGEON model is equal to $2.7 \times 10^{18} m^{-2}$ whereas for **Conf. 3** it is equal to $1.1 \times 10^{19} m^{-2}$. As shown in Table 3.10 the charge exchange reaction rates due to the pick up and ionosphere processes differ by almost three orders of magnitude. Moreover, the O_2 atmospheric density falls off by more than 2 orders of magnitude after the first 100s of kms (the low-altitude scale height of the EGEON model is equal to $\sim$ 20 km (see Milillo et al. (in press)). This means that the dominant charge-exchange loss takes place at low altitudes and is due to the slow, i.e. 10 km/s, O_2^+ (ionospheric) population. Therefore in our calculation we use the respected reaction rate. The O_2 volume integrated loss rates due to the dominant loss mechanisms (these are charge-exchange, electron impact ionization and electron impact dissociation, in order of efficiency) are presented in Table 3.12. For comparison, in Table 3.12, we also present the results obtained through other studies. The respective volume integrated loss rates calculated through different models are also presented. We note that in our estimates, the volume-integrated loss rates are proportional to the neutral column density and they depend on some more or less free parameters (e.g. the energy of the ionospheric particles). Given the uncertainty in the determination of such parameters, the derived estimations can be used to validate the whole approach of the loss calculations to first order, but cannot be considered as an independent estimation of the absolute loss of the atmosphere.

Table 3.12 shows that the ionosphere plasma-neutral interaction is the most important agent for the exospheric O_2 depletion. However, we note that the estimated rates corresponding to charge-exchange presented in Table 3.12 do not represent a net atmosphere loss as a single charge-exchange reaction results both in the loss of a relatively cold O_2 atmospheric molecule (via charging) and the production of an energetic O_2 molecule; the latter will leave the Europan gravity field only if its velocity is larger than the escape velocity and if its trajectory does not intersect the surface. We can assume that the first condition is satisfied almost always since the O_2^+ velocity (in the current study assumed to be equal to $\sim$ 10 km/s, following Sittler et al. (2013)) is generally larger than the gravitational escape velocity (equal to $\sim$ 2.02 km/s) and since this collisional process can be considered elastic, though the incoming ion will lose some momentum during the collision. The second condition, however, is not necessarily satisfied for every reaction. Therefore, the net exosphere loss rate due to charge exchange for the exosphere will result from the balance between the gain due to the freshly generated energetic O_2 molecules (i.e those that do not escape Europa's gravity field) and the loss due to the freshly ionized O_2. Due to this fact, the estimates presented in Table 3.12 are upper lim-

[1] Note that in this work the same nomenclature as in Plainaki et al. (2013) has been considered for the different configurations, between Jupiter, Europa and the Sun.

Table 3.12: Volume integrated O_2 loss rates calculated through different models. From Lucchetti et al. (in press).

Model	**Smyth & Marconi (2006)** ($10^{26}s^{-1}$)	**(Shematovich et al., 2005)** ($10^{26}s^{-1}$)	**(Saur et al., 1998)** ($10^{26}s^{-1}$)	**(Dols et al., 2016)** ($10^{26}s^{-1}$)	**This work** ($10^{26}s^{-1}$)
***O_2* loss processes**					
Ionization		4.6[1,2] ; 5.3[3,2]	1.2	4.8	2.2 - 8.8[4,5]
Dissociation		0.039		3	1.3 - 5.3[4,6]
Charge-exchange	2.7	0.88[1] ; 0.014[3]	7.3	29.31	13 - 51[4,7,8]

[1] This value corresponds to Model D in Shematovich et al. (2005).
[2] This value includes ionization, charge-exchange and sweeping effects.
[3] This value corresponds to Model B in Shematovich et al. (2005).
[4] The lower and upper limits in the rates estimated in this work correspond to cases (a) and (b), respectively, for the considered O_2 exosphere (see text).
[5] Plasma conditions corresponding to Case (2) were considered (see Table 3.7).
[6] Plasma conditions corresponding to Case (3) were considered (see Table 3.7).
[7] The charge-exchange volume integrated rates in this work were estimated for the reaction $O_2^+ + O_2 \rightarrow O_2 + O_2^+$ which is the most effective one according to Table 3.10. The ionosphere O_2^+ density given by Sittler et al. (2013) was considered in the calculation.
[8] Assuming that at least half of the fresh energetic O_2 molecules produced through charge-exchange have velocities directions favoring escape, the net loss due to this process is expected to have values equal to 1/2 of the ones presented here (see also text).

its for the loss of the O_2 atmosphere due to charge exchange. Recently, Dols et al. (2016) modeled symmetrical charge-exchange cascades between ionospheric O_2^+ and exospheric O_2 and showed that the total production rate of ejected neutrals could be even an order of magnitude larger than the production of ions. In the current calculation, we make the rough assumption that at least half of the fresh energetic O_2 molecules produced through charge-exchange have velocities directions favouring escape. In this case, we deduce that the expected loss of the exospheric O_2 due to charge-exchange has values equal to 1/2 of the ones presented in Table 3.12 hence ranging between $6.5 \times 10^{26}s^{-1}$ and $26 \times 10^{26}s^{-1}$. We note that the charge-exchange process in any case will lead to a modification of the energy distribution of the exospheric population since it favours, simultaneously the loss of cold populations and the gain of energetic ones. An accurate estimate of the spatial and temporal dependence of the exosphere loss as well as the determination of the O_2 energy distribution function resulting from the consideration of all loss processes, requires a detailed analytical or Direct Simulation Monte Carlo model (DSMC) and goes beyond the scope of this work.

As shown in Table 3.12, the O_2 volume integrated loss rates estimated in this study are by more than one order of magnitude larger than those calculated by Smyth & Marconi (2006) and by Shematovich et al. (2005). On the other hand, our results are consistent with those by Dols et al. (2016). This is because this study, as well as the study by Dols et al. (2016), includes the charge exchange loss process between a high density ionospheric O_2^+ population and the atmospheric O_2. Small differences between our estimated rates and those by Dols et al. (2016) are due to the atmospheric model used as a basis for the calculation. Dols et al. (2016) used the atmosphere column densities of Smyth & Marconi (2006) whereas we used the ones of EGEON, in Plainaki et al. (2013), revised due to yield corrections (see Milillo et al. (in press); Plainaki et al. (2015)). On the other hand, Saur et al. (1998) estimated the neutral losses due to both ionization and charge exchange. In order to make a comparison of the results presented in this work and those in Saur et al. (1998), some clarifications of the vocabulary and the method used by these authors are necessary. Regarding ionization, what was actually calculated by Saur et al. (1998) was the flux of the ionized neutrals hitting the surface of Europa or being convected out of Europa's atmosphere. Such a process is referred to as "pick up loss" in that paper. Regarding charge exchange, Saur et al. (1998) computed a flux of ions out of the exobase generated after a collision of an ion with a neutral. We note that in that calculation the authors considered only the charge exchange cross section, whereas the respective loss process was referred to as "atmospheric sputtering"[2]. On the basis of the above, it is reasonable to compare quantitatively our ionization and charge exchange results with the pick up loss and atmospheric sputtering results, respectively, presented in Table 3.8 in the Saur et al. (1998) paper. We find that the volume integrated ionization loss rate calculated by Saur et al. (1998) is consistent with our results. In addition, our net charge-exchange volume integrated loss rate (ranging from $6.5 \times 10^{26} s^{-1}$ to $26 \times 10^{26} s^{-1}$) is similar to the one of Saur et al. (1998), when considering the exosphere configuration **Conf. 1** (i.e. leading hemisphere is the illuminated one) and it is ~ 3 times larger in the exosphere configuration **Conf. 3** (i.e. trailing hemisphere is the illuminated one). Since the loss rate is proportional to the exosphere density, the difference between our results and those in Saur et al. (1998) can be explained by differences in the assumed neutral density and cross sections. For the **Conf. 1** atmosphere configuration the EGEON model gives a column density equal to $2.7 \times 10^{18} m^{-2}$, similar to the one assumed by Saur et al. (1998) (equal to $5 \times 10^{18} m^{-2}$) hence the averaged volume integrated loss rates are very similar. For the **Conf. 3** atmosphere configuration the EGEON model gives a column density equal to $11 \times 10^{18} m^{-2}$ which is 2.2 times higher than the one assumed by Saur et al. (1998). We note that such a dense exosphere is the result of the effectiveness of the radiolysis process leading to a major surface release (and hence

[2]Note that according to Johnson (1994) the term "atmospheric sputtering" should refer to the combination of many processes rather than a single one

exosphere generation) when the trailing hemisphere of the moon is illuminated, as shown in Plainaki et al. (2013). Nevertheless, the obtained rates (see Table 3.12) are not strictly proportional since energy dependent cross section were considered in this study. Saur et al. (1998) assumed an effective charge exchange cross section value corresponding to an ion velocity of 60 km/s, equal to $2.6 \times 10^{-19} m^2$. Moreover, on the basis of the method used in our work, our estimates (Table 3.12, 6^{th} column) depend on the column density of the considered neutral model (rather than its atmospheric scale height) as well as on the actual rate corresponding to the loss process. Other estimates (see Table 3.12) were based on different methods (e.g. numerical methods as in Dols et al. (2016). It is, however, very difficult to test principle dependencies of those estimations and to understand the extent to which the (volume integrated) results in the past works depended either on the neutral (plasma) models themselves (e.g. scale height variation) or on the considered efficiencies of the loss processes. To achieve such a distinction (that would permit a more in depth comparison between different studies) detailed knowledge on each past model is necessary. Such an investigation, however challenging, goes beyond the scope of the current study.

Add-on to current knowledge

The main conclusion of the current study is that one of the dominant loss processes of Europa's exosphere is coming from the charge-exchange between the tenuous O_2 atmosphere and its own atmosphere ions. However, this rather unexpected result should be treated with caution due to uncertainties in the determination of the energy distribution function and density of the pickups ions due to limited in situ measurements. It is known that electron densities up to 104 cm^{-3} were measured very close to the moon's surface, however, the determination of the dominant ion species is still open. O_2^+ could be the main ion, but in the very near-surface layer the situation is rather complicated due to the following two reasons: 1) O_2^+ can be lost via its dissociative recombination with the ionospheric (thermal) electrons; and 2) ionization chemistry in the $O_2 + H_2 + H_2O$ mixtures results in the domination of the O_2^+, O_2H^+ and H_3O^+ ions (Larsson et al., 2012). Although H_2 and H_2O are minor species, nevertheless they should change the ion composition near surface. Such reactions could reduce our above estimated charge-exchange rates up to one order of magnitude.

The physics of plasma-moon interactions in the Jupiter system is one of the major interests of the international scientific community, especially in view of the upcoming JUICE mission (Grasset et al., 2013). The understanding of the spatial and temporal variability of Europa's neutral environment as well as of the implications of its interactions with the moon's internal ocean, require detailed knowledge of the neutral-plasma interactions. The related existing observations, obtained with HST (Hall et al., 1998; McGrath et al., 2004; Saur et al., 2011) and to a lesser extent in situ (Kliore et al., 1997;

Kurth et al., 2001; Hansen et al., 2005), have provided important constraints for determining the atmospheric source and loss rates. However, due to a) the lack of a direct measurement of the main atmospheric species; b) the existence of several atmospheric models based on very different approaches (e.g. assuming either the collisional (e.g. Shematovich et al., 2005; Smyth & Marconi, 2006) or the collisionless (e.g. Cassidy et al., 2007; Plainaki et al., 2012) approximation); c) the existence of several plasma interaction models (e.g. Saur et al., 1998; Sittler et al., 2013; Dols et al., 2016); d) recent debates on the nature of Europa's neutral and plasma environments (see paper by Shemansky et al. (2014)), our current understanding of Europa's plasma-neutral interactions is still fragmentary.

In view of the future JUICE mission observations, the need for an overall revision of the source and loss mechanisms for the exosphere of Europa is urgent. In this context, we provided in the current study a rough estimation of the efficiency of the dominant interactions at Europa that can be used as a starting point in future modeling studies of the moon's environment. Such models could be used as basic tools for planning the future JUICE observations and, later, for interpreting the actual exosphere and plasma measurements.

3.4 Summary

The presence of a subsurface ocean is a primary topic on Europa, in addition the recent discovery of a transient plume at the south pole by HST observations (Roth et al., 2014b) has raised many questions regarding the interaction between the subsurface/surface and the outer environment of Europa in terms of active processes affecting the icy satellite. In view of the future JUICE/ESA mission and of our involvement in JANUS camera, in this chapter we focused on different topics related to the presence of a subsurface ocean in order to achieve further information about the satellite and be of help to the observation planning of JUICE/JANUS.

Firstly, we simulated the possible detection of a plume deposit on the surface of Europa by the JANUS instrument, the camera on board the JUICE mission. We study the detection of the plume deposit basing our assumption on the work of Fagents et al. (2000), that suggested that some surface features on Europa can be the result of cryovolcanic eruptions, i.e. plumes. Hence, we simulated a possible plume deposit of particles in terms of an albedo distribution because we expect a snow plume deposit with an albedo higher than the surrounding surface of Europa. We found that the simulated plume deposit could be detectable as bright spot by JANUS during the Europa flybys phase. In particular, we focus our attention on a sub-phase of E9 flyby, the AP-d sub-phase, making observation simulation in order to achieve the SNR of images that will be taken in FPAN filter. We demonstrate that plume deposit, which is composed mainly by snow,

will be visible in respect to the Europa surface during the flyby Ap-d sub-phase even with lower SNR than those expected.

Nevertheless, further studies about this issues will be performed in accordance with additional development of the JUICE mission and possible changes in JANUS observation strategies. In particular, in the next future we will focus our attention on other flybys phases in order to understand if we could observe this phenomenon not only in Ap-d phase. If it will be the case, we will monitor the variability of the phenomenon with time. In addition, limb observations will be studied in more detail once the JANUS observation scenario will be defined.

Then, in the second part of the Chapter, we obtained all loss rates characterising the main species of Europa's exosphere that could be relevant to the investigation of Europa's interaction with Jupiter's magnetospheric plasma and can be of use during the observations planning preparation for JUICE mission to Europa (Lucchetti et al., in press). In fact an accurate characterisation of the exospheric background is a mandatory prerequisite to study the transient plumes (Roth et al., 2014b), with their potential implications on the nature of the moon's inner ocean. We have studied the loss rates of the main components of Europa's tenuous atmosphere (O_2, H_2O, H_2) on the basis of energy-dependent reaction cross sections found in literature and, for the first time, updated plasma conditions obtained from the recent state to the art model by Bagenal et al. (2015). We performed calculations for electron impact dissociation and ionization processes, for charge-exchange (considering plasma torus, pick up and ionosphere ions) and for photo processes (for both cases of quite and active Sun). For the dominant (in the near-surface regions) O_2 species, the volume integrated loss rates were estimated, using the revised (for the surface release yields) O_2 exosphere described by the EGEON model, for two different configuration between Europa, Jupiter and the Sun (i.e. subsolar point coincides with the leading hemisphere apex and subsolar point coincides with the trailing hemisphere apex) (Plainaki et al., 2013). The main results can be summarized as follows:

1. For both H_2O and H_2 tenuous atmospheres, the loss rates depend on the highly variable plasma conditions. The cold plasma electron population is primarily responsible for H_2O and H_2 loss, in particular maximum loss is expected under median plasma conditions and median or high plasma conditions for H_2O and H_2, respectively.

2. For the O_2 exosphere, we find the $O_2 - O_2^+$ charge-exchange process may have a dominant role in the exosphere loss, in agreement with Dols et al. (2016) but contrary to what has been suggested by previous atmospheric models.. Using the revised O_2 column density based on the estimation from the EGEON model (Plainaki et al., 2013), we estimate that the $O_2 - O_2^+$ charge exchange rate is in

the range $(13 - 51) \times 10^{26} s^{-1}$, depending on the configuration between Europa, Jupiter and the Sun.

In view of future missions to the Galilean satellites, namely JUICE mission to Europa, the current estimates could be useful for the planning of observation strategies and, later, for the interpretation of the observations.

Work in progress

In the following, we briefly introduce a work in progress we are performing regarding the estimation of the icy shell thickness, which is one of the main open questions regarding Europa. We support the hypothesis of the presence of an ocean layer using the fractal percolation theory. This method allows to study the spatial distribution of vents and fractures in terms of their self-similar clustering, in other words vents and fractures show spatial distribution characterised by scale invariance.

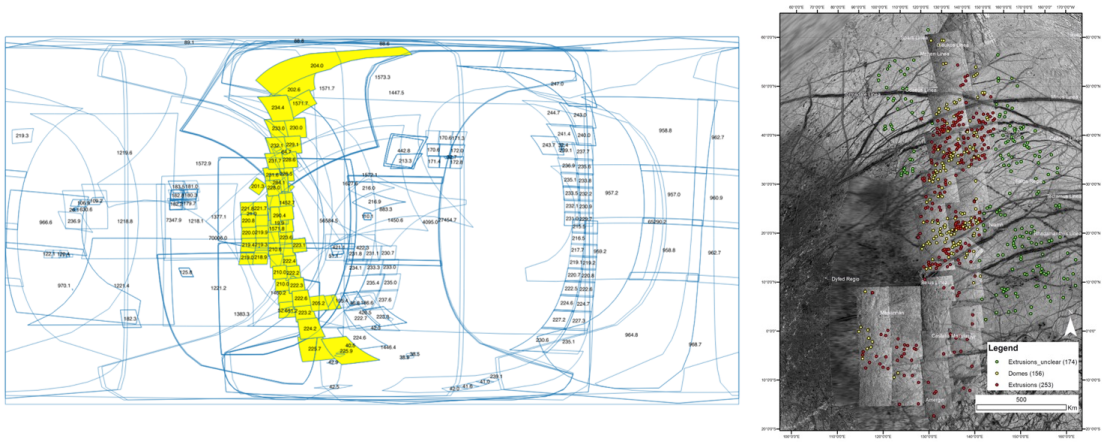

Figure 3.20: Left: Galileo SSI (solid state imager) resolution map of Europa. To investigate the possible depth of subsurface ocean, we chose the region at highest resolution from Galileo flyby with an average resolution ranging between 200 and 250 m/px. Right: Detailed of the mapped surface features (domes and extrusions).

The distribution of these vents reflects the presence of a liquid reservoir hydraulically connected to the surface via a fracture network. On Earth, a direct genetic and spatial link between subsurface fractures and vent occurrence has previously been observed (e.g. Tibaldi, 1995; Connor et al., 2000; Mazzarini, 2004; Mazzarini & Isola, 2010). Thus, the scale invariance in vent distribution is thought to reflect the fractal properties of the connected part of a fracture network that allows liquid to pass from deep reservoirs through the crust to the surface. This method was tested on Earth and already applied on Mars, in particular on Ascreus Moon (Pozzobon et al., 2014), and on Enceladus.

Our idea is to apply the same method on Europa, analysing the domes and extrusions that we see on the surface in order to determine the depth of the subsurface liquid ocean, Figure 3.20. Hence, the spatial distribution of vents should be analysed in terms of their self-similar clustering and a two-point correlation method must be used to measure the fractal dimension of the vents population (Mazzarini, 2004; Mazzarini & Isola, 2010). The correlation coefficient characterising the vents distribution will be defined by a lower and upper cut-off, that should represent a mechanical discontinuity and the thickness of the icy crust, thus connected to the liquid reservoir. Preliminary results suggest an icy shell thickness equal to 120 km, which is larger than what previously published. For this reason, we have to check and refine our fractal method and, in addition, we have to analyse also lineaments distribution with this fractal method (because also fractures distribution can be studied in term of self-similar clustering) in order to find if results coming from different surface features will be in agreement.

Conclusion

This PhD thesis focuses on the analysis of different structures and phenomena related to high energetic processes, which characterise the Solar System bodies. Specifically, this work concerns three main topics: (i) the numerical model of one of the most geological energetic process, i.e. impact cratering; (ii) the investigation of the fragmentation processes that could have formed boulders on comet Churyumov-Gerasimenko 67P; (iii) the analysis of a possible transient plume originating from cryovolcanic events on Europa, the Jovian icy satellite, combined with an accurate characterisation of its exospheric background.

Numerical modelling of impact craters

Impact cratering is a complex process and its current understanding combines both observational data and computer simulations. In this thesis we used the iSALE hydrocode, that is a code used for modelling highly dynamic events, and in particular the propagation of the shock wave as well as the behaviour of geologic materials over a broad range of stress and deformation states. In particular, we simulated two different impact structures present on terrestrial planets, specifically on Mercury and Mars. After an overview of the impact craters geological context, we obtained the crater profile from DTMs, which are generated using satellite images, and we used it to compare our output simulation results.

For the case of Mercury, we analysed a particular landform showing a steep-sided cone with associated pyroclastic deposits in order to investigate its origin. This morphology could suggest a genesis involving explosive volcanism, but through modelling we assessed the feasibility of another hypothesis. In fact, we demonstrated that the cone is the intrinsic central peak of an impact crater; indeed the cone lies within an encircling trough, which is in turn encircled by a ridge that could be interpreted as the rim crest of a 43 km crater diameter (Thomas et al., 2015). We found that the landform at this location is not a volcanic construct, but likely represents the extreme end-member of a large class of volcanic vents circumferential to impact-crater central peak structures, indicating that the crater-related faults control explosive volcanism at such locations. The hydrocode modelling was essential to determine the plausibility of our hypothesis.

We then considered Mars, and we studied the Firsoff crater located in Arabia Terra, i.e. a representative sample of other many craters presented in that region. This crater is heavily degraded and for this reason the impact modelling provides a better understanding of the subsequent geologic processes that led to crater post-impact modification, consequently defining which rheological structure of the Martian upper crust characterises Arabia Terra and if there are local conditions that favour the formation of central bulges. We have performed several simulations with different sets up in order to understand how different impact conditions affect the crater formation. We found two possible compositional scenarios that fit correctly the pristine crater profile of Firsoff: the first consists of a basaltic crust of fractured megaregolith whose thickness is at least 20 km, while the second introduces the presence of an anorthosite layer below the fractured basalt stratum. This latter compositional scenario is supported by recent discoveries of anorthosite patches on Martian highlands (Carter & Poulet, 2013). Since there are many craters similar to the Firsoff case, a further development of the work will be the study of other similar craters in Arabia Terra in order to strongly constrain the rheological structures we found through the modelling.

Boulders on comet 67P

We investigated the surface of comet Churyumov-Gerasimengo 67P focusing our attention on the possible energetic events that lead to the formation of boulders; i.e. blocks that are ubiquitous on the surface of the comet. Previous studies of boulders, which are found on asteroids and planets, are usually associated to impacts, but in 67P comet case the impact formation process is not sufficient and other formation processes must be invoked such as sublimation, fragmentation, outbursts and gravitational falls.

In this thesis, we used OSIRIS images to derive the size frequency distribution of boulders larger than 7 m performing global and localised studies. From these results we found that similar geomorphological setting display similar cumulative size-frequency distribution suggesting that energetic formation processes forming boulders, as well as thermal fracturing, pit formation or gravitational collapse, likely occurred in different areas of the comet (Pajola et al., 2015). Specifically, on the basis of the different cumulative size-frequency distribution, boulders were classified in the following way: (i) boulders associated to collapse/pit formation; (ii) boulders associated to gravitational events triggered by sublimation and/or thermal fracturing; (iii) boulders associated to the evolution of the origin material formed during both collapsing and gravitational events. In addition, we found that these energetic formation processes occur equally on different spatial scale of 67P, in fact the analysis of the Abydos site, the location where Philae is supposed to be, revealed a size frequency distribution of boulders up to 1 m that is strictly correlated to the geomorphological unit where Philae stands, in agreement with what previously found (Lucchetti et al., 2016).

When smaller spatial scaler are taken into account, we used CIVA images to investigate the formation of microscopic structures, i.e. grains that look like pebbles, in order to understand if the same energetic processes occur also on cm-scale. The size-frequency distribution of pebbles is not similar to the ones previously found, suggesting two different explanation: (i) pebbles could be formed primordially, or (ii) the fragmentation process maybe works in a different way on smaller spatial scale. In this context, our next step will be the development of a fragmentation model that could explain better the formation of pebbles and of boulders in general.

Europa

The presence of a subsurface ocean is a primary topic for Europa, in particular the interaction between subsurface/surface and outer environment of the satellite is still under investigation. In addition the recent discovery of a transient plume at the south pole by HST observations (Roth et al., 2014b) has raised further questions about this intriguing icy satellite. In view of the future ESA/JUICE mission and, in particular, of our involvement in the JANUS camera, we focused on two main topics in order to achieve additional information about the satellite and to be of help to the observation planning of JUICE/JANUS.

Firstly, we simulated the possible detection by the JANUS visible camera of a plume deposit, originating by cryovolcanic events, on the surface of Europa. We built up a simple model of a plume deposit and considered a specific sub-phase of the JUICE mission, i.e. the E9 Ap-d Europa flyby phase. We studied the possible detection of the plume deposit during this phase analysing its albedo distribution. Indeed, we expect the detection of a snow deposit that has a higher albedo than the surrounding Europa's surface. We calculated the SNR of possible observational scenarios during the Europa flyby and demonstrated that the simulated plume deposit will be identifiable as a bright spot by JANUS, even with lower SNR than those expected. Future studies about this issue will be performed, in particular we will investigate limb observations, once the JANUS observational scenario will be defined, and we will apply our model to other phases of the flyby in order to understand if we could observe the phenomenon not only in the phase considered in this work and, hence, monitoring its variability. The existence and the possible detection of these plumes is fundamental to better understand the interaction between the satellite subsurface and surface, in fact these transient phenomena are strictly related to the presence of a subsurface ocean and, hence, also to its depth.

Consequently, we investigated the exospheric background of Europa that is a mandatory prerequisite to study the transient plumes, in particular we provided a long list of reactions regarding the loss processes of Europa's tenuous atmosphere. The main results coming from this analysis involves the O_2 exosphere loss: we found that the charge-exchange process has a dominant role in the exosphere loss, contrarily to what

previously suggested by other works (Lucchetti et al., in press). The results coming from this work can be useful for the planning of observation strategies and, later, for the interpretation of the data coming from future missions to the Galilean satellites.

Future works

Eventually, a future work, which was briefly described in the previous chapter, will be the estimation of the icy shell thickness of Europa that is pivotal in adding hints about the nature of plumes. In fact, plumes have a liquid source beneath the icy crust of Europa and, within this context, the study of the surface lineaments and vents distribution can be used as a base to calculate the icy thickness of the satellites. We expect that the energetic cryovolcanism causes fractures and vents that reflect a fractal framework present in the Europa's surface allowing the rise of the liquid reservoir and therefore the occurrence of the plume. A fractal clustering analysis of surface features will be used to analyse their framework and, in particular, their spatial distribution will be utilised to verify their relationship to a fractured percolating network directly connected to the subsurface ocean. Such an approach has been already applied on Earth for volcanic vents and mud volcanoes, on vents present on Martian volcanoes to investigate the plumbing system deep structure, and on Enceladus, that shows many similarities with Europa. From this fractal method we will be able to estimate the icy shell thickness characterising Europa.

Appendix A

This Appendix A contains the refereed published articles where Alice Lucchetti has worked on and published during the 3 PhD years (2013-2015).

- **Loss rates of Europa's tenuous atmosphere**
  Planetary and Space Science, in press
  Authors: **Lucchetti A.**, Plainaki C., Cremonese G., Milillo A., Cassidy T., Jia X., Shematovich V.

- **Characterization of the Abydos region through OSIRIS high-resolution images in support of CIVA measurements**
  Astronomy & Astrophysics, Volume 585, id.L1, 5 pp. (2016)
  Authors: **Lucchetti A.**, Cremonese G., Jorda, L., Poulet, F., Bibring, J.-P., Pajola, M., La Forgia, F., Massironi M. and the OSIRIS team

- **Size-frequency distribution of boulders $\geq$10 m on comet 103P/Hartley 2**
  Astronomy & Astrophysics, Volume 585, id.A85, 8 pp. (2016)
  Authors: Pajola M., **Lucchetti A.**, Bertini I., Marzari F., A'Hearn M., La Forgia F.,; Lazzarin M., Naletto G., Barbieri C.

- **Size-frequency distribution of boulders $\geq$7 m on comet 67P/Churyumov-Gerasimenko**
  Astronomy & Astrophysics, Volume 583, id.A37, 17 pp. (2015)
  Authors: Pajola M., Vincent J.B., Guttler C., Lee J.C., Bertini I., Massironi M., Simioni E., Marzari F., Giacomini L., **Lucchetti A.**, Barbieri C., Cremonese G. and the OSIRIS team

- **A cone on Mercury: Analysis of a residual central peak encircled by an explosive volcanic vent**
  Planetary and Space Science, Volume 108, p. 108-116. (2015)
  Authors: Thomas R., **Lucchetti A.**, Cremonese G., Rothery D., Massironi M., Re C., Conway S.J., Anand M.

Bibliography

Abramov, O., & Kring, D. A. (2005). Impact-induced hydrothermal activity on early Mars. *Journal of Geophysical Research (Planets)*, *110*, 12. doi:10.1029/2005JE002453.

Ahrens, T. J., & O'Keefe, J. D. (1972). Shock melting and vaporization of lunar rocks and minerals. *Moon*, *4*, 214–249. doi:10.1007/BF00562927.

Ahrens, T. J., & O'Keefe, J. D. (1982). The interaction of the Cretaceous-Tertiary extinction bolide with the atmosphere, ocean, and solid earth. GSA special paper 190. *Geological Society of America*, (pp. 103 – 120).

Amsden, A., Ruppel, H., & Hirt, C. (1980). *SALE: A Simplified ALE Computer Program for Fluid Flow at All Speeds*. Los Alamos Scientific Laboratory, Report LA-8095. National Energy Software Center, Argonne National Laboratory. URL: http://books.google.it/books?id=LIDdHAAACAAJ.

Anderson, C. E. (1987). An overview of the theory of hydrocodes. *International Journal of Impact Engineering*, *5*, 33 – 59. URL: http://www.sciencedirect.com/science/article/pii/0734743X87900297. doi:http://dx.doi.org/10.1016/0734-743X(87)90029-7. Hypervelocity Impact Proceedings of the 1986 Symposium.

Anderson, J. D., Lau, E. L., Sjogren, W. L., Schubert, G., & Moore, W. B. (1997). Europa's differentiated internal structure: Inferences from two Galileo encounters. *Science*, *276*, 1236–1239. doi:10.1126/science.276.5316.1236.

Anderson, J. D., Schubert, G., Jacobson, R. A., Lau, E. L., Moore, W. B., & Sjogren, W. L. (1998). Europa's Differentiated Internal Structure: Inferences from Four Galileo Encounters. *Science*, *281*, 2019. doi:10.1126/science.281.5385.2019.

Andrews-Hanna, J. C., & Lewis, K. W. (2011). Early Mars hydrology: 2. Hydrological evolution in the Noachian and Hesperian epochs. *Journal of Geophysical Research*, *116*, E02007. URL: http://doi.wiley.com/10.1029/2010JE003709. doi:10.1029/2010JE003709.

Andrews-Hanna, J. C., Zuber, M. T., Arvidson, R. E., & Wiseman, S. M. (2010). Early Mars hydrology: Meridiani playa deposits and the sedimentary record of Arabia Terra. *Journal of Geophysical Research*, *115*, E06002. URL: http://doi.wiley.com/10.1029/2009JE003485. doi:10.1029/2009JE003485.

Arvidson, R. E., Poulet, F., Morris, R. V., Bibring, J. P., Bell, J. F., Squyres, S. W., Christensen, P. R., Bellucci, G., Gondet, B., Ehlmann, B. L., Farrand, W. H., Fergason, R. L., Golombeck, M., Griffes, J. L., Grotzinger, J., Guinness, E. a., Herkenhoff, K. E., Johnson, J. R., Klingelhöfer, G., Langevin, Y., Ming, D., Seelos, K., Sullivan, R. J., Ward, J. G., Wiseman, S. M., & Wolff, M. J. (2006). Nature and origin of the hematite-bearing plains of Terra Meridiani based on analyses of orbital and Mars Exploration rover data sets. *Journal of Geophysical Research E: Planets*, *111*, 1–19. doi:10.1029/2006JE002728.

Auger, A.-T., Groussin, O., Jorda, L., Bouley, S., Gaskell, R., Lamy, P. L., Capanna, C., Thomas, N., Pommerol, A., Sierks, H., Barbieri, C., Rodrigo, R., Koschny, D., Rickman, H., Keller, H. U., Agarwal, J., A'Hearn, M. F., Barucci, M. A., Bertaux, J.-L., Bertini, I., Cremonese, G., Da Deppo, V., Davidsson, B., Debei, S., De Cecco, M., El-Maarry, M. R., Fornasier, S., Fulle, M., Gutiérrez, P. J., Güttler, C., Hviid, S., Ip, W.-H., Knollenberg, J., Kramm, J.-R., Kührt, E., Küppers, M., La Forgia, F., Lara, L. M., Lazzarin, M., Lopez Moreno, J. J., Marchi, S., Marzari, F., Massironi, M., Michalik, H., Naletto, G., Oklay, N., Pajola, M., Sabau, L., Tubiana, C., Vincent, J.-B., & Wenzel, K.-P. (2015). Geomorphology of the Imhotep region on comet 67P/Churyumov-Gerasimenko from OSIRIS observations. A&A, *583*, A35. doi:10.1051/0004-6361/201525947.

Auster, H. U., Apathy, I., Berghofer, G., Remizov, A., Roll, R., Fornacon, K. H., Glassmeier, K. H., Haerendel, G., Hejja, I., Kührt, E., Magnes, W., Moehlmann, D., Motschmann, U., Richter, I., Rosenbauer, H., Russell, C. T., Rustenbach, J., Sauer, K., Schwingenschuh, K., Szemerey, I., & Waesch, R. (2007). ROMAP: Rosetta Magnetometer and Plasma Monitor. Space Sci. Rev., *128*, 221–240. doi:10.1007/s11214-006-9033-x.

Bagenal, F. (1994). Empirical model of the Io plasma torus: Voyager measurements. J. Geophys. Res., *99*, 11043–11062. doi:10.1029/93JA02908.

Bagenal, F., Dowling, T. E., & McKinnon, W. B. (2004). *Jupiter*.

Bagenal, F., Shemansky, D. E., McNutt, R. L., Jr., Schreier, R., & Eviatar, A. (1992). The abundance of O(2+) in the Jovian magnetosphere. Geophys. Res. Lett., *19*, 79–82. doi:10.1029/92GL00070.

Bagenal, F., Sidrow, E., Wilson, R. J., Cassidy, T. A., Dols, V., Crary, F. J., Steffl, A. J., Delamere, P. A., Kurth, W. S., & Paterson, W. R. (2015). Plasma conditions at Europa's orbit. Icarus, *261*, 1–13. doi:10.1016/j.icarus.2015.07.036.

Baker, D. M. H., & Head, J. W. (2013). New morphometric measurements of craters and basins on Mercury and the Moon from MESSENGER and LRO altimetry and image data: An observational framework for evaluating models of peak-ring basin formation. Planet. Space Sci., *86*, 91–116. doi:10.1016/j.pss.2013.07.003.

Banks, P. M., & Kockarts, G. (1973). *Aeronomy*.

Barabash, S., Lukyanov, A. V., C:son Brandt, P., & Lundin, R. (2001). Energetic neutral atom imaging of Mercury's magnetosphere 3. Simulated images and instrument requirements. Planet. Space Sci., *49*, 1685–1692. doi:10.1016/S0032-0633(01)00107-6.

Baragiola, R. A. (2003). Water ice on outer solar system surfaces: Basic properties and radiation effects. Planet. Space Sci., *51*, 953–961. doi:10.1016/j.pss.2003.05.007.

Belton, M. J. S., Klaasen, K. P., Clary, M. C., Anderson, J. L., Anger, C. D., Carr, M. H., Chapman, C. R., Davies, M. E., Greeley, R., & Anderson, D. (1992). The Galileo Solid-State Imaging experiment. Space Sci. Rev., *60*, 413–455. doi:10.1007/BF00216864.

Belton, M. J. S., Thomas, P., Carcich, B., Quick, A., Veverka, J., Jay Melosh, H., A'Hearn, M. F., Li, J.-Y., Brownlee, D., Schultz, P., Klaasen, K., & Sarid, G. (2013). The origin of pits on 9P/Tempel 1 and the geologic signature of outbursts in Stardust-NExT images. Icarus, *222*, 477–486. doi:10.1016/j.icarus.2012.03.007.

Benyoucef, D., & Yousfi, M. (2014). Ar + /ar, o 2 + /o 2 and n 2 + /n 2 elastic momentum collision cross sections: Calculation and validation using the semi-classical model. *Plasma Science and Technology*, *16*, 588. URL: http://stacks.iop.org/1009-0630/16/i=6/a=09.

Bibring, J.-P., Lamy, P., Langevin, Y., Soufflot, A., Berthé, M., Borg, J., Poulet, F., & Mottola, S. (2007). Civa. Space Sci. Rev., *128*, 397–412. doi:10.1007/s11214-006-9135-5.

Bibring, J.-P., Langevin, Y., Carter, J., Eng, P., Gondet, B., Jorda, L., Le Mouélic, S., Mottola, S., Pilorget, C., Poulet, F., & Vincendon, M. (2015). 67p/churyumov-gerasimenko surface properties as derived from civa panoramic images. *Science*, *349*. doi:10.1126/science.aab0671. arXiv:http://www.sciencemag.org/content/349/6247/aab0671.full.pdf.

Biele, J., Ulamec, S., Maibaum, M., Roll, R., Witte, L., Jurado, E., Muñoz, P., Arnold, W., Auster, H.-U., Casas, C., Faber, C., Fantinati, C., Finke, F., Fischer, H.-H., Geurts, K., Güttler, C., Heinisch, P., Herique, A., Hviid, S., Kargl, G., Knapmeyer, M., Knollenberg, J., Kofman, W., Kömle, N., Kührt, E., Lommatsch, V., Mottola, S., Pardo de Santayana, R., Remetean, E., Scholten, F., Seidensticker, K. J., Sierks, H., & Spohn, T. (2015). The landing(s) of philae and inferences about comet surface mechanical properties. *Science*, *349*. URL: http://www.sciencemag.org/content/349/6247/aaa9816.abstract. doi:10.1126/science.aaa9816. arXiv:http://www.sciencemag.org/content/349/6247/aaa9816.full.pdf.

Bierhaus, E. B., Zahnle, K., & Chapman, C. R. (2009). Europa's Crater Distributions and Surface Ages. In R. T. Pappalardo, W. B. McKinnon, & K. K. Khurana (Eds.), *Europa, Edited by Robert T. Pappalardo, William B. McKinnon, Krishan K. Khurana ; with the assistance of René Dotson with 85 collaborating authors. University of Arizona Press, Tucson, 2009. The University of Arizona space science series ISBN: 9780816528448, p.161* (p. 161).

Billings, S. E., & Kattenhorn, S. A. (2005). The great thickness debate: Ice shell thickness models for Europa and comparisons with estimates based on flexure at ridges. Icarus, *177*, 397–412. doi:10.1016/j.icarus.2005.03.013.

Bingham, E. C. (1916). Plastic flow. *Journal of the Franklin Institute*, *181*, 845 – 848. URL: http://www.sciencedirect.com/science/article/pii/S001600321690156X. doi:http://dx.doi.org/10.1016/S0016-0032(16)90156-X.

Bohren, C. F., & Huffman, D. R. (1998). *Absorption and Scattering of Light by Small Particles*.

Boslough, M., & Asay, J. (1993). Basic principles of shock compression. In J. Asay, & M. Shahinpoor (Eds.), *High-Pressure Shock Compression of Solids* High-Pressure Shock Compression of Condensed Matter (pp. 7–42). Springer New York. URL: http://dx.doi.org/10.1007/978-1-4612-0911-9_2. doi:10.1007/978-1-4612-0911-9_2.

Bray, V. (2009). *Impact Crater Formation on the Icy Galilean Satellites*. Ph.D. thesis Department of Earth Science and Engineering Imperial College London.

Britt, D. T., Yeomans, D., Housen, K., & Consolmagno, G. (2002). Asteroid Density, Porosity, and Structure. *Asteroids III*, (pp. 485–500).

Brož, P., & Hauber, E. (2012). A unique volcanic field in Tharsis, Mars: Pyroclastic cones as evidence for explosive eruptions. Icarus, *218*, 88–99. doi:10.1016/j.icarus.2011.11.030.

Brož, P., Čadek, O., Hauber, E., & Rossi, A. P. (2014). Shape of scoria cones on Mars: Insights from numerical modeling of ballistic pathways. *Earth and Planetary Science Letters*, *406*, 14–23. doi:10.1016/j.epsl.2014.09.002.

Brown, M. E. (2001). Potassium in Europa's Atmosphere. Icarus, *151*, 190–195. doi:10.1006/icar.2001.6612.

Brown, M. E., & Hill, R. E. (1996). Discovery of an extended sodium atmosphere around Europa. Nature, *380*, 229–231. doi:10.1038/380229a0.

Brown, W. L., Lanzerotti, L. J., & Johnson, R. E. (1982). Fast Ion Bombardment of Ices and its Astrophysical Implications. *Science*, *218*, 525–531. doi:10.1126/science.218.4572.525.

Brown, W. L., Lanzerotti, L. J., Poate, J. M., & Augustyniak, W. M. (1978). "sputtering" of ice by mev light ions. *Phys. Rev. Lett.*, *40*, 1027–1030. URL: http://link.aps.org/doi/10.1103/PhysRevLett.40.1027. doi:10.1103/PhysRevLett.40.1027.

Burger, M. H., Wagner, R., Jaumann, R., & Cassidy, T. A. (2010). Effects of the External Environment on Icy Satellites. Space Sci. Rev., *153*, 349–374. doi:10.1007/s11214-010-9645-z.

Carr, M. H., Belton, M. J. S., Chapman, C. R., Davies, M. E., Geissler, P., Greenberg, R., McEwen, A. S., Tufts, B. R., Greeley, R., Sullivan, R., Head, J. W., Pappalardo, R. T., Klaasen, K. P., Johnson, T. V., Kaufman, J., Senske, D., Moore, J., Neukum, G., Schubert, G., Burns, J. A., Thomas, P., & Veverka, J. (1998). Evidence for a subsurface ocean on Europa. Nature, *391*, 363. doi:10.1038/34857.

Carter, J., & Poulet, F. (2013). Ancient plutonic processes on Mars inferred from the detection of possible anorthositic terrains. *Nature Geoscience*, *6*, 1008–1012. doi:10.1038/ngeo1995.

Cassen, P., Reynolds, R. T., & Peale, S. J. (1979). Is there liquid water on Europa. Geophys. Res. Lett., *6*, 731–734. doi:10.1029/GL006i009p00731.

Cassidy, T., Coll, P., Raulin, F., Carlson, R. W., Johnson, R. E., Loeffler, M. J., Hand, K. P., & Baragiola, R. A. (2010). Radiolysis and Photolysis of Icy Satellite Surfaces: Experiments and Theory. Space Sci. Rev., *153*, 299–315. doi:10.1007/s11214-009-9625-3.

Cassidy, T. A., Johnson, R. E., McGrath, M. A., Wong, M. C., & Cooper, J. F. (2007). The spatial morphology of Europa's near-surface O $_2$ atmosphere. Icarus, *191*, 755–764. doi:10.1016/j.icarus.2007.04.033.

Cassidy, T. A., Paranicas, C. P., Shirley, J. H., Dalton, J. B., III, Teolis, B. D., Johnson, R. E., Kamp, L., & Hendrix, A. R. (2013). Magnetospheric ion sputtering and water ice grain size at Europa. Planet. Space Sci., *77*, 64–73. doi:10.1016/j.pss.2012.07.008.

Cintala, M. J., Wood, C. A., & Head, J. W. (1977). The effects of target characteristics on fresh crater morphology - Preliminary results for the moon and Mercury. In R. B. Merril (Ed.), *Lunar and Planetary Science Conference Proceedings* (pp. 3409–3425). volume 8 of *Lunar and Planetary Science Conference Proceedings*.

Collins, G., Ẃunneman, K., Elbeshausen, D., Ivanov, B., Melosh, H., & Davison, T. (2010). *iSALE: A multi-material, multi-rheology shock physics code for simulating impact phenomena.*.

Collins, G. S. (2001). Hydrocode Simulations of Complex Crater Collapse. In *Lunar and Planetary Science Conference* (p. 1752). volume 32 of *Lunar and Planetary Science Conference*.

Collins, G. S., Davison, T. M., & Ciesla, F. J. (2011). The Effects of Planetesimal Collisions. *Meteoritics and Planetary Science Supplement*, *74*, 5024.

Collins, G. S., & Melosh, H. J. (2003). Acoustic fluidization and the extraordinary mobility of sturzstroms. *Journal of Geophysical Research (Solid Earth)*, *108*, 2473. doi:10.1029/2003JB002465.

Collins, G. S., Melosh, H. J., & Ivanov, B. A. (2004). Modeling damage and deformation in impact simulations. *Meteoritics and Planetary Science*, *39*, 217–231. doi:10.1111/j.1945-5100.2004.tb00337.x.

Collins, G. S., Melosh, H. J., Morgan, J. V., & Warner, M. R. (2002). Hydrocode Simulations of Chicxulub Crater Collapse and Peak-Ring Formation. *Icarus*, *157*, 24–33. doi:10.1006/icar.2002.6822.

Collins, G. S., & Wünnemann, K. (2005). How big was the Chesapeake Bay impact? Insight from numerical modeling. *Geology*, *33*, 925. doi:10.1130/G21854.1.

Connor, C. B., Stamatakos, J. A., Ferrill, D. A., Hill, B. E., Ofoegbu, G. I., Conway, F. M., Sagar, B., & Trapp, J. (2000). Geologic factors controlling patterns of small-volume basaltic volcanism: Application to a volcanic hazards assessment at Yucca Mountain, Nevada. J. Geophys. Res., *105*, 417–432. doi:10.1029/1999JB900353.

Coplan, M. A., & Ogilvie, K. W. (1970). Charge Exchange for H^+ and H^+_2 in H_2O, CO_2, and NH_3. J. Chem. Phys., *52*, 4154–4160. doi:10.1063/1.1673624.

Cosby, P. C. (1993). Electron-impact dissociation of oxygen. J. Chem. Phys., *98*, 9560–9569. doi:10.1063/1.464387.

Coustenis, A., Tokano, T., Burger, M. H., Cassidy, T. A., Lopes, R. M., Lorenz, R. D., Retherford, K. D., & Schubert, G. (2010). Atmospheric/Exospheric Characteristics of Icy Satellites. Space Sci. Rev., *153*, 155–184. doi:10.1007/s11214-009-9615-5.

Crandall, S., & Mark, W. (1973). Random vibrations in mechaical systems. *Academic press, New York*, .

Cumming, W. A. (1952). The Dielectric Properties of Ice and Snow at 3.2 Centimeters. *Journal of Applied Physics*, *23*, 768–773. doi:10.1063/1.1702299.

Daglis, I. A., & Livi, S. (1995). Potential merits for substorm research from imaging of charge-exchange neutral atoms. *Annales Geophysicae*, *13*, 505–516. doi:10.1007/s00585-995-0505-1.

Dalton, J. B., Cruikshank, D. P., Stephan, K., McCord, T. B., Coustenis, A., Carlson, R. W., & Coradini, A. (2010). Chemical Composition of Icy Satellite Surfaces. Space Sci. Rev., *153*, 113–154. doi:10.1007/s11214-010-9665-8.

Davidsson, B., Sierks, H., & Güttler, C. e. a. (submitted). The primordial nucleus of comet 67p/churyumov–gerasimenko. A&A, .

Delamere, P. A., Bagenal, F., & Steffl, A. (2005). Radial variations in the Io plasma torus during the Cassini era. *Journal of Geophysical Research (Space Physics)*, *110*, 12223. doi:10.1029/2005JA011251.

Dence, M. R. (1973). Dimensional analysis of impact structures. *Meteoritics*, *8*, 343–344.

Denevi, B. W., Ernst, C. M., Meyer, H. M., Robinson, M. S., Murchie, S. L., Whitten, J. L., Head, J. W., Watters, T. R., Solomon, S. C., Ostrach, L. R., Chapman, C. R., Byrne, P. K., Klimczak, C., & Peplowski, P. N. (2013). The distribution and origin of smooth plains on Mercury. *Journal of Geophysical Research (Planets)*, *118*, 891–907. doi:10.1002/jgre.20075.

Denevi, B. W., Robinson, M. S., Solomon, S. C., Murchie, S. L., Blewett, D. T., Domingue, D. L., McCoy, T. J., Ernst, C. M., Head, J. W., Watters, T. R., & Chabot, N. L. (2009). The Evolution of Mercurys Crust: A Global Perspective from MESSENGER. *Science*, *324*, 613–. doi:10.1126/science.1172226.

Dent, B. (1973). Glacial exhumation of impact craters on the Canadian Shield. *Geological Society of America Bulletin*, *84*, 1667–1672.

Doggett, T., Greeley, R., Figueredo, P., & Tanaka, K. (2009). Geologic Stratigraphy and Evolution of Europa's Surface. In R. T. Pappalardo, W. B. McKinnon, & K. K. Khurana (Eds.), *Europa, Edited by Robert T. Pappalardo, William B. McKinnon, Krishan K. Khurana ; with the assistance of René Dotson with 85 collaborating authors. University of Arizona Press, Tucson, 2009. The University of Arizona space science series ISBN: 9780816528448, p.137* (p. 137).

Dols, V. J., Bagenal, F., Cassidy, T. A., Crary, F. J., & Delamere, P. A. (2016). Europa's atmospheric neutral escape: Importance of symmetrical O_2 charge exchange. Icarus, *264*, 387–397. doi:10.1016/j.icarus.2015.09.026.

Duvall, G. E., & Fowles, G. R. (1963). Shock Waves. In R. S. Bradley (Ed.), *High Pressure Physics and Chemistry, Volume 2* (p. 209). volume 2.

El-Maarry, M. R., Thomas, N., Gracia-Berná, A., Marschall, R., Auger, A.-T., Groussin, O., Mottola, S., Pajola, M., Massironi, M., Marchi, S., Höfner, S., Preusker, F., Scholten, F., Jorda, L., Kührt, E., Keller, H. U., Sierks, H., A'Hearn, M. F., Barbieri, C., Barucci, M. A., Bertaux, J.-L., Bertini, I., Cremonese, G., Da Deppo, V., Davidsson, B., Debei, S., De Cecco, M., Deller, J., Güttler, C., Fornasier, S., Fulle, M., Gutierrez, P. J., Hofmann, M., Hviid, S. F., Ip, W.-H., Knollenberg, J., Koschny, D., Kovacs, G., Kramm, J.-R., Küppers, M., Lamy, P. L., Lara, L. M., Lazzarin, M., Lopez Moreno, J. J., Marzari, F., Michalik, H., Naletto, G., Oklay, N., Pommerol, A., Rickman, H., Rodrigo, R., Tubiana, C., & Vincent, J.-B. (2015). Fractures on comet 67P/Churyumov-Gerasimenko observed by Rosetta/OSIRIS. Geophys. Res. Lett., *42*, 5170–5178. doi:10.1002/2015GL064500.

El-Maarry, M. R., Thomas, N., Giacomini, L., Massironi, M., Pajola, M., Marschall, R., Gracia-Berná, A., Sierks, H., Barbieri, C., Lamy, P. L., Rodrigo, R., Rickman, H., Koschny, D., Keller, H. U., Agarwal, J., A'Hearn, M. F., Auger, A.-T., Barucci, M. A., Bertaux, J.-L., Bertini, I., Besse, S., Bodewits, D., Cremonese,, G., Da Deppo, V., Davidsson, B., De Cecco, M., Debei, S., Güttler, C., Fornasier, S., Fulle, M., Groussin, O., Gutierrez, P. J., Hviid, S. F., Ip, W.-H., Jorda, L., Knollenberg, J., Kovacs, G., Kramm, J.-R., Kührt, E., Küppers, M., La Forgia, F., Lara, L. M., Lazzarin, M., Lopez Moreno, J. J., Marchi, S., Marzari, F., Michalik, H., Naletto, G., Oklay, N., Pommerol, A., Preusker, F., Scholten, F., Tubiana, C., & Vincent, J.-B. (2015). Regional surface morphology of comet 67p/churyumov-gerasimenko from rosetta/osiris images. *AA*, *583*, A26. URL: http://dx.doi.org/10.1051/0004-6361/201525723. doi:10.1051/0004-6361/201525723.

Elbeshausen, D., Wünnemann, K., & Collins, G. S. (2007). Three-Dimensional Numerical Modeling of Oblique Impact Processes: Scaling of Cratering Efficiency. In *Lunar and Planetary Science Conference* (p. 1952). volume 38 of *Lunar and Planetary Science Conference*.

Eliason, E. M. (1997). Production of Digital Image Models Using the ISIS System. In *Lunar and Planetary Science Conference* (p. 331). volume 28 of *Lunar and Planetary Science Conference*.

ESA (2014). *JUICE definition study report (Red Book)*. Technical Report ESA.

ESA Rosetta blog (2015). The quest to find philae. URL: http://blogs.esa.int/rosetta/2015/06/11/the-quest-to-find-philae-2/.

Evans, A. J., Andrews-Hanna, J. C., & Zuber, M. T. (2010). Geophysical limitations on the erosion history within arabia terra. *Journal of Geophysical Research: Planets*, *115*, n/a–n/a. URL: http://dx.doi.org/10.1029/2009JE003469. doi:10.1029/2009JE003469.

Fagents, S. A. (2003). Considerations for effusive cryovolcanism on Europa: The post-Galileo perspective. *Journal of Geophysical Research (Planets)*, *108*, 5139. doi:10.1029/2003JE002128.

Fagents, S. A., Greeley, R., Sullivan, R. J., Pappalardo, R. T., Prockter, L. M., & The Galileo SSI Team (2000). Cryomagmatic Mechanisms for the Formation of Rhadamanthys Linea, Triple Band Margins, and Other Low-Albedo Features on Europa. Icarus, *144*, 54–88. doi:10.1006/icar.1999.6254.

Fehsenfeld, F. C., Schmeltekopf, A. L., & Ferguson, E. E. (1967). Thermal-Energy IonNeutral Reaction Rates. VII. Some Hydrogen-Atom Abstraction Reactions. J. Chem. Phys., *46*, 2802–2808. doi:10.1063/1.1841117.

Figueredo, P. H., Chuang, F. C., Rathbun, J., Kirk, R. L., & Greeley, R. (2002). Geology and origin of Europa's "Mitten" feature (Murias Chaos). *Journal of Geophysical Research (Planets)*, *107*, 5026. doi:10.1029/2001JE001591.

Fite, W. L., & Brackmann, R. T. (1963). Electron collisions with atomic and molecular oxygen. In P. Hubert, & E. Crémieu-Alcan (Eds.), *Phenomena in Ionized Gases, VI International Conference, Volume I* (p. 21).

Forsberg-Taylor, N. K., Howard, A. D., & Craddock, R. A. (2004). Crater degradation in the Martian highlands: Morphometric analysis of the Sinus Sabaeus region and simulation modeling suggest fluvial processes. *Journal of Geophysical Research (Planets)*, *109*, 5002. doi:10.1029/2004JE002242.

Franchi, F., Rossi, A. P., Pondrelli, M., & Cavalazzi, B. (2014). Geometry, stratigraphy and evidences for fluid expulsion within Crommelin crater deposits, Arabia Terra, Mars. Planet. Space Sci., *92*, 34–48. doi:10.1016/j.pss.2013.12.013.

Fraser, G. W., Carpenter, J. D., Rothery, D. A., Pearson, J. F., Martindale, A., Huovelin, J., Treis, J., Anand, M., Anttila, M., Ashcroft, M., Benkoff, J., Bland, P., Bowyer, A., Bradley, A., Bridges, J., Brown, C., Bulloch, C., Bunce, E. J., Christensen, U., Evans, M., Fairbend, R., Feasey, M., Giannini, F., Hermann, S., Hesse, M., Hilchenbach, M., Jorden, T., Joy, K., Kaipiainen, M., Kitchingman, I., Lechner, P., Lutz, G., Malkki, A., Muinonen, K., Näränen, J., Portin, P., Prydderch, M., Juan, J. S., Sclater, E., Schyns, E., Stevenson, T. J., Strüder, L., Syrjasuo, M., Talboys, D., Thomas, P., Whitford, C., & Whitehead, S. (2010). The mercury imaging X-ray spectrometer (MIXS) on bepicolombo. Planet. Space Sci., *58*, 79–95. doi:10.1016/j.pss.2009.05.004.

French, B. M. (1998). *Traces of Catastrophe: A Handbook of Shock-Metamorphic Effects in Terrestrial Meteorite Impact Structures*.

Galli, A., Pommerol, A., Vorburger, A., Wurz, P., Tulej, M., Scheer, J., Thomas, N., Wieser, M., & Barabash, S. (2015). The first laboratory measurements of sulfur ions sputtering water ice. In *EGU2015-3752*.

Garvin, J. B., Sakimoto, S. E. H., & Frawley, J. J. (2003). Craters on Mars: Global Geometric Properties from Gridded MOLA Topography. In A. L. Albee, & H. H. Kieffer (Eds.), *Sixth International Conference on Mars* (p. 3277).

Geissler, P., Petit, J.-M., Durda, D. D., Greenberg, R., Bottke, W., Nolan, M., & Moore, J. (1996). Erosion and Ejecta Reaccretion on 243 Ida and Its Moon. Icarus, *120*, 140–157. doi:10.1006/icar.1996.0042.

Geissler, P. E., Greenberg, R., Hoppa, G., McEwen, A., Tufts, R., Phillips, C., Clark, B., Ockert-Bell, M., Helfenstein, P., Burns, J., Veverka, J., Sullivan, R., Greeley, R., Pappalardo, R. T., Head, J. W., Belton, M. J. S., & Denk, T. (1998). Evolution of Lineaments on Europa: Clues from Galileo Multispectral Imaging Observations. Icarus, *135*, 107–126. doi:10.1006/icar.1998.5980.

Giacomini, L., Massironi, M., Marchi, S., Fasset, C., & G., C. ().

Gillis-Davis, J. J., Blewett, D. T., Gaskell, R. W., Denevi, B. W., Robinson, M. S., Strom, R. G., Solomon, S. C., & Sprague, A. L. (2009). Pit-floor craters on Mercury: Evidence of near-surface igneous activity. *Earth and Planetary Science Letters*, *285*, 243–250. doi:10.1016/j.epsl.2009.05.023.

Goudge, T. A., Head, J. W., Kerber, L., Blewett, D. T., Denevi, B. W., Domingue, D. L., Gillis-Davis, J. J., Gwinner, K., Helbert, J., Holsclaw, G. M., Izenberg, N. R., Klima, R. L., McClintock, W. E., Murchie, S. L., Neumann, G. A., Smith, D. E., Strom, R. G., Xiao, Z., Zuber, M. T., & Solomon, S. C. (2014). Global inventory and characterization of pyroclastic deposits on Mercury: New insights into pyroclastic activity from MESSENGER orbital data. *Journal of Geophysical Research (Planets)*, *119*, 635–658. doi:10.1002/2013JE004480.

Grasset, O., Dougherty, M., Coustenis, A., Bunce, E., Erd, C., Titov, D., Blanc, M., Coates, A., Drossart, P., Fletcher, L., Hussmann, H., Jaumann, R., Krupp, N., Lebreton, J.-P., Prieto-Ballesteros, O., Tortora, P., Tosi, F., & Van, H. T. (2013). Jupiter icy moons explorer (juice): An esa mission to orbit ganymede and to characterise the jupiter system. *PLANETARY AND SPACE SCIENCE*, *78*, 1–21. URL: http://dx.doi.org/10.1016/j.pss.2012.12.002. doi:10.1016/j.pss.2012.12.002.

Greenberg, R., Geissler, P., Hoppa, G., Tufts, B. R., Durda, D. D., Pappalardo, R., Head, J. W., Greeley, R., Sullivan, R., & Carr, M. H. (1998). Tectonic Processes on Europa: Tidal Stresses, Mechanical Response, and Visible Features. Icarus, *135*, 64–78. doi:10.1006/icar.1998.5986.

Greenberg, R., Geissler, P., Tufts, B. R., & Hoppa, G. V. (2000). Habitability of Europa's crust: The role of tidal-tectonic processes. J. Geophys. Res., *105*, 17551–17562. doi:10.1029/1999JE001147.

Grieve, R. A. F. (1987). Terrestrial Impact Structures. *Annual Review of Earth and Planetary Sciences*, *15*, 245–270. doi:10.1146/annurev.ea.15.050187.001333.

Gurnett, D. A., Kurth, W. S., Roux, A., Bolton, S. J., Thomsen, E. A., & Groene, J. B. (1998). Galileo plasma wave observations near Europa. Geophys. Res. Lett., *25*, 237–240. doi:10.1029/97GL03706.

Hall, D. T., Feldman, P. D., McGrath, M. A., & Strobel, D. F. (1998). The Far-Ultraviolet Oxygen Airglow of Europa and Ganymede. ApJ, *499*, 475–481. doi:10.1086/305604.

Hall, D. T., Strobel, D. F., Feldman, P. D., McGrath, M. A., & Weaver, H. A. (1995). Detection of an oxygen atmosphere on Jupiter's moon Europa. Nature, *373*, 677–679. doi:10.1038/373677a0.

Hansen, C. J., Esposito, L., Stewart, A. I. F., Colwell, J., Hendrix, A., Pryor, W., Shemansky, D., & West, R. (2006). Enceladus' Water Vapor Plume. *Science*, *311*, 1422–1425. doi:10.1126/science.1121254.

Hansen, C. J., Shemansky, D. E., & Hendrix, A. R. (2005). Cassini UVIS observations of Europa's oxygen atmosphere and torus. Icarus, *176*, 305–315. doi:10.1016/j.icarus.2005.02.007.

Harb, T., Kedzierski, W., & McConkey, J. W. (2001). Production of ground state OH following electron impact on H_2O. J. Chem. Phys., *115*, 5507–5512. doi:10.1063/1.1397327.

Hartmann, W. K., & Kuiper, G. P. (1962). Concentric Structures Surrounding Lunar Basins. *Communications of the Lunar and Planetary Laboratory*, *1*, 51–66.

Hartmann, W. K., & Wood, C. A. (1971). Moon: Origin and evolution of multi-ring basins. *Moon*, *3*, 3–78. doi:10.1007/BF00620390.

Hasan, A. T., & Gray, T. J. (2007). Electron-Capture Cross Sections of Ground-State O2+ Recoil Ions in Slow Collisions with H2 and O2. *International Journal of Molecular Sciences*, (pp. 1158–1164).

Hasenaka, T., & Carmichael, I. S. E. (1985). The cinder cones of MichoacánGuanajuato, central Mexico: their age, volume and distribution, and magma discharge rate. *Journal of Volcanology and Geothermal Research*, *25*, 105–124. doi:10.1016/0377-0273(85)90007-1.

Hasted, J. B., & Hussain, M. (1964). Electron capture by multiply charged ions. *Proceedings of the Physical Society*, *83*, 911–924. doi:10.1088/0370-1328/83/6/303.

Head, J. W., Sherman, N. D., Pappalardo, R. T., Thomas, C., Greeley, R., & Galileo SSI Team (1998). Cryovolcanism on Europa: Evidence for the Emplacement of Flows and Related Deposits in the E4 Region (5N, 305W) and Interpreted Eruption Conditions. In *Lunar and Planetary Science Conference* (p. 1491). volume 29 of *Lunar and Planetary Science Conference*.

Heinisch, P., Auster, H.-U., & Richter, I. e. a. (2015). Attitude-Reconstruction of ROSETTA's lander PHILAE using two-point observations by ROMAP and RPC-MAG. In *EGU Abstracts* (p. 12166).

Hoppa, G. V., Greenberg, R., Tufts, B. R., & Geissler, P. E. (1999). Plume Detection on Europa: Locations of Favorable Tidal Stress. In *Lunar and Planetary Science Conference* (p. 1603). volume 30 of *Lunar and Planetary Science Conference*.

Housen, K. R., & Holsapple, K. A. (1990). On the fragmentation of asteroids and planetary satellites. Icarus, *84*, 226–253. doi:10.1016/0019-1035(90)90168-9.

Hubert, B., Gérard, J.-C., Gustin, J., Bisikalo, D. V., Shematovich, V. I., & Gladstone, G. R. (2012). Cassini-UVIS observation of dayglow FUV emissions of carbon in the thermosphere of Venus. Icarus, *220*, 635–646. doi:10.1016/j.icarus.2012.06.002.

Huebner, W. F., Keady, J. J., & Lyon, S. P. (1992). Solar photo rates for planetary atmospheres and atmospheric pollutants. Ap&SS, *195*, 1–289. doi:10.1007/BF00644558.

Hurford, T. A., Helfenstein, P., Hoppa, G. V., Greenberg, R., & Bills, B. G. (2007). Eruptions arising from tidally controlled periodic openings of rifts on Enceladus. Nature, *447*, 292–294. doi:10.1038/nature05821.

Hussmann, H., Spohn, T., & Wieczerkowski, K. (2002). Thermal Equilibrium States of Europa's Ice Shell: Implications for Internal Ocean Thickness and Surface Heat Flow. Icarus, *156*, 143–151. doi:10.1006/icar.2001.6776.

Ingersoll, A. P., & Ewald, S. P. (2011). Total particulate mass in Enceladus plumes and mass of Saturns E ring inferred from Cassini ISS images. Icarus, *216*, 492–506. doi:10.1016/j.icarus.2011.09.018.

Ionov, D. E., Bisikalo, D. V., Shematovich, V. I., & Huber, B. (2014). Ionization fraction in the thermosphere of the exoplanet HD 209458b. *Solar System Research*, *48*, 105–112. doi:10.1134/S0038094614020026.

Irvine, A. D., & Latimer, C. J. (1997). Charge-exchange processes involving ground- and excited-state O2+ and H2+ ions with H2 and O2. *International Journal of Mass Spectrometry and Ion Processes*, *164*, 115–120. doi:10.1016/S0168-1176(97)00025-6.

Itikawa, Y. (2009). Cross sections for electron collisions with oxygen molecules. *Journal of Physical and Chemical Reference Data*, *38*.

Itikawa, Y., & Mason, N. (2005). Cross Sections for Electron Collisions with Water Molecules. *Journal of Physical and Chemical Reference Data*, *34*, 1–22. doi:10.1063/1.1799251.

Ivanov, B., Deniem, D., & Neukum, G. (1997). Implementation of dynamic strength models into 2d hydrocodes: Applications for atmospheric breakup and impact cratering. *International Journal of Impact Engineering*, *20*, 411 – 430. URL: http://www.sciencedirect.com/science/article/pii/S0734743X97875112. doi:http://dx.doi.org/10.1016/S0734-743X(97)87511-2. Hypervelocity Impact Proceedings of the 1996 Symposium.

Ivanov, B. A. (2005). Numerical Modeling of the Largest Terrestrial Meteorite Craters. *Solar System Research*, *39*, 381–409. doi:10.1007/s11208-005-0051-0.

Ivanov, B. A., & Artemieva, N. (2002). Numerical modeling of the formation of large impact craters. Impact and Beyond, GSA special paper. Catastrophic Events and Mass Extinctions.

Ivanov, B. A., & Deutsch, A. (1999). Sudbury impact event: Cratering mechanics and thermal history. In B. O. Dressler, & V. L. Sharpton (Eds.), *Large Meteorite Impacts and Planetary Evolution II* (p. 389).

Ivanov, B. A., & Kostuchenko, V. N. (1998). Impact Crater Formation: Dry Friction and Fluidization Influence on the Scaling and Modification. In *Lunar and Planetary Science Conference* (p. 1654). volume 29 of *Lunar and Planetary Science Conference*.

Jaumann, R., Neukum, G., Behnke, T., Duxbury, T. C., Eichentopf, K., Flohrer, J., Gasselt, S. v., Giese, B., Gwinner, K., Hauber, E., Hoffmann, H., Hoffmeister, A., Köhler, U., Matz, K.-D., McCord, T. B., Mertens, V., Oberst, J., Pischel, R., Reiss, D., Ress, E., Roatsch, T., Saiger, P., Scholten, F., Schwarz, G., Stephan, K., Wählisch, M., & the HRSC Co-Investigator Team (2007). The high-resolution stereo camera (HRSC) experiment on Mars Express: Instrument aspects and experiment conduct from interplanetary cruise through the nominal mission. *Planetary and Space Science*, *55*, 928–952. doi:10.1016/j.pss.2006.12.003.

Jenness, J. (). Tools for graphics and shapes: Extension for arcgis. *Jeness Enterprises*, .

Johnson, P. V., & Kanik, I. (2001). Inelastic differential electron scattering cross sections of molecular oxygen (O_2) in the 20-100 eV impact energy range. *Journal of Physics B Atomic Molecular Physics*, *34*, 3041–3051. doi:10.1088/0953-4075/34/15/310.

Johnson, R. E. (1990). *Energetic Charged-Particle Interactions with Atmospheres and Surfaces*.

Johnson, R. E. (1994). Plasma-Induced Sputtering of an Atmosphere. Space Sci. Rev., *69*, 215–253. doi:10.1007/BF02101697.

Johnson, R. E., Carlson, R. W., Cooper, J. F., Paranicas, C., Moore, M. H., & Wong, M. C. (2004). Radiation effects on the surfaces of the Galilean satellites. In F. Bagenal, T. E. Dowling, & W. B. McKinnon (Eds.), *Jupiter. The Planet, Satellites and Magnetosphere* (pp. 485–512).

Johnson, R. E., Luhmann, J. G., Tokar, R. L., Bouhram, M., Berthelier, J. J., Sittler, E. C., Cooper, J. F., Hill, T. W., Smith, H. T., Michael, M., Liu, M., Crary, F. J., & Young, D. T. (2006). Production, ionization and redistribution of O $_2$ in Saturn's ring atmosphere. Icarus, *180*, 393–402. doi:10.1016/j.icarus.2005.08.021.

Jorda, L., Gaskell, R., & Capanna, C. e. a. (submitted). The global shape, density and rotation of comet 67p/churyumov-gerasimenko from pre perihelion rosetta/osiris observations. *Icarus*, .

Jorda, L., Lamy, P. L., Gaskell, R. W., Kaasalainen, M., Groussin, O., Besse, S., & Faury, G. (2012). Asteroid (2867) Steins: Shape, topography and global physical properties from OSIRIS observations. Icarus, *221*, 1089–1100. doi:10.1016/j.icarus.2012.07.035.

Kabin, K., Combi, M. R., Gombosi, T. I., Nagy, A. F., DeZeeuw, D. L., & Powell, K. G. (1999). On Europa's magnetospheric interaction: A MHD simulation of the E4 flyby. J. Geophys. Res., *104*, 19983–19992. doi:10.1029/1999JA900263.

Karkoschka, E. (1994). Spectrophotometry of the jovian planets and Titan at 300- to 1000-nm wavelength: The methane spectrum. Icarus, *111*, 174–192. doi:10.1006/icar.1994.1139.

Keller, H. U., Barbieri, C., Koschny, D., Lamy, P., Rickman, H., Rodrigo, R., Sierks, H., A'Hearn, M. F., Angrilli, F., Barucci, M. A., Bertaux, J.-L., Cremonese, G., Da Deppo, V., Davidsson, B., De Cecco, M., Debei, S., Fornasier, S., Fulle, M., Groussin, O., Gutierrez, P. J., Hviid, S. F., Ip, W.-H., Jorda, L., Knollenberg, J., Kramm, J. R., Kührt, E., Küppers, M., Lara, L.-M., Lazzarin, M., Moreno, J. L., Marzari, F., Michalik, H., Naletto, G., Sabau, L., Thomas, N., Wenzel, K.-P., Bertini, I., Besse, S., Ferri, F., Kaasalainen, M., Lowry, S., Marchi, S., Mottola, S., Sabolo, W., Schröder, S. E., Spjuth, S., & Vernazza, P. (2010). E-Type Asteroid (2867) Steins as Imaged by OSIRIS on Board Rosetta. *Science*, *327*, 190–. doi:10.1126/science.1179559.

Keller, H. U., Barbieri, C., Lamy, P., Rickman, H., Rodrigo, R., Wenzel, K.-P., Sierks, H., A'Hearn, M. F., Angrilli, F., Angulo, M., Bailey, M. E., Barthol, P., Barucci, M. A., Bertaux, J.-L., Bianchini, G., Boit, J.-L., Brown, V., Burns, J. A., Büttner, I., Castro, J. M., Cremonese, G., Curdt, W., da Deppo, V., Debei, S., de Cecco, M., Dohlen, K., Fornasier, S., Fulle, M., Germerott, D., Gliem, F., Guizzo, G. P., Hviid, S. F., Ip, W.-H., Jorda, L., Koschny, D., Kramm, J. R., Kührt, E., Küppers, M., Lara, L. M., Llebaria, A., López, A., López-Jimenez, A., López-Moreno, J., Meller, R., Michalik, H., Michelena, M. D., Müller, R., Naletto, G., Origné, A., Parzianello, G., Pertile, M., Quintana, C., Ragazzoni, R., Ramous, P., Reiche, K.-U., Reina, M., Rodríguez, J., Rousset, G., Sabau, L., Sanz, A., Sivan, J.-P., Stöckner, K., Tabero, J., Telljohann, U., Thomas, N., Timon, V., Tomasch, G., Wittrock, T., & Zaccariotto, M. (2007). OSIRIS The Scientific Camera System Onboard Rosetta. Space Sci. Rev., *128*, 433–506. doi:10.1007/s11214-006-9128-4.

Kempf, S., Beckmann, U., Moragas-Klostermeyer, G., Postberg, F., Srama, R., Economou, T., Schmidt, J., Spahn, F., & Grün, E. (2008). The E ring in the vicinity of Enceladus. I. Spatial distribution and properties of the ring particles. Icarus, *193*, 420–437. doi:10.1016/j.icarus.2007.06.027.

Kenkmann, T., & Scherler, D. (2002). New Structural Constraints on the Upheaval Dome Impact Crater. In *Lunar and Planetary Science Conference* (p. 1037). volume 33 of *Lunar and Planetary Science Conference*.

Kerber, L., Head, J. W., Blewett, D. T., Solomon, S. C., Wilson, L., Murchie, S. L., Robinson, M. S., Denevi, B. W., & Domingue, D. L. (2011). The global distribution of pyroclastic deposits on mercury: The view from {MESSENGER} flybys 1–3. *Planetary and Space Science*, *59*, 1895 – 1909. URL: http://www.sciencedirect.com/science/article/pii/S0032063311001073. doi:http://dx.doi.org/10.1016/j.pss.2011.03.020. Mercury after the {MESSENGER} flybys.

Kerber, L., Head, J. W., Solomon, S. C., Murchie, S. L., Blewett, D. T., & Wilson, L. (2009). Explosive volcanic eruptions on mercury: Eruption conditions, magma volatile content, and implications for interior volatile abundances. *Earth and Planetary Science Letters*, *285*, 263 – 271. URL: http://www.sciencedirect.com/science/article/pii/S0012821X09002611. doi:http://dx.doi.org/10.1016/j.epsl.2009.04.037. MESSENGER's First Flyby of Mercury.

Khurana, K. K., Kivelson, M. G., Stevenson, D. J., Schubert, G., Russell, C. T., Walker, R. J., & Polanskey, C. (1998). Induced magnetic fields as evidence for subsurface oceans in Europa and Callisto. Nature, *395*, 777–780. doi:10.1038/27394.

Kieffer, S. W., Lu, X., McFarquhar, G., & Wohletz, K. H. (2009). A redetermination of the ice/vapor ratio of Enceladus plumes: Implications for sublimation and the lack of a liquid water reservoir. Icarus, *203*, 238–241. doi:10.1016/j.icarus.2009.05.011.

Kim, J. K., & Huntress, W. T., Jr. (1975). Ion cyclotron resonance studies on the reaction of H_2^+ and D_2^+ ions with various simple molecules and hydrocarbons. J. Chem. Phys., *62*, 2820–2825. doi:10.1063/1.430817.

Kimmel, G. A., Orlando, T. M., Vézina, C., & Sanche, L. (1994). Low-energy electron-stimulated production of molecular hydrogen from amorphous water ice. J. Chem. Phys., *101*, 3282–3286. doi:10.1063/1.468430.

Kivelson, M. G., Bagenal, F., Kurth, W. S., Neubauer, F. M., Paranicas, C., & Saur, J. (2004). Magnetospheric interactions with satellites. In F. Bagenal, T. E. Dowling, & W. B. McKinnon (Eds.), *Jupiter. The Planet, Satellites and Magnetosphere* (pp. 513–536).

Kivelson, M. G., Khurana, K. K., Russell, C. T., Volwerk, M., Walker, R. J., & Zimmer, C. (2000). Galileo Magnetometer Measurements: A Stronger Case for a Subsurface Ocean at Europa. *Science*, *289*, 1340–1343. doi:10.1126/science.289.5483.1340.

Kliore, A. J., Hinson, D. P., Flasar, F. M., Nagy, A. F., & Cravens, T. E. (1997). The ionosphere of Europa from Galileo radio occultations. *Science*, *277*, 355–358. doi:10.1126/science.277.5324.355.

Kocharyan, G. G., Kostuchenko, V. N., & Ivanov, B. A. (1996). Mechanics of Rock Massive Disruption: Implementation to Planetary Cratering Processes. In *Lunar and Planetary Science Conference* (p. 677). volume 27 of *Lunar and Planetary Science Conference*.

Kofman, W., Herique, A., Goutail, J.-P., Hagfors, T., Williams, I. P., Nielsen, E., Barriot, J.-P., Barbin, Y., Elachi, C., Edenhofer, P., Levasseur-Regourd, A.-C., Plettemeier, D., Picardi, G., Seu, R., & Svedhem, V. (2007). The Comet Nucleus Sounding Experiment by Radiowave Transmission (CONSERT): A Short Description of the Instrument and of the Commissioning Stages. Space Sci. Rev., *128*, 413–432. doi:10.1007/s11214-006-9034-9.

Kresak, L. (1981). The lifetimes and disappearance of periodic comets. *Bulletin of the Astronomical Institutes of Czechoslovakia*, *32*, 321–339.

Krupp, N., Khurana, K. K., Iess, L., Lainey, V., Cassidy, T. A., Burger, M., Sotin, C., & Neubauer, F. (2010). Environments in the Outer Solar System. Space Sci. Rev., *153*, 11–59. doi:10.1007/s11214-010-9653-z.

Küppers, M., Moissl, R., Vincent, J.-B., Besse, S., Hviid, S. F., Carry, B., Grieger, B., Sierks, H., Keller, H. U., Marchi, S., & OSIRIS Team (2012). Boulders on Lutetia. Planet. Space Sci., *66*, 71–78. doi:10.1016/j.pss.2011.11.004.

Kurth, W. S., Gurnett, D. A., Persoon, A. M., Roux, A., Bolton, S. J., & Alexander, C. J. (2001). The plasma wave environment of Europa. Planet. Space Sci., *49*, 345–363. doi:10.1016/S0032-0633(00)00156-2.

La Forgia, F., Giacomini, L., Lazzarin, M., Massironi, M., Oklay, N., Scholten, F., Pajola, M., Bertini, I., Cremonese, G., Barbieri, C., Naletto, G., Simioni, E., Preusker, F., Thomas, N., Sierks, H., Lamy, P., Rodrigo, R., Koschny, D., Rickman, H., Keller, H. U., Agarwal, J., Auger, A.-T., A'Hearn, M. F., Barucci, M. A., Bertaux, J.-L., Besse, S., Bodewits, D., Da Deppo, V., Davidsson, B., Debei, S., De Cecco, M., El-Maarry, M. R., Ferri, F., Fornasier, S., Fulle, M., Groussin, O., Gutiérrez, P. J., Güttler, C., Hall, I., Hviid, S. F., Ip, W.-H., Jorda, L., Knollenberg, J., Kramm, J. R., Kührt, E., Küppers, M., Lara, L.-M., Lopez Moreno, J. J., Magrin, S., Marzari, F., Michalik, H., Mottola, S., Pommerol, A., Tubiana, C., & Vincent, J.-B. (2015). Geomorphology and spectrophotometry of philae's landing site on comet 67p/churyumov-gerasimenko. *AA*, *583*, A41. URL: http://dx.doi.org/10.1051/0004-6361/201525983. doi:10.1051/0004-6361/201525983.

Lamy, P., Faury, G., Jorda, L., Romeuf, D., Gaskell, R., Jurado, E., Garmier, R., Llebaria, A., Auger, A.-T., Capanna, C., & the OSIRIS Team (2015). Identification and Characterization of the landing site of Philae from OSIRIS-NAC Images. In *EPSC Abstracts*.

Larsson, M., Geppert, W. D., & Nyman, G. (2012). Ion chemistry in space. *Reports on Progress in Physics*, *75*, 066901. URL: http://stacks.iop.org/0034-4885/75/i=6/a=066901.

Le Feuvre, M., & Wieczorek, M. A. (2011). Nonuniform cratering of the Moon and a revised crater chronology of the inner Solar System. Icarus, *214*, 1–20. doi:10.1016/j.icarus.2011.03.010.

Leblanc, F., Johnson, R. E., & Brown, M. E. (2002). Europa's Sodium Atmosphere: An Ocean Source? Icarus, *159*, 132–144. doi:10.1006/icar.2002.6934.

Leblanc, F., Potter, A. E., Killen, R. M., & Johnson, R. E. (2005). Origins of Europa Na cloud and torus. Icarus, *178*, 367–385. doi:10.1016/j.icarus.2005.03.027.

Lee, P., Veverka, J., Thomas, P. C., Helfenstein, P., Belton, M. J. S., Chapman, C. R., Greeley, R., Pappalardo, R. T., Sullivan, R., & Head, J. W., III (1996). Ejecta Blocks on 243 Ida and on Other Asteroids. Icarus, *120*, 87–105. doi:10.1006/icar.1996.0039.

Lee, S. W., Thomas, P., & Ververka, J. (1986). Phobos, Deimos, and the moon - Size and distribution of crater ejecta blocks. Icarus, *68*, 77–86. doi:10.1016/0019-1035(86)90075-8.

Levison, H. F., & Duncan, M. J. (1994). The long-term dynamical behavior of short-period comets. Icarus, *108*, 18–36. doi:10.1006/icar.1994.1039.

Lipatov, A. S., Cooper, J. F., Paterson, W. R., Sittler, E. C., Hartle, R. E., & Simpson, D. G. (2010). Jovian plasma torus interaction with Europa: 3D hybrid kinetic simulation. First results. Planet. Space Sci., *58*, 1681–1691. doi:10.1016/j.pss.2010.06.015.

Lipatov, A. S., Cooper, J. F., Paterson, W. R., Sittler, E. C., Jr., Hartle, R. E., & Simpson, D. G. (2013). Jovian plasma torus interaction with Europa. Plasma wake structure and effect

of inductive magnetic field: 3D hybrid kinetic simulation. Planet. Space Sci., *77*, 12–24. doi:10.1016/j.pss.2013.01.009. arXiv:1212.3626.

Lishawa, C. R., Dressler, R. A., Gardner, J. A., Salter, R. H., & Murad, E. (1990). Cross sections and product kinetic energy analysis of H_2O^+-H_2O collisions at suprathermal energies. J. Chem. Phys., *93*, 3196–3206. doi:10.1063/1.458852.

Lucchetti, A., Cremonese, G., Jorda, L., Poulet, F., Bibring, J.-P., Pajola, M., La Forgia, F., Massironi, M., El-Maarry, M. R., Oklay, N., Sierks, H., Barbieri, C., Lamy, P., Rodrigo, R., Koschny, D., Rickman, H., Keller, H. U., Agarwal, J., A'Hearn, M. F., Barucci, M. A., Bertaux, J.-L., Bertini, I., Da Deppo, V., Davidsson, B., Debei, S., De Cecco, M., Fornasier, S., Fulle, M., Groussin, O., Gutierrez, P. J., Güttler, C., Hviid, S. F., Ip, W.-H., Knollenberg, J., Kramm, J.-R., Kührt, E., Küppers, M., Lara, L. M., Lazzarin, M., Lopez Moreno, J. J., Marzari, F., Mottola, S., Naletto, G., Preusker, F., Scholten, F., Thomas, N., Tubiana, C., & Vincent, J.-B. (2016). Characterization of the Abydos region through OSIRIS high-resolution images in support of CIVA measurements. A&A, *585*, L1. doi:10.1051/0004-6361/201527330.

Lucchetti, A., Plainaki, C., Cremonese, G., Milillo, A., Cassidy, T., Xianzhe, J., & Shematovich, V. (in press). Loss rates of Europa's tenuous atmosphere. Planet. Space Sci., .

Lundborg, N. (1968). Strength of rock–like materials. *Journal of Rock Mechanics and Mining Sciences*, .

Marchi, S., Massironi, M., Cremonese, G., Martellato, E., Giacomini, L., & Prockter, L. (2011). The effects of the target material properties and layering on the crater chronology: The case of raditladi and rachmaninoff basins on mercury. *Planetary and Space Science*, *59*, 1968 – 1980. URL: http://www.sciencedirect.com/science/article/pii/S0032063311001917. doi:http://dx.doi.org/10.1016/j.pss.2011.06.007. Mercury after the {MESSENGER} flybys.

Marchi, S., Morbidelli, A., & Cremonese, G. (2005). Flux of meteoroid impacts on Mercury. A&A, *431*, 1123–1127. doi:10.1051/0004-6361:20041800.

Massironi, M., Simioni, E., Marzari, F., Cremonese, G., Giacomini, L., Pajola, M., Jorda, L., Naletto, G., Lowry, S., El-Maarry, M. R., Preusker, F., Scholten, F., Sierks, H., Barbieri, C., Lamy, P., Rodrigo, R., Koschny, D., Rickman, H., Keller, H. U., A'Hearn, M. F., Agarwal, J., Auger, A.-T., Barucci, M. A., Bertaux, J.-L., Bertini, I., Besse, S., Bodewits, D., Capanna, C., da Deppo, V., Davidsson, B., Debei, S., de Cecco, M., Ferri, F., Fornasier, S., Fulle, M., Gaskell, R., Groussin, O., Gutiérrez, P. J., Güttler, C., Hviid, S. F., Ip, W.-H., Knollenberg, J., Kovacs, G., Kramm, R., Kührt, E., Küppers, M., La Forgia, F., Lara, L. M., Lazzarin, M., Lin, Z.-Y., Lopez Moreno, J. J., Magrin, S., Michalik, H., Mottola, S., Oklay, N., Pommerol, A., Thomas, N., Tubiana, C., & Vincent, J.-B. (2015). Two independent and primitive envelopes of the bilobate nucleus of comet 67P. Nature, *526*, 402–405. doi:10.1038/nature15511.

Mazrouei, S., Daly, M. G., & Barnouin, e. a. (2014). Block distributions on Itokawa. Icarus, *229*, 181–189. doi:10.1016/j.icarus.2013.11.010.

Mazzarini, F. (2004). Volcanic vent self-similar clustering and crustal thickness in the northern Main Ethiopian Rift. Geophys. Res. Lett., *31*, L04604. doi:10.1029/2003GL018574.

Mazzarini, F., & Isola, I. (2010). Monogenetic vent self-similar clustering in extending continental crust: Examples from the East African Rift System. *Geosphere*, *6*, 567–582. doi:10.1130/GES00569.1.

McEwen, A. S., Eliason, E. M., Bergstrom, J. W., Bridges, N. T., Hansen, C. J., Delamere, W. A., Grant, J. A., Gulick, V. C., Herkenhoff, K. E., Keszthelyi, L., Kirk, R. L., Mellon, M. T., Squyres, S. W., Thomas, N., & Weitz, C. M. (2007). Mars Reconnaissance Orbiter's High Resolution Imaging Science Experiment (HiRISE). *Journal of Geophysical Research (Planets)*, *112*, 5. doi:10.1029/2005JE002605.

McGetchin, T. R., Settle, M., & Chouet, B. A. (1974). Cinder cone growth modeled after Northeast crater, Mount Etna, Sicily. J. Geophys. Res., *79*, 3257–3272. doi:10.1029/JB079i023p03257.

McGrath, M. A., & Johnson, R. E. (1989). Charge exchange cross sections for the io plasma torus. *Journal of Geophysical Research: Space Physics*, *94*, 2677–2683. URL: http://dx.doi.org/10.1029/JA094iA03p02677. doi:10.1029/JA094iA03p02677.

McGrath, M. A., Lellouch, E., Strobel, D. F., Feldman, P. D., & Johnson, R. E. (2004). Satellite atmospheres. In F. Bagenal, T. E. Dowling, & W. B. McKinnon (Eds.), *Jupiter. The Planet, Satellites and Magnetosphere* (pp. 457–483).

McKinnon, W. B., & Alexopoulos, J. S. (1994). Some Implications of Large Impact Craters and Basins on Venus for Terrestrial Ringed Craters and Planetary Evolution. *LPI Contributions*, *825*, 81.

McSween, H. Y., Grove, T. L., & Wyatt, M. B. (2003). Constraints on the composition and petrogenesis of the Martian crust. *Journal of Geophysical Research (Planets)*, *108*, 5135. doi:10.1029/2003JE002175.

McSween, H. Y., Taylor, G. J., & Wyatt, M. B. (2009). Elemental Composition of the Martian Crust. *Science*, *324*, 736–. doi:10.1126/science.1165871.

Melosh, H. (2000). A new and improved equation of state for impact computations. In *Lunar and Planetary Science Conference*.

Melosh, H. (2011). *Planetary Surface Processes*. Cambridge Planetary Science. Cambridge University Press. URL: http://books.google.it/books?id=3bQD1DJgliIC.

Melosh, H. J. (1977). The Role of Slumping in Crater Modification. In *Lunar and Planetary Science Conference* (p. 658). volume 8 of *Lunar and Planetary Science Conference*.

Melosh, H. J. (1979). Acoustic fluidization - A new geologic process. J. Geophys. Res., *84*, 7513–7520.

Melosh, H. J. (1982). A schematic model of crater modification by gravity. J. Geophys. Res., *87*, 371–380. doi:10.1029/JB087iB01p00371.

Melosh, H. J. (1989). *Impact cratering: A geologic process*.

Melosh, H. J., & Gaffney, E. S. (1983). Acoustic fluidization and the scale dependence of impact crater morphology. J. Geophys. Res., *88*, 830. doi:10.1029/JB088iS02p0A830.

Melosh, H. J., & Ivanov, B. A. (1999). Impact Crater Collapse. *Annual Review of Earth and Planetary Sciences*, *27*, 385–415. doi:10.1146/annurev.earth.27.1.385.

Melosh, H. J., & McKinnon, W. B. (1978). The mechanics of ringed basin formation. Geophys. Res. Lett., *5*, 985–988. doi:10.1029/GL005i011p00985.

Melosh, H. J., & Ryan, E. V. (1997). NOTE: Asteroids: Shattered but Not Dispersed. Icarus, *129*, 562–564. doi:10.1006/icar.1997.5797.

Melosh, H. J., Ryan, E. V., & Asphaug, E. (1992). Dynamic fragmentation in impacts - Hydrocode simulation of laboratory impacts. J. Geophys. Res., *97*, 14735. doi:10.1029/92JE01632.

Metrich, N., & Wallace, P. (). Volatile abundances in basaltic magmas and their degassing paths tracked by melt inclusions. In *Rev. Mineral. Geochem.*.

Michalski, J. R., Cuadros, J., Niles, P. B., Parnell, J., Deanne Rogers, A., & Wright, S. P. (2013). Groundwater activity on Mars and implications for a deep biosphere. *Nature Geoscience*, *6*, 133–138. doi:10.1038/ngeo1706.

Michikami, T., Nakamura, A. M., Hirata, N., Gaskell, R. W., Nakamura, R., Honda, T., Honda, C., Hiraoka, K., Saito, J., Demura, H., Ishiguro, M., & Miyamoto, H. (2008). Size-frequency statistics of boulders on global surface of asteroid 25143 Itokawa. *Earth, Planets, and Space*, *60*, 13–20. doi:10.1186/BF03352757.

Milillo, A., Orsini, S., & Daglis, I. A. (2001). Empirical model of proton fluxes in the equatorial inner magnetosphere: Development. J. Geophys. Res., *106*, 25713–25730. doi:10.1029/2000JA900158.

Milillo, A., Plainaki, C., De Angelis, E., Mangano, V., Massetti, S., Mura, A., Orsini, S., & Rispoli, R. (in press). Analytical model of Europa's O2 exosphere. Planet. Space Sci., .

Milillo, A., Wurz, P., Orsini, S., Delcourt, D., Kallio, E., Killen, R. M., Lammer, H., Massetti, S., Mura, A., Barabash, S., Cremonese, G., Daglis, I. A., Angelis, E., Lellis, A. M., Livi, S., Mangano, V., & Torkar, K. (2005). Surface-Exosphere-Magnetosphere System Of Mercury. Space Sci. Rev., *117*, 397–443. doi:10.1007/s11214-005-3593-z.

Morabito, L. A., Synnott, S. P., Kupferman, P. N., & Collins, S. A. (1979). Discovery of currently active extraterrestrial volcanism. *Science*, *204*, 972. doi:10.1126/science.204.4396.972.

Moratto, Z. M., Broxton, M. J., Beyer, R. A., Lundy, M., & Husmann, K. (2010). Ames Stereo Pipeline, NASA's Open Source Automated Stereogrammetry Software. In *Lunar and Planetary Science Conference* (p. 2364). volume 41 of *Lunar and Planetary Science Conference*.

Morbidelli, A., & Rickman, H. (2015). Comets as collisional fragments of a primordial planetesimal disk. A&A, *583*, A43. doi:10.1051/0004-6361/201526116. arXiv:1504.04512.

Mottola, S., Arnold, G., Grothues, H.-G., Jaumann, R., Michaelis, H., Neukum, G., & Bibring, J.-P. (2007). The Rolis Experiment on the Rosetta Lander. Space Sci. Rev., *128*, 241–255. doi:10.1007/s11214-006-9004-2.

Mottola, S., Arnold, G., Grothues, H.-G., Jaumann, R., Michaelis, H., Neukum, G., Bibring, J.-P., Schröder, S. E., Hamm, M., Otto, K. A., Pelivan, I., Proffe, G., Scholten, F., Tirsch, D., Kreslavsky, M., Remetean, E., Souvannavong, F., & Dolives, B. (2015). The structure of the regolith on 67p/churyumov-gerasimenko from rolis descent imaging. *Science*, *349*. URL: http://www.sciencemag.org/content/349/6247/aab0232.abstract. doi:10.1126/science.aab0232. arXiv:http://www.sciencemag.org/content/349/6247/aab0232.full.pdf.

Nimmo, F., Porco, C., & Mitchell, C. (2014). Tidally Modulated Eruptions on Enceladus: Cassini ISS Observations and Models. AJ, *148*, 46. doi:10.1088/0004-6256/148/3/46.

Nittler, L. R., Starr, R. D., Weider, S. Z., McCoy, T. J., Boynton, W. V., Ebel, D. S., Ernst, C. M., Evans, L. G., Goldsten, J. O., Hamara, D. K., Lawrence, D. J., McNutt, R. L., Schlemm, C. E., Solomon, S. C., & Sprague, A. L. (2011). The Major-Element Composition of Mercurys Surface from MESSENGER X-ray Spectrometry. *Science*, *333*, 1847–. doi:10.1126/science.1211567.

Nyquist, H. (1928). Certain topics in telegraph transmission theory, .

Okeefe, J. D., & Ahrens, T. J. (1977). Impact-induced energy partitioning, melting, and vaporization on terrestrial planets. In R. B. Merril (Ed.), *Lunar and Planetary Science Conference Proceedings* (pp. 3357–3374). volume 8 of *Lunar and Planetary Science Conference Proceedings*.

O'Keefe, J. D., & Ahrens, T. J. (1993). Planetary cratering mechanics. J. Geophys. Res., *98*, 17011–17028. doi:10.1029/93JE01330.

O'Keefe, J. D., & Ahrens, T. J. (1999). Complex craters: Relationship of stratigraphy and rings to impact conditions. J. Geophys. Res., *104*, 27091–27104. doi:10.1029/1998JE000596.

Orlando, T. M., & Kimmel, G. A. (1997). The role of excitons and substrate temperature in low-energy (5-50 eV) electron-stimulated dissociation of amorphous D $_2$O ice. *Surface Science*, *390*, 79–85. doi:10.1016/S0039-6028(97)00511-6.

Orsini, S., & Milillo, A. (1999). Magnetospheric plasma loss processes in the Earth's ring current and energetic neutral atoms. *Nuovo Cimento C Geophysics Space Physics C*, *22*, 633–648.

Orsini, S., Milillo, A., Angelis, E. D., Lellis, A. M. D., Zanza, V., & Livi, S. (2001). Remote sensing of Mercury's magnetospheric plasma environment via energetic neutral atoms imaging. Planet. Space Sci., *49*, 1659–1668. doi:10.1016/S0032-0633(01)00104-0.

Pajola, M., Vincent, J.-B., Güttler, C., Lee, Jui-Chi, Bertini, Ivano, Massironi, Matteo, Simioni, Emanuele, Marzari, Francesco, Giacomini, Lorenza, Lucchetti, Alice, Barbieri, Cesare, Cremonese, Gabriele, Naletto, Giampiero, Pommerol, Antoine, El-Maarry, Mohamed R., Besse, Sébastien, Küppers, Michael, La Forgia, Fiorangela, Lazzarin, Monica, Thomas, Nicholas, Auger, Anne-Thérèse, Sierks, Holger, Lamy, Philippe, Rodrigo, Rafael, Koschny, Detlef, Rickman, Hans, Keller, Horst U., Agarwal, Jessica, A'Hearn, Michael F., Barucci, Maria A., Bertaux, Jean-Loup, Deppo, Vania Da, Davidsson, Björn, De Cecco, Mariolino, Debei, Stefano, Ferri, Francesca, Fornasier, Sonia, Fulle, Marco, Groussin, Olivier, Gutierrez, Pedro J., Hviid, Stubbe F., Ip, Wing-Huen, Jorda, Laurent, Knollenberg, Jörg, Kramm, J.-Rainer, Kürt, Ekkehard, Lara, Luisa M., Lin, Zhong-Yi, Moreno, Jose J. Lopez, Magrin, Sara, Marchi, Simone, Michalik, Harald, Moissl, Richard, Mottola, Stefano, Oklay, Nilda, Preusker, Frank, Scholten, Frank, & Tubiana, Cecilia (2015). Size-frequency distribution of boulders 7 m on comet 67p/churyumov-gerasimenko. *AA*, *583*, A37. URL: `http://dx.doi.org/10.1051/0004-6361/201525975`. doi:`10.1051/0004-6361/201525975`.

Pappalardo, R. T., Belton, M. J. S., Breneman, H. H., Carr, M. H., Chapman, C. R., Collins, G. C., Denk, T., Fagents, S., Geissler, P. E., Giese, B., Greeley, R., Greenberg, R., Head, J. W., Helfenstein, P., Hoppa, G., Kadel, S. D., Klaasen, K. P., Klemaszewski, J. E., Magee, K., McEwen, A. S., Moore, J. M., Moore, W. B., Neukum, G., Phillips, C. B., Prockter, L. M., Schubert, G., Senske, D. A., Sullivan, R. J., Tufts, B. R., Turtle, E. P., Wagner, R., & Williams, K. K. (1999). Does Europa have a subsurface ocean? Evaluation of the geological evidence. J. Geophys. Res., *104*, 24015–24056. doi:`10.1029/1998JE000628`.

Pappalardo, R. T., McKinnon, W. B., & Khurana, K. K. (2009). *Europa*.

Pappalardo, R. T., Vance, S., Bagenal, F., Bills, B. G., Blaney, D. L., Blankenship, D. D., Brinckerhoff, W. B., Connerney, J. E. P., Hand, K. P., Hoehler, T. M., Leisner, J. S., Kurth, W. S., McGrath, M. A., Mellon, M. T., Moore, J. M., Patterson, G. W., Prockter, L. M., Senske, D. A., Schmidt, B. E., Shock, E. L., Smith, D. E., & Soderlund, K. M. (2013). Science Potential from a Europa Lander. *Astrobiology*, *13*, 740–773. doi:`10.1089/ast.2013.1003`.

Parfitt, E. A., Wilson, L., & Head, J. W. (1993). Basaltic magma reservoirs: factors controlling their rupture characteristics and evolution. *Journal of Volcanology and Geothermal Research*, *55*, 1–14. doi:`10.1016/0377-0273(93)90086-7`.

de Pater, I., & Lissauer, J. (2001). *Planetary Sciences*. Cambridge University Press. URL: `https://books.google.co.uk/books?id=RaJdy3_VINQC`.

Pierazzo, E., Artemieva, N., Asphaug, E., Baldwin, E. C., Cazamias, J., Coker, R., Collins, G. S., Crawford, D. A., Davison, T., Elbeshausen, D., Holsapple, K. A., Housen, K. R., Korycansky, D. G., & Wünnemann, K. (2008). Validation of numerical codes for impact and explosion cratering: Impacts on strengthless and metal targets. *Meteoritics and Planetary Science*, *43*, 1917–1938. doi:`10.1111/j.1945-5100.2008.tb00653.x`.

Pierazzo, E., Artemieva, N., & Ivanov, B. (2005). Starting conditions for hydrothermal systems underneath Martian craters: Hydrocode modeling. In F. H. T. Kenkmann, & A. Deutsch (Eds.), *Special Paper 384: Large Meteorite Impacts III* (pp. 443–457).

Pierazzo, E., & Collins, G. S. (2004). *A brief introduction to hydrocode modelling* volume Cratering in Marine Environments and on Ice. Springer, Verlag, Berlin, pp 323 - 340.

Pike, R. J. (1977). Apparent depth/apparent diameter relation for lunar craters. In R. B. Merril (Ed.), *Lunar and Planetary Science Conference Proceedings* (pp. 3427–3436). volume 8 of *Lunar and Planetary Science Conference Proceedings*.

Pike, R. J. (1985). Some morphologic systematics of complex impact structures. *Meteoritics*, *20*, 49–68.

Pike, R. J. (1988). Geomorphology of impact craters on Mercury. In F. Vilas, C. R. Chapman, & M. S. Matthews (Eds.), *Mercury, University of Arizona Press* (pp. 165–273).

Plainaki, C., Milillo, A., Massetti, S., Mura, A., Jia, X., Orsini, S., Mangano, V., De Angelis, E., & Rispoli, R. (2015). The H_2O and O_2 exospheres of Ganymede: The result of a complex interaction between the jovian magnetospheric ions and the icy moon. Icarus, *245*, 306–319. doi:10.1016/j.icarus.2014.09.018.

Plainaki, C., Milillo, A., Mura, A., Orsini, S., & Cassidy, T. (2010). Neutral particle release from Europa's surface. Icarus, *210*, 385–395. doi:10.1016/j.icarus.2010.06.041. arXiv:0911.4602.

Plainaki, C., Milillo, A., Mura, A., Orsini, S., Massetti, S., & Cassidy, T. (2012). The role of sputtering and radiolysis in the generation of Europa exosphere. Icarus, *218*, 956–966. doi:10.1016/j.icarus.2012.01.023.

Plainaki, C., Milillo, A., Mura, A., Saur, J., Orsini, S., & Massetti, S. (2013). Exospheric O_2 densities at Europa during different orbital phases. Planet. Space Sci., *88*, 42–52. doi:10.1016/j.pss.2013.08.011.

Poirier, J.-P. (1994). Light elements in the Earth's outer core: A critical review. *Physics of the Earth and Planetary Interiors*, *85*, 319–337. doi:10.1016/0031-9201(94)90120-1.

Pommerol, A., Thomas, N., El-Maarry, M. R., Pajola, M., Groussin, O., Auger, A.-T., Oklay, N., Fornasier, S., Feller, C., Davidsson, B., Gracia-Berná, A., Jost, B., Marschall, R., Poch, O., Barucci, M. A., Bertaux, J.-L., La Forgia, F., Keller, H. U., Kührt, E., Lowry, S. C., Mottola, S., Naletto, G., Sierks, H., Barbieri, C., Lamy, P. L., Rodrigo, R., Koschny, D., Rickman, H., Agarwal, J., A'Hearn, M. F., Bertini, I., Boudreault, S., Cremonese, G., Da Deppo, V., De Cecco, M., Debei, S., Güttler, C., Fulle, M., Gutierrez, P. J., Hviid, S. F., Ip, W.-H., Jorda, L., Knollenberg, J., Kovacs, G., Kramm, J.-R., Küppers, E., Lara, L., Lazzarin, M., Lopez Moreno, J. L., Marzari, F., Michalik, H., Preusker, F., Scholten, F., Tubiana, C., & Vincent, J.-B. (2015). OSIRIS observations of meter-sized exposures of H_2O ice at the surface of 67P/Churyumov-Gerasimenko and interpretation using laboratory experiments. A&A, *583*, A25. doi:10.1051/0004-6361/201525977.

Pondrelli, M., Rossi, A. P., Le Deit, L., Fueten, F., Van Gasselt, S., Glamoclija, M., Cavalazzi, B., Hauber, E., Franchi, F., & Pozzobon, R. (2015). Equatorial Layered Deposits in Arabia Terra, Mars: Facies and process variability. *Geological Society of American Bulletin*, . doi:10.1130/B31225.1.

Pondrelli, M., Rossi, A. P., Ori, G. G., van Gasselt, S., Praeg, D., & Ceramicola, S. (2011). Mud volcanoes in the geologic record of Mars: The case of Firsoff crater. *Earth and Planetary Science Letters*, *304*, 511–519. doi:10.1016/j.epsl.2011.02.027.

Porco, C., DiNino, D., & Nimmo, F. (2014). How the Geysers, Tidal Stresses, and Thermal Emission across the South Polar Terrain of Enceladus are Related. AJ, *148*, 45. doi:10.1088/0004-6256/148/3/45.

Porco, C. C., Helfenstein, P., Thomas, P. C., Ingersoll, A. P., Wisdom, J., West, R., Neukum, G., Denk, T., Wagner, R., Roatsch, T., Kieffer, S., Turtle, E., McEwen, A., Johnson, T. V., Rathbun, J., Veverka, J., Wilson, D., Perry, J., Spitale, J., Brahic, A., Burns, J. A., Del Genio, A. D., Dones, L., Murray, C. D., & Squyres, S. (2006). Cassini Observes the Active South Pole of Enceladus. *Science*, *311*, 1393–1401. doi:10.1126/science.1123013.

Postberg, F., Kempf, S., Hillier, J. K., Srama, R., Green, S. F., McBride, N., & Grün, E. (2008). The E-ring in the vicinity of Enceladus. II. Probing the moon's interiorThe composition of E-ring particles. Icarus, *193*, 438–454. doi:10.1016/j.icarus.2007.09.001.

Potter, R., Collins, G., Kiefer, W., McGovern, P., & Kring, D. (2012). Constraining the size of the south pole-aitken basin impact. *Icarus*, *220*, 730 – 743. URL: http://www.sciencedirect.com/science/article/pii/S001910351200214X. doi:http://dx.doi.org/10.1016/j.icarus.2012.05.032.

Potter, R. W. K. (2012). *Numerical modelling of basin-scale impact crater formation*. Ph.D. thesis Department of Earth Science and Engineering, Imperial College London.

Poulet, F., Bibring, J.-P., Carter, J., Eng, P., Gondet, B., Jorda, L., Langevin, Y., Le Mouélic, S., & Pilorget, C. (2015). Surface of the comet 67P from PHILAE/CIVA images as clues to the formation of the comet nucleus. In *EGU Abstracts* (p. 9517).

Pozzobon, R., Mazzarini, F., Massironi, M., & Marinangeli, L. (2014). Self-similar clustering distribution of structural features on ascraeus mons (mars): implications for magma chamber depth. *Geological Society, London, Special Publications*, *401*. doi:10.1144/SP401.12.

Pozzobon, R., Mazzarini, F., Massironi, M., Rossi, A. P., Marinangeli, L., & Pondrelli (submitted). Fluids mobilization at Firsoff Crater, Mars: depth of pressurized water table from mounds clustering, .

Pozzobon, R., Mazzarini, F., Rossi, A. P., Lucchetti, A., Pondrelli, M., Marinangeli, L., Martellato, E., Cremonese, G., & Massironi, M. (2013). Genesis and fluid source in Arabia crater mounds: mapping, fractal analysis, and impact simulations. In *AGU Fall Meeting* (p. 1797270).

Preusker, F., Scholten, F., Matz, K.-D., Roatsch, T., Willner, K., Hviid, S. F., Knollenberg, J., Jorda, L., Gutiérrez, P. J., Kührt, E., Mottola, S., A'Hearn, M. F., Thomas, N., Sierks, H., Barbieri, C., Lamy, P., Rodrigo, R., Koschny, D., Rickman, H., Keller, H. U., Agarwal, J., Barucci, M. A., Bertaux, J.-L., Bertini, I., Cremonese, G., Da Deppo, V., Davidsson, B., Debei, S., De Cecco, M., Fornasier, S., Fulle, M., Groussin, O., Güttler, C., Ip, W.-H., Kramm,

J. R., Küppers, M., Lara, L. M., Lazzarin, M., Lopez Moreno, J. J., Marzari, F., Michalik, H., Naletto, G., Oklay, N., Tubiana, C., & Vincent, J.-B. (2015). Shape model, reference system definition, and cartographic mapping standards for comet 67p/churyumov-gerasimenko – stereo-photogrammetric analysis of rosetta/osiris image data. *AA*, *583*, A33. URL: http://dx.doi.org/10.1051/0004-6361/201526349. doi:10.1051/0004-6361/201526349.

Prockter, L., & Schenk, P. (2005). Origin and evolution of Castalia Macula, an anomalous young depression on Europa. Icarus, *177*, 305–326. doi:10.1016/j.icarus.2005.08.003.

Quick, L. C., Barnouin, O. S., Prockter, L. M., & Patterson, G. W. (2013). Constraints on the detection of cryovolcanic plumes on Europa. Planet. Space Sci., *86*, 1–9. doi:10.1016/j.pss.2013.06.028.

Re, C., Roncella, R., Forlani, G., Cremonese, G., & Naletto, G. (2012). Evaluation of Area-Based Image Matching Applied to DTM Generation with Hirise Images. *ISPRS Annals of Photogrammetry, Remote Sensing and Spatial Information Sciences*, (pp. 209–214). doi:10.5194/isprsannals-I-4-209-2012.

Riley, J., Hoppa, G. V., Greenberg, R., Tufts, B. R., & Geissler, P. (2000). Distribution of chaotic terrain on Europa. J. Geophys. Res., *105*, 22599–22616. doi:10.1029/1999JE001164.

Robbins, S. J., & Hynek, B. M. (2012). A new global database of mars impact craters â1 km: 2. global crater properties and regional variations of the simple-to-complex transition diameter. *Journal of Geophysical Research: Planets*, *117*, n/a–n/a. URL: http://dx.doi.org/10.1029/2011JE003967. doi:10.1029/2011JE003967.

Rodríguez, J. A. P., Sasaki, S., Dohm, J. M., Tanaka, K. L., Strom, B., Kargel, J., Kuzmin, R., Miyamoto, H., Spray, J. G., Fairén, A. G., Komatsu, G., Kurita, K., & Baker, V. (2005). Control of impact crater fracture systems on subsurface hydrology, ground subsidence, and collapse, Mars. *Journal of Geophysical Research (Planets)*, *110*, 6003. doi:10.1029/2004JE002365.

Rodriguez, J. A. P., Tanaka, K. L., Yamamoto, A., Berman, D. C., Zimbelman, J. R., Kargel, J. S., Sasaki, S., Jinguo, Y., & Miyamoto, H. (2010). The sedimentology and dynamics of crater-affiliated wind streaks in western arabia terra, mars and patagonia, argentina. *Geomorphology*, *121*, 30 – 54. URL: http://www.sciencedirect.com/science/article/pii/S0169555X09003274. doi:http://dx.doi.org/10.1016/j.geomorph.2009.07.020. Planetary Dune Systems.

Roelof, E. C. (1987). Energetic neutral atom image of a storm-time ring current. Geophys. Res. Lett., *14*, 652–655. doi:10.1029/GL014i006p00652.

Roelof, E. C., Mitchell, D. G., & Williams, D. J. (1985). Energetic neutral atoms (E approximately 50 keV) from the ring current - IMP 7/8 and ISEE 1. J. Geophys. Res., *90*, 10991. doi:10.1029/JA090iA11p10991.

Rossi, A. P., Neukum, G., Pondrelli, M., van Gasselt, S., Zegers, T., Hauber, E., Chicarro, A., & Foing, B. (2008). Large-scale spring deposits on Mars? *Journal of Geophysical Research (Planets)*, *113*, 8016. doi:10.1029/2007JE003062.

Roth, L., Retherford, K. D., Saur, J., Strobel, D. F., Feldman, P. D., McGrath, M. A., & Nimmo, F. (2014a). Orbital apocenter is not a sufficient condition for HST/STIS detection of Europa's water vapor aurora. *Proceedings of the National Academy of Science*, (pp. 5123–E5132). doi:10.1073/pnas.1416671111.

Roth, L., Saur, J., Retherford, K. D., Strobel, D. F., Feldman, P. D., McGrath, M. A., & Nimmo, F. (2014b). Transient Water Vapor at Europa's South Pole. *Science*, (pp. 171–174). doi:10.1126/science.1247051.

Rothery, D., Marinangeli, L., Anand, M., Carpenter, J., Christensen, U., Crawford, I. A., De Sanctis, M. C., Epifani, E. M., Erard, S., Frigeri, A., Fraser, G., Hauber, E., Helbert, J., Hiesinger, H., Joy, K., Langevin, Y., Massironi, M., Milillo, A., Mitrofanov, I., Muinonen, K., Näränen, J., Pauselli, C., Potts, P., Warell, J., & Wurz, P. (2010). Mercury's surface and composition to be studied by BepiColombo. Planet. Space Sci., *58*, 21–39. doi:10.1016/j.pss.2008.09.001.

Rubin, M., Jia, X., Altwegg, K., Combi, M. R., Daldorff, L. K. S., Gombosi, T. I., Khurana, K., Kivelson, M. G., Tenishev, V. M., Tóth, G., Holst, B., & Wurz, P. (2015). Self-consistent multifluid MHD simulations of Europa's exospheric interaction with Jupiter's magnetosphere. *Journal of Geophysical Research (Space Physics)*, *120*, 3503–3524. doi:10.1002/2015JA021149.

Saur, J., Feldman, P. D., Roth, L., Nimmo, F., Strobel, D. F., Retherford, K. D., McGrath, M. A., Schilling, N., Gérard, J.-C., & Grodent, D. (2011). Hubble Space Telescope/Advanced Camera for Surveys Observations of Europa's Atmospheric Ultraviolet Emission at Eastern Elongation. ApJ, *738*, 153. doi:10.1088/0004-637X/738/2/153.

Saur, J., Strobel, D. F., & Neubauer, F. M. (1998). Interaction of the Jovian magnetosphere with Europa: Constraints on the neutral atmosphere. J. Geophys. Res., *103*, 19947–19962. doi:10.1029/97JE03556.

Schenk, P. M. (2002). Thickness constraints on the icy shells of the galilean satellites from a comparison of crater shapes. Nature, *417*, 419–421.

Schilling, N., Neubauer, F. M., & Saur, J. (2007). Time-varying interaction of Europa with the jovian magnetosphere: Constraints on the conductivity of Europa's subsurface ocean. Icarus, *192*, 41–55. doi:10.1016/j.icarus.2007.06.024.

Schilling, N., Neubauer, F. M., & Saur, J. (2008). Influence of the internally induced magnetic field on the plasma interaction of Europa. *Journal of Geophysical Research (Space Physics)*, *113*, 3203. doi:10.1029/2007JA012842.

Schmidt, R. M., & Housen, K. R. (1987). Some recent advances in the scaling of impact and explosion cratering. *International Journal of Impact Engineering*, *5*, 543–560.

Scholz, C. A., Karp, T., Brooks, K. M., Milkereit, B., Amoako, P. Y. O., & Arko, J. A. (2002). Pronounced central uplift identified in the Bosumtwi impact structure, Ghana, using multichannel seismic reflection data. *Geology*, *30*, 939. doi:10.1130/0091-7613(2002)030<0939:PCUIIT>2.0.CO;2.

Schubert, G., Spohn, T., & Reynolds, R. T. (1986). Thermal histories, compositions and internal structures of the moons of the solar system. In J. A. Burns, & M. S. Matthews (Eds.), *Satellites* (pp. 224–292).

Schultz, P. H. (1976). Floor-fractured lunar craters. *Moon*, *15*, 241–273. doi:10.1007/BF00562240.

Schultz, R. A. (1993). Brittle strength of basaltic rock masses with applications to Venus. J. Geophys. Res., *98*, 10883. doi:10.1029/93JE00691.

Schwenzer, S. P., Abramov, O., Allen, C. C., Clifford, S. M., Cockell, C. S., Filiberto, J., Kring, D. A., Lasue, J., McGovern, P. J., Newsom, H. E., Treiman, A. H., Vaniman, D. T., & Wiens, R. C. (2012). Puncturing Mars: How impact craters interact with the Martian cryosphere. *Earth and Planetary Science Letters*, *335*, 9–17. doi:10.1016/j.epsl.2012.04.031.

Schwenzer, S. P., & Kring, D. A. (2009). Impact-generated hydrothermal systems capable of forming phyllosilicates on Noachian Mars. *Geology*, *37*, 1091–1094. doi:10.1130/G30340A.1.

Seed, H. B., & Goodman, R. E. (1964). Earthquake stability of slopes of cohesionless soils. *Journal of the Soil Mechanics and Foundations Division*, *90*, 43–56.

Senft, L. E., & Stewart, S. T. (2009). Dynamic fault weakening and the formation of large impact craters. *Earth and Planetary Science Letters*, *287*, 471–482. doi:10.1016/j.epsl.2009.08.033.

Shemansky, D. E. (1987). Ratio of oxygen to sulfur in the Io plasma torus. J. Geophys. Res., *92*, 6141–6146. doi:10.1029/JA092iA06p06141.

Shemansky, D. E., Yung, Y. L., Liu, X., Yoshii, J., Hansen, C. J., Hendrix, A. R., & Esposito, L. W. (2014). A New Understanding of the Europa Atmosphere and Limits on Geophysical Activity. ApJ, *797*, 84. doi:10.1088/0004-637X/797/2/84.

Shematovich, V. I., Johnson, R. E., Cooper, J. F., & Wong, M. C. (2005). Surface-bounded atmosphere of Europa. Icarus, *173*, 480–498. doi:10.1016/j.icarus.2004.08.013.

Shirai, T., Tabata, T., & Tawara, T. (2001). Analytic cross sections for electron collisions with CO, CO_2, and H_2O relevant to edge plasma impurities. *Atomic Data and Nuclear Data Tables*, *79*, 143–184. URL: http://www.sciencedirect.com/science/article/pii/S0092640X01908666. doi:http://dx.doi.org/10.1006/adnd.2001.0866.

Sierks, H., Barbieri, C., Lamy, P. L., Rodrigo, R., Koschny, D., Rickman, H., Keller, H. U., Agarwal, J., AHearn, M. F., Angrilli, F., Auger, A.-T., Barucci, M. A., Bertaux, J.-L., Bertini, I., Besse, S., Bodewits, D., Capanna, C., Cremonese, G., Da Deppo, V., Davidsson, B., Debei, S., De Cecco, M., Ferri, F., Fornasier, S., Fulle, M., Gaskell, R., Giacomini, L., Groussin, O., Gutierrez-Marques, P., Gutirrez, P. J., Gttler, C., Hoekzema, N., Hviid, S. F., Ip, W.-H., Jorda, L., Knollenberg, J., Kovacs, G., Kramm, J. R., Khrt, E., Kppers, M., La Forgia, F., Lara, L. M., Lazzarin, M., Leyrat, C., Lopez Moreno, J. J., Magrin, S., Marchi, S., Marzari, F., Massironi, M., Michalik, H., Moissl, R., Mottola, S., Naletto, G., Oklay, N., Pajola, M.,

Pertile, M., Preusker, F., Sabau, L., Scholten, F., Snodgrass, C., Thomas, N., Tubiana, C., Vincent, J.-B., Wenzel, K.-P., Zaccariotto, M., & Ptzold, M. (2015). On the nucleus structure and activity of comet 67p/churyumov-gerasimenko. *Science*, *347*. URL: http://www.sciencemag.org/content/347/6220/aaa1044.abstract. doi:10.1126/science.aaa1044. arXiv:http://www.sciencemag.org/content/347/6220/aaa1044.full.pdf.

Sierks, H., Lamy, P., Barbieri, C., Koschny, D., Rickman, H., Rodrigo, R., A'Hearn, M. F., Angrilli, F., Barucci, M. A., Bertaux, J.-L., Bertini, I., Besse, S., Carry, B., Cremonese, G., Da Deppo, V., Davidsson, B., Debei, S., De Cecco, M., De Leon, J., Ferri, F., Fornasier, S., Fulle, M., Hviid, S. F., Gaskell, R. W., Groussin, O., Gutierrez, P., Ip, W., Jorda, L., Kaasalainen, M., Keller, H. U., Knollenberg, J., Kramm, R., Kührt, E., Küppers, M., Lara, L., Lazzarin, M., Leyrat, C., Moreno, J. J. L., Magrin, S., Marchi, S., Marzari, F., Massironi, M., Michalik, H., Moissl, R., Naletto, G., Preusker, F., Sabau, L., Sabolo, W., Scholten, F., Snodgrass, C., Thomas, N., Tubiana, C., Vernazza, P., Vincent, J.-B., Wenzel, K.-P., Andert, T., Pätzold, M., & Weiss, B. P. (2011). Images of Asteroid 21 Lutetia: A Remnant Planetesimal from the Early Solar System. *Science*, *334*, 487–. doi:10.1126/science.1207325.

Sittler, E. C., Cooper, J. F., Hartle, R. E., Paterson, W. R., Christian, E. R., Lipatov, A. S., Mahaffy, P. R., Paschalidis, N. P., Coplan, M. A., Cassidy, T. A., Richardson, J. D., Fegley, B., & Andre, N. (2013). Plasma ion composition measurements for Europa. Planet. Space Sci., *88*, 26–41. doi:10.1016/j.pss.2013.01.013.

Sittler, E. C., & Strobel, D. F. (1987). Io plasma torus electrons - Voyager 1. J. Geophys. Res., *92*, 5741–5762. doi:10.1029/JA092iA06p05741.

Smith, B. A., Soderblom, L. A., Beebe, R., Boyce, J., Briggs, G., Carr, M., Collins, S. A., Johnson, T. V., Cook, A. F., II, Danielson, G. E., & Morrison, D. (1979a). The Galilean satellites and Jupiter - Voyager 2 imaging science results. *Science*, *206*, 927–950. doi:10.1126/science.206.4421.927.

Smith, B. A., Soderblom, L. A., Johnson, T. V., Ingersoll, A. P., Collins, S. A., Shoemaker, E. M., Hunt, G. E., Masursky, H., Carr, M. H., Davies, M. E., Cook, A. F., Boyce, J. M., Owen, T., Danielson, G. E., Sagan, C., Beebe, R. F., Veverka, J., McCauley, J. F., Strom, R. G., Morrison, D., Briggs, G. A., & Suomi, V. E. (1979b). The Jupiter system through the eyes of Voyager 1. *Science*, *204*, 951–957. doi:10.1126/science.204.4396.951.

Smith-Konter, B., & Pappalardo, R. T. (2008). Tidally driven stress accumulation and shear failure of Enceladus's tiger stripes. Icarus, *198*, 435–451. doi:10.1016/j.icarus.2008.07.005.

Smyth, W. H., & Marconi, M. L. (2006). Europa's atmosphere, gas tori, and magnetospheric implications. Icarus, *181*, 510–526. doi:10.1016/j.icarus.2005.10.019.

Sohl, F., Spohn, T., Breuer, D., & Nagel, K. (2002). Implications from Galileo Observations on the Interior Structure and Chemistry of the Galilean Satellites. Icarus, *157*, 104–119. doi:10.1006/icar.2002.6828.

Spaun, N. A., Head, J. W., III, Pappalardo, R. T., & Galileo SSI Team (1999). Chaos and Lenticulae on Europa: Structure, Morphology and Comparative Analysis. In *Lunar and Planetary Science Conference*. volume 30 of *Lunar and Planetary Inst. Technical Report*.

Spencer, J. R., Pearl, J. C., Segura, M., Flasar, F. M., Mamoutkine, A., Romani, P., Buratti, B. J., Hendrix, A. R., Spilker, L. J., & Lopes, R. M. C. (2006). Cassini Encounters Enceladus: Background and the Discovery of a South Polar Hot Spot. *Science*, *311*, 1401–1405. doi:10.1126/science.1121661.

Spohn, T., & Schubert, G. (2003). Oceans in the icy Galilean satellites of Jupiter? Icarus, *161*, 456–467. doi:10.1016/S0019-1035(02)00048-9.

Spray, J. G., & Thompson, L. M. (1995). Friction melt distribution in a multi-ring impact basin. Nature, *373*, 130–132. doi:10.1038/373130a0.

Spudis, P. D., & Guest, J. E. (1988). Stratigraphy and geologic history of Mercury. In F. Vilas, C. R. Chapman, & M. S. Matthews (Eds.), *Mercury, University of Arizona Press* (pp. 118–164).

Spudis, P. D., Hawke, B. R., & Lucey, P. (1984). Composition of Orientale basin deposits and implications for the lunar basin-forming process. J. Geophys. Res., *89*, 197. doi:10.1029/JB089iS01p0C197.

Steffl, A. J., Bagenal, F., & Stewart, A. I. F. (2004). Cassini UVIS observations of the Io plasma torus. II. Radial variations. Icarus, *172*, 91–103. doi:10.1016/j.icarus.2004.04.016. arXiv:1301.3813.

Straub, H. C., Renault, P., Lindsay, B. G., Smith, K. A., & Stebbings, R. F. (1996). Absolute partial cross sections for electron-impact ionization of H_2, N_2, and O_2 from threshold to 1000 eV. Phys. Rev. A, *54*, 2146–2153. doi:10.1103/PhysRevA.54.2146.

Strom, R. G., Trask, N. J., & Guest, J. E. (1975). Tectonism and volcanism on Mercury. J. Geophys. Res., *80*, 2478–2507. doi:10.1029/JB080i017p02478.

Tanaka, K. L., Robbins, S. J., Fortezzo, C. M., Skinner, J. A., & Hare, T. M. (2014). The digital global geologic map of Mars: Chronostratigraphic ages, topographic and crater morphologic characteristics, and updated resurfacing history. Planet. Space Sci., *95*, 11–24. doi:10.1016/j.pss.2013.03.006.

Tawara, H., Kato, T., & Nakai, Y. (1985). Cross Sections for Electron Capture and Loss by Positive Ions in Collisions with Atomic and Molecular Hydrogen. *Atomic Data and Nuclear Data Tables*, *32*, 235. doi:10.1016/0092-640X(85)90007-5.

Taylor, G. J., Martel, L. M. V., Karunatillake, S., Gasnault, O., & Boynton, W. V. (2010). Mapping Mars geochemically. *Geology*, *38*, 183–186. doi:10.1130/G30470.1.

Teolis, B. D., Niemann, H. B., Waite, J. H., Gell, D. A., Perryman, R. S., Kasprzak, W. T., Mandt, K. E., Yelle, R. V., Lee, A. Y., Pelletier, F. J., Miller, G. P., Young, D. T., Bell, J. M., Magee, B. A., Patrick, E. L., Grimes, J., Fletcher, G. G., & Vuitton, V. (2015). A

Revised Sensitivity Model for Cassini INMS: Results at Titan. Space Sci. Rev., . doi:10.1007/s11214-014-0133-8.

Thomas, N., Sierks, H., Barbieri, C., Lamy, P. L., Rodrigo, R., Rickman, H., Koschny, D., Keller, H. U., Agarwal, J., A'Hearn, M. F., Angrilli, F., Auger, A.-T., Barucci, M. A., Bertaux, J.-L., Bertini, I., Besse, S., Bodewits, D., Cremonese, G., Da Deppo, V., Davidsson, B., De Cecco, M., Debei, S., El-Maarry, M. R., Ferri, F., Fornasier, S., Fulle, M., Giacomini, L., Groussin, O., Gutierrez, P. J., Gttler, C., Hviid, S. F., Ip, W.-H., Jorda, L., Knollenberg, J., Kramm, J.-R., Khrt, E., Kppers, M., La Forgia, F., Lara, L. M., Lazzarin, M., Moreno, J. J. L., Magrin, S., Marchi, S., Marzari, F., Massironi, M., Michalik, H., Moissl, R., Mottola, S., Naletto, G., Oklay, N., Pajola, M., Pommerol, A., Preusker, F., Sabau, L., Scholten, F., Snodgrass, C., Tubiana, C., Vincent, J.-B., & Wenzel, K.-P. (2015). The morphological diversity of comet 67p/churyumov-gerasimenko. *Science*, *347*. URL: http://www.sciencemag.org/content/347/6220/aaa0440.abstract. doi:10.1126/science.aaa0440. arXiv:http://www.sciencemag.org/content/347/6220/aaa0440.full.pdf.

Thomas, P. C., Veverka, J., Robinson, M. S., & Murchie, S. (2001). Shoemaker crater as the source of most ejecta blocks on the asteroid 433 Eros. Nature, *413*, 394–396. doi:10.1038/35096513.

Thomas, R. J., Lucchetti, A., Cremonese, G., Rothery, D. A., Massironi, M., Re, C., Conway, S. J., & Anand, M. (2015). A cone on Mercury: Analysis of a residual central peak encircled by an explosive volcanic vent. Planet. Space Sci., *108*, 108–116. doi:10.1016/j.pss.2015.01.005.

Thomas, R. J., Rothery, D. A., Conway, S. J., & Anand, M. (2014). Mechanisms of explosive volcanism on Mercury: Implications from its global distribution and morphology. *Journal of Geophysical Research (Planets)*, *119*, 2239–2254. doi:10.1002/2014JE004692.

Thompson, S. L., & Lauson, H. S. (1972). *Improvements in the CHART-D radiation-hydrodynamic code III: Revised analytical equation of state.*. Sandia National Laboratories, Report SC-RR-710714.

Tibaldi, A. (1995). Morphology of pyroclastic cones and tectonics. J. Geophys. Res., *100*, 24. doi:10.1029/95JB02250.

Tillotson, J. (1962). *Metallic Equations of State for Hypervelocity Impact*. General Atomic, Division of General Dynamics, John Jay Hopkins Laboratory for Pure and Applied Science, Report GA-3216. URL: http://books.google.it/books?id=fX81ygAACAAJ.

Turner, B. R., & Rutherford, J. A. (1968). Charge transfer and ion-atom interchange reactions of water vapor ions. J. Geophys. Res., *73*, 6751–6758. doi:10.1029/JA073i021p06751.

Urrutia Fucugauchi, J., & Pérez Cruz, L. (2009). Multiring-forming large bolide impacts and evolution of planetary surfaces. *International Geology Review*, .

van de Hulst, H. C. (1957). *Light Scattering by Small Particles*.

Vance, D. W., & Bailey, T. L. (1966). Inelastic Collisions of H^+_2 and N^+_2 Ions with Hydrogen Molecules. J. Chem. Phys., *44*, 486–493. doi:10.1063/1.1726714.

Vincent, J.-B., Bodewits, D., Besse, S., Sierks, H., Barbieri, C., Lamy, P., Rodrigo, R., Koschny, D., Rickman, H., Keller, H. U., Agarwal, J., A'Hearn, M. F., Auger, A.-T., Barucci, M. A., Bertaux, J.-L., Bertini, I., Capanna, C., Cremonese, G., da Deppo, V., Davidsson, B., Debei, S., de Cecco, M., El-Maarry, M. R., Ferri, F., Fornasier, S., Fulle, M., Gaskell, R., Giacomini, L., Groussin, O., Guilbert-Lepoutre, A., Gutierrez-Marques, P., Gutiérrez, P. J., Güttler, C., Hoekzema, N., Höfner, S., Hviid, S. F., Ip, W.-H., Jorda, L., Knollenberg, J., Kovacs, G., Kramm, R., Kührt, E., Küppers, M., La Forgia, F., Lara, L. M., Lazzarin, M., Lee, V., Leyrat, C., Lin, Z.-Y., Lopez Moreno, J. J., Lowry, S., Magrin, S., Maquet, L., Marchi, S., Marzari, F., Massironi, M., Michalik, H., Moissl, R., Mottola, S., Naletto, G., Oklay, N., Pajola, M., Preusker, F., Scholten, F., Thomas, N., Toth, I., & Tubiana, C. (2015). Large heterogeneities in comet 67P as revealed by active pits from sinkhole collapse. Nature, *523*, 63–66. doi:10.1038/nature14564.

Vincent, J. B., Oklay, N., Marchi, S., Hoefner, S., & Sierksl, H. (2014). Craters on comets. Planet. Space Sci., .

Wahlberg Jansson, K., & Johansen, A. (2014). Formation of pebble-pile planetesimals. A&A, *570*, A47. doi:10.1051/0004-6361/201424369. arXiv:1408.2535.

Waite, J. H., Combi, M. R., Ip, W.-H., Cravens, T. E., McNutt, R. L., Kasprzak, W., Yelle, R., Luhmann, J., Niemann, H., Gell, D., Magee, B., Fletcher, G., Lunine, J., & Tseng, W.-L. (2006). Cassini Ion and Neutral Mass Spectrometer: Enceladus Plume Composition and Structure. *Science*, *311*, 1419–1422. doi:10.1126/science.1121290.

Watanabe, N., Horii, T., & Kouchi, A. (2000). Measurements of D_2 Yields from Amorphous D_2O Ice by Ultraviolet Irradiation at 12 K. ApJ, *541*, 772–778. doi:10.1086/309458.

Weider, S. Z., Nittler, L. R., Starr, R. D., McCoy, T. J., Stockstill-Cahill, K. R., Byrne, P. K., Denevi, B. W., Head, J. W., & Solomon, S. C. (2012). Chemical heterogeneity on Mercury's surface revealed by the MESSENGER X-Ray Spectrometer. *Journal of Geophysical Research (Planets)*, *117*, 0. doi:10.1029/2012JE004153.

Wieczorek, M. A., Neumann, G. A., Nimmo, F., Kiefer, W. S., Taylor, G. J., Melosh, H. J., Phillips, R. J., Solomon, S. C., Andrews-Hanna, J. C., Asmar, S. W., Konopliv, A. S., Lemoine, F. G., Smith, D. E., Watkins, M. M., Williams, J. G., & Zuber, M. T. (2013). The Crust of the Moon as Seen by GRAIL. *Science*, *339*, 671–675. doi:10.1126/science.1231530.

Wieczorek, M. A., & Phillips, R. J. (1999). Lunar Multiring Basins and the Cratering Process. Icarus, *139*, 246–259. doi:10.1006/icar.1999.6102.

Wilson, L., & Head, J. W. (1981). Ascent and eruption of basaltic magma on the earth and moon. J. Geophys. Res., *86*, 2971–3001. doi:10.1029/JB086iB04p02971.

Wilson, L., Head, J. W., & Pappalardo, R. T. (1997). Eruption of lava flows on Europa: Theory and application to Thrace Macula. J. Geophys. Res., *102*, 9263–9272. doi:10.1029/97JE00412.

Wilson, L., Head, J. W., & Tye, A. R. (2014). Lunar Regional Pyroclastic Deposits: Evidence for Eruption from Dikes Emplaced into the Near-Surface Crust. In *Lunar and Planetary Science Conference* (p. 1223). volume 45 of *Lunar and Planetary Science Conference*.

Wilson, L., Sparks, R. S. J., & Walker, G. P. L. (1980). Explosive volcanic eruptions ? IV. The control of magma properties and conduit geometry on eruption column behaviour. *Geophysical Journal*, *63*, 117–148. doi:10.1111/j.1365-246X.1980.tb02613.x.

Worthington, A. (1963). *A study of splashes: Including his 1894 lecture: The splash of a drop and allied phenomena*. Macmillan. URL: https://books.google.ch/books?id=JxJRAAAAMAAJ.

Wray, J. J., Hansen, S. T., Dufek, J., Swayze, G. A., Murchie, S. L., Seelos, F. P., Skok, J. R., Irwin, R. P., & Ghiorso, M. S. (2013). Prolonged magmatic activity on Mars inferred from the detection of felsic rocks. *Nature Geoscience*, *6*, 1013–1017. doi:10.1038/ngeo1994.

Wuennemann, K., Collins, G., & Osinski, G. (2008). Numerical modelling of impact melt production in porous rocks. *Earth and Planetay Science Letters*, *269*, 529–538. URL: http://dx.doi.org/10.1016/j.epsl.2008.03.007. doi:10.1016/j.epsl.2008.03.007.

Wünnemann, K., Collins, G. S., & Melosh, H. J. (2006). A strain-based porosity model for use in hydrocode simulations of impacts and implications for transient crater growth in porous targets. *Icarus*, *180*, 514–527. doi:10.1016/j.icarus.2005.10.013.

Wünnemann, K., & Ivanov, B. A. (2003). Numerical modelling of the impact crater depth-diameter dependence in an acoustically fluidized target. *Planetary and Space Science*, *51*, 831–845. doi:10.1016/j.pss.2003.08.001.

Yoon, J.-S., Song, M.-Y., Han, J.-M., Hwang, S. H., Chang, W.-S., Lee, B., & Itikawa, Y. (2008). Cross Sections for Electron Collisions with Hydrogen Molecules. *Journal of Physical and Chemical Reference Data*, *37*, 913–931. doi:10.1063/1.2838023.

Zimmer, C., Khurana, K. K., & Kivelson, M. G. (2000). Subsurface Oceans on Europa and Callisto: Constraints from Galileo Magnetometer Observations. Icarus, *147*, 329–347. doi:10.1006/icar.2000.6456.

Zolotov, M. Y. (2011). On the chemistry of mantle and magmatic volatiles on Mercury. Icarus, *212*, 24–41. doi:10.1016/j.icarus.2010.12.014.

Zuber, M. T., Smith, D. E., Solomon, S. C., Muhleman, D. O., Head, J. W., Garvin, J. B., Abshire, J. B., & Bufton, J. L. (1992). The Mars Observer laser altimeter investigation. J. Geophys. Res., *97*, 7781–7797. doi:10.1029/92JE00341.